BIOGEOCHEMISTRY OF MEROMICTIC PIT LAKES AND PERMEABLE REACTIVE BARRIERS AT THE CLUFF LAKE URANIUM MINE

by

Konstantin Von Gunten

A thesis submitted in partial fulfillment of the requirements for the degree of

Doctor of Philosophy

Department of Earth and Atmospheric Sciences
University of Alberta

ABSTRACT

Mining generates not only vast amounts of waste rock and tailings but is also responsible for far-reaching contamination of soil, groundwater, and surface water, which often requires remediation. This thesis focused on the biogeochemistry of two types of remediation technologies applied at the decommissioned Cluff Lake uranium (U) mine in Northern Saskatchewan.

The first remediation technique is pit lakes from open-pit mining operations. Pits created by mining are left to flood with surface and groundwater to prevent excessive oxidation of exposed rocks and release of contaminants. At Cluff Lake, two such pits exist, the older D-pit and the younger DJX-pit, which are geochemically different. The pits are contaminated with U, arsenic (As), and nickel (Ni) and were previously described as meromictic. It was found that in the D-pit, meromixis stability, pH conditions, and contaminant distribution were controlled by Fe cycling. In the DJX-pit, two chemoclines were characterized, both being linked to sharp U and Ni concentration gradients. Meromixis was stabilized by calcium (Ca) carbonate dissolution and precipitation. It was found that aluminum oxyhydroxide colloids might play an important role in contaminant removal.

The role of colloids in contaminant sequestration and their accumulation in sediments was further investigated. The most common colloidal particles found in the pits consisted of Ca-O, Fe-O, and Ca-S-O. A high abundance of metals was found in colloidal fractions, especially in aged samples, suggesting that colloids can act as metal accumulators. With the help of sediment traps, the precipitation of Fe-O, Fe-S, Al-Si, and Ce-P phases, with traces of U and Ni, was demonstrated. The stability of metals in bottom sediment followed the order Ni<U<As. U-bearing phases confirmed by spectroscopy and diffraction, such as vandendriesscheite and monazite, were found to increase the overall U stability. Sediment chemistry was the primary driver for microbial community composition in the sediments, with low species richness and diversity in deeper and more contaminated sediments. The meromictic pit lakes were found to be an efficient remediation method, but future development of the pits need to be monitored to assure ongoing remediation success and to prevent the release of sequestered contaminants.

The second remediation technology was a permeable reactive barrier (PRB). Two such barriers, made of peat, gravel, lime, and limestone, were installed in a mining-affected wetland. Previously installed groundwater wells allowed an in-depth analysis of groundwater passing through the first PRB. Both PRBs were effective in removing U, Cu, and Zn from groundwater but were less efficient for Ni and Co. In the alkaline environment of the PRB, significant portions of Ni, Co, Cu, U, and Fe were associated with colloids, while in the more acidic environments of the surrounding wetland, ionic species and complexes dominated. The presence of colloidal fractions favored the removal of Cu and U, which were found to more strongly bind to the solid phase, suggesting ongoing metal sequestration processes. Uranium removal was further enhanced by chemical and biological U(VI) reduction in the oxygen-depleted conditions of the PRBs. The less efficient removal of Ni and Co, being major target metals, was explained by their high solubility, their limited association with colloids, and unfavorable redox and pH conditions created by the alkaline PRBs, considerations that are critical in the design of future PRBs for the remediation of similar systems.

The biogeochemical approach used in this thesis was found suitable to investigate the role of elemental cycling, contaminant mobilization, and the role of microorganisms to assess the efficiency of two common remediation techniques for mining sites in northern Canada. While meromixis was found to be effective in stabilizing contaminants in the pit lakes, any perturbation of this delicate system, such as acid generation, could compromise its performance. This study demonstrated how important it is to properly design a permeable reactive barrier. Chemical incompatibilities (e.g., inappropriate pH conditions for sulfide precipitation), unreactive carbon sources, and issues arising during the scale-up of barrier systems could lead to underperformance and ineffectiveness of the technology in removing target compounds from groundwater. The results from this work could provide an important toolset to assess the suitability of remediation techniques for similar mining sites and to evaluate potential risks with regard to changing environmental conditions, which could affect their performance.

PREFACE

Since its discovery, uranium became an important resource. It developed a somewhat bad reputation in the general public due to its radioactivity, its history of being a critical component for the manufacturing of nuclear weapons and its more recent use in depleted uranium projectiles used by various militaries. It is, however, an important metal for Canada's and world's economy due to its indispensable use as a supplier of energy. This function generates other problems, much less known to the public, namely the contamination of the environment caused by uranium mining. As with all mining activities, when U is mined, geological material is exposed to the surface conditions, e.g., humidity, temperature changes, and physical stress, which lead to its oxidation and dissolution of metals (e.g., U, Pb, Ni, Co) and metalloids (e.g., As, Se, Sb) from the rock, leading to a phenomenon known as acid mine drainage. In such way, contaminants can reach surface- and groundwater, soil and air, with imminent contact to organisms causing toxicity effects and disrupting surface biogeochemical cycles. Where a legal framework exists and where financial means and skilled workers are available, such contamination can be mitigated with remediation (clean-up operations) and reclamation (return of the landscape to its original state) techniques, which can be very successful or sometimes fail due to lack of diligence or unexpected outcomes.

This thesis deals with two types of remediation technologies and investigates associated biogeochemical cycles in a decommissioned uranium mine at Cluff Lake. The first remediation technique is pit lakes, which are created after open pit mines are flooded. The idea behind such lakes is the formation of a meromictic water body, in which the deeper water does not seasonally mix with the surface water, a feature that allows isolating deeper, contaminated water from shallow water that might come in contact with flora and fauna.

The second remediation technique is permeable reactive barriers, which are generally used to treat contaminated groundwater. Reactive medium (e.g., zerovalent iron, lime, organic material) is buried in the flow path of an affected groundwater plume, so that contaminants in the water can react with it. This required the medium to be highly permeable, to not impede the groundwater flow and additionally the medium has to be properly chosen based on the contaminant.

This thesis consists of four chapters. The first chapter is an introduction to uranium biogeochemistry and mining and to the field site investigated in this thesis, the Cluff Lake uranium mine. Each of the following chapters focused on a certain biogeochemical aspect of the Cluff Lake decommissioning and remediation activities. All projects were supervised by Kurt Konhauser and Daniel Alessi.

The second chapter focuses on the aqueous biogeochemistry of two pit lakes at Cluff Lake. This chapter was published in the Canadian Journal of Earth Sciences, 55(5):463-474 (National Research Council Research Press) with the co-authors Tyler Warchola, Mark Donner, Manuel Cossio, Weiduo Hao,

Christopher Boothman, Jonathan Lloyd, Tariq Siddique, Camille Partin, Shannon Flynn, Arden Rosaasen, Kurt Konhauser and Daniel Alessi. Tyler Warchola performed Fe(II)/Fe(III) analyzes, Mark Donner analyzed As and Se speciation under the supervision of Tariq Siddique, Manuel Cossio assisted during field work, Weiduo Hao provided support during sample processing and assisted in gathering necessary historical information, Christopher Boothman and Jonathan Lloyd assisted with the DNA extractions from water samples, sequencing 16S rRNA genes and the bioinformatics. Camille Partin assisted in gathering necessary geological background information, Shannon Flynn assisted during ICP-MS analyzes of water samples and Arden Rosaasen provided historical monitoring records and pit lake models.

The third chapter focuses on the sediments and colloids biogeochemistry in the two pit lakes at Cluff Lake. This chapter was submitted to the Geochmica et Cosmochimica Acta (Elsevier) with the co-authors Brendan Bishop, Isabel Plata-Enriquez, Samrat Alam, Peter Blanchard, Leslie Robbins, Renfei Feng, Kurt Konhauser, and Daniel Alessi. Brendan Bishop assisted during field work and sample processing, Isabel Plata-Enriquez assisted during sequential extractions of sediment samples, Samrat Alam, Peter Blanchard, Leslie Robbins, and Renfei Fend assisted during synchrotron-based analyzes.

The fourth chapter focuses on the biogeochemistry of two permeable reactive barriers near the Cluff Lake mine. This chapter was submitted to the Journal of Geophysical Research - Biogeosciences with the co-authors Brendan Bishop, Samrat Alam, Luyu Zhang, Karlis Muehlenbachs, Kurt Konhauser, and Daniel Alessi. Brendan Bishop assisted during field work and sample processing; Luyu Zhang performed soil incubations and gas measurements under the supervision of Samrat Alam and Konstantin von Gunten. Karlis Muehlenbachs provided isotopic gas results.

Methods that were developed in the frame of this thesis were also used in other projects that are not part of this thesis. Digestion and sequential extraction methods used in Chapters 2-4 were modified to cope with highly organic samples and were used to analyze the metal speciation in biochar and asphalt. Those projects yielded the following publications:

- von Gunten, K., Alam, M.S., Hubmann, M., Ok, Y.S., Konhauser, K.O., and Alessi, D.S., 2017. Modified sequential extraction for biochar and petroleum coke: Metal release potential and its environmental implications. Bioresource Technology, 236, 106-110.
- von Gunten, K., Konhauser, K.O., and Alessi, D.S. Potential of asphalt concrete as a source of trace metals. Revision submitted to Environmental Geochemistry and Health.

Bioinformatics methods used in Chapters 3-4 were previously tested and used on forest soils in Ontario to characterize the microbiology of so-called “forest rings”. Furthermore, they were applied for another project investigating the effects of biochar on ferralsols of the Atlantic forest in Brazil. Those projects yielded the following publications:

- von Gunten, K., Hamilton, S.M., Zhong, C., Nesbø, C., Li, J., Muehlenbachs, K., Konhauser, K.O., and Alessi, D.S., 2018. Electron donor-driven bacterial and archaeal community patterns along forest ring edges in Ontario, Canada. Environmental Microbiology Reports, 10(6): 663-672.
- von Gunten, K., Hubmann, M., Ineichen, R., Gao, Y., Konhauser, K.O., Alessi, D.S. Biochar-induced changes in metal mobility and uptake by perennial plants in a ferralsol of Brazil's Atlantic forest. Biochar, 2, preprint.

ACKNOWLEDGMENTS

Foremost, I would like to thank my academic supervisors Daniel Alessi and Kurt Konhauser for supporting me in completing the projects for this thesis. Their open-mindedness and their willingness to explore new fields allowed me to dive into many different research aspects and collaborate with many researchers, companies and institutions.

Orano Canada Inc. (formerly AREVA Resources Canada), supported the projects by providing historical data, facilitating site access, helping in organizing on-site lodging and by providing safety equipment. Great thanks in this regard go to Arden Rosaasen, Kebbi Hughes, and Sarah Benson. Canada North Environmental Services Limited Partnership (CanNorth) helped by providing sampling equipment. Special thanks go to Jocelyn Howery. The work at the Canadian Light Source was supported financially by CLS travel awards to Samrat Alam, Leslie Robbins, and Konstantin von Gunten. Scientific and technical support was provided by the VESPERS team. Special thanks go to Peter Blanchard.

Christopher Boothman and Jonathan Lloyd provided initial microbiological data for the Cluff Lake pit lakes (water and sediments), which helped me to develop my own method applied in this thesis. Stable isotopes of water and carbon were analyzed by Casey Buchanan, Duane Froese, Olga Levner, and Karlis Muehlenbachs. Tariq Siddique kindly provided his equipment for the analysis of water and gases and Alsu Kuznetsova provided the corresponding training. Mark Donner helped in analyzing the oxidation states of arsenic and selenium. Brendan Bishop and Manuel Cossio were a big help in the field during the campaigns in 2016-2018.

Further scientific advice and support were provided by Isabel Plata-Enriquez, Tyler Warchola, Samrat Alam, Salman Safari, Luzu Zhang, Katherine Snihur, Camille Partin, Shannon Flynn, Camilla Nesbø, Katie Nichols, Chad Cuss, Gabrielle Dublet, Alexandre Bagnoud, Weiduo Hao, Neil MacPherson, Cheng Zhong, Guangcheng Chen, Nathan Gerein, Andrew Locock, Renfei Feng and Allan Harms. I highly appreciate the support of other members of the Alessi and Konhauser research groups. Big thanks go to my friends and family and especially to my partner Magdalena Hubmann, who not only motivated me to do this work but also gave valuable scientific advices.

Financial support for the projects in this thesis was mainly provided by the Natural Sciences and Engineering Research Council of Canada (NSERC) grants to Daniel Alessi and Kurt Konhauser (RGPIN-04134, RGPIN-165831, EGP 511159-17), and by a 2015-2016 Ashley and Janet Cameron Research and Education Seed Fund grant to Daniel Alessi. UAlberta North provided research awards to Tyler Warchola (2016-2017) and Konstantin von Gunten (2018-2019). Travel Awards from the Ashley and Janet Cameron Fund, the Graduate Student Association and the Faculty of Graduate Studies and Research allowed me to travel to international conferences and to present my work.

TABLE OF CONTENTS

LIST OF TABLES

LIST OF FIGURES

LIST OF ABBREVIATIONS

AF4 – Assymetrical Flow Field Flow Fractionnation

BTEX – Benzene, Toluene, Ethylbenzene, and Xylene

CLS – Canadian Light Source

DMA – Dimethylated Arsenic

DSWQO – Decommissioning Surface Water Quality Objectives

EDS – Energy-dispersive X-ray Spectroscopy

IC – Ion Chromatography

ICP-MS – Inductively Coupled Plasma Mass Spectometry

MMA – Monomethylated Arsenic

NAPL – Non-aqueous phase liquids

PRB – Permeable Reactive Barrier

rRNA – Ribosomal Ribonucleic Acid

S/TEM – Scanning Transmission Electron Microscopy

SEM – Scanning Electron Microscopy

TIC – Total Inorganic Carbon

TN – Total Nitrogen

TOC – Total Organic Carbon

VESPERS – Very Sensitive Elemental and Structural Probe Employing Radiation from a Synchrotron

XANES – X-ray Absorption Near Edge Spectroscopy

XAS – X-ray Absorption Spectroscopy

XRD – X-ray diffraction

XRF – X-ray fluorescence

ZVI – Zerovalent Iron

1 INTRODUCTION

1.1 Overview

This thesis focuses on the post-decommissioning biogeochemistry of U at the Cluff Lake mine, and its co-occurring contaminants As and Ni. The introduction given here provides both, background information on the biogeochemistry of U, as well as an overview on uranium mining techniques targeted deposits. To provide context for the research studies, the environmental importance of colloids is reviewed and an introduction to meromictic pit lakes, permeable reactive barriers, both remediation techniques discussed in this thesis, is given. In the final part, the Cluff Lake field site is introduced and important historical monitoring information is summarized.

1.2 Uranium biogeochemistry

1.2.1 Uranium systematics

Uranium has an average concentration in the crust of approximately 2.8 ppm, which makes this element more abundant than gold or silver (Taylor, 1964). In seawater, U is more abundant than Cu, Ni or Zn, with concentrations approximating 3.3 µg/L, while in rivers, it is much less abundant with typical concentrations below 0.3 µg/L (Ku *et al.*, 1977). Uranium has three long-lived isotopes, ^{234}U, ^{235}U and ^{238}U, with a natural distribution of approximately 0.000055:0.00725:1, and half-lives that range from 250 thousand to 4.5 billion years (Richter *et al.*, 1999).

Uranium in the environment usually exists as U(IV) or U(VI) species, which exhibit different aqueous mobilities. U(IV) is sparingly soluble and is often present as the mineral uraninite (isometric UO_2, low water content) or pitchblende (massive amorphous UO_2, high water content), which are often mined as primary sources of U. It is also found as non-crystalline U(IV) species in association with mineral and microbial surfaces, and as colloids (Wang *et al.*, 2013; Alessi *et al.*, 2014a). U(VI), on the other hand, is mobile and bioavailable. At all pH values, U(VI) exists as a free uranyl cation (UO_2^{2+}) or forms mononuclear complexes (e.g., UO_2OH^+) at low U concentrations ($<10^{-8}$ M) or polynuclear species (e.g., $(UO_2)_3(OH)_5^+$) at higher concentrations (Kumar *et al.*, 2011). As shown in Figure 1.1, in most terrestrial natural systems (pH 6-7) U(VI) species are dominated by strong and soluble carbonate complexes, such as $UO_2CO_3^0$ or $UO_2(CO_3)_2^{2-}$ (Newsome *et al.*, 2014a). U(VI) can also form relatively soluble U(VI)-bearing minerals, such as schoepite or meta-schoepite (Wang *et al.*, 2016).

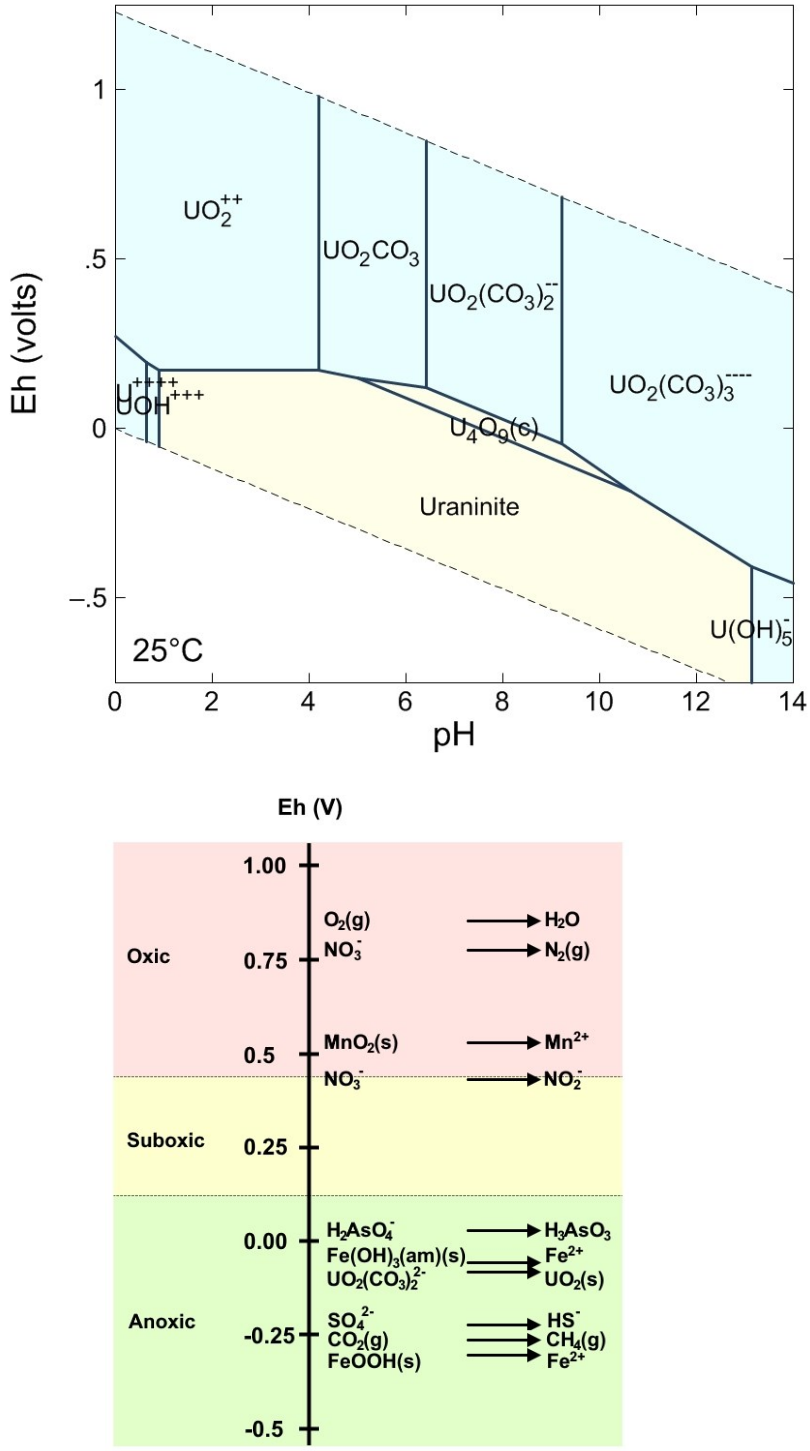

Figure 1.1: (Top) Eh-pH diagram for U under typical surface conditions. Diagram created at standard conditions using the Geochemist's Workbench edition 12.0 with a[U]=10^{-8} M, a[HCO_3^-]=$10^{-3.5}$ M. (Bottom) A typical Eh ladder at pH 7 showing the positions of As and U redox couples in relation to others (modified from Borch et al., 2010)

The transition between U(IV) and U(VI) redox states, and corresponding changes in solubility can be influenced by numerous processes. Uranium can be transformed into less soluble U(IV) via its reduction

by ferrous iron (Fe^{2+}), sulfide (HS^-), various organic compounds, and by microorganisms employing metabolisms related to dissimilatory Fe(III) and sulfate reduction coupled to organic matter or hydrogen oxidation (Borch *et al.*, 2010). U(VI) can even be reduced by inactive spores (Dalla Vecchia *et al.*, 2010). U(IV), on the other hand, can be abiotically oxidized to U(VI) by oxygen (O_2), nitrate (NO_3^-), ferric iron (Fe^{3+}), and manganese oxide (MnO_2), and biotically by denitrifying bacteria (Figure 1.1, Borch *et al.*, 2010). The latter was demonstrated with the denitrifying *Thiobacillus denitrificans*, however the process is not fully understood (Beller, 2005). Therefore, the exposure of mined U to atmospheric conditions creates soluble and highly mobile U(VI) species that promote its transport in the broader environment.

1.2.2 Uranium mining: history and importance

Despite controversies surrounding its mining and use, U remains one of the most important energy resources of the modern world, delivering about 10% (over 2600 TWh) of the global demand for electricity in 2017 (IEA, 2018b) and its importance is expected to stay the same in the coming decades (Table 1.1). By 2017, the leader in U production was Kazakhstan, with 39% of the overall production, followed by Canada with 22% (World Nuclear Association, 2018b).

Table 1.1: Electricity production by source and major producers (IEA, 2018a/b).

Electricity source	Production	Major electricity producers 2016
Coal	38%	China, USA, India
Oil	4%	Saudi Arabia, Japan, Iraq
Gas	23%	USA, Russia, Japan
Nuclear	10%	USA, France, China
Renewables	32%	China, USA, Brazil
Others	3%	

Long before the official discovery of U compounds in 1789 in Berlin (Klaproth, 1789), many of their variations were observed and described by miners and often referred to as a black, lead-heavy ore type, which was directly mined since 1850 for the coloration of artwork, mostly glassware (Dahlkamp, 2013). Briefly after the discovery of radium (Ra) in uranium ore (Curie and Curie, 1898), U mining began to grow for the recovery of this radioactive metal for the production of luminescent paints. One gram of Ra required the extraction of approximately three tons of U. Before World War II, the Shinkolobwe in today's Democratic Republic of the Congo, Port Radium in Canada and Jáchymov in today's Czech Republic became the most important U deposits of that time (Dahlkamp, 2013). After the end of World War II, nuclear weapons manufacturing and research initiated a period of intensive exploration for U, which, between 1950 and 1982 led to the discovery of the majority of today's known deposits.

Uranium is typically recovered by three methods: (1) open pit mining, (2) underground mining, and (3) *in-situ* leaching by water amended with acid and oxidizing agents (NEA/IAEA, 2018). Open pit U mining is profitable down to approximately 250 m depth and is often combined with underground mining (currently

down to 600 m) to exploit deeper parts of the deposits (WNA, 2018b). *In-situ* leaching can be applied in porous, unconsolidated material. In terms of solvent selection, hydrogen peroxide, sulfuric acid, or alkaline leaching can be applied, the latter as an alternative in limestone and gypsum-rich deposits where acid-neutralization would be too great. Through these methods, U is dissolved and pumped out together with the solvent (WNA, 2018b). Due to minimal surface disturbance, this method is believed to have the smallest environmental impact, given that the leaching solution is properly recovered, recycled and treated, which is not yet ensured in many countries that have lower environmental standards.

After mining, U is transported to U mills, where the ore is ground to a fine slurry, which is subsequently leached with sulfuric acid, a process that yields yellowcake, a fine powder enriched in U_3O_8 (CNA, 2015). U_3O_8 is further refined or chemically cleaned from impurities and formed into uranium trioxide, UO_3. For use in heavy water reactors, such as the CANada Deuterium Uranium (CANDU) reactors, UO_3 is converted into UO_2. For reactors running with light water, enrichment of the ^{235}U isotope is necessary and therefore, UO_3 is converted to uranium hexafluoride, UF_6 (CNA, 2015).

Pit and underground mining exposes waste rock materials to oxidizing conditions at the surface. Uranium and other metals-containing tailings are generated during milling and refining. Oxidation of waste rock and tailings can cause air, water and soil contamination with U, its daughter isotopes, such as ^{230}Th, and other co-contaminants, such as As (Moffett and Tellier, 1977). The long half-lives of U isotopes (e.g., 704 million years for ^{235}U) and their daughters (e.g., 83,000 years for ^{230}Th) can lead to radiation threats over extended periods of time. Acute and chronic toxicity effects to flora, fauna, and humans through ingestion, inhalation, or direct contact and consequent bioaccumulation are all possible impacts of U contamination (WHO, 2001). Thus, it is important to study the geochemical properties of former mine sites in order to understand and mitigate the potential impacts of U mining operations.

1.2.3 Uranium deposits

Uranium is usually mined from U(IV)-dominated minerals, such as uraninite (UO_2), pitchblende (U_3O_8) and brannerite (UTi_2O_6). Therefore, the formation of U deposits requires the reduction of the more mobile U(VI), which can occur under various geological conditions, leading to a large variety of U deposits, normally named by the host rock (WNA, 2018a). Major deposit types and their properties are summarized in Table 1.2. Historically in Canada, intrusive, metamorphite, and conglomerate deposit types played an important role, with major findings near Bancroft (Ontario), Port Radium (Northwest Territories) and Elliot Lake (Ontario), respectively (CNSC, 2018). Mines in the Bancroft area (e.g., Dyno, Madawaska) were decommissioned and remediated in the 1980s and 1990s, Port Radium remediation was finished in 2007, and decommissioning of the Elliot Lake mines was accomplished in the early 2000s (CNSC, 2018). Today, the vast majority of Canadian U is associated with unconformity-related deposits in the Athabasca basin, Saskatchewan, with the most productive mines at McArthur River and Cigar Lake. In the future, the Thelon Basin U deposits in the Northwest Territories and Nunavut, which are geologically similar, might gain more importance (CNSC, 2018). Other potentially important deposits are the Michelin metasomatite

albitite-hosted U deposits in Newfoundland and Labrador (Sparkes *et al.*, 2017), and the sandstone type Matoush deposit in Quebec (Alexandre *et al.*, 2015).

Table 1.2: Uranium deposit types and examples (Cowan, 1976; CNSC, 2018).

Deposit type	Properties	Notable deposits/mine examples
Intrusive	Associated with intrusive rocks, such as granite and pegmatite	Bancroft area (Ontario, Canada)
Granite-related	Mainly vein deposits in granite and adjacent rocks	Jáchymov mines (Czech Republic)
Polymetallic iron-oxide breccia complex	Hematite-rich granite breccia	Olympic Dam (Australia)
Volcanic-related	In volcanic rocks of faults and shear zones near volcanic calderas	Streltsovska (Стрельцовское рудное поле) ore deposits (Russia)
Metasomatite	Unevenly distributed U in hydrothermally-affected rocks	Zhovti Vody (Жовті Води) mine (Ukraine)
Metamorphite	Metamorphic-type in non-granite-related metasediments or metavolcanics.	Port Radium (Northwest Territories, Canada)
Proterozoic unconformity	Between faulted and brecciated metasedimentary rocks and Proterozoic overlying sandstones	Athabasca basin (Saskatchewan, Canada)
Collapse breccia pipe	Vertical, circular collapse structures up to 1000 m deep, filled with fine sediments	Grand Canyon Orphan mine (Arizona, USA)
Sandstone	Uranium mineralization occurs near mudstone units, which are interbedded in medium- to coarse-grained sandstone	Oklo mine (“natural fission reactor”) in the Franceville Basin (Gabon)
Palaeo-quartz-pebble conglomerate	Detrital U in archaean to early palaeoproterozoic conglomerates that overlie granitic and metamorphic rocks	Elliot Lake (Ontario, Canada)
Surficial	Tertiary and younger deposits with low-concentrated U mineralization on sand and clay with secondary cementing minerals	Langer Heinrich mine (Namibia)
Lignite-coal	Mostly amorphous U in lignite and coal on intermixed silt/clay or in adjacent carbonaceous rocks	Freital coal mine (Germany)
Carbonate	In limestone and/or dolomite, related to fractures, faults and folds	Tummalapalle (India)
Phosphate	Very low U concentrations in sedimentary phosphorites of mostly marine origin	Bakouma mine (Central African Republic)
Black shale	Uranium adsorbed onto organic material and clays in marine organic-rich shale or coal-rich pyritic shale	Alum shale formation (Sweden)

1.2.4 Uranium mitigation techniques

It is estimated that worldwide, more than two billion tons of uranium contaminated mine tailings threaten human and environmental health (Borch *et al.*, 2010). In addition, contamination of depleted uranium in warzones is a serious problem. Efforts were taken to decontaminate such places, but large contaminated areas and several hot-spots remain close to environmental receptors (Bleise *et al.*, 2003). Other uranium contamination sources involve improperly stored/dumped nuclear warheads and depleted uranium ammunition. In addition, long-term solutions are needed to safely store low-, medium- and high-level (spent fuel) radioactive wastes from energy production, research and medicine. In terms of remediation of such sites, the ultimate goal is often to fix soluble U into insoluble minerals (uraninite) or to biomass, which can subsequently be removed from the environment. Such methods include the formation of anoxic ponds and/or the use of microorganisms for bioreduction, biomineralization, biosorption, and bioaccumulation (Newsome *et al.*, 2014a).

Biomineralisation by bacteria and fungi was found to promote the formation of sparingly soluble uranyl phosphate minerals, which are stable under a broad range of geochemical conditions (Fomina *et al.*, 2008; Newsome *et al.*, 2014a). For the formation of such minerals, specific bacteria (e.g., *Serratia sp.*) need to be supplied with phosphate, e.g., in form of organophosphates, which is then cleaved by bacterial enzymes and transferred to dissolved uranyl ions. Biosorption has been used to remediate contaminated water, for example, in waste water treatment plants, since uranium shows a strong affinity for adsorption to microbial surfaces; the sorption affinity of U to bacteria is less than for Ni but higher than for Cu, Cd, Cr or Pb (Lopez *et al.*, 2000). The sorption potential of uranyl cations to microbial surfaces strongly depends on the availability of negatively charged functional groups, competition to sorption sites with other cations (including protons) and desorption, which can happen as fast as sorption (Bai *et al.*, 2016). Uranium bioaccumulation involves the fast sorption of uranyl cations to the surface of a cell, the subsequent transport of the cations through the periplasm and the assimilation of U in the cell membrane (Newsome *et al.*, 2014a). The process is believed to be a toxicity-related phenomenon, caused by the permeability increase of microbial cells after exposure to U.

As for many metals, plants can be used to phytoremediate U. Phytoremediation includes phytoextraction (removal of contaminants from soil and accumulation in roots and shoots), rhizofiltration (absorption of contaminants though plant roots) and phytostabilization (bioavailability reduction through detoxification mechanisms and the production of humic substances) (Gadd, 2010). Through the excretion of proteins, carbohydrates and organic acids, plants can also promote microbial growth in soils, enhancing microbial bioremediation processes. The accumulation of metals in plant tissue can vary substantially between and within plant species (Violante *et al.*, 2010). Some authors classify plants into three categories: (1) excluders, or plants that grow under high contaminant conditions by maintaining a low contaminant concentration in the shoots until a critical soil value is reached, after which unrestricted root-to-shoot contaminant transport can take place; (2) accumulators, or plants that accumulate heavy metals

in aerial parts; and (3) indicators, which take up metals in a regulated manner, so that with higher contaminant concentrations higher root uptake takes place (Huang *et al.*, 1998, Violante *et al.*, 2010). For group (2), the accumulators, an extreme form exists: hyperaccumulators, or plants which accumulate metals to even higher concentration than in the substrate and to higher levels than observed in other organisms (Li *et al.*, 2011). A so called phytoremediation factor was defined by Li *et al.* (2011), which not only respects the capability of the plant to take up metals but includes also the biomass produced. For example, they defined a uranium phytoremediation factor of 7.6 for *Cyperus iria*, a uranium hyperaccumulator, with plant uranium concentrations of about 36 µg/g. Although not a hyperaccumulator, *Phragmites australis* received a higher uranium phytoremediation factor of 16.6, since it produces more biomass in which uranium can be accumulated (up to 21 µg/g). Li *et al.* (2011) consider this species as the most potent for the remediation of U, Th, Ba and Pb (without amendments, as will be discussed below).

Amendments can be used to accelerate the phytoextraction process. For example, organic acids (e.g., citric acid, acetic acid) can enhance U uptake due to U dissolution and chelation and the removal of inorganic coatings from soil particles that might suppress U mobilization (Huang *et al.*, 1998). In their experiments, Huang *et al.* (1998) found that plants of the Brassicaceae family were able to reach equilibrium concentrations after only 3 days, with 1000 times higher uranium concentrations (up to 5000 µg/g) in stems than in control plants.

After uranium is taken up by plants, the contaminated parts must be removed from the environment. Thus, understanding how different plant species take up uranium and in which plant part the contaminant is accumulated is important for remedial plans. Plants which accumulate uranium in the roots would have to be removed as a whole, in contrast to accumulators which have the highest contaminant concentrations in the aerial parts and could be cut off at the soil surface. Finally, the removed plant parts have to be treated, e.g., incinerated. Remaining ashes should then be filtered and properly stored. Recovery of uranium from the ash as a resource could be a possibility in the future.

Remobilization of reduced U(IV) through re-oxidation can be prevented when diffusional barriers suppress the delivery of oxidants, or when preferential reductants, such as FeS, are present in high concentrations (Williams *et al.*, 2013). Previous laboratory work on U mobility has demonstrated that U can be immobilized by reduction to U(IV) under anaerobic conditions (*e.g.*, Tang *et al.*, 2013). Field experiments at the uranium-contaminated Rifle, Colorado and Oak Ridge, Tennessee experimental sites have both shown that metal-reducing bacteria (e.g., anaerobic heterotrophs) were able to immobilize uranium when provided with a reduced carbon source, such as acetate or soybean oil (Newsome *et al.*, 2014a). Arsenic and Ni are often found to be associated with U, but can display a higher potential for mobility and different immobilization pathways, such as sorption to ferrihydrite or by the formation of secondary minerals, such as calcium arsenates and arsenic sulfides (Kipp *et al.*, 2009; Troyer *et al.*,

2014). These metals may even become major contaminants in mining affected regions (Donahue *et al.*, 2000). For those reasons, both elements will be briefly introduced in the subsections below.

1.2.5 Arsenic and nickel - two common co-contaminants

Arsenic

Arsenic abundance in continental crust is about 1.5-2 ppm and it is a constituent of approximately 250 mineral species, the majority of which are arsenates (e.g., containing AsO_4^{3-}) (NRC, 1977). Arsenopyrite (FeAsS) is the most common As mineral, making As one of the major co-contaminants in acid mine drainage due to sulfide oxidation. The natural content of As in soils ranges between 0.1 ppm to 40 ppm but can naturally be as high as 8000 ppm (NRC, 1977).

In water, arsenic is most commonly present in two oxidation states, as the less mobile arsenate, As(V), or as the more mobile arsenite, As(III) (Figure 1.2). Thermodynamically, As(V) should be the dominant species in surface waters, however the actual As(V):As(III) ratio is around 0.1-10:1, mostly due to biological As(V) reduction (NRC, 1977), a process that under certain conditions can yield more energy than Fe(III) reduction (Figure 1.1). Various bacterial (e.g., *Desulfotomaculum sp.*) and archaean (e.g., *Pyrobaculum sp.*) species were shown to reduce As(V) (Huang, 2014). Furthermore, under reducing conditions, dissolution of Fe oxyhydroxides can lead to a release of co-precipitated and adsorbed As, thus leading to increased As concentrations in low oxygen environments, a process that can be critical for As contamination in groundwater (Raessler, 2018). The formation of secondary precipitates with Fe(II) can partially mitigate As release by its removal as $Fe_3(AsO_4)_2$, however, this process can be suppressed in environments rich of Fe(II) chelators, such as organic matter in wetlands (Huang, 2014). The reverse process, i.e., the oxidation of As(III) to As(V) can also be mediated biologically, by chemolithoautotrophic bacteria, either as part of dissimilation or as a detoxification mechanism (Borch *et al.*, 2010; Raessler, 2018), for example by *Acidithiobacillus ferrooxidans* (Huang, 2014).

Besides oxidation and reduction, As can be biologically methylated and demethylated, forming highly volatile monomethylated and dimethylated species, a process that is estimated to contribute to 36% of the total As emissions worldwide (Huang, 2014). These speciation changes govern not only the mobility of As but also its toxicity, which can be summarized as following: monomethylarsenite MMA(III) > dimethylarsenite DMA(III) > As(III) > As(V) > monomethylarsenate MMA(V) > dimethylarsenate DMA(V) (Raessler, 2018). The toxicity of As in an organism mostly comes from its similarity to phosphate and the consequent false incorporation into various enzymes that in the majority of cases lead to their inactivation (Ratnaike, 2003). Nevertheless, As is likely a micronutrient in animal bodies, likely involved in gene silencing selenium-related processes (Hunter, 2008).

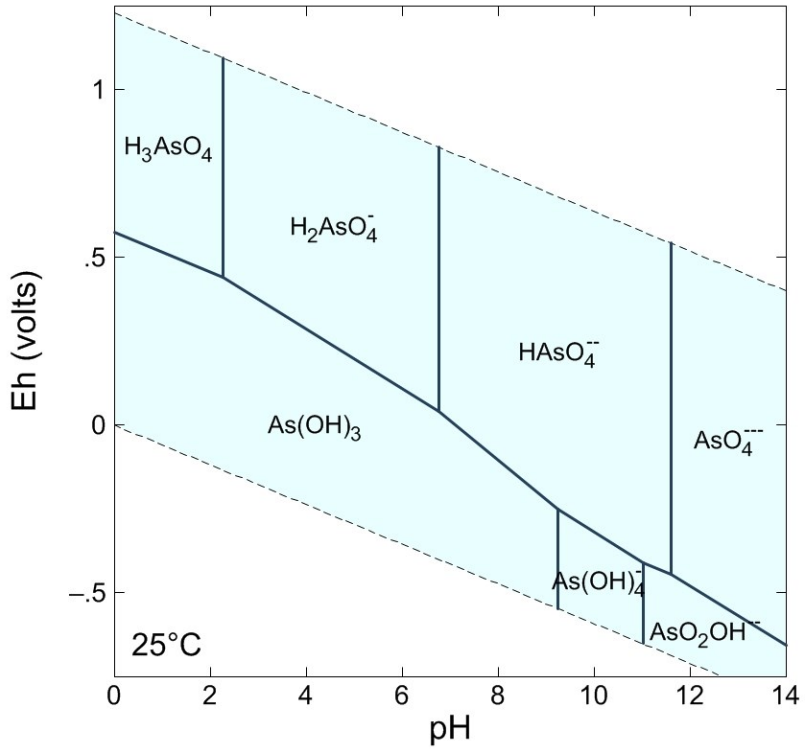

Figure 1.2: Eh-pH diagram As under typical surface conditions. Diagram created at standard conditions using the Geochemist's Workbench edition 12.0 with a [As]=10^{-8} M.

Nickel

Nickel is a fairly abundant element in Earth's crust with an average concentration of 75 ppm (Taylor, 1964). Nickel has an abundance of 10-40 ppm in soils and 0.1-100 ppb in surface water (Macomber and Hausinger, 2011). At surface conditions, Ni is dominantly present in the Ni^{2+} form (Figure 1.3) making it highly mobile in many environments. Its mobility is generally higher than of other divalent cations, such as Zn, Cu, and Pb (Harter, 1983) and is increased by complexation with organic matter (Iyaka, 2011). Nickel mobility can be controlled by the formation of insoluble sulfides in anoxic, S-rich environments (e.g., hot springs), as shown in Figure 1.3, or in high pH environments, where it can form insoluble hydroxides and carbonates (Harter, 1983). Nickel also sorbs readily to biomass, more so than uranium or arsenic (Violante *et al.*, 2010), making it a good candidate for bioremediation by biosorption. Furthermore, it is an important micronutrient for many microorganisms (e.g., methanogens), plants, and likely even animals (Scheller *et al.*, 2010; Iyaka, 2011). At the same time, Ni is highly toxic for many microorganisms, and in higher concentrations to plants and animals, with the toxicity being caused by its substitution in metalloproteins, blockage of catalytic groups in non-metalloenzymes and by causing oxidative stress (Macomber and Hausinger, 2011).

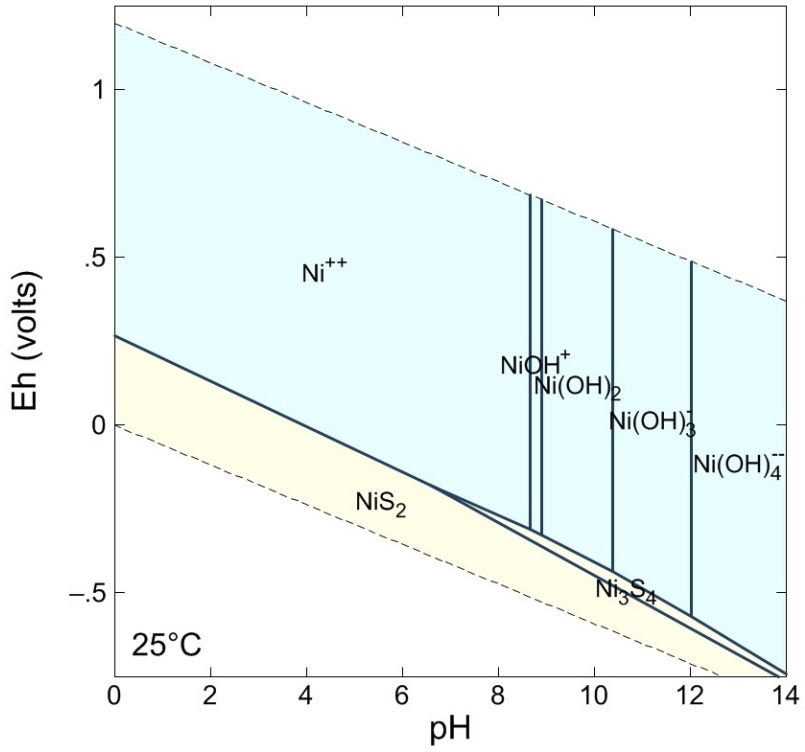

Figure 1.3: Eh-pH diagram for Ni under typical surface conditions. Diagram created at standard conditions using the Geochemist's Workbench edition 12.0 with a [Ni]=$10^{-8.5}$ M, a [SO_4^{2-}]=10^{-3} M.

1.3 Environmental importance of colloidal particles

Colloid chemistry and interactions are critical aspects of metal cycling, and understanding the extent to which colloids can sorb and transport metals is essential for determining their role in the functioning of meromictic pit lakes as a decommissioning measure. Colloids are generally defined as particles with a size range between 1 nm - 10 µm. Gustafsson and Gschwend (1997) further defined colloids as "any constituent that provides a molecular milieu into and onto which chemicals can escape from the bulk aqueous solution, while its vertical movement is not significantly affected by gravitational settling." This definition considers metals adsorbed and absorbed by non-settling mineral particles, humic substances, and non-motile microorganisms, but excludes metals complexed by organic acids, as those are generally considered to be truly dissolved.

Early colloidal research focused on the presence and separation of colloids by dialysis and found that metals such as Si, Al, Fe, Cu, Cr, and U were found to behave differently in terms of solution phase reactions than those that comprise the truly dissolved fraction (Graham, 1861). However, only over 100 years later, the importance of colloids in the environmental transport of organic constituents (Sharp, 1973; Baker *et al.*, 1986) and trace metals (Honeyman, 1991) was finally recognized.

Colloids can change the "classical" behavior of metals in aqueous media in several ways. Colloidal particles can act as reaction centers, which lower kinetic energy barriers, as demonstrated by the

reduction of U(VI) bound to the surface of hematite colloids by Fe(II) (Liger *et al.*, 1999). Some metals, when sorbed to colloids, can be mobilized under conditions previously thought to prevent their mobilization, as shown for reduced and generally insoluble U(IV) in an anoxic environment of a uranium (U) contaminated peat bog (Wang *et al.*, 2013). Similarly, Pu(III) and Pu(IV) mobility in natural aquatic systems was increased through colloidal transport and, consequently, a decreased Pu fraction was adsorbed to the solid phase (Nelson *et al.*, 1985). The eventual accumulation of colloidal particles and subsequent formation of precipitating particulates can remove metals from the aqueous medium via a scavenging process referred to as "colloidal pumping" (Honeyman and Santschi, 1991; Dai *et al.*, 1995). Such processes operate on longer time scales and can contribute to removal of metals from the mixolimnia of meromictic lakes, leading to an accumulation of trace metals in bottom sediments (von Gunten *et al.*, 1997, Castro and Moore, 2000, Pelletier *et al.*, 2009). This can, in turn, increase metal toxicity to benthic fauna (Cain *et al.*, 2013; Croteau *et al.*, 2013).

Although colloidal particles and their importance for metal cycling has been investigated in rivers (e.g., Dai *et al.*, 1995; Ross and Sherrell, 1999) and wetlands (e.g., Pokrovsky *et al.*, 2004; Wang *et al.*, 2013), studies regarding on their behavior in lakes are limited (e.g., Gimpel *et al.*, 2003). Colloidal metal transport is particularly understudied in artificial lacustrine systems, such as mining pits. In these systems, they may play an important role in metal transport due to extensive groundwater exchange with nearby areas, allowing colloidal-bound metals to escape the pits and enter the groundwater. In addition, colloidal abundance can increase due to local surface runoff and related soil disturbances. In a mining environment, revegetation during land reclamation may provide a fresh input of low molecular weight organic acids that can promote colloid formation (Slowey *et al.*, 2007). Such organic acids can additionally liberate metals from waste rock, leading to a concomitant increase in metal concentrations and colloids.

1.4 Major remediation techniques

1.4.1 Meromictic pit lakes and their applications

Open mining pits can eventually fill with surface runoff (e.g., spring melt), rain- and groundwater, forming pit lakes. This can also be induced artificially by flooding as a remediation technique, for example to treat acid mine drainage (Fisher and Lawrence, 2006; Pelletier *et al.,* 2009). A characteristic feature of such pit lakes is that they have steeply sided walls and considerable depth (Schultze *et al.*, 2016). Relative depth is often calculated for pit lakes, which is defined as the ratio of the maximum depth to the circular diameter of the surface d_{eq}[1], and which, for pit lakes, is usually 11% and higher (Pieters and Lawrence, 2014).

Such lakes can become meromictic, whereby the water body is separated by a chemocline into an upper mixolimnion that expresses seasonal turnover, and a lower monimolimnion with limited water

[1] $d_{eq} = \sqrt{\left(\frac{4}{\pi}\right) A}$, where A is the lake surface area

exchange with the overlaying water mass. The mixolimnion itself usually consists of the epilimnion and the hypolimnion, which are separated by the thermocline, a temperature gradient (Schultze *et al.*, 2016). These layers vary considerably in density and chemical composition. The formation of meromixis depends on various factors, in addition to the shape of the lake basin, including protection against wind, climatic conditions, ice melt and runoff, and groundwater inputs (Pieters and Lawrence, 2014; Schultze *et al.*, 2016; Boehrer *et al.*, 2017). Meromixis is not always a stable condition; the regular mixing of the mixolimnion can push the chemocline down, whereas the turnover of the monimolimnion, initiated by the input of less saline groundwater or geothermal heating, can lead to its rise (Pieters and Lawrence, 2014).

The selective manipulation of the meromixis stability in pit lakes can be used as an *in situ* remediation tool, and has been applied for the containment of highly contaminated brines and acid mine drainage (Geller *et al.*, 2012). Usually some minimal management is necessary to control the meromixis and to avoid lake turnover. This can include the application of lime and flocculants to promote contaminant precipitation in deeper water layers (Wiessner *et al.*, 2014), the addition of fertilizers or a carbon source to promote algal or bacterial growth and contaminant removal from the upper layers (Schultze *et al.*, 2016), or the addition of fresh or salt water to stabilize or induce stratification (Fisher and Lawrence, 2006). Nevertheless, published meromixis related biogeochemical data are scarce and not all geochemical relations in pit lakes are well understood (Schultze *et al.*, 2016).

1.4.2 Permeable reactive barriers

Permeable reactive barriers (PRBs) are an *in situ* remediation technology applied for the remediation of both organic and inorganic contaminants in groundwater (Powell *et al.*, 1998). Typically a trench is excavated perpendicular to the flow of contaminated groundwater and then backfilled with a mixture of reactive and permeable material. The reactive medium is chosen based on the contaminant that need to be treated. Examples are given in Table 1.3.

Contaminants are removed by sorption or precipitation, or, if the contaminant is organic, they are degraded by redox processes (Powell *et al.*, 1998). The transport behavior of trace metals in an aqueous environment is strongly affected by redox conditions, pH, available ligands (e.g., organic acids), and potential sorption sites (Borch *et al.*, 2010; Violante *et al.*, 2010).

In the majority of cases, zero-valent iron (ZVI) is used as a reactive medium due to its high reducing potential (ITRC, 2011); for example, chlorinated compounds are reductively dechlorinated. Some inorganics that are less mobile in their reduced states (e.g., U, Cr) are chemically reduced and are removed from solution by precipitation. Arsenic, on the other hand, can be removed by ZVI through sorption to ZVI corrosion products and by co-precipitaion with ferric and ferrous iron (ITRC, 2011). Organic substrates (biobarriers) can be used to promote microbial growth, which then promotes the biological degradation of organic contaminants and the transformation of inorganics into their less mobile forms by bioreduction. Furthermore, inorganic contaminants can be immobilized by precipitation with

metabolic products, such as hydrogen sulfide (form sulfate reduction) (ITRC, 2011). Various organic materials can be used, such as mulch, compost, or sawdust. Combinations of ZVI with biobarriers can be employed to increase removal efficiency and to immobilize a wider range of contaminants with one PRB.

Various reactive media can be used for the sorption of aqueous contaminants, such as phosphate minerals (e.g., apatites, $Ca_5(PO_4)_3(F,Cl,OH)$), zeolites (e.g., natrolite, $Na_2Al_2Si_3O_{10}{\cdot}2H_2O$), organophilic clays (modified clays with improved hydrophobicity), or furnace slag, a by-product of steel production, which is rich in calcium oxide and hydroxide and silicon dioxide (ITRC, 2011). Lime and limestone can be used to control barrier pH, as well as waste products such as fly-ash, a by-product of combustion rich in Si- and Al-minerals and lime, or recycled concrete (Golab *et al.*, 2006).

Table 1.3: Examples of contaminants and suitable reactive media in PRBs (Golab et al., 2006; ITRC, 2011). ZVI: zero-valent iron. BTEX: benzene, toluene, ethylbenzene, and xylene. NAPLs: Non-aqueous phase liquids.

Contaminant	Potential reactive media	Treatment processes
Chlorinated ethenes and ethanes	ZVI, biobarriers, ZVI-organic combination	Reductive dechlorination and degradation
BTEX	Biobarriers	Reductive degradation
NAPLs	Organophilic clays	Sorption
Arsenic	ZVI, slag, zeolite, ZVI-organic combination	Sorption, co-precipitation
Hexavalent chromium	ZVI, slag, zeolite, ZVI-organic combination	Reduction of Cr(VI) to Cr(III), precipitation and sorption
Uranium and cationic metals	ZVI, biobarriers, apatite, ZVI-carbon combination	Reduction (e.g., U, Cu), precipitation and sorption
Nitrate	Biobarriers, apatite, ZVI-organic combination	Chemical reduction, denitrification, sorption
Acid mine drainage	Zeolite, slag, fly-ash, limestone, lime, recycled concrete	Neutralization, precipitation and sorption

It is important that the reactive medium is filled into the barrier trench in a way that does not impede groundwater flow (i.e., high permeability), which otherwise would reduce the PRB efficiency due the groundwater flowing around the PRB. Therefore, the reactive medium is usually mixed with some high porosity material, e.g., sand or gravel (Powell *et al.*, 1998). Secondly, the surface area of the reactive medium should be as high as possible to increase reaction rates between it and the target contaminants (ITRC, 2011).

1.5 Field site introduction

1.5.1 Geological setting

The research studies discussed in this thesis are associated with the decommissioned Cluff Lake uranium mine in Northern Saskatchewan, Canada. Cluff Lake is located in Canada's most important uranium mining area, the Paleo- and Mesoproterozoic Athabasca Basin, in northwestern Saskatchewan (Figure 1.4). The Athabasca unconformity-related deposits that were introduced above provide approximately one third of all currently U mined (Donahue *et al.*, 2000). Basement orthogneisses at the Cluff Lake site were exposed during the formation of the Carswell structure in the Paleozoic, likely caused by a meteorite impact (Harper, 1982). The deposit at Cluff Lake, located approximately 75 km south of Athabasca Lake, was one of the first locations in the Athabasca Basin where U deposits were discovered in 1969 with ore grades of up to 4% (Jefferson *et al.*, 2007). Uranium is mainly found as the following four uraniferous minerals: uraninite-sulfide (dated at ~1150 Ma), uraninite-Te-Se-Bi (~1050 Ma), pitchblende-sulfide, and pitchblende-hematite (both ~380 Ma) (Bell, 1985; Ruhlmann, 1985). The ore found in the Athabasca Basin contains also relatively high grades of Ni (up to 2%) and As (up to 1.2%) due to oxidation of the primary minerals gersdorffite (NiAsS), niccolite (NiAs), bravoite ($FeNiS_2$), and chalcopyrite ($CuFeS_2$) (Donahue *et al.*, 2000).

Figure 1.4: Location of the Cluff Lake mine, the Athabasca Basin and the Carswell Structure.

1.5.2 Climatic conditions and hydrogeological considerations

Given the importance of rainfall and temperature for the mobilization of contaminants in surface- and groundwater, one needs to consider the climatic zone of the field site and the major drainage pathways. Cluff Lake lies within the boreal shield ecozone dominated by boreal forest. Common vegetation includes jack pine, paper birch, white spruce, balsam fir, and trembling aspen. Cluff Lake has short summers with only about 90 frost-free days (WFD, 2019). Average daily temperatures range between 14°C and 17°C in the summer and between −17°C and −20°C in the winter. Recorded extreme temperatures in summer and winter were 36°C (1982) and −49°C (1991), respectively. Yearly precipitation is on average 451 mm, with snowfall from October to May sometimes causing snow accumulation in excess of 60 cm (WFD, 2019).

The surface of the site consists mainly of peat and permeable glacial till, up to 7 m thick (AREVA, 2009). Creeks and rivers, which pass through the mining area (Beaver Creek, Boulder Creek, Earl Creek, Peter River, and Claude Creek) discharge into Cluff Lake. Water exits the lake at the south end into Cluff Creek, which ultimately discharges into the Douglas River (AREVA, 2013). Snake Lake, located near the tailings management area, also discharges into Douglas River after passing through a system of wetlands and lakes. The Douglas River ultimately discharging into Lake Athabasca. Previous groundwater modeling by AREVA (AREVA, 2013) suggests that the main direction of groundwater flow at the mining area trends from north to south.

1.5.3 Mining and decommissioning activities

Mining operations were active between 1979 and 2002, led by Compagnie Générale Des Matières Nucléaires (COGEMA), which in 2001 became AREVA Resources Canada (CNSC, 2003) and in 2018 ORANO. During 22 years of mining operations, approximately 28.3 million kg of U_3O_8 were extracted (SMA, 2016). At the peak of operations, the site consisted of an air strip, an exploration camp and a mining area north of Cluff Lake (58° 22.5' N, 109° 32' W; spread over 810 ha; shown in Figure 1.5), a milling complex, and a tailings management area between Snake Lake and Cluff Lake in the west (58° 21.5' N, 109° 37' W; 640 ha) and the Germaine camp at the southern end of Cluff Lake (58° 19.7' N, 109° 34.7' W; 50 ha) (CNSC, 2003). The mining area included the open pit mines on the D, Claude, and Dominique-Janine (DJN and DJX) orebodies, and the underground mines on the ore bodies OP and Dominique-Peter (DP). The milling complex and the tailings management area consisted of two tailing ponds (solids, liquids), an above-ground tailings management facility, and corresponding treatment systems (CNSC, 2003).

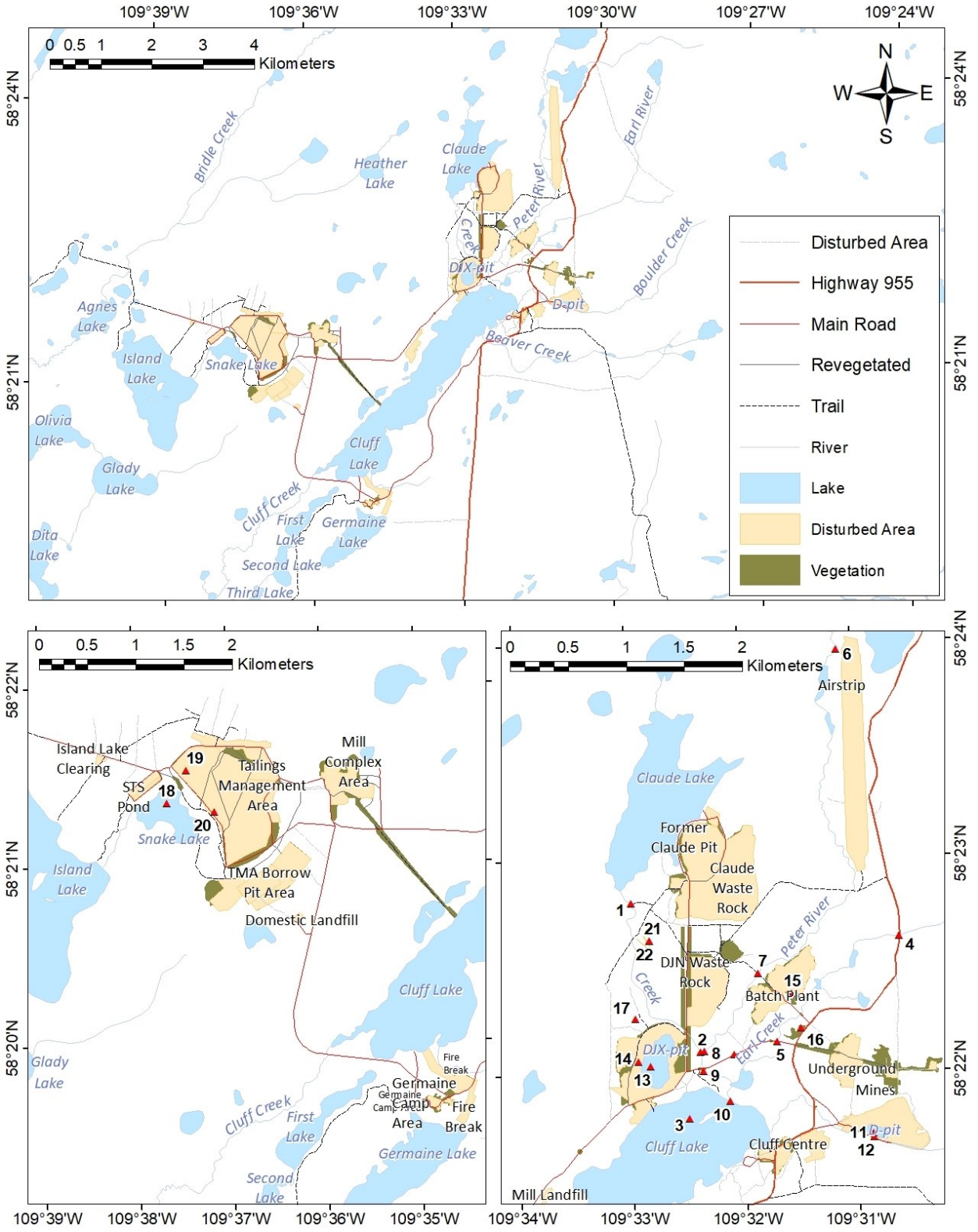

Figure 1.5: Overview of the Cluff Lake mine (top) and detailed maps on the tailings management area (bottom left) and the mining site (bottom right). Triangles and numbers represent selected sampling stations mentioned in Table 1.4.

Table 1.4: Selected monitoring results (metals) for locations in Figure 1.5. Table data from 2010-2012 from AREVA (2009, 2013). Data from 2015 and 2016 provided by AREVA (personal communication). Data from 2017 was sampled by the author (see Chapter 2).

No.	Station	Description	Year	As µg/L	Fe mg/L	Mn mg/L	Ni mg/L	Sulfate mg/L	U µg/L	Al mg/L	pH
1	CDE1000S	Surface water Claude Creek	2016	0.5	0.81	1.39	0.002	190	3.3	0.007	7.7
2	CDE2100S	Surface water Claude Creek	2015	0.2	0.23	0.21	0.011	420	0.1	0.013	6.2
3	CFF1010S	Surface water Cluff Lake	2010	0.2	0.03	<0.01	0.001	11	0.8	0.001	7.3
4	ERL1000S	Surface water Earl Creek	2012	<0.1	4.68	0.14	0.001	1	<0.1	0.020	7.3
5	ERL3000S	Surface water Earl Creek	2012	<0.1	0.88	0.04	<0.001	3	<0.1	0.002	7.5
6	PTR1000S	Surface water Peter River	2012	<0.1	0.01	<0.01	<0.001	1	<0.1	0.003	7.4
7	PTR1500S	Surface water Peter River	2012	<0.1	0.23	<0.01	<0.001	1	<0.1	0.003	7.8
8	PTR1900S	Surface water Peter River	2015	0.1	0.52	0.06	0.002	6	0.6	0.026	7.5
9	PTR3000S	Surface water Peter River	2015	0.1	0.81	0.16	0.003	33	0.5	0.032	7.6
10	PTR4000S	Surface water Peter River	2016	0.1	0.45	0.07	0.002	12	0.6	0.009	6.9
11	BLD2000S	Surface water D-pit	2015	2.1	1.33	0.22	0.003	7	71.0	0.014	8.4
12	DWW0041G	Groundwater near D-pit	2015	1.4	1.24	0.60	0.002	5	19.0	0.016	6.4
13	MNW6100S	Surface water DJX-pit	2015	1.0	0.04	<0.01	0.068	210	131.0	0.012	8.3
14	HYD9846AG	Groundwater near DJX-pit	2015	<0.1	<0.01	0.02	<0.001	34	0.1	0.005	7.5
15	MNW2050G	Groundwater of covered area	2012	<0.1	0.05	0.01	<0.001	52	<0.1	0.002	8.8
16	MNW2100G	Groundwater of covered area	2012	<0.1	2.20	0.24	<0.001	160	0.2	0.005	7.8
17	MNW6210G	Groundwater near DJX-pit	2012	<0.1	0.01	0.07	<0.001	880	<0.1	0.002	9.1
18	ISL2000S	Surface water Snake Lake	2012	<0.1	0.09	<0.01	0.002	190	<0.1	0.005	8.9
19	HYD10-04AG	Groundwater in TMA	2012	<0.1	33.00	1.30	<0.001	620	<0.1	<0.005	6.7
20	HYD0192G	Groundwater in TMA	2012	<0.1	37.60	2.10	0.005	1030	0.49	<0.005	6.9
21	HYD07-11G	Groundwater in wetland	2017	7.2	1.00	4.70	0.400	-	<1.0	0.067	6.4
22	HYD06-03G	Groundwater in wetland	2017	1.9	6.60	14.90	6.900	-	915.9	9.845	4.6

Physical decommissioning activities at Cluff Lake were undertaken between 2004 and 2006. During this time, large areas were resloped, and tailings and backfilled pits were covered with compacted waste rock, on top of which local glacial till (layers of approximately 1 m) or reclaimed organic material was deposited (AREVA, 2009). These areas were then revegetated with native and non-native species, usually mixtures of shallow rooting legumes and grass species to prevent erosion by water and wind, as well as lowering the potential of acid mine drainage formation. The D-pit and DJX-pit were turned into pit

lakes in the context of remediation. Two experimental permeable reactive barriers (up to 130 m wide) were built in 2006 and 2007 in a peat bog between the Claude waste rock pile and Claude Creek to capture the metals leaching from the Claude Waste rock pile, but were only partially successful in arresting metal transport (AREVA, 2013), as will be discussed in Chapter 4. Since 2006, the site has been monitored up to four times a year, with the final goal being to transfer site responsibility to the Provincial Institutional Control Program (Huffman, 2014). Since 2013 no full-time personnel presence has been maintained on site. By 2018, 93 groundwater wells, 12 dosimeter and Radon sampling stations, and 33 designated surface sampling locations were present on the Cluff Lake field site (AREVA, 2013).

1.5.4 Historical monitoring data and trends

Mining area

According to historical monitoring results for the Cluff Lake mining area, the highest metal concentrations were found in the north-western creeks and in the mining pits (Table 1.4). Metal concentrations in Claude Creek were lower downstream of the wetland south of Claude Lake, suggesting that the wetland retains a large fraction of the metals of concern. The pH values varied from 6.2 to 9.1 in the mining area, with the lowest values found in Claude Creek (pH 6.2), the D-pit groundwater (pH 6.4), and the Peter River (pH 6.9). The two flooded pits had the highest measured concentrations of U, Ni, and As in the mining area as will be discussed in a later chapter. D-pit was sampled at several depths since 1992 (Figure 1.6). Until 2004, monitoring was performed on a monthly basis, after which the sampling rate decreased to 2-4 times a year (see Figure 1.6). Heavy rainfall in 1996 and 1997 led to higher metal inputs into the pit from the adjacent waste rock pile and contributed to concentration peaks for U (up to 0.8 ppm), Fe (up to 0.06 ppm), As (up to 1.2 ppm), and Al (up to 0.14 ppm) (AREVA, 2013). The metals of concern, namely As, U, and Ni, rapidly decreased after this major precipitation event and have been steadily decreasing since then. However, since 2009, a slight increase in the U concentrations was observed at the surface of the pit (0.03 ppb per year). By contrast, Fe is slowly rising in the deeper water layers after a major concentration drop in 1995 (4 ppb per year increase in Fe concentrations at 20 m depth since 2009). In 2015, reported Fe concentrations in groundwater were up to 1.2 ppm, and ranged from 1.3 to 54 ppm in surface water. In 2015, U, As, and Ni surface water concentrations were approximately 71 ppb, 2.1 ppb, and 3.3 ppb (Table 1.4), respectively, which is within the established Decommissioning Surface Water Quality Objectives (DSWQO) of 100-200 ppb for U (hardness dependent), 50 ppb for As, and 25 ppb for Ni (hardness dependent). As of 2015, U, As, and Ni concentrations in the nearby groundwater well were 19 ppb, 1.4 ppb, and 2.2 ppb, respectively.

Metal concentrations were generally higher in the DJX-pit than in the D-pit, except for As. In 1999, when the DJX-pit was partially flooded, U and Ni water concentrations were 6.6 ppm and 0.38 ppm, respectively (AREVA, 2009). Historical trends since 2005 of selected metals in the DJX-pit are shown in Figure 1.7. Over this period of 10 years, the concentration did not significantly change, with the exception of a few spikes most probably caused by precipitation events. In the middle of the pit (36-40 m), some

parameters, such as sulfate, Ni, and Mn concentrations showed slight increases and stabilized at 600 ppm, 1 ppm, and 2 ppm, respectively. Since 2009 surface U concentrations were decreasing at a rate of about 0.03 ppb per year. According to sampling data from 2015, the concentrations in the middle of the water column (at 40 m depth) for U, As, and Ni were 342 ppb, 0.4 ppb, and 1030 ppb, respectively. At the water surface the recorded values were 131 ppb, 68 ppb, and 1 ppb (Table 1.4), respectively, meeting the established DSWQO. DJX-pit also has the highest sulfate concentrations in the mining area (420 ppm on surface).

At the Claude Lake discharge, in 2016, the concentration of U was 3.3 ppb (Table 1.4). It then decreased progressively downstream towards Cluff Lake, where concentrations dropped to 0.5 to 0.8 ppb. Marginally elevated As concentrations were found upstream of Claude Creek (0.5 ppb) and decreased progressively downstream (<0.1 ppb). Iron concentrations within the mining area were generally lower than 1 ppm, the exception being D-pit surface and ground water, where concentrations were 1.33 ppm and 1.24 ppm, respectively. Cluff Lake experienced several metal concentration highs in the surface water since 2000 (Figure 1.8), which were likely linked to precipitation events.

Tailings management area

The watershed, where the tailings management area (TMA) is located, is draining into Snake Lake (Figure 1.5). In its surroundings, based on recent monitoring results, the highest U, As, Fe, and sulfate concentrations were found in the solids pond pore water with 0.49 ppb, 0.003 ppb, 37.6 ppm, and 1030 ppm, respectively (AREVA, 2013). In the Snake Lake itself, however, metal concentrations were generally low. The pH values were nearly neutral in the groundwater of the solids and liquids ponds and slightly basic in Snake Lake.

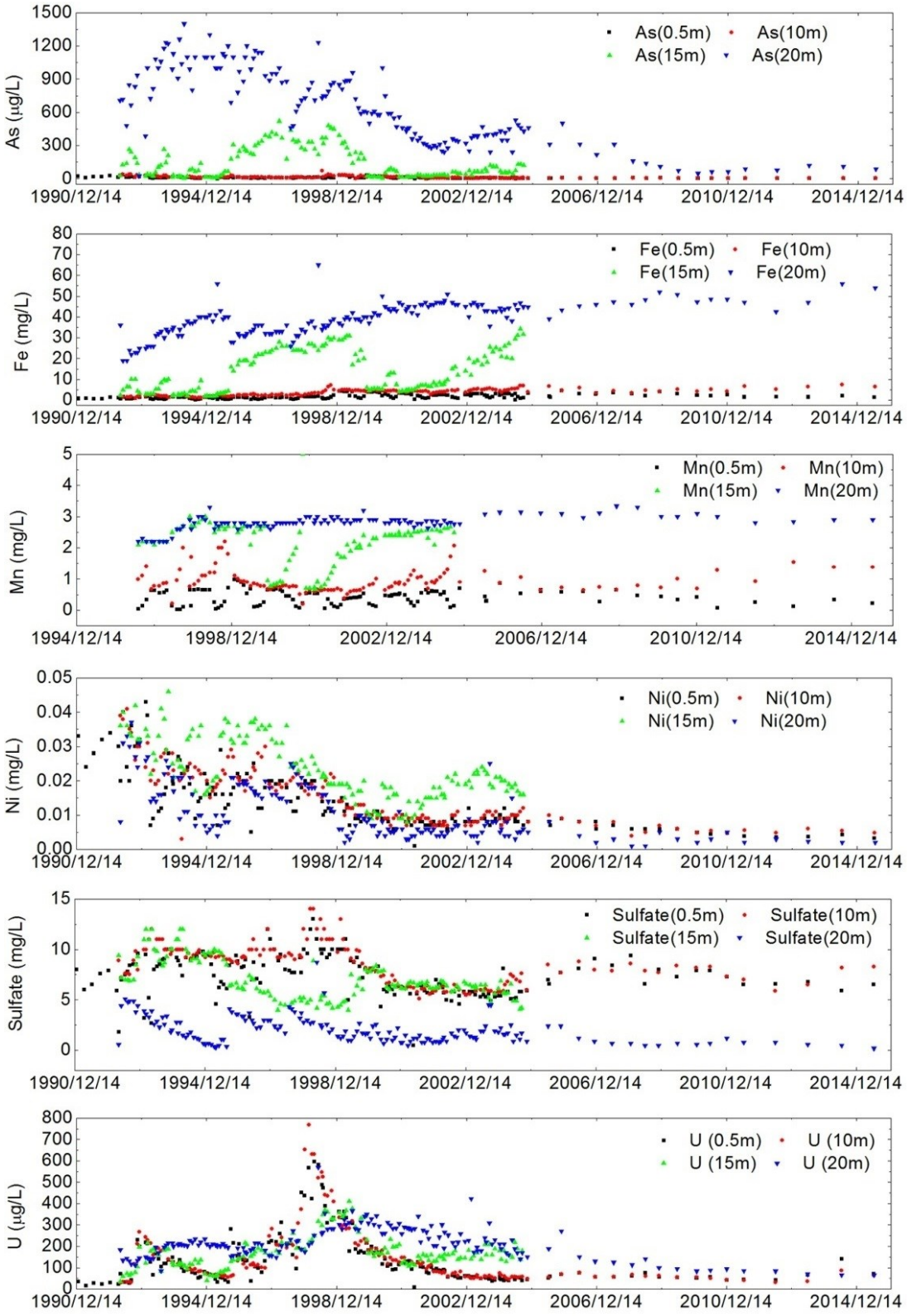

Figure 1.6: D-pit concentration trends since 1990 for As, Fe, Mn, Ni, sulfate, and U (based on data provided by AREVA).

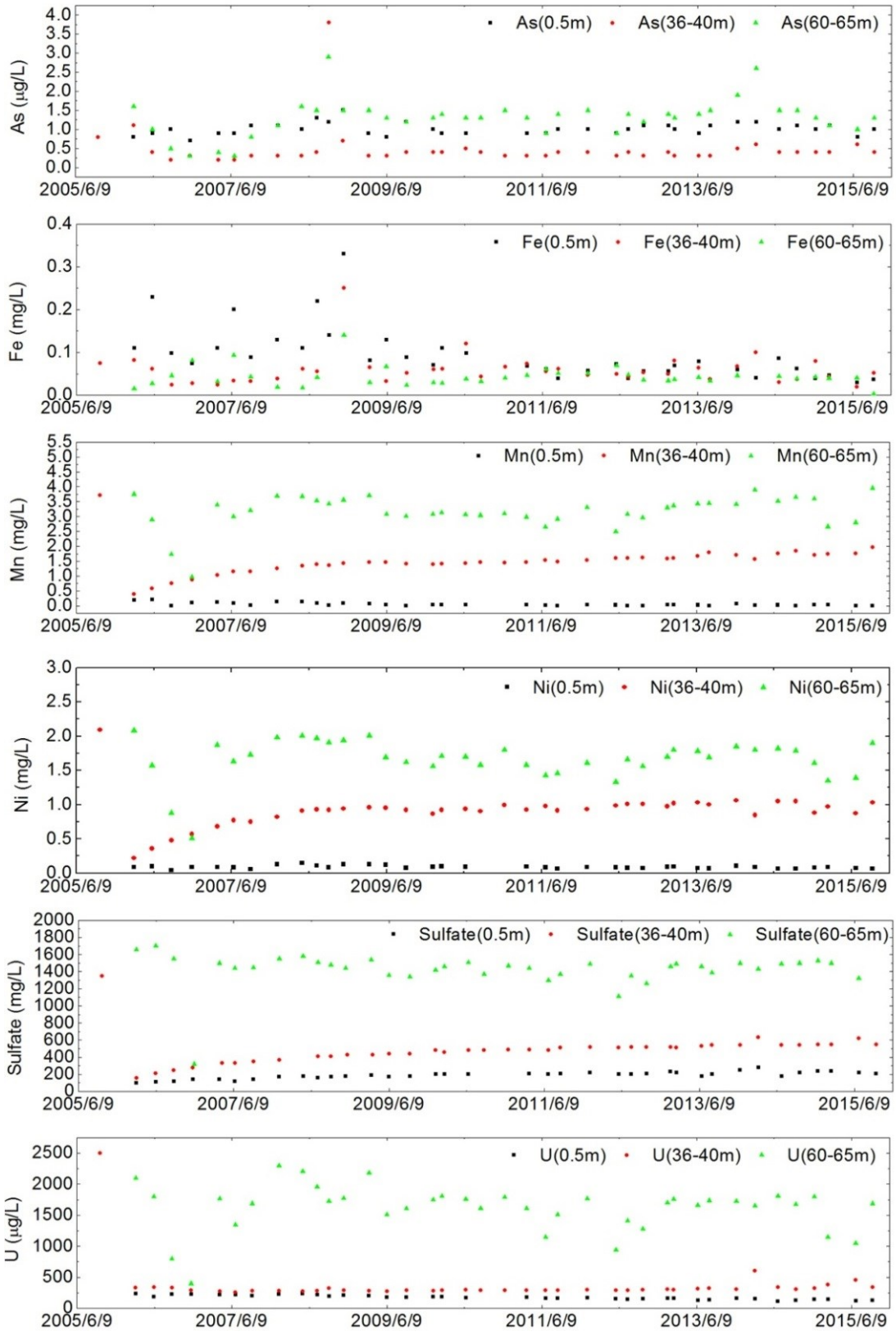

Figure 1.7: DJX-pit historical trends since 2005 for As, Fe, Mn, Ni, sulfate and U (based on data provided by AREVA).

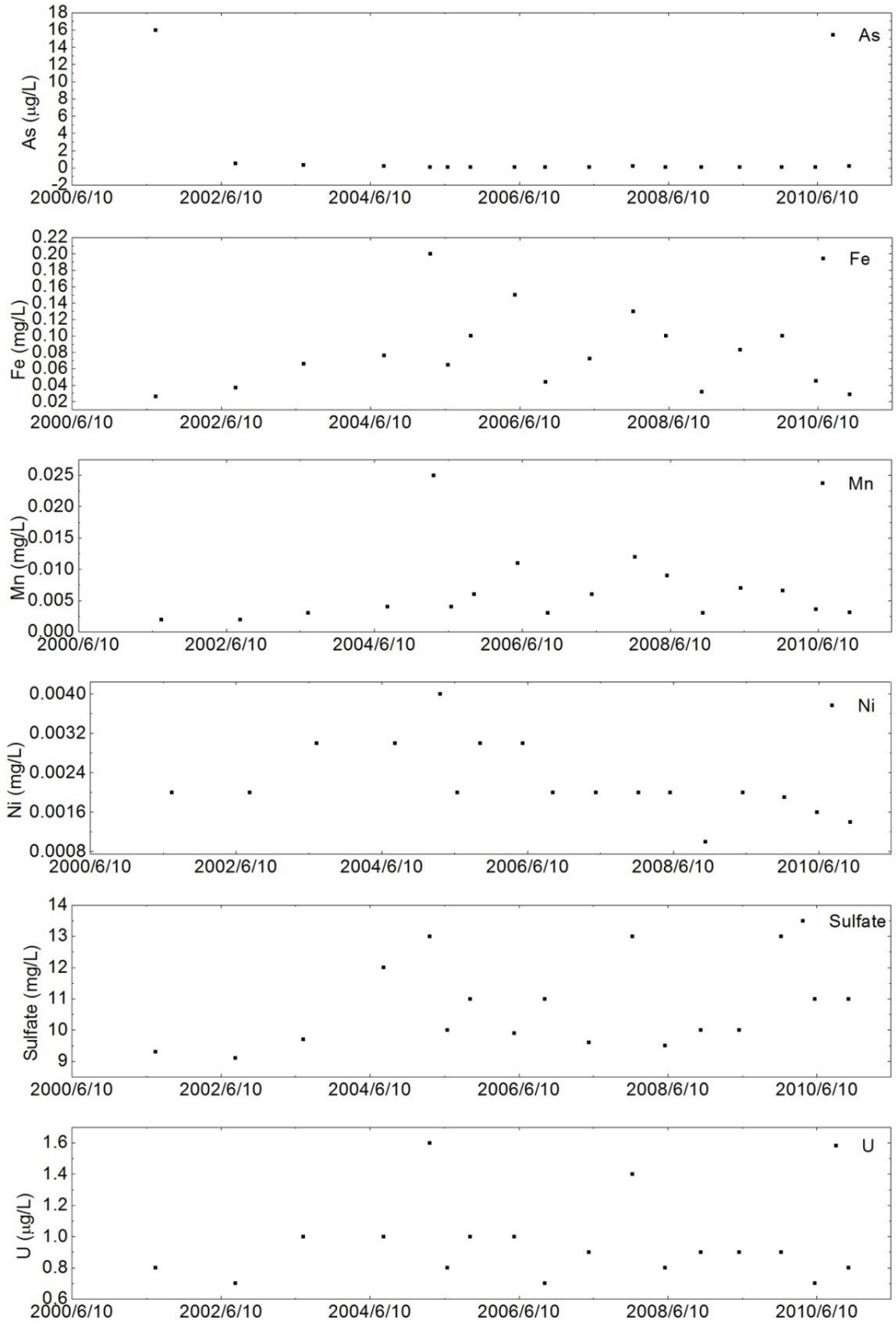

Figure 1.8: Metal concentrations in surface water of Cluff Lake since the year 2000 (based on data provided by AREVA).

1.6 Concluding remarks

Despite its importance for the Canadian and world economies, uranium recovery and processing involves considerable environmental disturbances and can generate wide-spread contamination of U, its decay products and co-contaminants, such as As and Ni. The mobility and sequestration of such contaminants has been well investigated, however, as will be elaborated in the studies that follow, those processes are not well understood in cold climates, as in the case of the decommissioned U mine at Cluff Lake. This abandoned but still monitored mine, with 22 years of mining history, has a valuable long-term monitoring record that allows us to compare the current biogeochemisty of the pit lakes and wetlands with previous observations. Today, Cluff Lake utilizes several common remediation techniques including pit lakes and permeable reactive barriers. The site documentation allows us to investigate their long-term performance and make predictions for future decommissioning of Cluff Lake and numerous other metals-contaminated mine sites located in cold regions.

Based on the background site data discussed above, the following hypotheses were made with regards to the pit lakes (Chapters 2 and 3):

- Meromictic pit lakes in cold climates are an effective (bio)remediation technology (i.e., contaminants are efficiently sequestered in pit lake sediments)
- Processes linked to the chemocline of meromictic pit lakes drive contaminant sequestration
- Colloidal particles are major contributors of metal and metalloid sequestration in cold climate pit lakes

For the project related to the permeable reactive barrier technology (Chapter 4), the following hypotheses were made:

- The wetland environment and the chosen reactive medium are unfavorable for Ni and Co removal
- Colloidal particles influence the performance of permeable reactive barriers

2 BIOGEOCHEMISTRY OF U, NI, AND AS IN TWO MEROMICTIC PIT LAKES AT THE CLUFF LAKE URANIUM MINE, NORTHERN SASKATCHEWAN

2.2 Summary

Open pits, which remain after U mining operations cease, can form meromictic lakes which develop suitable conditions for the containment of dissolved and colloidal metals. In this study, the distribution and speciation of U, Ni, and As in the water column of two meromictic pit lakes was investigated at the decommissioned Cluff Lake mine in northern Saskatchewan. The 28 m deep and older D-pit had a chemocline at 13 m depth, below which it turned anoxic and its meromixis was controlled by Fe cycling. Below the chemocline both Fe(III) and As(V) were reduced to Fe(II) and As(III), respectively. Iron cycling had a large effect on U distribution because reducing conditions prevented sulfide oxidation and a drop in pH in deeper layers. Metal-reducing bacteria were found to be present at, and below, the chemocline. In the deeper (90 m), larger and more recently flooded DJX-pit, two chemoclines were observed at depths of 15 and 65 m. Both were linked to sharp U and Ni concentration gradients. Unlike the D-pit, a transition to reducing conditions was not observed in the DJX-pit's water column. However, colloidal U, primarily associated with aluminum oxyhydroxides, was found below the first chemocline. Overall, the meromixis-type determined the distribution and speciation of metals and bacteria in the investigated pit lakes, thus providing insights into the use of pit lakes as a potential bioremediation strategy.

2.3 Introduction

2.3.1 Objectives

As elaborated in Chapter 1, Canada is one of the largest U producers in the world. The U mining process exposes excavated rock to surface oxidizing conditions, which can result in the mobilization and accumulation of metals and metalloids in nearby environments. Knowledge of the geochemical processes and reactions of potential contaminants at former mine sites is important to mitigate impacts from future mining operations. Despite the significant literature pertaining to U transport and bioremediation in laboratory studies and temperate field environments, such as the Rifle site in Colorado (Williams *et al.*, 2011; Bargar *et al.*, 2013; Alessi *et al.*, 2014a) and the Oak Ridge site in Tennessee (Watson *et al.*, 2013; Leigh *et al.*, 2014), little is known about the transport and fate of U in subarctic regions, such as those where Canada's U resources are mined. As previously discussed, As and Ni are often found to be associated with U deposits and can become major contaminants in such mining districts (Donahue *et al.*, 2000). Accordingly, our motivation was to study U, Ni, and As mobility and speciation in two chemically-stratified (meromictic) pit lakes in a subarctic climate at the decommissioned Cluff Lake mine, located in the Athabasca Basin in northern Saskatchewan (Figure 1.4). These lakes are two examples of mine pit lakes with different histories, sizes, geometries, stratification behaviors and U, Ni, and As metal

distributions. Additionally, this study investigates the role of colloidal particles in the geochemical cycling of those metals.

2.3.2 Characteristics of the pit lakes: D-pit and DJX-pit

In this study, we focused on two pit lakes at the Cluff Lake site, which were briefly mentioned in Chapter 1 (Figure 1.5): D-pit (formed 36 years ago) and DJX-pit (formed 17 years ago). Mining of D-pit occurred between 1979 and 1981 (AREVA, 2009), during which time the nearby Boulder Creek was diverted to allow for pit development. In 1983 the creek overflowed during spring thaw and flooded the D-pit (AREVA, 2009). A waste rock pile located adjacent to the pit was revegetated between 1983 and 1985, but minor metal leaching from the covered waste pile has been reported (AREVA, 2009). The D-pit lake has a surface area of 15,400 m^2 and an approximate depth of 28 m.

The DJX-pit was composed of two open pits: DJN-Pit, which was mined from 1989 to 1991, and DJX-pit, mined from 1994 to 1997. To develop the DJN-Pit, the adjacent Claude Creek was diverted into the nearby Peter River. The DJN-Pit was subsequently used for waste rock disposal (containing <0.03% U) from the adjacent DJX-pit, which showed high potential for acid generation (AREVA, 2009). After mining ceased in the DJX-pit, it was seasonally dewatered to minimize water inflow to the nearby DJ underground mine (1994-2002). With the cessation of mining, the DJN-pit and the DJX-pit were flooded with water from the adjacent Cluff Lake (AREVA, 2009), and today they form one water body, which will hereafter be referred to as DJX-pit. The water level in the 90 m deep pit has stabilized below the level of nearby Cluff Lake, forming a pit lake with a surface area of approximately 85,900 m^2 (AREVA, 2013).

2.4 Materials and Methods

2.4.1 Water sampling and measurement of field parameters

In June 2016, water was sampled from D-pit and DJX-pit from a boat in the center of the pit. A plastic tube was lowered into the pit together with a measuring tape and the probe of a multi-parameter water quality meter (YSI Professional Plus). D-pit was sampled from 0.5-23 m in 1 m intervals, while DJX-pit was sampled from 0.5-82 m in 2 to 5 m intervals. Temperature, pH, oxidation-reduction potential (ORP), dissolved oxygen, and conductivity were recorded using the water quality meter at each depth. Sampled water was pumped through the tubing using a MasterFlex E/S portable sampler (Cole-Parmer) and collected in the boat.

For metal quantification and arsenic speciation analysis, the water was filtered (0.45 µm nylon membranes, Agilent Technologies) and collected into acidified (0.05 M HCl) 50 mL polypropylene (PP) tubes (Fisher Scientific), which were wrapped in aluminum foil to prevent photo-oxidation of redox-sensitive species. For carbon, nitrogen, and anion analyses, unfiltered water samples were collected without acidification. Separate non-acidified samples, filtered through 0.45 µm membranes, were collected into 250 mL polypropylene copolymer (PPCO) centrifuge bottles (Thermo Fisher), wrapped in aluminum

foil, for asymmetrical flow field-flow fractionation (AF4). For iron speciation, 1 mL of water was directly filtered (0.45 µm) into 2 mL Eppendorf tubes and acidified with 1 mL of 2 M HCl for preservation. Results, collected in June 2016, were compared to preliminary field measurements (temperature, pH, conductivity) and water analyses (selected depths for cations, anions, carbon, and nitrogen, only) conducted in September of 2015 using similar methods (exception: 0.2 µm filters used). Field measurements for DJX-pit were also performed in September 2016. Groundwater was sampled in June 2016 from wells located close to the two investigated pits (Figure 1.5). The well south of D-pit was DWW0041G (7 m deep, N 58.3617°, W 109.5154°) and will hereafter be referred to as groundwater well 1 (GW1). Two groundwater wells close to the DJX-pit were sampled: the well north of the DJX-pit (GW2) is labeled as MNW6210G (17 m deep, N 58.3709°, W 109.5494°) and the well west of the DJX-pit (GW3) is labeled as HYD9846AG (4 m deep, N 58.3675°, W 109.5489°). Three well volumes were pumped to adequately purge the well before sampling (Vail, 2013).

2.4.2 Water chemistry

The unfiltered and unacidified water samples were analyzed for total carbon (TC), total inorganic carbon (TIC), and total nitrogen (TN) using a Shimadzu TOCV-N CHS/SCN Model Total Organic Carbon Analyzer with potassium nitrate and potassium hydrogen phthalate as calibration standards, and potassium acid phthalate certified reference material for quality control (detection limit: 0.1 ppm). Total organic carbon (TOC) was calculated by determining the difference between TC and TIC. Splits of the same samples were filtered (0.45 µm) for anion analysis by ion chromatography using a DX 600 (Dionex) with a 4 mm analytical column AS9-HC and a guard column AG9-HC (detection limit: 0.2-1.0 ppm). Filtered and acidified water samples were analyzed with an Inductively Coupled Plasma Mass Spectrometer (ICP-MS/MS) Triple Quadrupole system (Agilent Technologies 8800). Single-element standards (Spex CertiPrep, Ricca Chemical Company) were diluted in 2% HNO_3 (trace metal grade, Fisher Scientific) and 0.5% HCl (trace metal grade, Fisher Scientific), and used for external calibration. See Table A.1 for all used analyte masses and MS/MS modes.

2.4.3 Speciation of metals and metalloids

Selected samples (filtered, preserved in 1 M HCl) from both pits were subjected to a standard ferrozine assay based on the methods of Stookey (1970), Viollier *et al.* (2000), and Porsch and Kappler (2011), in order to determine iron speciation. Total Fe-content was determined by adding 400 µL of hydroxylamine hydrochloride (10% in 1M HCl) to 100 µL of each sample (preserved in 1 M HCl), which were left for 30 min in the dark. 500 µL of ferrozine (0.1% in 50% ammonium acetate) were added, followed by another 5 min incubation in the dark. Fe(II) concentrations were determined by adding 400 µL of 1M HCl to 100 µL of each sample, followed by 500 µL of ferrozine. After 5 min of incubation time in the dark, the samples were analyzed on the spectrophotometer. The ferrozine complex was quantified spectrophotometrically at 562 nm using an Evolution 60S UV-Vis Spectrophotometer (Thermo Scientific). Calibration curves for total

Fe and Fe(II) (0 to 1000 µM) were generated using $(NH_4)_2Fe(SO_4)_2 \cdot 6H_2O$ in 1M HCl, and confirmed by ICP-MS/MS.

Filtered and acidified samples were analyzed using a high performance ion chromatograph (IC; Thermo Scientific Dionex ICS-5000$^+$) paired with a quadrupole inductively coupled plasma mass spectrometer (iCAP Q ICP-MS, Thermo Scientific) operated in kinetic energy discrimination mode with helium as the collision gas. Arsenic species were separated using a Dionex Ion Pac AS7 anion exchange column (4 mm ID x 250 mm length) and AG7 guard column (4 mm ID x 50 mm length), with dilute HNO_3 as the mobile phase. Samples were also analyzed for total concentrations of trace metals using an iCAP Q ICP-MS. More detailed method information can be found in Donner *et al.* (2017). Thermodynamic modeling of metal speciation was conducted using the PHREEQC 3.3.7 software and the Minteq (2009) database. Modeling was done for D-pit at depths of 0.5 m, 5 m, 10 m, 13 m, and 20 m, and for DJX-pit at 0.5 m, 50 m, and 80 m. For the inputs, measured cation and anion concentrations (in mol/L), pH, and oxidation-reduction potential (ORP) values were used (see Table A.2 for more details).

2.4.4 Asymmetrical flow field-flow fractionation

Filtered water samples collected for colloidal analysis were analyzed for the distribution of metals in the dissolved and colloidal (oxyhydroxides and organic matter) fractions. The analysis was completed using asymmetrical flow field-flow fractionation (AF4) equipped with an auto injector (AF200 and PN5300, respectively, Postnova Analytics), coupled to a UV-Visible absorbance detector (G4212 DAD, Agilent Technologies) and a quadrupole inductively-coupled mass spectrometer (iCAP Q ICP-MS; Thermo Scientific). The AF4 fractionation procedure is described elsewhere (Guéguen and Cuss, 2011). Ultrapure water and HCl were used to adjust the pH and conductivity of the ultrapure ammonium carbonate carrier fluid buffer (Sigma-Aldrich) in order to match the properties of the analyzed samples. Specifically, these adjustments were pH 7 and a conductivity of 300 µS/cm for D-pit and DJX-pit surface samples, and pH 6 and 1500 µS/cm for DJX-pit deep water samples based on Neubauer *et al.* (2013). The areas of the free, organic matter-associated, and oxyhydroxide-associated peaks were determined using statistical deconvolution as described in Cuss and Guéguen (2012).

2.4.5 Rock sample analysis

To obtain information about surrounding bedrock, rock samples (RockD, RockDJX) were collected on the steep shores of both pits in close proximity to the water, in order to acquire a qualitative measure of the metal contents in the circumambient rock of the pit. The rocks were ground with a mortar and pestle, and the mineralogy was determined by an Ultima IV XRD unit (Rikagu) from 5-90° 2θ using a cobalt X-ray source (λ = 1.790260). Data interpretation was performed with the JADE 9.5 software and using the 2013 ICDD and 2015-1 ICSD databases. To quantify metals concentrations for a qualitative sample comparison of the rock samples, 0.1 g of finely ground rock was digested with aqua regia (6 mL 37% HCl and 2 mL 70% HNO_3 at 130 °C) and analyzed by ICP-MS/MS.

2.4.6 16S-rRNA gene profiling

Prokaryotic diversity in the pit lakes was determined using 16S rRNA gene sequencing on selected unfiltered water samples from September 2015. DNA was extracted from the water samples using the PowerWater DNA Isolation Kit (Mobio). Fifteen mL of each water sample was filtered through 0.2 µm membranes using a vacuum unit and the membranes were processed according to kit instructions. Sequencing was performed by a dual-index paired-end sequencing approach on an Illumina MiSeq sequencer based on the method by Kozich *et al.* (2013). Post processing was done using a pipeline consisting of the following applications: Cutadapt and FastQC (quality control), Sickle (quality trimming), SPADes (Illumina MiSeq errors correction), Pandaseq (merging of paired reads), Qiime with UPARSE and Vsearch (removal of singletons and chimeras, building of OTU tables and phylogenetic trees, and for Shannon diversity).

2.5 Results

2.5.1 Limnology of D-pit and DJX-pit

Schematic diagrams of D-pit and DJX-pit can be seen in Figure 2.1, and are useful for understanding the different scales of the two locations. In September 2015, D-pit expressed one thermocline around 5 m and one major halocline between 12-13 m, accompanied by a pH decrease from 8.1 to 7.8 (Figure 2.2, left column). In June 2016, D-pit expressed a similar halocline at 12-15 m depth. Between 2-12 m depth a pH decrease from pH 7.3 to 6.2 was recorded. The dissolved oxygen concentrations in D-pit increased slightly within the first 2 m, decreased rapidly between 2-5 m, and then continued to decrease at a less rapid rate between 5-10 m. Corresponding to the oxygen curve, the ORP dropped from +200 mV (oxic conditions) to -300 mV (reducing conditions) between 12-20 m of depth. In this case, the upper 15 m can be referred to as mixolimnion, which by definition is affected by seasonal mixing.

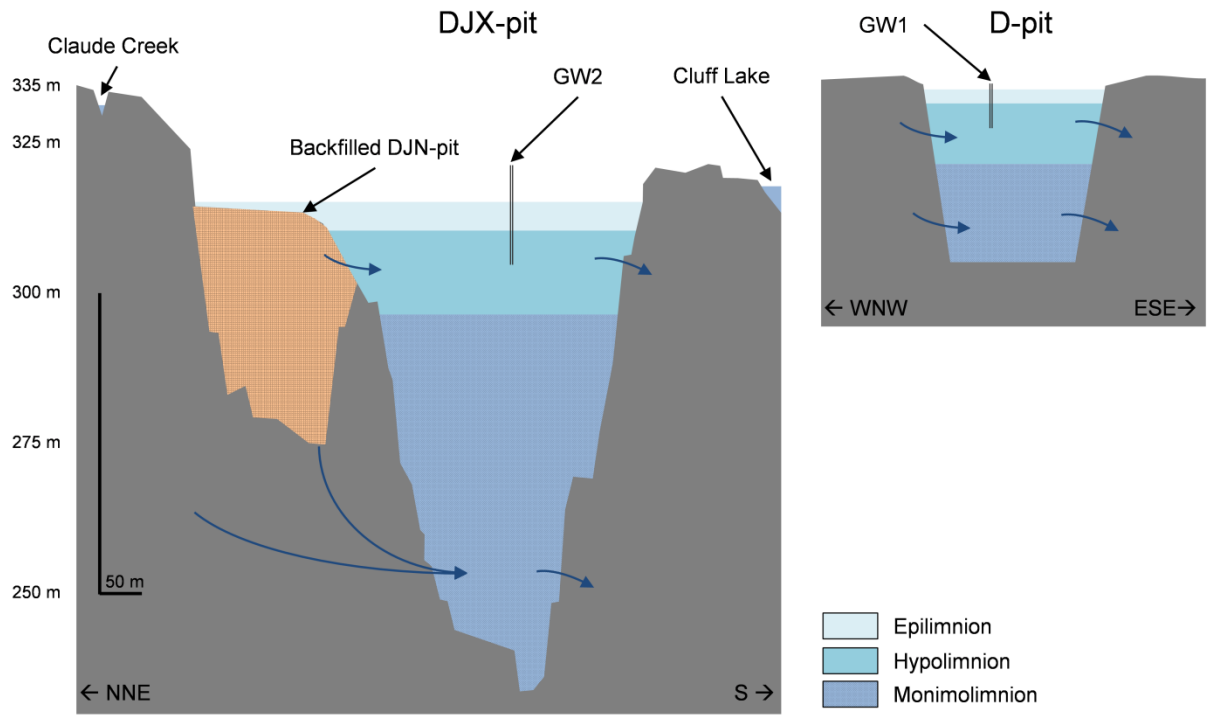

Figure 2.1: Schematic cross section through the DJX-pit (information provided by AREVA) and D-pit (rough estimation) showing the 3 different water layers in each pit. For comparison, the relative vertical positions and dimensions of the groundwater wells GW1 and GW2 are shown. The orientation of the cross sections is shown at the bottom. Vertical exaggeration is 6.5x. The curved blue arrows indicate potential groundwater inflow pathways. See Figure A.1 for a 3D DJX-pit model and for spatial location of GW2.

The DJX-pit showed a thermocline between 0-10 m in all data sets (Figure 2.2, right column). In June 2016, the depth of the thermocline was similar to September 2015, but was associated with a stronger temperature gradient. Across all data sets, four haloclines were identified around the following depths: 5 m, 17 m, 55 m, and 65 m. The halocline at 5 m depth was closely associated with an increase in oxygen (e.g., up to 11.6 mg/L in June 2016), likely due to primary production, which was followed by an oxygen decline to 20 m (as low as 4.4 mg/L) and a more moderate decline to the bottom (<0.9 mg/L). The pH was generally lower than in D-pit and decreased from pH 7.5 at 5 m depth to pH 5.5 below the halocline at 17 m depth. In the DJX-pit, the ORP was positive throughout the measured column (150-280 mV), which may result from redox interactions, e.g., by Mn(III/IV), NO_3^- (Schürling *et al.*, 2013) or even sulfate, because under low pH conditions, sulfate-reducing environments might result in higher measured ORP values (Church *et al.*, 2007, Falagán *et al.*, 2013).

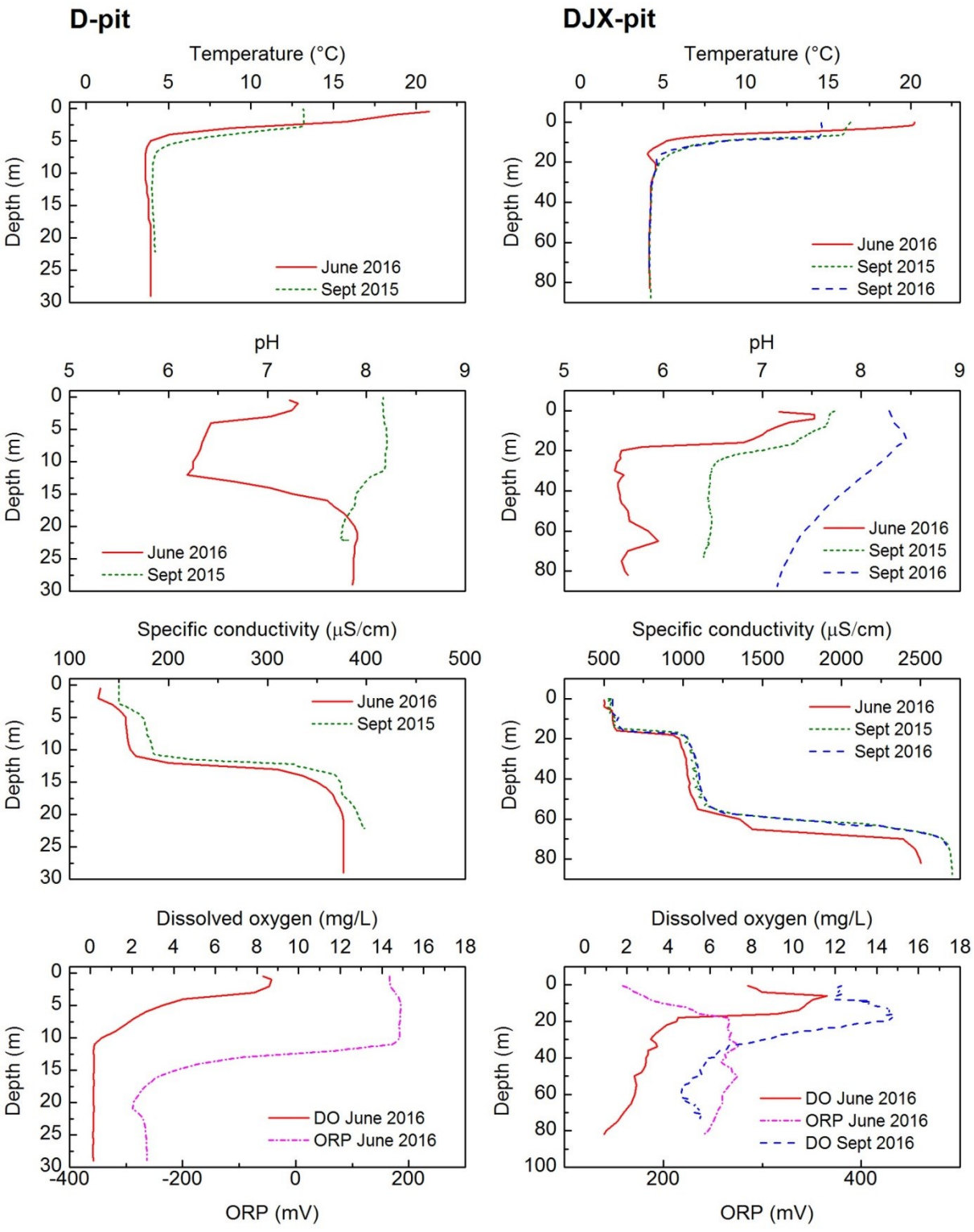

Figure 2.2: Limnological results (temperature, pH, specific conductivity, dissolved oxygen, and oxidative-reductive potential (ORP)) for D-pit (left) and DJX-pit (right) measured at the Cluff Lake site. Note the differences in depth (vertical scale) between the two pits.

2.5.2 *Distribution of metals and ligands*

In the D-pit, total carbon was 22 ppm at the surface, rising to 47 ppm at 17 m (Figure 2.3, left column and Table A.3). It was dominated by inorganic species; organic carbon remained between 4-13 ppm. No phosphate was detected in D-pit, likely due to precipitation with Fe (Jaeger, 1994). Sulfate was detectable above 13 m, coinciding with the depth of the halocline and the change of the ORP from positive to negative. Below this depth, no SO_4^{2-} or NO_3^- could be detected, however, N was present, indicating that more reduced nitrogen species are present. The reduction of SO_4^{2-} can result in the precipitation of iron sulfide phases with low solubility, forming in the presence of Fe^{2+} and the negative ORP below the chemocline (Sobolewski, 1999). In the D-pit, concentrations of B, Na, Mg, K, Ca, Mn, and Fe increased with depth (Table A.4 and Figure 2.3, left column). A significant increase in Fe concentrations was observed below 12 m depth, coinciding with a drop in ORP values and oxygen concentrations. This suggests that there was a shift towards Fe(III)-reducing conditions, as supported by the Fe speciation results discussed below. Further, Mn concentrations steadily increased from 0.2 ppm to 3.3 ppm. Nickel concentrations were low at the surface of the D-pit, with a concentration maximum of 9 ppb measured at the chemocline; Ni then became undetectable below 15 m (Figure 2.3, left column). The As concentration profile was similar to that of Fe, with the former increasing in concentration with depth from 2 ppb to 91 ppb and showing a small decrease at 20 m (76 ppb). The concentration profile of U was strongly linked to changes in pH. The drop to pH 6.2 between 4 and 12 m was associated with a decrease in U concentrations from 120 ppb at the surface to 64 ppb at 7 m depth. Below 11 m, U concentrations increased with increasing pH to 131 ppb (13 m) and stabilized below 16 m to around 90 ppb. A similar concentration trend was observed for Si (Table A.4).

In the DJX-pit, total carbon ranged from 5.4-13.8 mg/L (Figure 2.3, right column and Table A.5). DJX-pit carbon composition was similarly dominated by inorganic carbon; however, this trend reversed after 70 m, where the presence of organic carbon became more predominant. TOC was generally lower in deeper water layers of the DJX-pit compared to D-pit, in conjunction with the presence of oxygen. Sulfate-S values reached 78 mg/L at the 15 m halocline, up to 172 mg/L in the upper monimolimnion, and up to 476 mg/L near the bottom of the pit (82 m). Trace amounts of Se, V, Cd, Pb, Sb, Tl were detected by iCAP Q ICP-MS (Table A.6). The deep water of DJX-pit was rich in B, Na, Mg, K, Ca (dominant metal), and Mn, but depleted in Fe compared to the D-pit (Figure 2.3, right column and Table A.7). This pattern was likely due to the presence of oxygen in the deep-water layers of DJX-pit, leading to the precipitation of Fe(III) oxyhydroxides. Concentration curves of U, Ni, and Mn had similar shapes, with the two major chemoclines evident at 15 m and 65 m (Figure 2.3, right column). Based on the high Mn concentrations, the bottom water layers of DJX-pit were potentially in the redox transition zone between oxic and Mn(IV)-reducing conditions.

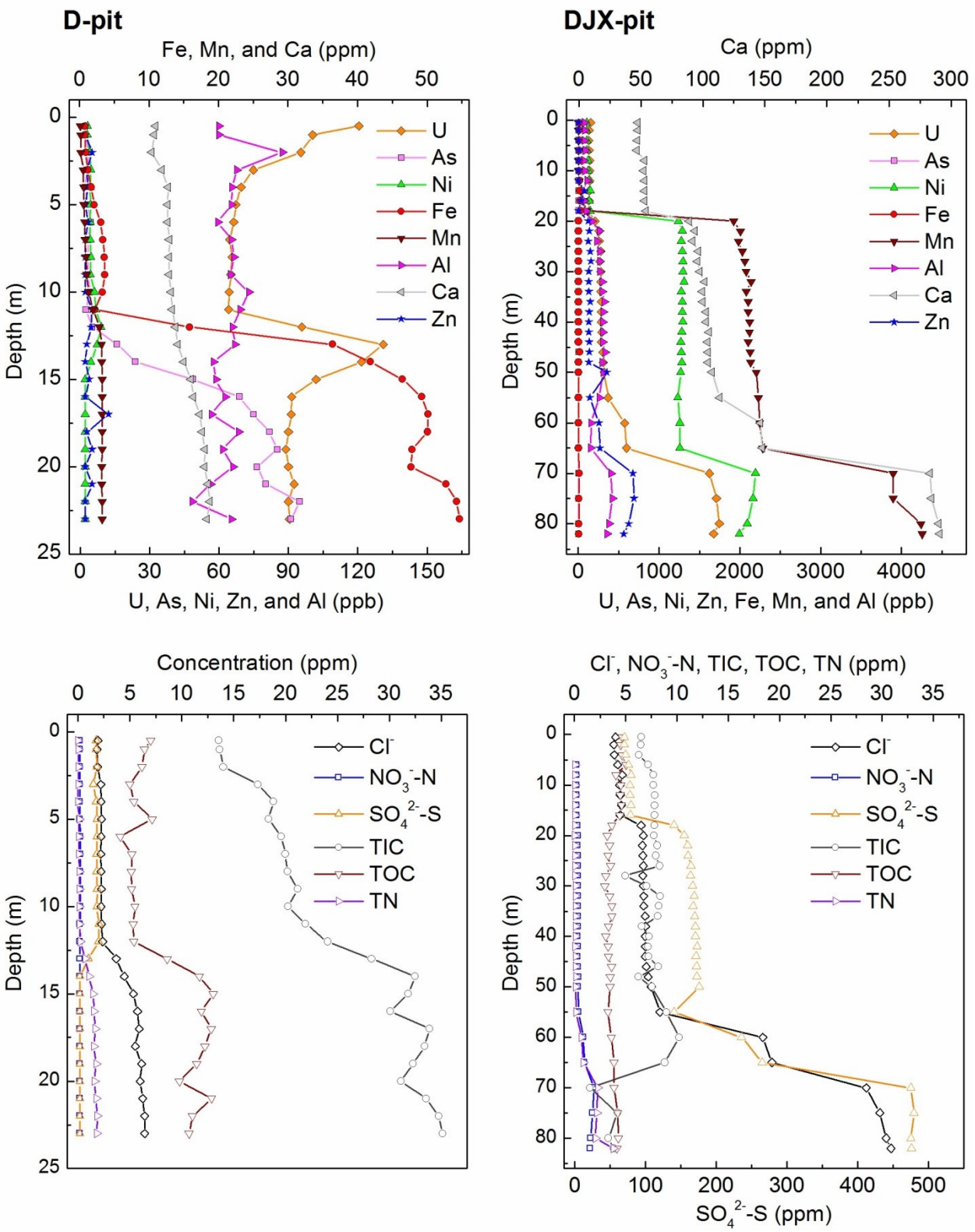

Figure 2.3: Measured cations, anions, carbon and nitrogen in the D-pit (left) and the DJX-pit (right) in June 2016.

In general, the DJX-pit metal concentration profiles indicate that stratification is an important control for metal distribution. A slight decrease was observed in the concentrations of U, Ni, and Zn (also Cu, as shown in Table A.7), which could indicate the beginning of the development of an anoxic zone below 82 m, where those metals might be precipitating as sulfides. Supporting this conclusion are the trace amounts of As at 80 m depth, which are nearly double those at the surface of the DJX-pit (Table A.6). The lower chemocline (65 m) was sharp, and was well developed for most metals in the DJX-pit (exceptions: Li, Al, and Si). This lower zone could be due to remnant mine water from the time when the pit was used for temporary mine water storage prior to being flooded with freshwater from Cluff Lake. Arsenic and Fe concentrations were low (<2 ppb and <28 ppb, respectively) throughout the water column. Results for DJX-pit obtained in September 2015 indicated higher Fe concentrations (4.6 ppm at 70 m, see Table A.8) compared to the June 2016 results (7 ppb), while Mn concentrations were marginally lower (3.6 ppm vs. 3.9 ppm at 70 m). Oxygen concentrations in the DJX-pit were lower in September 2015 (personal communication, CanNorth), suggesting that the bottom of the DJX-pit is not consistently oxygenated every year (see Discussion).

Metal concentrations, anions, carbon, and nitrogen results for the three sampled groundwater wells are shown in Table A.3 to Table A.7. A Piper diagram showing the water composition of these samples in relation to the pit water samples is shown in Figure 2.4. The well GW1, close to D-pit, was rich in Na (2.2 ppm), Mg (7.2 ppm), and Ca (11.4 ppm), while the Fe concentration was only 0.5 ppm. Well GW2, located at the northern end of DJX-pit, was rich in Na (125.9 ppm), Mg (49.5 ppm), K (12.5 ppm), and Ca (155.4 ppm), and had higher concentrations of Fe and Br compared to the pit water. GW3 had, in general, lower metal concentrations.

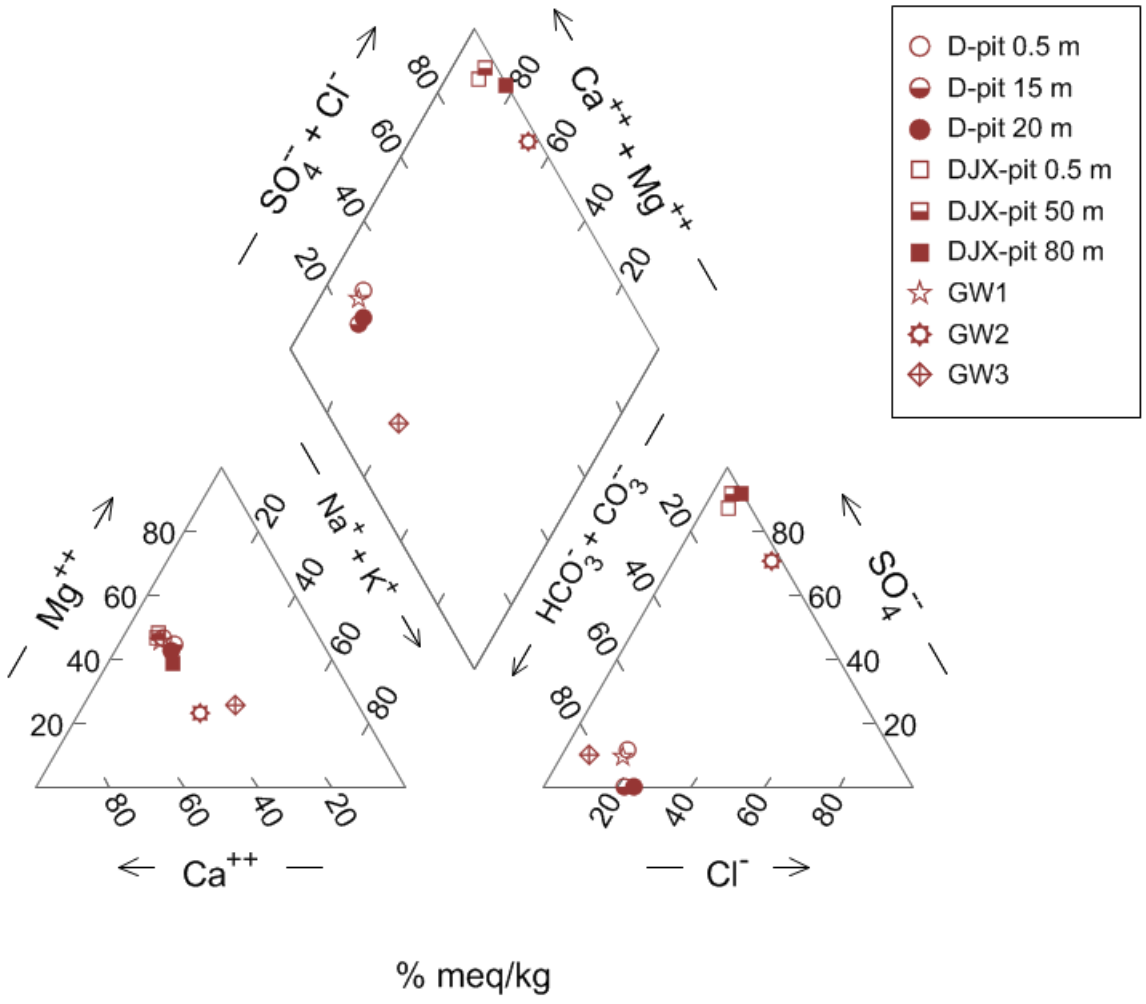

Figure 2.4: Piper diagram of selected D-pit and DJX-pit water samples and the 3 groundwater samples GW1 (DWW0041G), GW2 (MNW6210G), GW3 (HYD9846AG). Subdivisions based on Sadashivaiah et al. (2008). Carbonate and hydrogen carbonate data for GW2 and GW3 from AREVA (2013). Distinguishable groups can be seen in the diagrams. D-pit water and GW1 are found in the Magnesium-bicarbonate subdivision of the diamond. Water from the DJX-pit, however, is in the Calcium-chloride type subdivision, together with GW2. GW3 is on the border between the Magnesium-bicarbonate and the mixed-type subdivisions.

2.5.3 Analysis of rock samples from the pits

The major minerals identified in sample RockD from the shores of D-pit were quartz, anatase, clinochlore, muscovite, hematite, and sodalite (Figure A.2). RockDJX from DJX-pit displayed a similar major mineral composition, but lacked magnesiosilicate. Elemental analysis showed a high abundance of Al, Mg, K, and Fe, which was consistent with their mineral compositions (Table 2.1). In terms of U, Ni, and As, the two rock samples showed different patterns. RockD contains 10.8 ppm As, 15.3 ppm Ni, and 3.4 ppm U, while RockDJX had lower As and U concentrations (<0.5 ppm and 1.2 ppm, respectively), but higher Ni concentrations (26.4 ppm). The U concentrations of these two samples were typical of the continental crust average of 2.7 ppm (Taylor and McLennan, 1985).

The relative abundance of Al, Fe, As, and Ni in the water columns of the two pits match well with the concentrations found in the adjacent rock samples (Table 2.1). Rock samples and the water in DJX-pit had high concentrations of Al and Ni, while D-pit rock samples and water were more enriched in Fe and As. Some elements, however, showed opposite trends, such as Zn, Mn, and U.

Table 2.1: Metal contents in the rock samples from D-pit (RockD) and DJX-pit (RockDJX) determined by aqua regia digestion.

Element	RockD (ppm)	RockDJX (ppm)
Na	14.7	12.9
Mg	1705.7	5776.5
Al	3860.2	12049.8
K	1277.6	1352.3
Ca	470.2	120.7
V	35.8	11.3
Cr	37.4	12.8
Mn	646.7	16.4
Fe	20679.3	3266.6
Co	5.0	3.5
Ni	15.3	26.4
Cu	2.3	1.7
Zn	60.6	24.1
As	10.8	<0.5
Br	2.3	1.3
Sr	8.1	3.2
Ba	19.8	5.2
Pb	1.8	<0.5
U	3.4	1.2

2.5.4 Speciation of metals

In D-pit, Fe(II) concentrations increased with depth, with 78-80% of total Fe as Fe(II) in deeper water layers (Table 2.2). The results for D-pit demonstrate that there is a distinct shift in Fe speciation towards Fe(II) species below the depth where the ORP switches from positive to negative near 12 m. The groundwater close to D-pit (GW1) was dominated by Fe(III), with only 31% Fe(II). In DJX-pit, neither Fe(II) nor total Fe were detected by the ferrozine method, and only traces of Fe could be found using ICP-MS/MS. Water in well GW3, located west of the DJX-pit, also had no detectable Fe.

Table 2.2: Fe(II) and total Fe concentration determined by the ferrozine absorption method in the D-pit and the groundwater well close to it (GW1: DWW0041G. "n.d.": not detected).

Depth (m)	Total Fe	Fe(II)	
	ppm	ppm	% (of total)
0.5	n.d.	n.d.	-
5	0.92 ± 0.31	0.09 ± 0.13	9.7
10	1.26 ± 0.54	0.28 ± 0.22	22.7
15	52.25 ± 2.21	41.83 ± 1.02	80.1
20	51.59 ± 2.69	40.02 ± 1.60	77.6
GW1	0.93 ± 0.06	0.29 ± 0.03	31.4

IC-ICP-MS for D-pit samples showed the abundance of As(III) and As(V). In general, the sum of As(III) and As(V) were close to the total As concentration at each depth (Table 2.3). A marked shift in As speciation was observed between depths of 10 m to 13 m. The high concentrations of As in the D-pit below the chemocline are the result of the reducing conditions in the monimolimnion, which not only promote the reduction of Fe(III) but also the reduction and release of any bound As(V) species to the more mobile As(III) form. Arsenic speciation determination was problematic in the DJX-pit due to the presence of unknown As species and their co-elution with known peaks at determined retention times.

Table 2.3: IC-ICP-MS results for As speciation in the D-pit and total As based on iCAP Q ICP-MS.

Depth (m)	Total As	As(V)		As(III)	
	ppb	ppb	% (of total)	ppb	% (of total)
0.5	1.58	0.94	59.5	0.54	34.2
5	2.45	1.12	45.7	0.63	25.7
10	3.56	1.68	47.2	0.95	26.7
13	16.52	2.91	17.6	14.41	87.2
15	46.83	8.72	18.6	41.47	88.6
18	75.38	12.91	17.1	70.38	93.4
20	69.87	12.05	17.2	61.38	87.8
23	85.43	12.15	14.2	77.05	90.2

Thermodynamic modeling with PHREEQC showed a charge balance difference of >10% close to the D-pit chemocline and below (Table A.2), indicating that not all charge bearing components were fully identified and modeled. For example, colloid-bound metals and organometallic species might have a strong influence due to their abundance and high surface charge. As shown in Table 2.4, the model predicted the dominant U(VI) species to be $UO_2(CO_3)_2^{2-}$ and $UO_2CO_3^0$ for the top 10 meters of each pit. In D-pit, at the chemocline and at 20 m depth, $U(OH)_5^-$ was expected to dominate, whereas in the DJX-pit, $UO_2CO_3^0$, UO_2^{2+}, and $UO_2SO_4^0$ were predicted to become the dominant species in deeper layers. In the D-pit, the saturation index was positive for U_4O_9, UO_2, and $USiO_4$ at and below the chemocline. In the DJX-pit, U_3O_8 and U_4O_9 were saturated at 80 m depth. Precipitation of U(IV) species may explain the observed concentration drops in the D-pit of U and Si below 13 m depth (Table A.4). Compared to IC-ICP-MS results, As(V) species were overestimated for the D-pit surface water and underestimated for the deeper water layers. On the other hand, As(III) species were underestimated by the calculations above the chemocline at 13 m depth. $HAsO_4^{2-}$ and $H_2AsO_4^-$ were calculated to be the dominant As species in the DJX-pit at all depths. Nickel was predicted to be predominately $NiCO_3^0$ in the D-pit (up to 96%) and Ni^{2+} in the DJX-pit (up to 80%), but in the DJX-pit, due to high SO_4^{2-} concentrations, $NiSO_4^0$ (up to 28%) was also predicted.

Table 2.4: PHREEQC modeling results for U, As, and Ni at selected depths. The distribution of major calculated species (in %) and the saturation indices for solid species are shown. A similar table with molar concentrations can be found in the Appendix A (Table A.2).

			D-pit					DJX-pit		
Element	Ox. state	Species	0.5 m	5 m	10 m	13 m	20 m	0.5 m	50 m	80 m
U	U(IV)	$U(OH)_5^-$	0%	0%	0%	98%	100%	0%	0%	0%
		$U(OH)_4$	0%	0%	0%	1%	0%	0%	0%	0%
	U(VI)	$UO_2(CO_3)_2^{2-}$	83%	34%	24%	0%	0%	71%	1%	0%
		UO_2CO_3	14%	65%	75%	0%	0%	26%	77%	56%
		$UO_2(CO_3)_3^{4-}$	3%	1%	0%	0%	0%	2%	0%	0%
		UO_2OH^+	0%	0%	0%	0%	0%	1%	6%	9%
		UO_2^{2+}	0%	0%	0%	0%	0%	0%	10%	17%
		UO_2SO_4	0%	0%	0%	0%	0%	0%	4%	11%
	Saturation indices	U_3O_8	-3.7	-4.6	-4.3	-3.0	-16.0	-1.3	-2.8	0.6
		U_4O_9	-6.4	-4.1	-3.1	14.3	4.3	-2.4	-3.7	1.7
		UO_2	-2.7	-1.7	-1.3	5.4	4.0	-1.6	-1.9	-0.4
		$USiO_4$	-3.7	-2.4	-2.0	4.8	3.3	-2.8	-2.5	-1.0
As	As(III)	H_3AsO_3	0%	0%	1%	100%	98%	0%	0%	0%
		$H_2AsO_3^-$	0%	0%	0%	0%	2%	0%	0%	0%
	As(V)	$HAsO_4^{2-}$	77%	32%	25%	0%	0%	77%	8%	10%
		$H_2AsO_4^-$	23%	68%	75%	0%	0%	23%	92%	90%
Ni		$NiCO_3$	79%	31%	22%	50%	96%	52%	0%	0%
		Ni^{2+}	19%	63%	72%	45%	4%	40%	80%	72%
		$NiHCO_3^+$	2%	5%	5%	5%	1%	2%	0%	0%
		$NiSO_4$	0%	0%	1%	0%	0%	6%	19%	28%

2.5.5 Colloidal metal fractions

Colloidal fraction analyses for D-pit indicated high variability with depth with regards to the distribution of metals between free ions, dissolved organic matter (DOM) and oxyhydroxide fractions (Table A.10 and Table A.11). For most of the metals investigated, the free ion phase was the dominant species. An exception was Al, which was predominantly in the DOM and oxyhydroxides size fractions, which may indicate the presence of colloidal aluminosilicates (Filella, 2006). This was particularly evident in D-pit, where DOM contributed up to 67% (5 m) of the Al, while oxyhydroxide contributions made up the remaining 33% (0.5-5 m). In contrast, in the DJX-pit the DOM size fraction (up to 59%) and the oxyhydroxide fraction (up to 23%) only played a role in Al partitioning in the surface waters (0.5-10 m).

For U, Ni, and As, the colloidal distribution in the two pit lakes was different (Figure 2.5). In the mixolimnion of the D-pit, U was mostly associated with the oxyhydroxide size fraction (up to 12%), with a small contribution by DOM (up to 3%). At 0.5 m, 5 m, and 10 m, there was a progressive increase for U in the oxyhydroxide size fraction with 0%, 7%, and 12% being colloidal, respectively (Figure 2.5). This fraction then dropped to 2% at the chemocline. This pattern was inversely related to the pH (Figure 2.2)

and U concentrations (Figure 2.3) in the mixolimnion of the D-pit. Nickel was scarce in the D-pit water column, however, up to 34% of Ni in the mixolimnion, and all Ni found at 20 m depth was in colloidal form (DOM). For As in the D-pit, the oxyhydroxide size fraction played an important role, hosting up to 42% of the total As in the oxic water layers. Below the chemocline (13 m) As was mostly found as a free ion, suggesting that in contrast to U, As was not binding to reduced particulate organic matter.

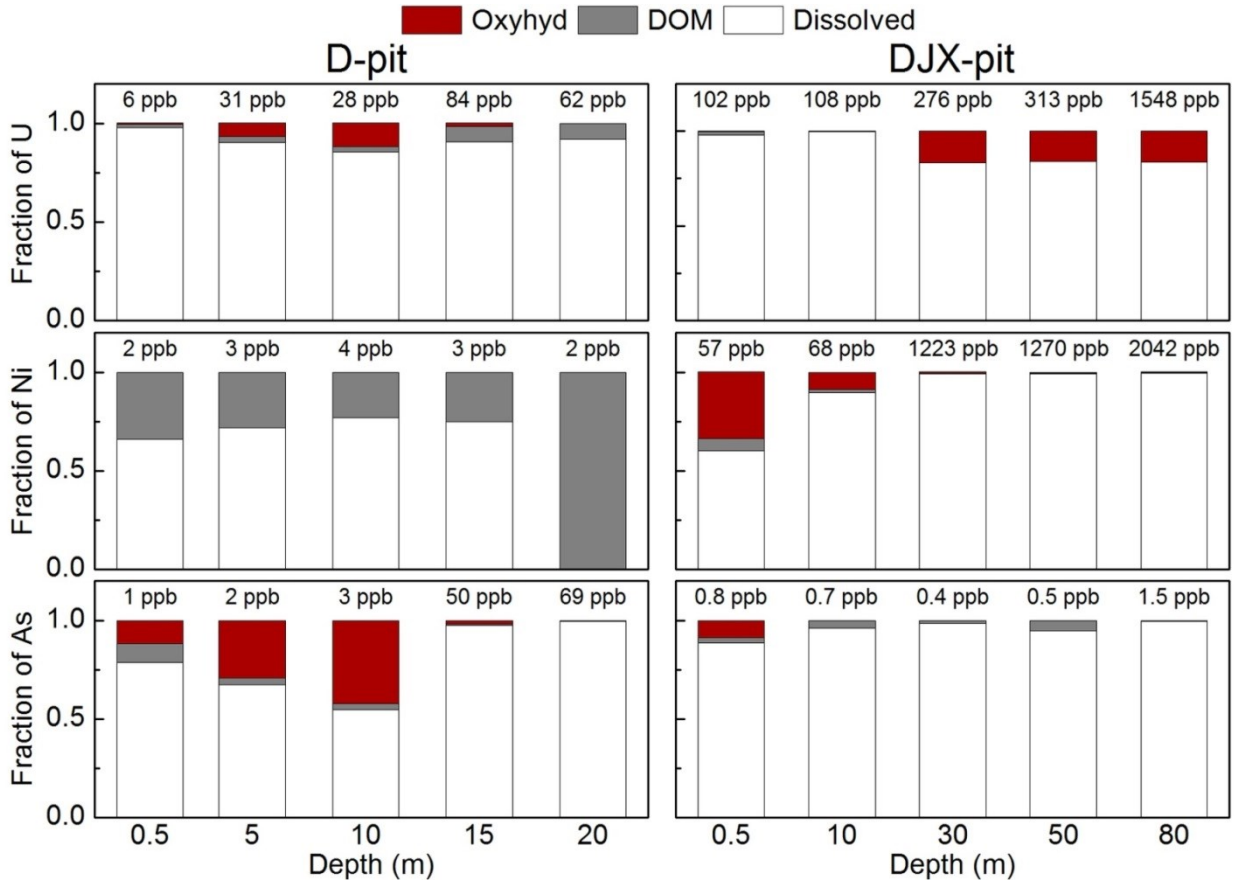

Figure 2.5: Colloidal distribution of dissolved, organic matter associated (DOM), and oxyhydroxide associated (Oxyhyd) U, Ni, and As in the D- and DJX-pit lakes. Distribution of other metals can be found in Table A.10 and Table A.11. Example fractograms for U, Ni, and As are presented in Figure A.3.

In the DJX-pit, colloidal U (associated with oxyhydroxides) was only relevant in the samples below the upper chemocline (>30 m) where it contributed approximately 16% of total U. The same colloidal material also carried minor amounts of Al (0.9-1.8 ppb), but no Fe or Mn (Table A.11), which might indicate that the U-bearing colloids were Al oxyhydroxides. Despite high (>2.1 ppm) Ni concentrations below 20 m depth of the DJX-pit, colloidal Ni was only present above 30 m. At 0.5 m, Ni was bound to colloidal DOM (6%) and oxyhydroxides (33%). Below 10 m the colloidal Ni contribution was <1%, which might suggest that DOM-sized colloids are more important for Ni transport (as in D-pit); however, those particles are respired in deeper layers of the oxygenated DJX-pit. Arsenic concentrations were <1.5 ppb and colloidal As was only detected in the surface water sample (0.5 m), dominantly in the form of oxyhydroxides (9%).

Other metals that were largely represented in the oxyhydroxide fraction were Fe in the mixolimnia of the D-pit (32%) and DJX-pit (25%), and Co in the mixolimnion of the DJX-pit (24%). Despite the high concentrations of Mn in both pit lakes, only the D-pit showed the presence of colloidal Mn (up to 6%). Therefore, the observed oxyhydroxides are expected to contain mainly Al, and some Fe (mostly D-pit). The presence of such colloids was also predicted by PHREEQC calculations, which indicated oversaturation for mineral phases, including boehmite, diaspore, nontronite, and hematite (data not shown).

2.5.6 Microbial communities

The relative distribution of phylogenetic classes, as determined by 16S rRNA gene sequencing, revealed a high microbial diversity within the two pit lakes (Figure 2.5). Qualitatively, the classes with the highest representation in the water column were Alphaproteobacteria, Betaproteobacteria, Gammaproteobacteria, Actinobacteria, and Flavobacteria. Metal reduction studies in groundwater have suggested that Actinobacteria are most active at circumneutral pH and when NO_3^- is absent (Williams *et al.*, 2013), which was the case for the two pit lakes. In the D-pit, the classes Acidobacteria, Holophagae, and Acidimicrobia were found in greater abundance than in the DJX-pit, whereas the latter showed a higher abundance of Sphingobacteria. The calculated Shannon diversity indices were highest close to the chemoclines in both pits (Figure A.4). Specifically, the highest indices were found for D-pit at 5 m depth (7.1), followed by DJX-pit at 70 m (6.9) and D-pit at 15 m (6.4). Lowest diversity indices were calculated for DJX-pit at 20 m (5.0) and D-pit at 0 m (4.6). The highest microbial diversity in the D-pit was, therefore, linked to the thermocline around 5 m and the redox transition zone with the highest ORP gradient at 15 m. Similarly, in DJX-pit, the diversity increase was related to the deep chemocline at 65 m. These findings are consistent with other authors (Falagán *et al.*, 2013, 2014) that showed that highest diversity and abundance in meromictic lakes is linked to the chemoclines.

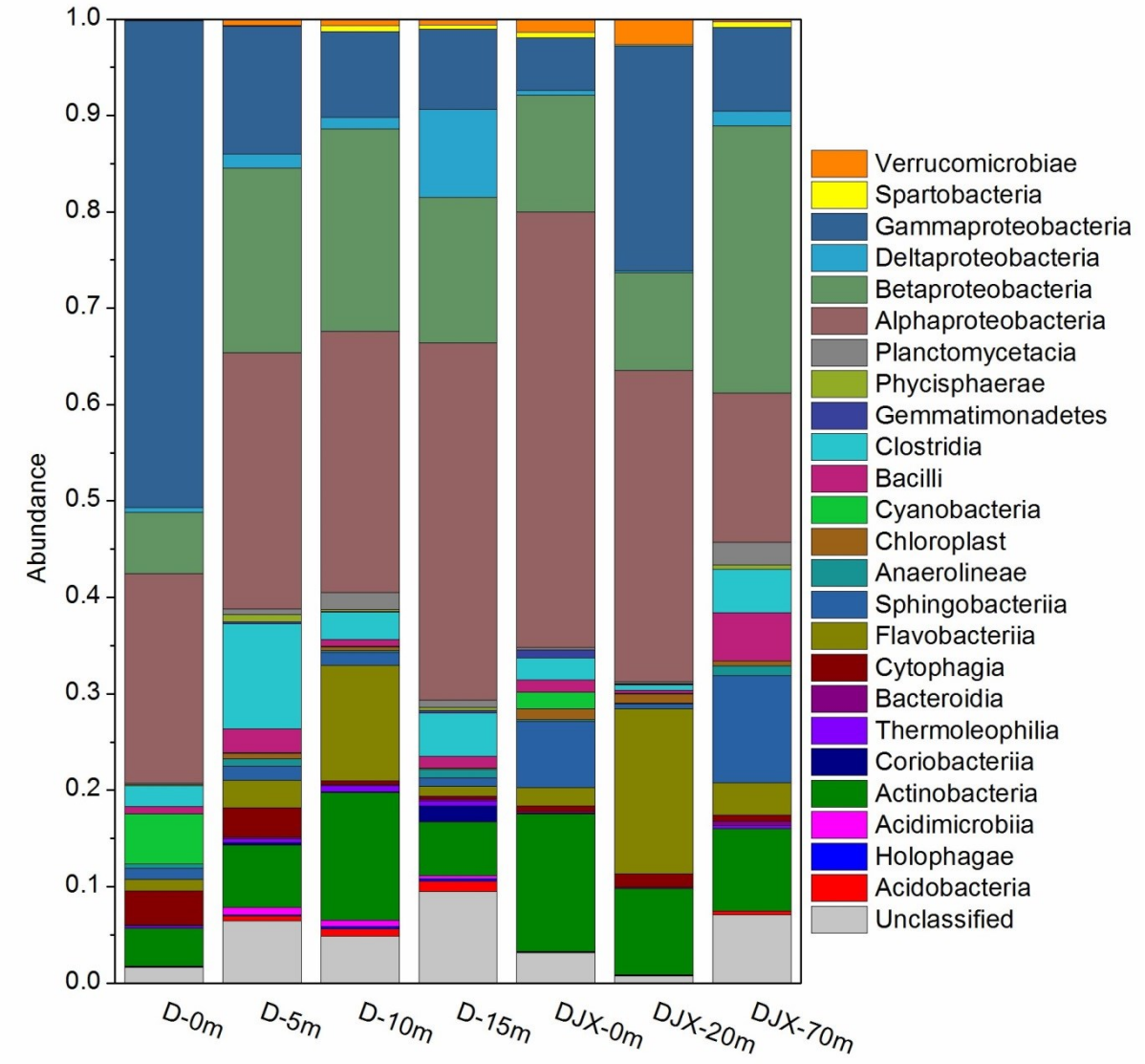

Figure 2.6: Distribution and abundance of microbial communities by phylogenetic class in the waters of the D-pit and DJX-pit by 16S rRNA assay, showing a markedly diverse microbial population.

Dominant prokaryotic taxa are summarized in Table A.12. One of the most abundant species in both pits was a close relative to *Arthrobacter sp.*, an Mn(II)-oxidizing species which has been previously identified at uranium mine sites (Bohu *et al.*, 2016). Its highest abundance was observed at 20 m depth of the DJX-pit, where an increase in Mn concentrations from 0.1 ppm to over 2 ppm occurred, suggesting that increased mobility of Mn made it more bioavailable to bacteria. With the presence of oxygen at this depth in the DJX-pit, oxidation of complexed Mn(II) would be possibile. A close relative to another dominant species, *Alkaliphilus peptidifermentans strain Z-7036*, was particularly abundant at the depth of the thermocline. This spore-forming aerotolerant anaerobic organism is known to reduce Fe(III) (Zhilina *et al.*, 2009). Microorganisms closely related to those associated with U(VI) reduction, such as *Desulfosporosinus orientis* (also SO_4^{2-} reducing), *Clostridium acetobutylicum, Geobacter uraniireducens*,

Geobacter metallireducens, and *Geobacter sulfurreducens* (Williams *et al.*, 2013), were also found in both pit lakes. Species of the named genera were previously shown to be stimulated during in situ U(VI) reduction experiments (e.g., Xu *et al.*, 2010; Van Nostrand *et al.*, 2011; Alessi *et al.*, 2014a). With the exception of the close relative to *Geobacter sulfurreducens*, the species discussed above were more abundant in D-pit than DJX-pit, especially close to the chemocline (10 m sample). *Geobacter uraniireducens* is mainly an Fe(III)-and Mn(IV)-reducing microorganism, which can grow at temperatures above 10°C (Shelobolina *et al.*, 2008). Its growth might be seasonally limited to the water layers above the thermoclines of the pits at 5 m (D-pit) and 20 m (DJX-pit), respectively. The pH range below 5 m depth may further limit growth, as *Geobacter uraniireducens* is best suited to pH conditions between 6.0-7.7. Despite those limitations, a microorganism most closely related to *Geobacter uraniireducens* was present in all water depths of both pit lakes. A bacterium related to *Geobacter metallireducens*, a strict anaerobic bacterium capable of reducing Fe(III), Mn(IV), and U(IV) (Lovley *et al.*, 1993a), was detected in deeper layers of the DJX-pit (70 m) and D-pit (15 m). Also capable of U(VI) reduction, *Desulfosporosinus orientis DSM 765* is a strictly anaerobic Gram-negative bacterium, which can grow chemoheterotrophically using SO_4^{2-} or thiosulfate as electron acceptors, or autotrophically with hydrogen and SO_4^{2-} (Stackebrandth *et al.*, 1997). A close relative to this bacterium was less abundant in the DJX-pit than the D-pit, even with the higher concentrations of U and SO_4^{2-}, highlighting its preference for anoxic environments.

One Betaproteobacterium species was most closely related to *Rhodoferax ferrireducens*. This phototrophic bacterium was more abundant in D-pit, especially at the chemocline, which was consistent with the concentrations of Fe(II) found in this pit. Another bacterium, which is often found with higher Fe concentrations is *Sideroxydans lithotrophicus*, which is known to oxidize Fe(II) (Emerson and Moyer, 1997); a close relative was abundant in deeper layers of the D-pit where higher Fe concentrations prevailed, suggesting that the increased bioaccessibility of Fe in those layers, combined with potential oxygen diffusion at the chemocline, would favor its presence. Bacteria possibly capable of As(III) oxidation were found in both pits, such as representatives of the genus *Rhizobium* (Campos *et al.*, 2009; data not shown) or some *Pseudomonas* strains (Paul *et al.*, 2014). A Betaproteobacterium most closely related to the As(III)-oxidizing bacterium *C05* was only found in the D-pit and predominantly in the mixolimnion. Representatives of the previously described genera *Geobacter*, *Desulfosporosinus,* and additionally *Alkaliphilus,* are all capable of dissimilatory As(V) reduction (Giloteaux *et al.*, 2013). Microorganisms from these genera were found in both pits, but they were more abundant in the zone close to the chemocline of the D-pit.

2.6 Discussion

2.6.1 Geochemical metal cycling

In both pit lakes, meromixis influences the cycling of the major contaminants, especially U and As. Both pit lakes had pH >7 at the surface and were likely influenced by photosynthesis and CO_2 exchange

with the atmosphere that can lead to strong carbonate complexation of U. Due to intrinsic acid generation from the surrounding waste rocks and aerobic respiration of organic materials, the pH dropped with increasing depth (Figure 2.2). However, the sharp change in the ORP in the D-pit prevented the acidification below the chemocline as a consequence of Fe(III) and SO_4^{2-} reduction, metabolisms that both lead to the generation of bicarbonate (Boehrer and Schultze, 2008; Geller *et al.*, 2012). Iron in general was one of the drivers for the stratification of the D-pit (Boehrer and Schultze, 2008; Bohrer *et al.*, 2017). Additionally, this Fe cycling could be the key driver for U concentration changes in this pit, as summarized in Figure 2.7. The Fe and U redox couples have similar potentials and small changes in water chemistry can turn reducing agents into oxidizing agents (Du *et al.*, 2011). For instance, Fe(II) could diffuse upwards through the chemocline to reduce U(VI) (Liger *et al.*, 2009). This leads to U(IV) precipitates forming above the chemocline, which could then drive down the total U concentration just above the chemocline. U(IV) precipitates might subsequently get oxidized back to soluble U(VI) by forming Fe(III)-bearing colloids, causing an increase in total U at 13 m depth; this is supported by oxygenic photosynthesis at this depth (Figure A.5). Below the chemocline, alkaline conditions lead to strong carbonate complexation of U(VI), which was supported by the increasing TIC concentrations (Figure 2.3). Carbonate complexation prevents U(VI) from being reduced completely by Fe(II) and S(-II) (Anderson *et al.*, 1989). The reductive dissolution of amorphous Fe(III) oxyhydroxides, and other Fe minerals in the D-pit, release mineral-bound and co-precipitated As causing its concentrations to rise below 13 m depth. Reducing conditions also favored the formation of organic colloids that can contribute to the Ni and As transport (Figure 2.5).

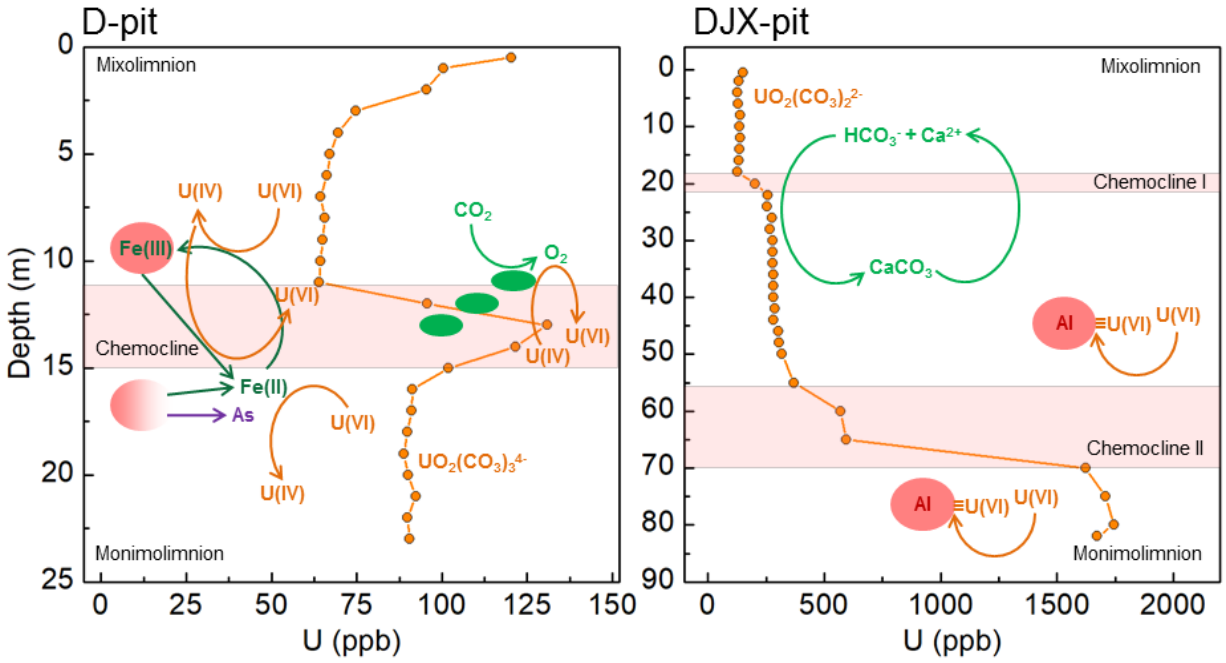

Figure 2.7: Schematic summary of ongoing processes influencing the stratification and distribution of U in both pits. In the D-pit (left) the Fe cycling drives the reduction and oxidation of U in the mixolimnion and at the chemocline, together with photosynthesis. Carbonate complexation in deeper water layers keep U(VI) in solution even under anoxic solutions. In the DJX-pit (right) Ca cycling is the driving force behind the stratification and Al oxyhydroxides drive the accumulation of U in deeper water layers.

Colloids in the D-pit might also contribute to U cycling by scavenging U(VI) from the water column. Indeed, speciation models for the mixolimnion predicted a decrease in negatively charged U(VI) species due the decreasing pH (Table 2.4). The anionic species, $UO_2(CO_3)_2^{2-}$ and $UO_2(CO_3)_3^{4-}$, are calculated to make up approximately 86% of all U species at 0.5 m. This fraction decreased to 35% at 5 m and 24% at 10 m, concomitant with the neutrally charged $UO_2CO_3^0$ becoming the dominant species. At a pH of 6.0-6.5, $UO_2CO_3^0$ is more likely to sorb to hydroxyl groups of the oxyhydroxide colloids, which can agglomerate to form larger particles and remove U from solution. At the chemocline, aqueous U(IV) was predicted to be present mostly as $U(OH)_5^-$. However, the abundance of Fe or Al oxyhydroxide colloids progressively decreased with depth, and in the monimonlimnion, DOM became the dominant U bearing colloidal phase (up to 8% of total U). In the D-pit, the oxyhydroxides also played an important role for As, and hosted up to 42% of the total As in the mixolimnion (Figure 2.5), which was likely due to As co-precipitation onto Fe oxyhydroxide particles (Slowey *et al.*, 2007).

Meromixis in the DJX-pit was predicted by Dessouki *et al.* (2005), who performed phosphate fertilization experiments in the pit before it was completely flooded. In the DJX-pit no change in ORP was observed and the pH dropped to 5.5 after the first chemocline (Figure 2.2). This pit illustrates a “stairs-like” meromixis type that could be influenced by Ca (Boehrer and Schultze, 2008; Boehrer *et al.*, 2017). The formation and precipitation of $CaCO_3$ in the upper 20 m, and its subsequent dissolution below the chemocline, might lead to the accumulation of Ca in deeper water layers, which further stabilized the stratification (Figure 2.7). The DJX-pit might also be influenced by Mn cycling (Boehrer and Schultze, 2008; Boehrer *et al.*, 2017). Mn(IV)-oxides could be precipitating in the well oxygenated water but then get reduced to Mn(II) at the very bottom of the water column, inducing a rise of Mn concentrations which would increase stratification stability. A similar “stairs-like” meromixis was found in the Cueva de la Mora pit lake in Spain, which was not only due to double-diffusive convection processes but was likely also induced by sulfate- and metal-laden groundwater inputs entering the mine through intersecting galleries (Schultze *et al.*, 2017). Al-bearing colloids could be responsible for additional U accumulation in deeper water layers (Figure 2.5). Similarly, removal of As by precipitating Al oxyhydroxides was proposed by Sánchez-España *et al.* (2016) in the San Telmo acidic pit lake (Spain).

In general, due to the oxic conditions, colloidal transport of metals in the DJX-pit was limited to oxyhydroxide particles. There are a number of potential hypotheses that may explain the presence of oxygen in the lower layers of DJX-pit. For example, oxygen may still be present from the days of flooding, due to the low oxygen demand of deeper DJX-pit layers, or there may be oxygenated groundwater inputs to the lower layers (Geller *et al.*, 2012). Some of the wells located north of the DJX-pit, lying in an area that is hydrologically upgradient of the pit, were tested in June 2017 and found to contain oxygen. Examples are the wells shown in Figure 1.5: HYD07-11G (11.8 m deep) with 3.1 mg/L oxygen and HYD06-03G (5.0 m deep) with 3.5 mg/L oxygen. Additionally, the bedrock in the mining area is fractured and weathered (AREVA, 2009), which may favor input of oxygenated groundwater. Therefore, the DJX-pit

may not truly be meromictic, since, under this scenario, renewal of the monimolimnion with oxygen-containing water is quite uncommon. Although groundwater inputs might destabilize the pit's stratification by reducing the salinity in the monimolimnion (Pieters and Lawrence, 2014), the opposite appears to be the case in the DJX-pit. The concentrations of SO_4^{2-}, Cl^-, B, Na, Ca, and Br found in the groundwater well GW2 (Table A.5 and Table A.7), north of the DJX-pit, suggests that higher salinity groundwater is moving from the north towards the DJX-pit. This plume might be partially responsible for the chemocline at 65 m depth, bringing in not only the above mentioned anions and cations, but also Ni and U that had eluted from the waste rock in the backfilled DJN-pit and the adjoining bedrock (Figure 2.1). The observation of oxygen in the DJX-pit might be explained by occasional mixing processes. The shallower portion of the pit, over the backfilled DJN, could be cooling faster in the winter causing this oxygenated water to slide down toward deeper layers and leading to episodic deep water renewal, a process previously observed in Lake Malawi (Boehrer and Schultze, 2008). However, further investigations of the shallower portions of the pit would be needed to refine the understanding of this and other potential sources of oxygen in the lower layers of the DJX-pit.

The high relative depth of both pit lakes is likely a key contributor to their stable stratification (Pieters and Lawrence, 2014). D-pit and DJX-pit have relative depths of 20% and 27%, respectively and formation of an ice cover every year promotes stable chemoclines in both pits. Factors that might disturb meromixis in the case of D-pit and DJX-pit are rock falls, landslides (Figure A.6), surface water inputs, and potential changes in groundwater flow.

2.6.2 Microbial communities in comparison to acidic pit lakes and additional remarks

The overall microbial composition in the Cluff Lake pits was different from previously studied acidic (pH 2.5-4.5) pit lakes, such as Cueva de la Mora and Guadiana in Spain (Falagán *et al.*, 2013, 2014). Bacteria dominant in those two lakes, including *Leptospirillum sp.*, *Acidithiobacillus sp.*, *Metallibacterium sp.*, *Thiomonas sp.*, and *Desulfomonile sp.*, were not detected in the Cluff Lake pits. Generally, compared to the acidic pit lakes, Acidobacteria and Deltaproteobacteria were less abundant in the Cluff Lake pits (Figure 2.6). On the other hand, bacteria reported to be related to *Desulfosporosinus sp.* (see above) were found, and they were more dominant in the pH-neutral D-pit, likely due to the anoxic conditions found there (Falagán *et al.*, 2014). Relatives of the acidophilic and aerobic bacterium *Alicyclobacillus sp.* (Chang and Kang, 2004), which was previously identified in acidic pit lakes (Falagán *et al.*, 2013, 2014) were also found at the chemocline of the D-pit. Falagán *et al.* (2014) identified various archaea of the order Thermoplasmatales and the phyla Thaumarchaeota and Crenarchaeota in the acidic pit lakes. In this study, relatives of Thermoplasmates were identified mostly in the DJX-pit and Thaumarchaeota were only detected in the water column of the D-pit. Crenarchaeota were not detected in either of the pits.

16S rRNA analysis confirmed the presence of U(VI) reducers, however, the situation is less clear concerning U(IV) oxidizers. Relatives to the well-known U(IV) oxidizer *Thiobacillus denitrificans* were not detected, although the possibly present *Geobacter metallireducens* is known to be able to oxidize uranium

under nitrate-abundant conditions (Borch *et al.*, 2009). However, based on previously discussed data, such conditions were not prevalent in the two pits. Except for the deeper water layers of the DJX-pit, nitrate was not abundant in the water columns. This nitrate in the deeper DJX-pit layers could be accumulated residue from nitrogen-containing blasting agents used in the mining process (Bailey *et al.*, 2013).

The detection of a relative of *Acidovorax defluvii strain BSB411* could be related to low abundance of nitrate in the upper water layers of both pits, because *Acidovorax defluvii* is known to carry out nitrate reduction (Schulze *et al*, 1999). Another potential and highly represented nitrate reducer was a relative to *Massilia brevitalea (T); byr23-80* (Zul *et al.*, 2008), which was highest abundant in the D-pit at 5 m depth. However *Massilia brevitalea* would produce nitrite, which was not detected in either of the two pits. A relative to the Gram-negative, methanotrophic bacterium *Methylobacter tundripaludum strain SV96* (Wartiainen *et al.*, 2006) showed a strong presence in the D-pit at 10 m and 15 m, suggesting that methane might be produced in the water column of the pit.

2.6.3 Potential for enhanced remediation

The meromictic behavior of the investigated pit-lakes opens potential opportunities by enhancing the use of pit lakes as a remediation strategy by promoting metal precipitation in the monimolimnia (Fisher and Lawrence, 2006; Pieters and Lawrence 2014). For example, the application of fertilizer over longer time periods would enhance algal growth in the mixolimnion, which may lead to enhanced metal removal from this layer through metal sorption and uptake by algal cells, as demonstrated previously over a shorter term in the DJX-pit by Dessouki *et al.* (2005). Fertilization with phosphorus was observed to increase the removal of metals (e.g., U, Ni, Zn, Mn, Cu, As) from the surface water and their accumulation the sediments. Metal removal through fertilization was also achieved in the Island Copper Mine pit lake (Canada) through the addition of nitrogen and phosphorus (Schultze *et al.*, 2017). An additional effect of fertilization could be the stimulation of sulfate-reducing bacteria (such as *Desulfosporosinus orientis*) in the monimolimnion, which would promote the formation of insoluble sulfide minerals, such as NiS, in the DJX-pit. Arsenic sulfides might form and could lead to the coprecipitation of As(III) with ferrous sulfides in the D-pit, as been seen in the Cueva de la Mora pit (Schultze *et al.*, 2016). Similarly, in the Island Copper Mine pit lake, metal removal from the mixolimnion through the formation of sulfides at the chemocline was found to be an efficient process (Schultze *et al.*, 2017).

The formation of insoluble sulfides might also lead to the development of a significant U sink, as sulfide particles can remove U from the water column though sorption (Wersin *et al.*, 1994; Diez-Ercilla *et al.*, 2014). Moreover, reducing conditions could promote the precipitation of U(IV) through *Desulfosporosinus orientis*, *Geobacter* species or other U(VI)-reducing organisms, when sufficient electron donors are available (Williams *et al.*, 2013). Differing remediation approaches would likely be required between D-pit and DJX-pit, as their redox conditions vary considerably. The presence of oxygen in deeper layers of the DJX-pit, if it persists, could influence remediation outcomes. The formation of anoxia in the DJX-pit

through fertilization could initiate the formation of sulfides and U(IV) precipitation, but they are likely to already take place in the D-pit. In contrast, the addition of sulfate, e.g., as gypsum (Lueders and Friedrich, 2002; Kijjanapanich *et al.*, 2014), to D-pit might provide an electron acceptor for SO_4^{2-} reducing bacteria, including those which are known to actively reduce U(VI). Additionally, iron sulfides (e.g., mackinawite) might form and abiotically reduce U(VI) (Bargar *et al.*, 2013; Veeramani *et al.*, 2013; Alessi *et al.*, 2014a). Although reducing conditions are known to increase the bioaccessibility of As, in the long term, precipitates such as orpiment (As_2S_3) and realgar (AsS) might partially remove As from the water column.

2.6.4 Further future considerations

The chemoclines in both pits are very dynamic as can be seen in AREVA (2013) and more recent data (not published). From 2007 to 2015 the D-pit chemocline rose from 14.75 m depth (AREVA, 2013) to approximately 10.25 m (unpublished data), which corresponds to a rise of 0.56 m/year. At the same time the elevation of the surface water was not changing considerably, on average -4 cm/year (AREVA, 2013). However in 2016, a deeper chemocline was observed (12.25 m), indicating that a stabilization of the upper layer might be taking place. On the other hand, both chemoclines of the DJX-pit are travelling deeper. The upper chemocline went from 13 m in 2006 (AREVA, 2013) to 16.5 m in 2015 (unpublished data), which corresponds to a lowering rate of 0.39 m/year. The lower chemocline went from 57.5 m in 2006 (AREVA, 2013) to 62 m in 2015 (unpublished data), with an average lowering rate of 0.50 m/year. However, conclusions cannot be easily drawn for DJX-pit because of the quickly changing surface elevation. For example, the surface rose from 312.5 m in 2006 to 319.5 m in 2012 with an average rising rate of 1.16 m/year (AREVA, 2013).

The rising chemocline in the D-pit might have consequences for its future stability. According to Fisher and Lawrence (2006) the critical upper layer (mixolimnion) depth can be calculated, at which the chemocline will be eroded and the monimolimnion will be intermixed with the mixolimnion. This depth is depending on the wind forces predominating in the area and the pit geometry. The predominant wind speed can be estimated to be 5 m/s based on the regional wind rose (AREVA, 2013). The density of the water layers was estimated by weighing the collected samples and by correcting the measured density by the temperature[2]. With this the critical upper layer depths can be estimated to be 0.33 m and 1.84 m for D-pit and DJX-pit, respectively. With the previously mentioned rising rate (0.56 m/year) of the chemocline in the D-pit, this depth might be reached in 2071, if no slowdown would be taking place. By considering the lowering of the chemocline in 2016, an average chemocline rising rate of 0.36 m/year can be calculated and the critical depth might only be reached in the year 2102.

2.7 Concluding remarks

Our study provides new insights on the geochemical behavior of dissolved and colloidal metals in meromictic pit lakes in a subarctic climate. Meromixis was found to determine the metal distribution,

[2] http://www.engineeringtoolbox.com/fluid-density-temperature-pressure-d_309.html

speciation and colloidal formation in the pit lakes at Cluff Lake. The redox state and mineral composition of the bedrocks of the pits have led to the formation of two types of stratification. Strong reducing conditions in the monimolimnion of the D-pit led to increased As concentrations (mostly As(III) species), but did not promote the precipitation of reduced U minerals, likely due to U stabilization by carbonate complexation. The chemocline of this pit is a highly dynamic zone, governed by the cycling of Fe. In contrast, the oxic conditions and high Ca and Mg concentrations in the DJX-pit with a staircase-like stratification, led to low As concentrations in the water column and an accumulation of U and Ni at the pit bottom. In both pits the association of metals with colloidal particles could be observed. Potential U(VI)-reducing microorganisms were mostly found near the chemocline of the D-pit and in deeper layers of the DJX-pit, and some of those microorganisms are known to reduce As(V). Further investigations at the Cluff Lake mine pits should focus on the speciation and size distribution of contaminant bearing colloids, and the U, As, and Ni distribution and speciation in the sediments of the pit lakes.

3 COLLOIDAL TRANSPORT MECHANISMS AND SEQUESTRATION OF U, NI, AND AS IN MEROMICTIC MINE PIT LAKES

3.2 Summary

This study investigated the biogeochemistry U, and the co-occurring elements Ni and As, in colloids and sediments from two meromictic mine pit lakes that have considerably different depths and geochemistry. In order to characterize the processes controlling metal speciation and cycling in the pits, the distribution and speciation of the elements in colloidal size fractions were analyzed using micro- and ultrafiltration in combination with transmission electron microscopy. Sediment traps collected fresh sediments over the course of one year below the chemocline of the pit lakes and were subsequently analyzed by scanning electron microscopy (SEM) and digestions for morphology and composition. The most common particles found in the shallower pit consisted of Ca-O and Fe-O colloids, while the particles in the deeper pit were composed of Ca-S-O. Filtration results showed a higher abundance of metals in larger colloidal fractions in aged samples, suggesting that colloids can act as metal accumulators. Sediment traps showed the formation of Fe-O, Fe-S, Al-Si, and Ce-P phases, which were observed to sorb U and Ni. The overall U removal was calculated to be 0.9 g/m^2/year in both pits, despite considerably different geochemical conditions between the two, and the maximum removal rates for As (shallow pit) and Ni (deeper pit) were estimated to be 4.7 g/m^2/year and 0.6 g/m^2/year, respectively. Bottom sediments were also collected from both pits, and characterized using sequential extractions, SEM, synchrotron-based X-ray absorption spectroscopy and diffraction techniques. These techniques showed that the stability of metals in the sediment follows the order Ni<U<As. Nickel, found in the exchangeable and acid soluble fractions, could be easily mobilized by changes in aqueous ionic strength and pH. Similarly, pH and redox changes in the water may strongly affect U, due to its dominance in the acid soluble and reducible sediment fractions. U(VI) mineral phases confirmed by spectroscopy and diffraction, such as vandendriesscheite and monazite, which were likely associated with the oxidizable sediment fraction, may increase overall U stability. Arsenic was more strongly bound to the sediments and mostly present in the oxidizable and residual (highly recalcitrant) fractions. 16S rRNA gene sequencing demonstrated that sediment chemistry was the primary driver of microbial community composition in the sediments, with low species richness and diversity in deeper and more contaminated sediments. The collective results demonstrate the importance of colloidal particles for metal sequestration processes, highlighting the need for improved characterization of colloids in environmental studies and routine monitoring campaigns.

3.3 Introduction

Pit lakes, created by open pit mining, can become meromictic (see Chapter 1 for details on meromixis), whereby they have a permanently stratified deep water layer (monimolimnion) which does not mix with the upper water layer (mixolimnion). Important for this chapter is that meromixis can promote the removal of

metal contaminants from the mixolimnion through metal cycling at the chemocline, the highly dynamic boundary between the mixolimnion and the monimolimnion, which can have large physicochemical gradients. Metals can be transported from the mixolimnion into the monimolimnion and become trapped in the latter due to its permanent stratification, and eventually these metals can be sequestered into the pit bottom sediments due to saturation- or nucleation-induced precipitation (Soni *et al.*, 2014; see also Chapter 2). The development of anaerobic conditions within the monimolimnion can also promote the reductive immobilization of certain metal species.

Colloid chemistry and interactions are critical aspects of metal cycling, and understanding the extent to which colloids can sorb and transport metals is essential for determining their role in the functioning of meromictic pit lakes as a decommissioning measure. The sorption of metals to colloids, eventual accumulation of such particles and subsequent formation of precipitating particulates can remove metals from the aqueous medium via a scavenging process referred to as “colloidal pumping” (see Chapter 1).

To investigate colloidal processes and metal sequestration in meromictic lakes and their relevance as a decommissioning strategy, we studied the previously introduced (Chapters 1 and 2) artificial meromictic pit lakes, D-pit and DJX-pit, formed by open pit mining and located at the decommissioned Cluff Lake uranium mine in Northern Saskatchewan, Canada (Figure 3.1). These lakes are distinct from each other in terms of both chemistry and geometry. Work done in Chapter 2 showed that Fe- and Al-containing colloidal particles were likely involved in metals sequestration processes at the chemoclines of the two pits, while another older study demonstrated that active fertilization and microbial growth could decrease contaminant metal concentrations in the mixolimnion of the DJX-pit (Dessouki *et al.*, 2005). However, neither study investigated the nature of the interactions between metals and colloids or the colloid morphologies. To further understand these relationships and their net effect on sequestration in reclaimed pit mines, we investigated the biogeochemistry of metal contaminants (with U, Ni, and As being of major concern) in the two pit lakes at Cluff Lake, using water filtrations, sediment traps, electron microscopy techniques and sequential extractions of bottom sediments (Tessier *et al.*, 1979; Pichler *et al.*, 2001; Kipp *et al.*, 2009), as well as synchrotron-based X-ray spectroscopy and diffraction. This study reveals how metal transport by colloidal particles can promote metal sequestration in pit lakes and provides estimates for metal removal rates in these systems. Furthermore, new insights into the stability of metals in sediments and important secondary minerals are discussed.

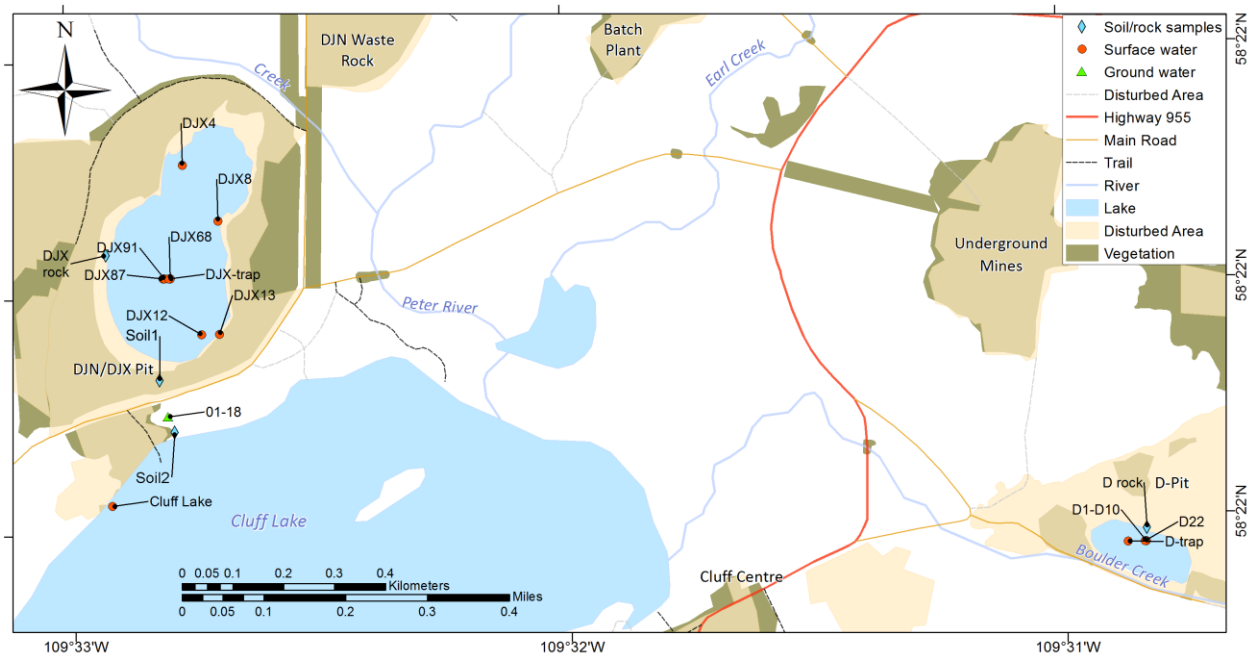

Figure 3.1: Sampling locations in and around the two pit lakes (D-pit and DJX-pit) at Cluff Lake, northern Saskatchewan, Canada.

3.4 Materials and Methods

3.4.1 Description of the pits

D-pit, the smaller of the two pits (maximum 28 m deep) was actively mined for U between 1979 to 1981, and eventually flooded in 1983 (AREVA, 2013). A chemocline is present at a depth of 13 m, with an anoxic monimolimnion below that has elevated pH values (pH 7.3 to 7.9) compared to the mixolimnion (pH 6.2 to 6.4). The major metals of concern in this lake were previously identified as U, with highest concentrations at the chemocline (up to 131 ppb), and As, with up to 95 ppb in the monimolimnion (see Chapter 2 for details). The chemocline and the monimolimnion are influenced by Fe redox processes, suggesting that the biogeochemistry of the pit bottom is controlled by Fe(III) reduction.

The DJX-pit is deeper (91 m), was mined periodically from 1989 to 1997 and allowed to flood in 2002 (AREVA, 2013). The lake in the DJX-pit lake has two major chemoclines, one at 18 to 20 m, and the second between 65 and 75 m, with stratification being controlled by carbonate dissolution and precipitation processes. Oxygen is present even near the bottom of the pit (0.9-1.9 mg/L; see Chapter 2 for details), while the pH in the mixolimnion is neutral in contrast to the values in the monimolimnion (pH 5.6 to 6). The monimolimnion is dominated by sulfate (up to 476 ppm), which is in stark contrast to the D-pit (<0.1 ppm). Major metals of concern are U and Ni, with the highest concentrations in the deeper monimolimnion (1744 ppb and 2193 ppb, respectively). Other metals with elevated concentrations include Mn, Co, and Zn with concentrations up to 4 ppm, 424 ppb, and 687 ppb, respectively. A regional groundwater model (AREVA, 2013) suggests some groundwater exchange between the DJX-pit and

nearby Cluff Lake. Groundwater wells (e.g., Well 01-18 in Figure 3.1) were installed between the two water bodies to monitor the groundwater quality. The trace metals U, As, and Ni are of primary concern in the two pits and were therefore the primary focus of this study.

3.4.2 Sampling

In June 2017, water samples were collected from the center of the D-pit and the DJX-pit from a boat using a MasterFlex E/S portable sampler (Cole-Parmer) and plastic tubing. Water was sampled from depths that were chosen to capture major geochemical changes along the chemoclines as determined in Chapter 2. Three depths were sampled in the D-pit: 5 m (mixolimnion), 13 m (chemocline), and 20 m (monimolimnion). Four depths were sampled in the DJX-pit: 5 m (mixolimnion), 20 m (upper chemocline), 40 m (upper monimolimnion), and 65 m (lower monimolimnion).

To investigate how metals, which may be transported by groundwater from DJX-pit towards a natural lake (Cluff Lake), are immobilized in a till-dominated soil, we collected soil samples and groundwater in the flow path between the two. The 9 m deep groundwater well 01-18, situated between DJX-pit and Cluff Lake (Figure 3.1) was sampled with the MasterFlex E/S portable sampler after purging three times the well volume according to Vail (2013). Saturated soil samples from the locations Soil1 (south of DJX-pit, depth 25 cm) and Soil2 (north of Cluff Lake, depth 80 cm) were collected in June 2018 using a hand shovel and transported in polypropylene centrifuge tubes. To understand the potential relationship between the geochemistry of U ores and resulting water chemistry, rock samples (D rock, DJX rock) were collected along the shores of both pits and U ore samples from Cluff Lake were analyzed as described below. Further details on the rock and ore samples are provided in Appendix B.

Bottom sediments were collected from the pit bottoms using an Ekman dredge. Samples from D-pit were retrieved in September 2015 from the middle of the pit and are hereafter referred to as D-1 to D-10 (Figure 3.1). A new sediment sample was collected from 22 m depth in June 2017 and labeled D-22. Sediment samples from the DJX-pit were collected in June 2016 (shallow) and June 2017 (deep) from depths and locations provided in Table 3.1. The sediments were stored in polypropylene centrifuge tubes and placed on ice for transport back to the University of Alberta, and subsequently stored at -20°C until further processing.

Table 3.1 Sediment and soil sample information: dates, depths and locations. Anaerob.: anaerobically dried for XAS.

Sample name(s)	Location	Sampling date	Depth (m)	Anaerob
D-1 to D-10	D-pit	Sept 2015	not recorded	No
D-22	D-pit	June 2017	22	Yes
D-trap	D-pit	2017-2018	17	No
DJX-13a, DJX-13b	DJX-pit	June 2016	13	No
DJX-12a, DJX-12b	DJX-pit	June 2016	12	No
DJX-8	DJX-pit	June 2016	8	No
DJX-4a, DJX-4b, DJX-4c	DJX-pit	June 2016	4	No
DJX-68	DJX-pit	June 2017	68	No
DJX-87	DJX-pit	June 2017	87	No
DJX-91	DJX-pit	June 2017	91	Yes
DJX-trap	DJX-pit	2017-2018	47	No
Soil1	S of DJX-pit	June 2018	0.25	No
Soil2	N of Cluff Lake	June 2018	0.80	No

In June 2017, sediment traps were placed in D-pit and DJX-pit at 17 m and 47 m, respectively. These depths were selected to be below the upper chemoclines (see Chapter 2). The sediment traps were constructed from 50 mL centrifuge tubes attached to a PET funnel (Figure B.10). An aluminum tube filled with rocks and sand was attached below as a stabilizing weight. The rope holding the trap was attached to a buoy, which was attached to the center buoy in each pit. Plastic water logs held both buoys at a constant distance to prevent the ropes from becoming entangled. Both sediment traps were recovered after 374 days. In the DJX-pit, only approximately 25 mL of sediments were recovered and after detaching the funnel under water, the tube was capped and sealed with Teflon tape (Figure B.10). More than 50 mL sediments were found in the D-pit sediment trap, therefore, to prevent losses, the excess sediments with additional liquid was poured in additional 50 mL tubes, which were sealed as described above. Captured sediments were transported on ice. In the laboratory, samples were stored in an anaerobic glove box (98% N_2 and 2% H_2) prior to processing.

3.4.3 Colloidal size distribution and microscopy

To investigate the distribution of metals in different colloidal size fractions, aliquots of lake water were filtered on the boat immediately following sampling. Unfiltered aliquots were also collected for analysis. Dead-end filters (0.45 µm and 0.2 µm) were used for separating the larger size fractions, while reusable ultrafiltration cartridges (Pellicon XL, Millipore, 500 kDa and 10 kDa), both fed with the 0.2 µm permeate, were used for separating the smaller size fractions (Wang *et al.*, 2013). The cartridges were flushed between the filtrations (50 mL 0.1 M hydrochloric acid, 50 mL 0.1 M sodium hydroxide, 50 mL of ultrapure water) and then preconditioned with at least 10 mL of the sample. Filtrations were performed differently in

June 2017 and June 2018. The June 2017 filtrations were performed using syringes and syringe filters (Agilent) for larger size fractions. As there was a concern that the brief exposure to oxygen might alter the colloidal distribution, the filtrations were repeated in June 2018 using in-line filters (Waterra) prepared in a closed, sequential setup, in which permeate from one filter was subsequently fed into the next without air exposure. Using the same setup, groundwater from the well 01-18 (Figure 3.1) was filtered in June 2018.

Previous studies have determined that temperature changes can cause colloidal aggregation and agglomeration, ultimately leading to precipitation (von Gunten and Schneider, 1991; Tranvik, 1994). To determine if this process affects the colloidal size distribution of metals in the two pit lakes, filtrations of aged (mature) colloids were performed by collecting unfiltered water samples in June 2017 in serum bottles in a nitrogen purged glove bag (Fisher Scientific) (Wang *et al.*, 2013). In order to age the colloids, these samples were sealed and stored in an anaerobic glove box (98% N_2 and 2% H_2) at room temperature for one month. Samples were then filtered in the glove box following the same method as used in the field in 2017 (with syringes). After storing the water samples for 7.5 months in the glove box, precipitates were observed in samples from D-pit (20 m) and DJX-pit (65 m). The precipitates were retrieved by centrifugation (15000 *g*, 10 min) and dried at 60 °C. They were then carbon coated and analyzed by scanning electron microscopy coupled with energy dispersive X-ray spectroscopy (SEM-EDS) as described below.

All filtrates were diluted as necessary, acidified to a final concentration of 2% nitric acid, with the metals then being analyzed using an Agilent 8800 Triple Quadrupole ICP-MS as described in Chapter 2. Size fraction ranges were calculated by using the differences between the larger and the smaller fractions. The June 2018 permeates were also analyzed for the total organic carbon (TOC; Shimadzu TOC-V analyzer) using the non-purgeable organic carbon method. To characterize colloidal particles, transmission electron microscopy (TEM; JEOL JEM-ARM200CF S/TEM) and energy dispersive X-ray spectroscopy (EDS) were performed using water from fresh samples collected in June 2017.

3.4.4 Aqueous U speciation analysis

Because U and other redox sensitive metals have varying affinities toward colloidal particles depending on their speciation, it is important to investigate their oxidation states; however, this poses methodological challenges. Although thermodynamic speciation modeling is widely applied (e.g., Ramos *et al.*, 2012), it cannot explain kinetically limited systems and is prone to large deviations from observations, especially when colloidal particles are involved (Gustafsson and Gschwend, 1997). In the two lakes studied here, the speciation of Fe and As was previously investigated using laboratory techniques (see Chapter 2), yet no data were obtained for U. To separate reduced from oxidized U in the field, the method developed by Anderson (1984) was applied, which exploits the redox properties of U(III) and U(IV) that cause them to favorably co-precipitate with lanthanide fluorides, such as LaF_3 and NdF_3 under acidic conditions, leaving U(V) and U(VI) in solution (Foti and Freiling, 1963). Since other ions in the solution can compete with the fluoride anions, proper calibration of the assay is necessary. Water was

pumped on the boat into a nitrogen purged glove bag. Inside the glove bag, water collected from the various depths was partitioned into 50 mL polypropylene tubes and acidified to 0.6 M HCl. To be able to use similar reagent amounts for all samples in the field, DJX-pit water was diluted 10x with nitrogen purged, ultrapure water prior to acidification. Next, 3.5 mmol of neodymium nitrate hexahydrate ($Nd(NO_3)_3 \cdot 6H_2O$) was added to each tube (Anderson, 1984). Following dissolution, 0.9 mL of 47% hydrofluoric acid (HF) was added, and the solutions were mixed by shaking and left at ambient temperature for 45 min, after which white/purple precipitates accumulated at the bottom of the tube. The supernatant was then filtered into 15 mL tubes using 0.45 µm nylon syringe filters, and 0.075 g of boric acid was added. This filtrate was then analyzed for U using the Agilent 8800 Triple Quadrupole ICP-MS. The separation method was calibrated in the laboratory with three U concentrations ranging from 10-150 ppb. To completely reduce the U, 50 µL of 20% $Ti(III)Cl_3$ in 2M HCl (Fisher Scientific) was added to each mL of oxic solution (Anderson, 1984). In addition, because Ca is known to generate interferences with this method due to the precipitation of CaF_2, an additional calibration series was made with three artificial U-Ca solutions that covered the range of the undiluted D-pit and DJX-pit samples (3.7 ppm, 11.8 ppm, 19.8 ppm). All calibration curves were forced through the origin and for Ca values between the prepared ones, the slopes were linearly approximated. The results obtained from the samples were then fit to the resulting calibration curves using linear combination fitting of the oxidized and corresponding reduced calibration curves.

3.4.5 Chemistry of solid samples

General chemistry

Sediments from the sediment traps were mixed in their containers and the total volume was recorded. The dry masses of the solids were then determined by air-drying (under 98% N_2 and 2% H_2) for a week and weighing. Bottom sediment samples and soil samples were dried at 105 °C, sieved (<2 mm), and crushed using a mortar and pestle. Total carbon (TC), total organic carbon (TOC), and total nitrogen (TN) were analyzed by a Costech Model EA 4010 Elemental Analyzer. Total inorganic carbon (TIC) was calculated by subtracting TOC from TC.

Sequential extractions

Sequential extraction was performed on selected samples from each pit according to Tessier *et al.* (1979) with modifications by Li *et al.* (1995). The extractions were conducted in triplicates using finely ground sediment samples (1 g each sample) in 50 mL polypropylene centrifuge tubes. After each extraction step, the resulting residues were used for the following extraction step. Exchangeable metals (fraction 1) were extracted at room temperature over 20 min with 8 mL of 0.5 M magnesium chloride ($MgCl_2$, ACS grade, Fisher Scientific) with continuous agitation. Metals bound to carbonates (fraction 2, acid soluble) were extracted at room temperature over a 5 h period, using 8 mL of 1 M sodium acetate ($C_2H_3NaO_2$, adjusted to pH 5 with acetic acid, ACS grade, Fisher Scientific) with continuous agitation.

Metals bound to Fe-Mn-oxides (fraction 3, reducible) were extracted at 95°C in a heating block for 6 h, with 20 mL of 0.04±0.01 M hydroxylammonium hydrochloride ($NH_2OH \cdot HCl$, ACS grade, Fisher Scientific) with occasional agitation each hour. Metals bound to organic matter and sulfide (fraction 4, oxidizable) were extracted by adding 3 mL of 0.02 M HNO_3 and 5 mL of 30% H_2O_2 (30%, ACS grade, Fisher Scientific), and by subsequently heating the sample slowly to 85℃. The sample was kept at this temperature for 2 h with occasional agitation. An additional 3 mL of H_2O_2 (adjusted to pH 2 with HNO_3 and NaOH) was added and the mixture was heated at 85℃ for an additional 3 h (with agitation). The mixture was allowed to cool, and left to react for 30 min at room temperature with a solution of 4 mL ultrapure water and 5 mL of 3.2 M ammonium acetate ($C_2H_3O_2NH_4$, HPLC grade, Fisher Scientific) in 20±3% (v/v) HNO_3 with continuous agitation. To retrieve the extracts from fractions 1 to 4, the tubes with the suspensions were centrifuged at 17000 relative centrifugal force (rcf) for 20 min. Supernatants were pipetted in clean centrifuge tubes and diluted to 50 mL with 2% HNO_3 and 0.5% HCl: 5 mL for fractions 1 and 2, and 15 mL for fractions 3 and 4. The remaining liquid was discarded. Before starting with the next step, the remains were flushed. This was done by adding 8-10 mL of ultrapure water and suspending the remains by shaking. The tubes were then centrifuged again and the supernatant was discarded. Control samples (no sediment added) were set-up for each step of the sequential extraction to account for metals in the extraction solutions. The final fraction (fraction 5) was calculated by subtracting the amount in the previous four fractions from the total amount of metals (see below).

During the extractions of a D-pit sediment (D-10), one sample was sacrificed after each extraction step for analysis by SEM-EDS (see below) to observe major changes in U.

All extraction and digestion solutions were filtered through 0.2 µm nylon syringe filters and analyzed on an Agilent 8800 Triple Quadrupole ICP-MS (see Table B.1 for instrumental settings).

Total digestions

The totals were determined by the digestion of small amounts of sediments with hydrofluoric acid (HF) and alkaline fusion (for As, Si). This was done with sediment samples previously analyzed by sequential extractions and with dried sediments from the sediment traps.

0.1 g of the dry sediment sample were digested with 5 mL HNO_3 (70%) and 5 mL HF (47-51%, ACS grade, Fisher Scientific) at 130°C. After all liquid evaporated, 3 mL HCl (37%) and 1 mL HNO_3 (70%) were added to dissolve the remains. The solution was heated to near dryness at 130°C, and finally diluted to 50 mL with 2% HNO_3 and 0.5% HCl.

To prevent evaporation losses with HF for Si and As (Wang *et al.*, 1997; von Gunten *et al.*, 2017), alkaline fusion was performed based on a method by GBC Scientific Equipment (2013). To perform the fusion, a sodium hydroxide (NaOH, ACS grade, Fisher Scientific) melt was created to prevent the fusion melt from foaming and frothing. 1.5 g of NaOH was melted in a nickel crucible over a Bunsen burner and

left to cool. 0.1 g of sample, an additional 0.5 g of NaOH, and 0.5 g of sodium peroxide (Na_2O_2, ACS grade, Fisher Scientific) ,were added into the crucible. The crucibles were covered with a lid and heated again for 5 min. After cooling the crucibles were flushed outside with 6 M HCl and then placed into 250 mL polypropylene beakers together with the lid. Ultrapure water and 6 M HCl were added until all suspended particles dissolved. The cleaned crucibles were removed and the volume of the liquid was corrected to 50 mL with ultrapure water. The solutions were diluted 2-20 times with a solution containing 2% HNO_3 and 0.5% HCl prior to analysis to prevent strong matrix effects. The recovery of the total digestion methods was verified by digesting the reference sediment STSD-3 (CANMET Mining and Mineral Sciences Laboratories) (Table B.1).

Organic acid extractions

To distinguish between highly and poorly crystalline Fe compounds in the residual fraction, weak organic acid extractions with 7-35 mM oxalic and citric acids were performed (Borggaard, 1992; Joseph *et al.*, 1996; Larios *et al.*, 2013). For the extractions, 0.5-1.0 g of dry sediments (D-6 and D-9) were placed into 15 mL centrifuge tubes. Acids (Fisher Scientific) were added in concentrations of 0.1 mmol/g dry sediment and 0.5 mmol/g dry sediments and dissolved in 15 mL of ultrapure water, which finally corresponded to 7-25mM of acid in solution (Table B.16). The tubes were placed on a rotational shaker for 96 h. After centrifugation (4600 rcf), the supernatant was filtered through 0.2 µm nylon syringe filters prior to analysis.

3.4.6 Mineralogy and microscopy

Bottom sediment subsamples for physical analyses were dried at 60 °C, sieved (<2 mm), and crushed using a mortar and pestle. Sediments from traps were only dried at 25 °C. Mineralogy of the samples was analyzed on a Rikagu Ultima IV X-ray diffraction (XRD) unit with a cobalt X-ray source (λ = 1.790260). Data was interpreted using the JADE 9.5 software package and the databases: 2013 ICDD, 2015-1 ICSD.

In order to investigate the morphology of the sediments and potential U accumulation, selected sediments with high U concentrations from D-pit, DJX-pit, and both sediment traps were analyzed by SEM-EDS. For this purpose, bottom sediments were embedded into EPO-TEC 301 resin thin sections of 30 µm thickness on glass slides. Regions of uranium accumulation in the thin sections were identified using SEM-EDS (Zeiss EVO MA 15 and Sigma 300 VP-FESEM). All SEM-EDS analyzes were performed without carbon coating to be able to reuse the slides for the synchrotron X-ray analyses without additional alteration of the surface. The instruments were run in variable pressure mode with nitrogen gas at 25 kV (detection limit 0.5 wt%).

3.4.7 Spectroscopic analyses

Synchrotron-based X-ray analyses were performed at the Very Sensitive Elemental and Structural Probe Employing Radiation from a Synchrotron (VESPERS) beamline at the Canadian Light Source

(CLS) in Saskatoon, Canada with thin sections from selected D-pit and DJX-pit sediments, and powder samples for bulk analysis (Feng *et al.*, 2007 and 2010). Micro-X-ray fluorescence (XRF) maps of the thin sections were collected using a polychromatic X-ray beam with an energy range of 2-30 keV and a beam spot size of ~3 µm. Samples were mounted in the focus of the X-ray beam at an angle of 45° from the horizontal plane. XRF spectra were collected with a single element silicon drift detector (Vortex-90EX; HITACHI) positioned 45° to the incident X-ray beam in horizontal plane. Laue diffraction patterns were collected from selected U hotspots using a Dectris Pilatus 1M Pixel Array Detector positioned 90° to the incident X-ray beam in vertical plane. Visualization of the maps and correlation calculations between elements (Pearson's linear product-moment correlation) were done using MATLAB R2015b. The diffraction patterns were analyzed using the XMAS v.6 software (Tamura, 2014).

Micro X-Ray Absorption Near Edge Structure (µ-XANES) at the U LIII-edge, As K-edge, and Ni K-edge were measured in fluorescence mode using a four-element silicon drift detector (Vortex-ME4, HITACHI). The energy of incident X-ray were scanned using a double crystal Si(111) monochromator ($\Delta E/E = 10\text{-}4$). The detector was positioned 90° to the incident X-ray beam in horizontal plane. Samples were positioned in the focus of the incoming X-ray beam at an angle of 45° in both the vertical and horizontal directions. Five to six µ-XANES scans were collected for each hotspot. Bulk XANES spectra were collected using a bigger beam of 0.8 mm x 0.8 mm in size. For bulk XANES, Teflon holders with a 3 mm slot in the middle were used. Ground sediment samples were packed into the slot and secured with Kapton tape on both sides. Samples were again positioned in front of the incident X-ray beam at a 45° angle with the fluorescence detector positioned 90° relative to the incident X-ray beam in horizontal plane. Bulk XANES measurements were performed at the U LIII-edge and the As-K edge using either a four-element Vortex silicon drift detector or a liquid nitrogen cooled 13-element germanium detector (Canberra). For each sample, 5-10 scans at a spot with the highest absorbance at the corresponding edge energy were performed. Post-processing of the XANES spectra was performed using Athena (Demeter 0.9.24 XAS Processing Software; Ravel and Newville, 2005). The spectra were corrected by the energy shift, normalized, and compared to standard XANES spectra using linear combination fitting (see Appendix B for more details on VESPERS-related analyses). As there was a concern that the drying procedures might influence sediment mineralogy, selected sediment samples from June 2017 were dried at room temperature in an anaerobic chamber containing 98% nitrogen and 2% hydrogen. The dried sediments were then immediately processed for XRF and µ-XANES as described above.

To verify the findings obtained by VESPERS, electron microprobe analyses were performed using a CAMECA SX100 microprobe. Selected carbon coated slides from each pit (bottom sediments) with known U grain locations (from SEM-EDS) were used. Additional EDS and wavelength dispersive X-ray spectroscopy were performed to differentiate the overlapping X-ray peaks of S, Pb, As, and Mg.

3.4.8 Microbiology

To investigate the composition of the microbial communities in the sediments, DNA was isolated from wet bottom sediment samples from D-pit (September 2015 samples), the shallow portion of DJX-pit (June 2016), and the deep portion of DJX-pit (June 2017). The FastDNA^{TM} SPIN Kit for soil (MP Biomedicals) was used and 16S rRNA was amplified by the polymerase chain reaction (PCR) according to the 16S Metagenomic Sequencing Library Preparation Guide by Illumina (Illumina, 2016) and using the 2x HiFi hotStart ReadyMix (Kapa Biosystems). A negative control was included in all amplification experiments. DJX-91m subsamples were processed twice, resulting in two datasets from this depth (DJX91a, DJX91b). Universal bacterial and archaeal primers targeting the V4/V5 hyper variable region were used: F515 (5′-GTGCCAGCMGCCGCGGTAA-3′) and R806 (5′-GGACTACHVGGGTWTCTAAT-3′) (Caporaso *et al.*, 2012). Sequencing was performed at The Applied Genomics Core (TAGC) laboratory at the University of Alberta using the Illumina MiSeq platform with the Illumina NexteraXT library preparation kit.

For data processing, MetaAmp version 2.0 (Dong *et al.*, 2017) was applied. The amplicons were trimmed to a length of 250 base pairs, a minimum length overlap of 40 base pairs was chosen and the operational taxonomic unit (OTU) clustering was done at the 97% similarity level. R version 3.4.1 with the PHYLOSEQ package (McMurdie and Holmes, 2013; R Core Team, 2017) were used to visualize the data as described by von Gunten *et al.* (2018). In order to investigate how environmental parameters are correlated with the community compositions, constrained ordinations plots (Anderson and Willis, 2003; Ramette, 2007) were prepared using the following environmental parameters (sediment concentrations): Fe, S, Ca, U, Ni, As, TOC. METAGENassist (Arndt *et al.*, 2012) was used to predict metabolisms and oxygen requirements of the sample microbial communities. Basic local alignment search tool (NCBI BLAST, https://blast.ncbi.nlm.nih.gov/) was used to align selected sequences (Altschul *et al.*, 1990; Zhang *et al.*, 2000). Raw sequencing data for sequenced samples was uploaded onto the National Center for Biotechnology Information (NCBI) database and can be found under accessions SRX3981803 to SRX3981811.

3.5 Results

3.5.1 Water samples

Colloidal water distribution

In D-pit, total U concentrations increased from the surface to the chemocline at 13 m to 130-160 ppb and decreased again to about 50% of the chemocline value at 20 m depth (Figure 3.2). The majority of U in fresh samples was in the dissolved form. Arsenic gradually increased with depth to 40-90 ppb and was distributed over all size fractions. Closer to the surface, larger As-bearing colloids dominated the size fractions, especially those in the 500 kDa-0.2 µm range. Overall, lower concentrations of As were detected in June 2018 and a dominance of the 500 kDa-0.2 µm fraction was observed. This difference could be attributed to oxidation processes during the brief sample exposure to the atmosphere that might have

occurred in June 2017. Iron in the D-pit was distributed in a similarly diverse way as As, ranging up to 51-53 ppm in total, which suggests a similar mechanism of colloidal immobilization. Low concentrations of Ni were detected in the D-pit (<10 ppb), with most of it being associated with the <10 kDa size fraction, with some contributions of the larger 10 kDa-0.2 μm fractions.

U in the DJX-pit also increased with depth and reached a peak of 1-1.7 ppm at a depth of 65 m and was dominantly associated with the <10 kDa fraction. Nickel similarly gradually increased up to 1.3-1.9 ppm, with the majority of it being in the <10 kDa fraction, indicating the dominance of small colloids and dissolved species. In June 2018, colloids in the range of 10-500 kDa carrying Ni were found. Concentrations of As and Fe were low in the DJX-pit (1 ppb and <161 ppb, respectively), making it impossible to resolve the colloidal distribution.

A markedly different size distribution was observed for the aged samples that were filtered after one month of storage at room temperature (Figure 3.2). For U in the samples from D-pit, the smaller 500 kDa - 0.2 μm size fraction became more dominant than the 0.2-0.45 μm size fraction in the surface water sample. The distribution of As in the larger fractions (0.2-0.45 μm and >0.45 μm) modestly increased. On the other hand, Ni in the D-pit became more abundant in the 10-500 kDa fraction. Iron became more abundant in the <10 kDa colloidal fraction, substituting the larger 10-500 kDa and 500 kDa-0.2 μm fractions. For aged DJX-pit samples, in some cases more than 50% of U was detected in the larger colloidal fractions, especially the 500 kDa-0.2 μm size fraction. Colloidal Ni >10 kDa only started to emerge with 6-10% contribution compared 0-2% in fresh 2018 samples and was related to larger size fractions (0.2-0.45 μm and >0.45 μm). Mo (up to 86 ppb) showed a similar distribution to U, especially in the matured samples (up to 40% colloidal), which indicates that Mo and U are exhibiting similar chemical behavior in the DJX-pit. Their similar charge could lead to similar interactions with colloids, and the formation of thiomolybdate phases (for example in deeper DJX-pit layers) could decrease the solubility of Mo and cause its precipitation (Erickson and Helz, 2000). Aluminum in the mature samples was present in the larger colloidal fractions and in lower concentrations, indicating the aggregation of smaller Al-bearing colloids and the precipitation of Al-containing phases.

D-pit precipitates collected from the 20 m sample after the 7.5 month aging experiment (Figure 3.3 and Table B.23) were rich in Fe and O, with an average Fe/O molar ratio of 0.2. This ratio most closely matched the iron hydroxide mass ratio of a hydrous ferric oxide such as ferrihydrite ($Fe(OH)_3$; Fe/O: 0.3). The lower ratio could be explained by residual water in the sample and other oxides. DJX-pit precipitates were more diverse. The particles shown in Figure 3.3 were rich in Al and Si (8.1 wt% and 10.0 wt%, respectively) and contained minor amounts of Mg (1.1 wt%), K (2.4 wt%), and Fe (1.2 wt%). Based on the Al/Si, Al/K, and Si/K molar ratios, the precipitates are similar to kaolinite ($Al_2Si_2O_5(OH)_4$) and muscovite ($KAl_3Si_3O_{10}(OH)_2$), which were also found in the deep (> 68 m) sediments of the DJX-pit. Some particles showed a high abundance of S (10.1 wt%) and Ca (12.2 wt%) and may be attributed to the precipitation of gypsum ($CaSO_4 \cdot 2H_2O$).

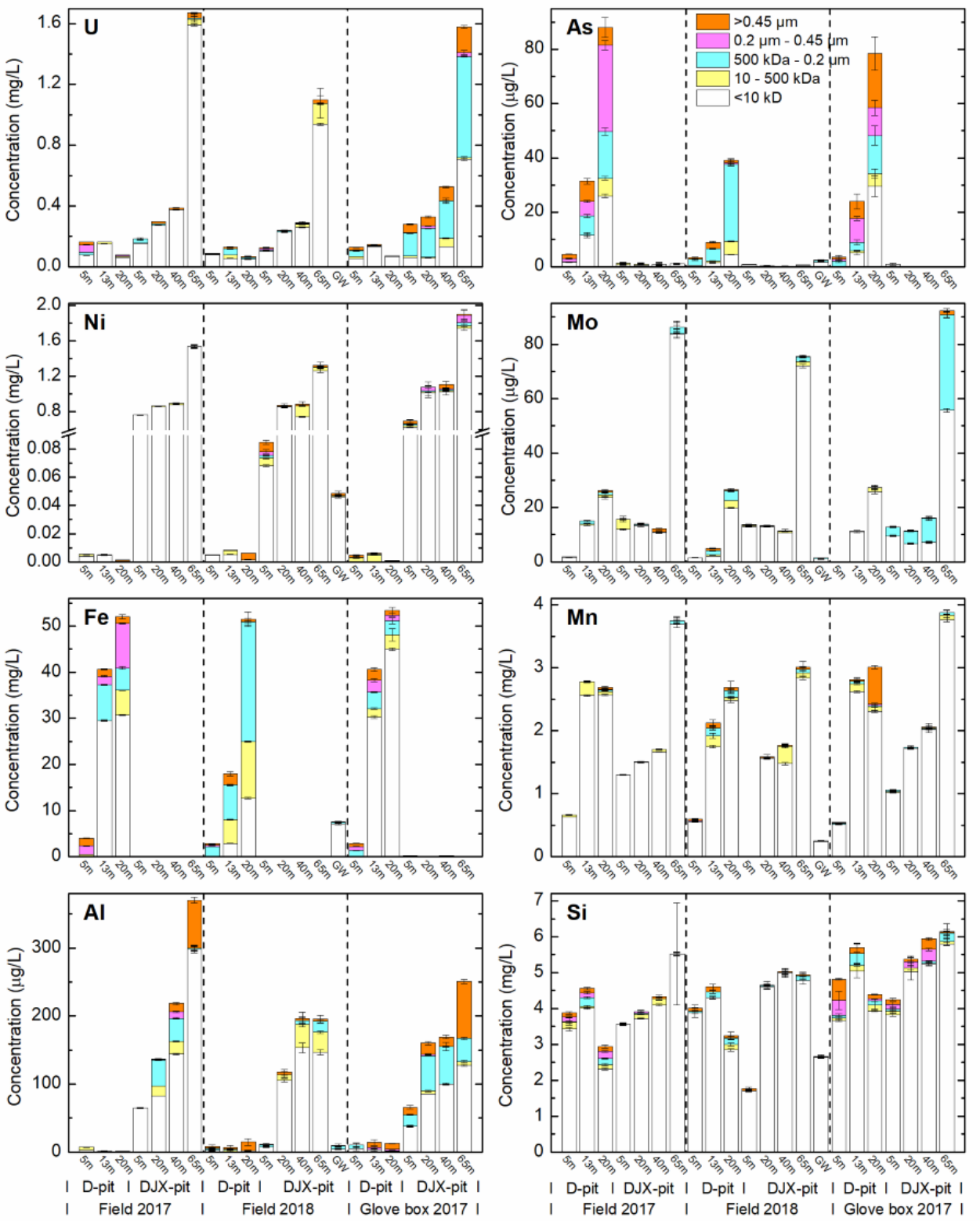

Figure 3.2: Colloidal size fractionation results for selected metals. The data is grouped by sampling date and pit (D-pit, DJX-pit). The error bars represent instrumental errors (ICP-MS, n=3). Note y-axis breaks for Ni (elevated in the DJX-pit). Data on other elements can be found in Tables B.26-B.28.

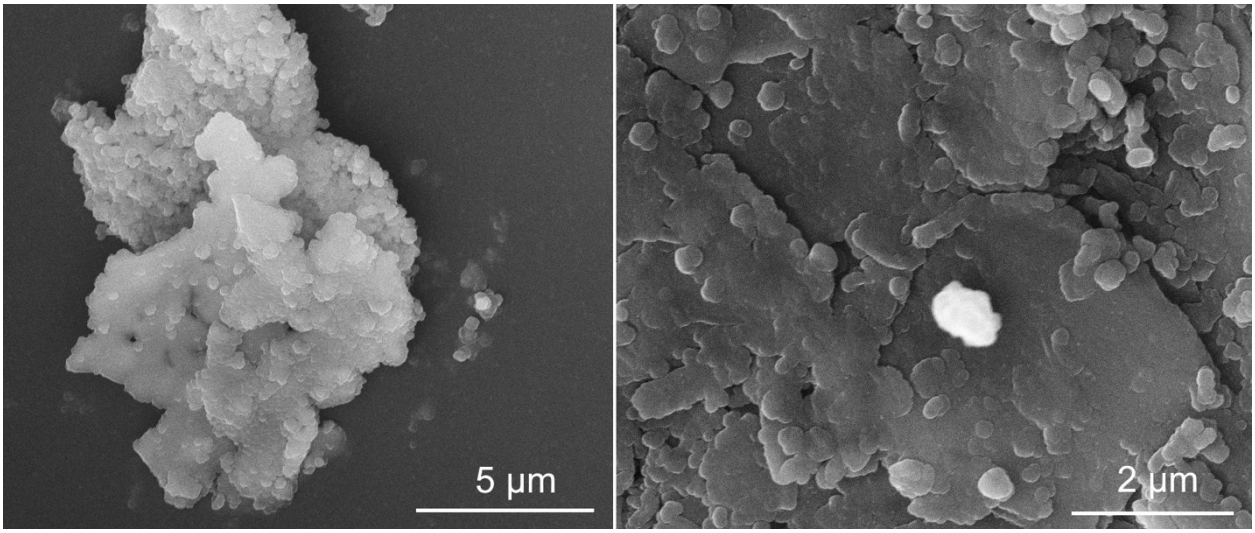

Figure 3.3 Selected SEM images of precipitates formed at room temperature after 7.5 months from D-pit (left) and DJX-pit (right) from 20 m and 65 m water depth, respectively.

Filtration results from the groundwater well 01-18 show that the major water chemistry is similar to the surface water of the DJX-pit (Figure 3.2, Table B.28), specifically, concentrations of Mg, S, K, and Ca. This implies that the two are hydrogeologically connected. The distribution of trace metals, such as Ni, Mo, and Mn, are only present in the <10 kDa fraction, suggesting that the aquifer between DJX-pit and Cluff Lake was efficiently removing colloid-bound metals. Similar results were found by Hollings *et al.* (1999) in groundwater at the Rabbit Lake uranium mine. No U was detected in the groundwater well 01-18 water.

S/TEM confirmed the presence of colloidal particles in D-pit at depths of 5 m, 13 m, and 20 m, and in DJX-pit at 60 m and 65 m, with colloidal particles ranging in size from 20-300 nm. EDS mapping on selected colloids (Figure 3.4) revealed major differences between colloidal particles present in the two pits. Colloidal particles found in the D-pit were dominated by Fe-O and Fe-O-Ca phases, with minor occurrences of Si-O in the 13 m water sample, while in the DJX-pit, colloids were mostly Ca-O and Ca-O-S phases. Although the DJX-pit water is depleted in Fe, Fe-O particles were detected. Arsenic, Ni, and U concentrations were below the detection limit for S/TEM-EDS imaging of the colloidal particles. No carbon-dominated colloids were detected, suggesting a minor role of organic matter colloids in the two pit lake systems. Filtrations and TOC analysis of June 2018 samples confirmed the lack of larger carbon particles in the D-pit and DJX-pit surface samples, but showed some 10-500 kDa C particles in deeper layers of both pits (Figure B.7), suggesting that some C-rich colloids might be present at these depths having a similar size distribution as As and Fe.

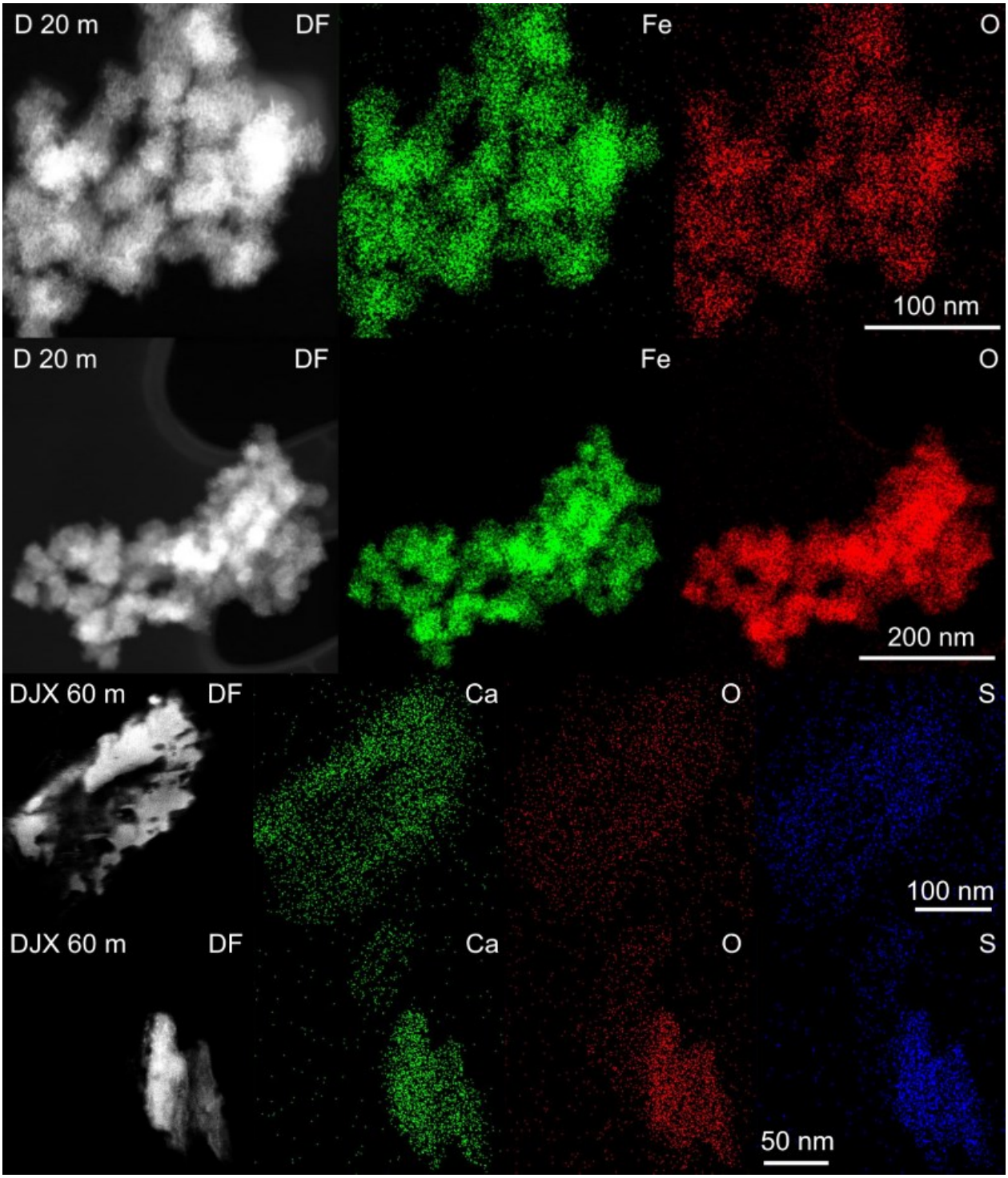

Figure 3.4 Selected TEM images of colloids found in fresh water in D-pit (top) and DJX-pit (bottom).

Aqueous U speciation

In the surface water of the D-pit, both extraction techniques (with Ca and without) demonstrated that U(VI) was the dominant species (Table B.22). The results obtained with the Ca calibration curve suggest higher U(VI) abundance and seem more reasonable, as the top water layers of D-pit were well mixed and oxidized and only small amounts of U(IV) would be expected. At the chemocline, where the redox conditions change, a transition from U(VI) to U(IV) was observed and the monimolimnion was dominated by U(IV). The results for DJX-pit, which does not become anoxic below the chemocline as D-pit, suggest that no U(IV) was present in the mixolimnion and the upper monimolimnion (i.e., DJX-pit water samples from 5 m, 20 m, and 40 m depths). In the 65 m sample, about 72% of U was in U(IV) form.

For some samples, less U precipitated than would be expected for a pure U-Ca solution based on the calibration curves. This resulted in some U(VI) values in excess of 100% (127-176%). The presence of certain dissolved species may interfere with the precipitation behavior of U in the sample solutions. For example, it is likely that Mg, Sr, and traces of lanthanides (such as Ce coming from rocks and sediments, e.g., see Table B.15) are also competing for F^-, and unlike Ca, they were not accounted for during the calibration. In addition, the presence of organic matter and stable colloids might further influence the calibration and results. Uranium is known to co-precipitate with Ca (Perry *et al.*, 1981), which makes it difficult to isolate the effect of Ca during NdF_3 co-precipitation. Moreover, replicating the sample solution chemistry in the simulated solutions used to make up calibration standards is especially challenging. For these reasons, the obtained results should be interpreted with caution, and viewed qualitatively rather than as a strict quantitative measure of the abundances of U(IV) and U(VI).

3.5.2 Bottom sediments

Sediment mineralogy and chemistry

In the bottom sediments, abundant feldspar minerals were identified, including anorthite, albite, orthoclase, and microcline (Table B.2). The latter three were predominantly found in DJX-pit samples. Clay minerals present included muscovite, clinochlore, kaolinite, and illite, with the latter primarily found in DJX-pit, whereas hematite and dolomite were present mostly in D-pit samples. Only a few samples had TC abundances >1% (i.e., D-6: 1.5%, DJX-13a: 2.0%, DJX-8: 4.2%, DJX-4a: 1.2%, and DJX-68: 1.0%). In these samples, the TC was dominantly present as TOC.

The distribution of elements in the sediment fractions as determined by sequential extraction showed substantial differences between the two pits, and within DJX-pit large variations between sample pools (deep vs. shallow) were also observed (Figure 3.5, details in Table B.3 to Table B.12). In both pits, U was mainly present in three fractions, the carbonate (acid soluble) fraction with 28-77% of total U, the amorphous Fe/Mn oxide (reducible) fraction with 17-50%, and the residual fraction with 1-41%. The Fe/Mn oxide (reducible) fraction was identified as the major U-bearing phase in deep sediment sample DJX-68 (32-50%), while in shallow samples, U was mainly in the carbonate fraction (67-77%). The residual

fraction was less substantial in the shallow DJX-pit samples (4-13 m depth) with only 1-2% of total U bound in this phase. Although not abundant in the water of DJX-pit, As was present at similar total concentrations in D-pit and the deep DJX-pit sediment samples. Arsenic was identified mainly in the residual fraction (29-95%) of the sediments from both pits, followed by the amorphous Fe/Mn oxide fraction (3-36%). DJX-91 also showed a high abundance of As in the organic matter/sulfide fraction (33%). Phosphorus had a noticeably similar distribution, as well as total concentrations, to that of As (Table B.3 to Table B.12). Nickel, although present in only trace levels in D-pit water, had similar total concentrations in the sediments as compared to the DJX-pit samples. Similar to other transition metals (Cu, Co, Mn) and S, a considerable fraction of the total concentration was found in each of the five sediment fractions. In the D-pit and shallow DJX-pit samples, Ni had a notable presence in the highly mobile, exchangeable fraction (5-38%) and the acid soluble carbonate fraction (5-42%). The more resilient reducible Fe/Mn oxide fraction contained 15-62% Ni. Ni in the residual fraction was only substantial in D-pit and deep DJX-pit samples, with concentrations varying between 36-64%. Iron was consistently present in the residual fraction (74-88%) with a smaller contribution from the amorphous Fe/Mn oxide (reducible) fraction (9-33%). Ca was mainly present in the residual fractions (28-76%), except for shallow sediments from the DJX-pit, where the exchangeable fraction contained more Ca (20-53%).

Extractions with citric and oxalic acids performed on sediments D-6 and D-9, showed that with 18-35 mM acid, U and As could be extracted in greater abundances than by sequential extraction steps 1-4 (Table B.16). This indicates that some of the U and As assigned to the residual fraction in the sequential extractions may be associated with poorly crystalline Fe oxide compounds. This was observed for up to 100% of U and up to 35% of As in the residual fraction, but not for Ni.

Bulk XANES

Linear combination fitting of synchrotron U L_3-edge XANES data of bulk sediment samples showed that the majority of U in the D-pit in the sediments was U(VI) (85%), with the remaining 15% being U(IV) (Table B.18 and Table B.19). Similar results were found in the DJX-pit for the samples DJX-13a, DJX-8, and DJX-4c, with an average value of 79% for U(VI) and 21% for U(IV). Arsenic K-edge XANES for D-pit samples indicated that a little more than half (58%) was present as reduced As(III), while the remainder was As(V) (Table B.20). The As(III) proportion in the DJX-pit sediments was, on average, 29%.

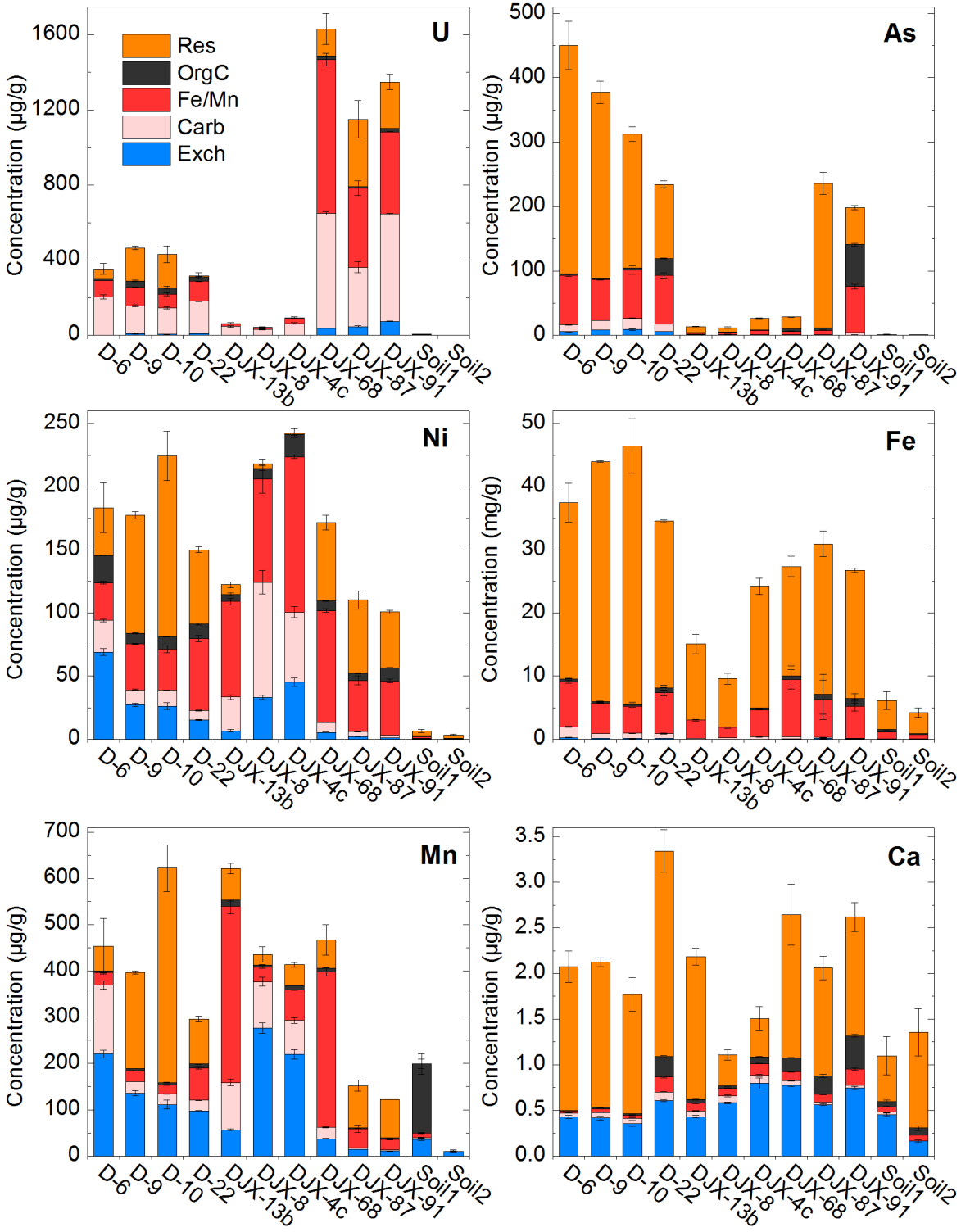

Figure 3.5 Sediment sequential extraction summary for U, As, Ni, Fe, Mn, and Ca. Fraction, from least to most recalcitrant are: exchangeable (Exch), acid soluble carbonates (Carb), reducible Fe/Mn oxide (Fe/Mn), oxidizable organic matter/sulfide (OrgC), and the residual fraction (Res). Error bars represent 1 standard deviation (n=3). Data on more elements can be found in Table B.3 to Table B.12.

SEM-EDS, µ-XANES and Laue diffraction on U-hotspots

SEM-EDS analysis on sediments collected from the pits detected U-rich grains ranging in size from 5-50 µm, examples of which are shown in Figure 3.6. A summary of the grain composition is provided in Table B.17. EDS analysis indicated that U-rich grains predominantly consisted of O (37-72%), U (3-22%), and Pb (1-3%). In three grains, up to 3% Ti was detected. Four grains contained traces of U and were identified as monazite-(Ce), represented by the chemical formula (Ce, La, Nd, Th)PO_4. In such grains, Th(IV) can be partially substituted with U(IV) (van Emden *et al.*, 1997). Sequential extraction of the sediments indicated that the U-rich grains were dissolved in the fourth extraction step (hydrogen peroxide and ammonium acetate), as shown in Figure B.4, suggesting that the U was associated with the oxidizable sediment fraction.

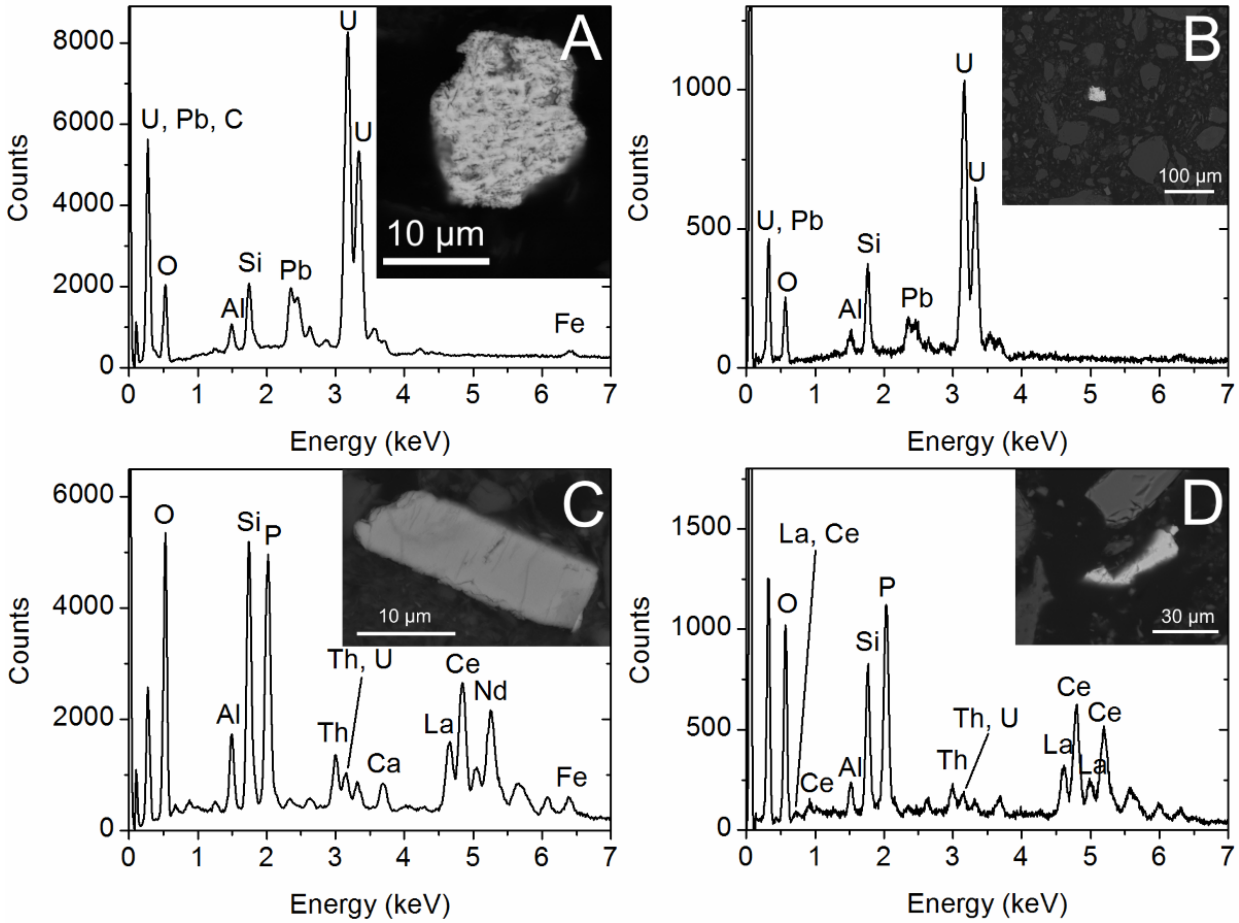

Figure 3.6 Examples of U-rich grains detected by SEM-EDS. Top: U-Pb accumulations found in samples D-10 (A) and DJX-4c (B). Bottom: monazite grains found in samples D-6 (C) and DJX-13a (D).

Contrary to bulk XANES results (Figure B.1), U L_3-edge µ-XANES (Figure 3.7; Figure B.1) on the identified U-grains from D-pit samples indicated that, on average, 67% of the U was present as U(IV) with the remaining 33% as U(VI) (Table B.18). Results from anaerobically dried sediments were similar to those obtained for air dried samples. For the shallow DJX-pit sediments, 44% U(IV) was measured (Table

B.19). Arsenic K-edge µ-XANES indicated that the U hotspots in D-pit samples mounted on glass slides yielded a generally higher proportion of As(III) (on average 78%) as compared to the quartz slides (on average 45%), as shown in Table B.20, likely due to background As in the glass slides having an As(III) fraction of 70%. For one DJX-pit U hotspot that had sufficiently good data for fitting, the As(III) fraction averaged 33%. Similar to the bulk samples, the majority of analyzed samples displayed a reduced component that corresponded best with As(III). The remaining As component was fit to As(V). Due to low As concentrations, most signals of DJX hotspots were too noisy to obtain reliable fits. Although Ni is not known to be redox sensitive under common environmental conditions, and the concentration of Ni was fairly low in the U accumulations, Ni XANES fitting was attempted for four U-hotspots in sample D-10 (Table B.21). The averaged XANES curves indicate various Ni(II) binding environments in the sediments, however, we were not able to resolve them further (Figure B.3).

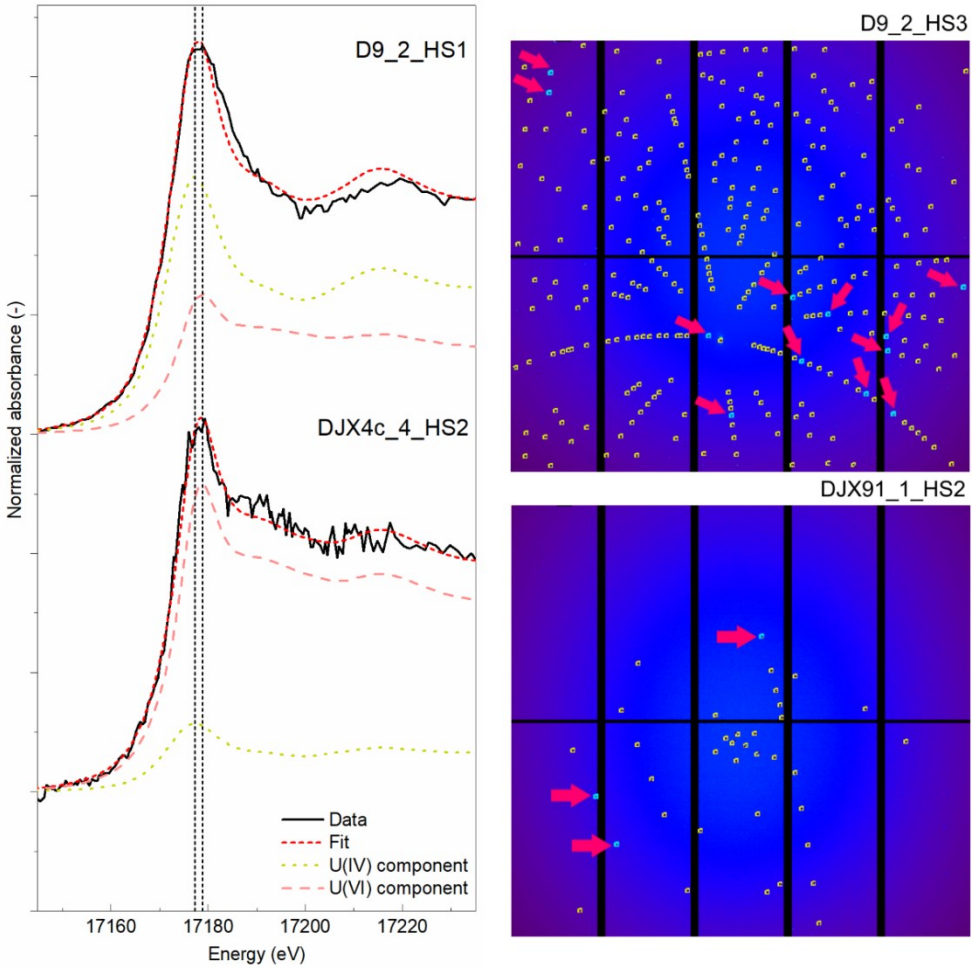

Figure 3.7 VESPERS fit data and Laue diffraction patterns. Left: examples of U L_3-edge XANES fits on the U hotspots D9_2_HS1(D-pit bottom sediments, unknown depth) and DJX4c_4_HS2 (DJX-pit bottom sediments, 4 m depth). The averaged data (solid line, black), obtained fit (dashed, red) and the fit components (dotted and dashed, green and pink) are shown. See Figure B.1 for more examples. Right: indexed Laue diffraction patterns for D9_2_HS3 and DJX91_1_HS2 using the vandendriesscheite crystal structure. Not fitted reflections are colored bright blue and marked with arrows.

In D-pit grains, U correlated strongly with Pb (79%), Th (63%), and As (69%) (Table B.18 and Table B.19). The correlation of U with Ni was, on average, 54%, and correlations with Ca and Fe were generally low (22% and 16%, respectively). In the DJX-pit grains, the correlation between elements was lower. Uranium correlations with Pb, Th, and As were 41%, 14%, and 45%, respectively. Correlations between U and Fe or Ni in the DJX-pit were similar to grains from the D-pit; however, the correlation between U and Ca was higher for DJX-pit grains (46%).

Indexations of Laue diffraction patterns from U minerals (Figure 3.7) yielded satisfying results for the mineral vandendriesscheite, a lead uranyl oxic hydrate ($Pb(UO_2)_{10}O_6(OH)_{11}\cdot 11(H_2O)$), with a similar crystal structure to metaschoepite (Burns, 1997). For several grains, a better indexation was obtained for gauthierite, another lead uranyl oxic hydrate ($KPb[(UO_2)_7O_5(OH)_7]\cdot 8H_2O$) (Olds *et al.*, 2017). Results were similar for sediments from both pits (Table B.18 and Table B.19). Microprobe analysis with wavelength dispersive X-ray spectroscopy confirmed that the U-rich grains were generally abundant in Pb, but not S or As (Figure B.5 and Figure B.6). The occurrence of Ti in some grains was additionally confirmed.

Microbial communities

Fundamental differences were observed between the microbial communities in D-pit and DJX-pit (Figure 3.8). D-pit sediments were dominated by the classes Bacilli, Clostridia, and Deltaproteobacteria, with example families *Planococcaceae*, *Clostridiaceae*, and *Geobacteraceae*, respectively (Table B.25) Samples from the DJX-pit were dominated by Alphaproteobacteria, Betaproteobacteria, Planctomycetacia, and Sphingobacteriia, with dominant families including *Bradyrhizobiaceae*, *Comamonadaceae*, *Planctomycetaceae*, and *Chitinophagaceae*. Spartobacteria and Acidobacteria were present in the largest proportions in shallow DJX-pit (4-12 m) samples, and a low abundance of Planctomycetacia was measured in the deep DJX-pit (91 m) samples. Species abundance and diversity were highest in the shallow DJX-pit samples and both parameters decreased with depth, leaving DJX-pit 91 m with the lowest values (Table B.25).

METAGENassist analysis (Figure B.8) indicated a stronger abundance of anaerobic microbes in the D-pit sediments, as expected due to anoxic conditions in the water column below the chemocline. Correspondingly, D-pit sediments showed a higher abundance of methanogens and syntrophic organisms. Examples for OTUs related to methanogens were *Methanosarcina lacustris Z-7289* (BLAST on OTU1060) a hydrogenotrophic and methylotrophic archaean, *Methanobacterium lacus strain AL-21* (BLAST on OTU1169) a hydrogenotrophic archaean, or *Methanosaeta* (OTU365), an acetoclastic archaean (Holmes and Smith, 2016). DJX-pit samples had more OTUs consistent with sulfate and sulfur reducers, likely due to the high abundance of sulfate in this pit. By far the most dominant group in all samples comprised ammonia oxidizers. Constrained ordination analysis indicated that the samples can be separated into three groups: D-pit, DJX-pit shallow portion, DJX-pit deep portion (Figure B.9). Iron and As concentrations correlated with the D-pit sample positions on the ordinate plot, whereas the deep DJX-pit samples were significantly correlated with U concentrations.

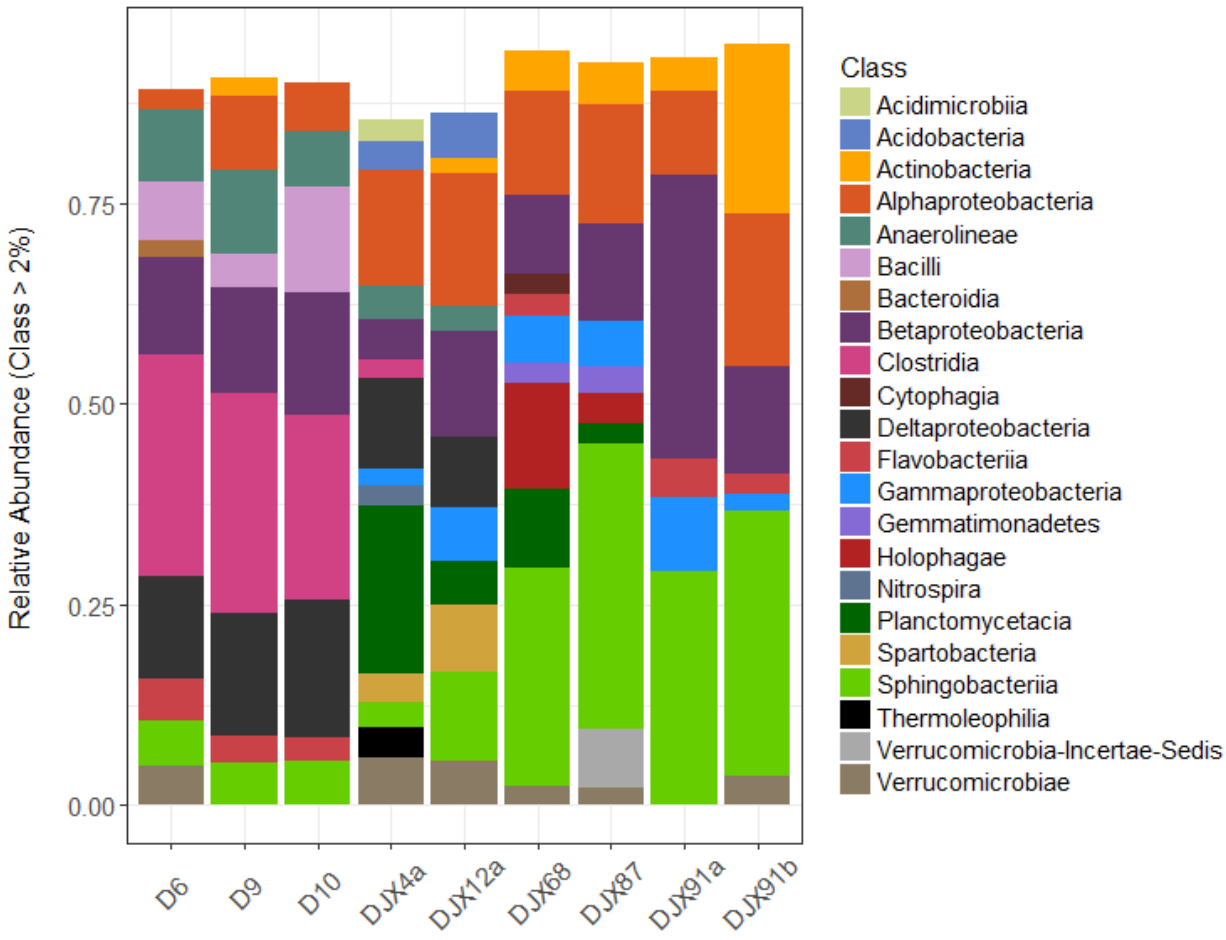

Figure 3.8 Bacterial class distribution in samples from the D-pit (D6-D10, unknown depth), the shallow portion of the DJX-pit (DJX4a, DJX12a) and the deep portion of the DJX-pit (DJX68-DJX91). See Table 3.1 for depth information. Only groups with an abundance >2% are shown.

As shown in Table B.25, the most abundant OTUs in the D-pit were OTU5 (6.6-11.0%) similar to *Clostridium-sensu-stricto-13,* OTU8 (4.7-5.4%) similar to *Rhodoferax,* and OTU13 (2.8-9.7%, family *Planococcaceae*). *Clostridium* has a strictly anaerobic metabolism and is unable to perform dissimilatory sulfate reduction (Andreesen *et al.*, 1989). BLAST results suggested a high similarity to *Clostridium estertheticum*. OTU8 is closely related to *Rhodoferax ferrireducens strain cHCR18ad,* as suggested by BLAST, a psychrotolerant, facultatively anaerobic bacterium capable of Fe(III) reduction from the *Comamonadaceae* family (Finneran *et al.*, 2003). This species was previously described in D-pit water (Chapter 2). Although OTU6 was closely related to *Geobacter* and was highly abundant in the D-pit samples (1.5-9.7%), the BLAST search did not yield evidence for known U(VI) reducers, such as *Geobacter sulfurreducens*.

The most abundant OTUs in the shallow DJX-pit sample (DJX4a) were OTU49 (3.1%) related to the Chloroflexi group KD4-96, OTU27 (2.9%) related to Bacteroidetes group VadinHA17, and OTU33 (1.6%, not shown) similar to the genus *Gaiella*. *Gaiella* species are strictly aerobic (Albuquerque *et al.*, 2011). In

the other shallow DJX-pit sample DJX12a, the top OTUs were OTU55 (2.5%) related to *Chthoniobacter*, OTU8 (2.4%, see above), and OTU237 (1.6%) similar to another microbe from the *Comamonadaceae* family. BLAST results suggested the species *Roseateles depolymerans*, an obligate anaerobic, photosynthetic bacterium (Suyama *et al.*, 1999).

In the deeper DJX-pit sediments (68-87 m), the following three OTUs were dominant: OTU1 (7.0-14.2%) related to the family *Chitinophagaceae*, OTU7 (3.7-8.7%) related to the Chloroflexi group KD4-96, and OTU10 (2.1-8.2%) related to the family *Holophagaceae*. OTU1 was also second most abundant OTU in the deep DJX-pit sediments (91 m) with an abundance of 9.3-19.0%. Other important OTUs at this depth were OTU2 (up to 31.0%) related to the Alphaproteobacteria order Rhizobiales, and OTU9 (up to 7.0%) similar to *Candidatus-Nitrotoga* from the family *Gallionellaceae*. *Nitrotoga* are widely abundant and likely nitrite oxidizing bacteria (Lücker *et al.*, 2015). BLAST results on OTU2 suggested the species *Methylorosula polaris*, an aerobic, facultatively methylotrophic psychrotolerant bacterium, previously found in wetland soils (Berestovskaya *et al.*, 2012).

3.5.3 Soil samples

Sequential extractions on soil samples collected between DJX-pit and Cluff Lake showed generally low metal abundances compared to the sediment samples (Figure 3.5). For example, the soil closer to DJX-pit (Soil1) only contained 6.4 μg/g U and 6.6 μg/g Ni. In this sample, the majority of U (52%) was found in the carbonate-bound fraction, followed by the Fe/Mn oxide fraction (30%), similar to the sediments (Table B.13). Nickel and Co were mostly bound to the residual fraction (58% and 59%, respectively), followed by the Fe/Mn oxide fraction (22% and 23%, respectively). They were therefore not as mobile as in the pit sediments where the exchangeable fraction was larger. Closer to Cluff Lake (Soil2), even lower concentrations of U and Ni were recorded at 0.5 μg/g, and 3.4 μg/g, respectively (Table B.14). In this sample, U was found dominantly in the residual fraction (47%), followed by the carbonate-bound fraction (25%) and the Fe/Mn oxide fraction (21%). Nickel (and Co) were distributed similarly to sample Soil1.

3.5.4 Sediments from sediment traps

Sediment quantification and chemistry

The sediment traps yielded a total 2.3 g and 0.6 g of dry sediments from D-pit and DJX-pit, respectively, after 374 days of deployment. Thus, average deposition rates were extimated to be 6.6 g/m^2/day (D-pit, 17 m) and 1.7 g/m^2/day (DJX-pit, 47 m). In general, the water chemistry matched a system in equilibrium with the fresh sediments in the two pits (Table 3.2). D-pit sediments were found to be rich in As, Fe, and Mn, compared to the DJX-pit sediments, which in turn, were more concentrated in bulk elements such as Al, Ca, K, Mg, S, and the trace elements Co, Cu, Mo, Ni, Zn, and U.

Table 3.2 Concentrations of selected elements in the sediment traps (per g dry weight) and the corresponding total mass deposited within one year based on a calculated deposition rate shown in the bottom line. For more elemental concentrations, see Table B.15.

	D-pit		DJX-pit	
	µg/g	g/m^2/year	µg/g	g/m^2/year
Al	15098.7	36.105	47347.1	29.826
As	1953.6	4.672	55.3	0.035
Co	17.0	0.041	459.7	0.290
Cu	17.6	0.042	254.6	0.160
Fe	223316.7	534.004	45138.1	28.435
Mn	2252.9	5.387	1893.1	1.193
Mo	19.1	0.046	207.2	0.131
Ni	46.5	0.111	896.4	0.565
P	792.7	1.896	639.5	0.403
Pb	15.8	0.038	29.3	0.018
S	3828.4	9.155	20919.0	13.178
U	377.8	0.903	1449.7	0.913
Zn	12.7	0.030	175.7	0.111
Rate (g/m2/year)		2391.2		630.0

Mineralogy and SEM-EDS

SEM-EDS analyses on the sediments from sediment traps revealed that D-pit sediments were dominated by Fe oxide and Fe sulfide phases (Figure 3.9). In addition, monazite-like grains were detected, which contained lanthanides (e.g., La, Ce, Nd) and the actinide Th. Such grains are similar to those that were previously described in the bottom sediments of the pits. In DJX-pit, Fe was not as dominant as in D-pit. Instead, many clay-like particles were detected. Additionally, Fe sulfide particles (Figure 3.9) were detected, some of which contained Ni (up to 3.9%) and Co (up to 5.0%). One particle, having a composition similar to an aluminosilicate, showed detectable amounts of U (0.3 %), suggesting that those silicates are capable of sorbing U from the pit water. Monazite-like grains, enriched in light-weight lanthanides were also observed in the DJX-pit.

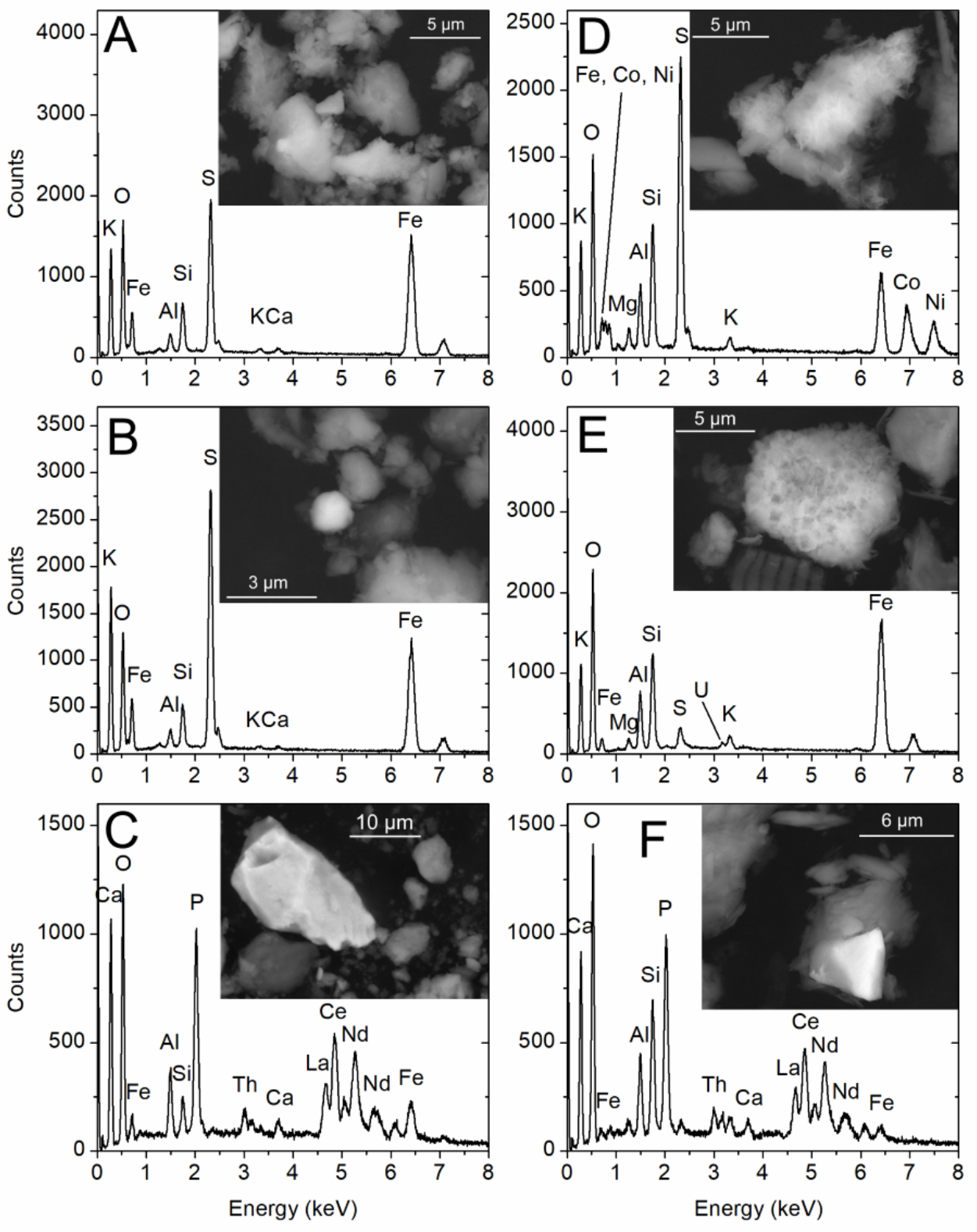

Figure 3.9 SEM-EDS images on selected spots found in the sediments collected by sediment traps in the D-pit (A, B, C) and DJX-pit (D, E, F). C and F show potential grains of monazite-(Ce). D and E show grains containing Ni, Co, and U. EDS results on those and other grains are summarized in Table B.24.

3.6 Discussion

3.6.1 Colloidal metal transport

The distribution of metals and metalloids over the different colloidal size fractions is a result of their chemistry (e.g., charge) and their affinity to specific colloidal types. The observed colloidal metals suggests that in the fresh water samples the majority of trace metals, such as U and Ni, were in the dissolved form or associated with small colloids (<10 kDa). Arsenic, on the other hand, having an affinity to co-precipitate with Fe phases, was associated with colloids >10 kDa, likely Fe oxyhydroxides, as suggested by similar colloidal size distribution. These results are similar to those reported by Hollings *et al.* (1999), who investigated the colloidal fractions in waters at the Rabbit Lake U mine and found that U, Ni, and As in water with little disturbance (e.g., deeper layers of tailings pond) were mostly in the fraction <0.02 µm, i.e., likely truly dissolved. In the current study, S/TEM-EDS results indicated that the colloidal pool in D-pit is dominated by Fe-O particles, whereas in DJX-pit, colloids are mostly composed of Al-Si-Ca-S-O particles. Colloidal aging at room temperature for one month led to a general shift towards larger colloids and a decrease in metal concentrations, presumably the result of flocculation and subsequent precipitation (Figure 3.2). Such shifts are likely to happen in the pits with time, when colloidal particles are exposed to different temperature conditions, especially at the thermoclines (in close proximity to the chemoclines) where warmer surface water is in contact with deeper, colder water. As suggested by the colloidal pumping theory (Dai *et al.*, 1995), larger aged colloids are more prone to being removed from the water column.

As observed in incubated water bottles and the sediment traps, sediments forming over time in D-pit were dominated by Fe oxyhydroxides (Figure 3.10). In DJX-pit, the sediments were chemically similar to minerals such as kaolinite, muscovite, and gypsum, the latter being predicted to form in the water column based on thermodynamic modeling (Chapter 2). Gypsum is known to form in leachates in contact with dolomitic host rocks (Gupta and Singh, 2003), which is the case for both pits. Despite the obvious chemical differences between the pits, our observations suggest that primarily Fe sulfide phases might be efficient in removing trace metals, such as U, Co, and Ni, from the water column below the chemocline (Figure 3.9). This process is known and was previously described in mining affected lakes (Huerta-Diaz *et al.*, 1998) and groundwater (Saunders *et al.*, 2018). Based on calculations done using data from the sediment traps (Table 3.2), we can estimate that the removal of U from the water column in both pits is very similar, 0.9 g/m^2/year at the corresponding depths, even though the U concentrations above the deployment depths in the two pits are clearly different, e.g., <131 ppm and <307 ppm, in D-pit and DJX-pit, respectively (Chapter 2). As the DJX-pit sediment trap was deeper and the pit has higher aqueous U concentrations, one may expect a higher rate of U accumulation. However, it is likely that other U removal processes (discussed below) in addition to the above-discussed removal by Fe-S phases, occur in the D-pit, contributing to on overall higher removal efficiency.

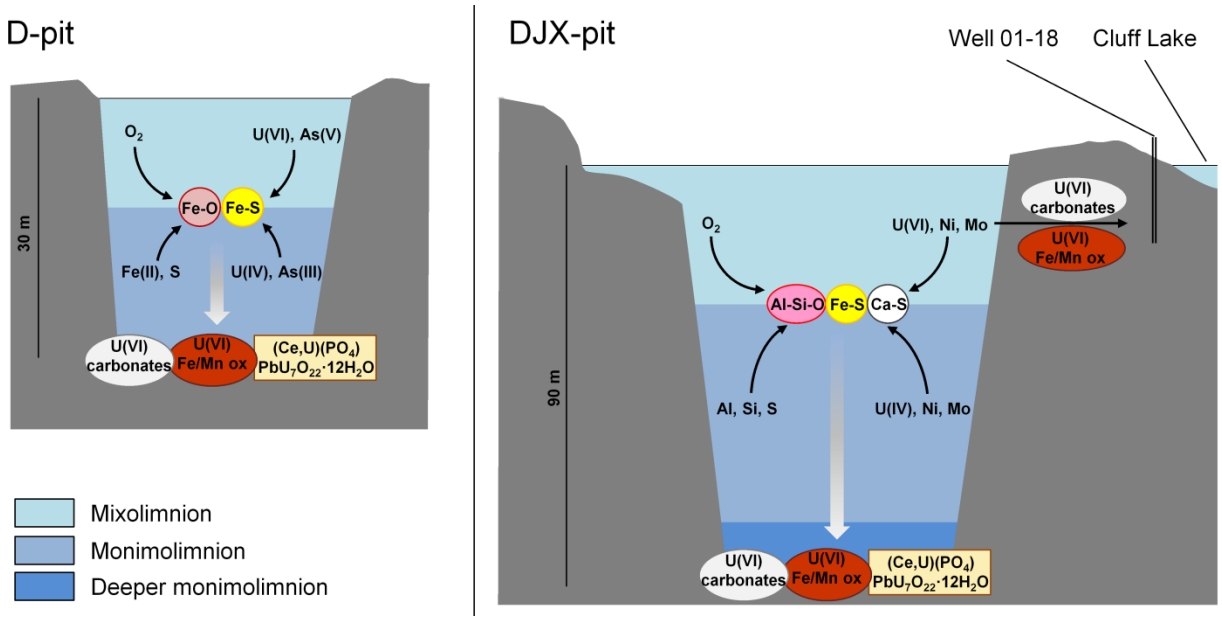

Figure 3.10 Schematic diagram of colloid formation and transport processes and the corresponding phases and minerals in the two pit lakes D-pit and DJX-pit. Note: schematic is not to scale.

In D-pit, Fe-O phases may play an important role in trace metal cycling. Such Fe-O might sorb As (up to 4.7 g/m^2/year, Table 3.2) and with it U, as U is known to bind to arsenate phases (Gupta and Singh, 2003). Tang and Reeder (2009) observed an increased affinity of U(VI) to aluminum oxides pretreated with As(V). Such coated Al particles are likely to form in the D-pit environment, where an Al removal rate was calculated as 36.1 g/m^2/year. In addition, at the investigated sediment trap depths, more U(IV) might be expected in D-pit compared to DJX-pit, as suggested by the oxidation state measurements of U. Here, U may be present as U(IV) hydroxide, as the environmental conditions (i.e., ORP: -263 mV, pH: 7.9; numbers from Chapter 2), would favor this species (Langmuir, 1978). In addition, the high abundance of Fe(II) in D-pit supports the presence of U(IV), as Fe^{2+} has been shown to reduce U (Du *et al.*, 2011), favoring its accumulation and precipitation.

In DJX-pit, the removal of U by aluminosilicates (Wilmarth *et al.*, 2003), which was previously hypothesized in Chapter 2, could indeed be taking place. Aluminosilicates were observed in the collected sediments (Figure 3.9), and Al and U were found in similar colloidal size distributions, especially in the deep and aged DJX-pit water samples (Figure 3.2). In addition to U, Mo is also precipitating in DJX-pit (0.1 g/m^2/year) and it is known that Mo oxyanions behave in a chemically similar manner to U oxyanions (Brassier-Lecarme *et al.*, 1997). Previous studies have indicated that U and Mo both strongly sorb to organic matter and clay minerals (Morrison and Spangler, 1992), supporting the hypothesis that aluminosilicates could be removing U in DJX-pit. Under more strongly reducing conditions, U is removed via mineral precipitation to a greater extent than Mo, unless Fe-Mn oxyhydroxides are present that can promote Mo removal from the water column (Algeo and Tribovillard, 2009). Indeed, some Fe-O colloids were observed in the DJX-pit by S/TEM-EDS, suggesting that this process might be taking place in the

deep, oxygen-limited DJX-pit water layers. Although phosphate fertilization experiments by Dessouki *et al.* (2005) did not show an increase in Mo precipitation, due to the low affinity of Mo to biogenic particles (e.g., algae), our observations suggest that Mo might be affected by colloidal pumping because of the sorption to inorganic colloidal particles.

In the aged D-pit sample, Ni shifted from mostly dissolved species towards colloidal particles of 10-500 kDa, thereby increasing the potential for Ni removal which was calculated to be around 0.1 g/m^2/year. This process likely contributes to the low concentration in the monimolimnion of the D-pit. Although present in much higher concentrations in DJX-pit, the removal of Ni was only 6 times larger, 0.6 g/m^2/year. Nickel removal in DJX-pit is likely limited due to the prevalence of dissolved Ni, even in the stored and aged samples, which was likely contributed by the lower pH conditions in the monimolimnion. This observation is also supported by the low concentrations of Ni and its near absence in the residual fraction within the shallow sediments of the DJX-pit (Figure 3.5).

3.6.2 Sequestration of metals in the sediments

Metals and metalloids precipitating out of the water column will eventually accumulate in pit lake bottom sediments (Laird *et al.*, 2014), where their speciation will ultimately determine their environmental fate. The strong presence of U in the carbonate fraction suggests the presence of uranyl carbonates (Vandenhove *et al.*, 2014) or the incorporation of U in carbonate minerals (Tessier *et al.*, 1979, Abdelouasa *et al.*, 1998). However, the fundamentally different distribution of Ca compared to U, and XRD results, do not suggest a significant presence of Ca-bearing carbonates. No carbonate crystals with sorbed or co-precipitated U were found by either SEM-EDS or Laue diffraction. Similarly, Vandenhove *et al.* (2014) did not observe any correlation between $CaCO_3$ and U within the carbonate fraction. Instead, this U may be present in the form of uranyl carbonates or hydrated carbonates that are adsorbed to the surface of silicate minerals (Abdelouasa *et al.*, 1998). Uranium in this carbonate fraction can be considered stable under many environmental conditions due to the low solubility of carbonate minerals under neutral to basic pH conditions (Troyer *et al.*, 2014). Such conditions prevail in the D-pit, where neutral pH values exist at the bottom (Chapter 2). However, in DJX-pit, the pH is more acidic (pH 5.6 below 20 m), which may lead to the remobilization of solid and suspended carbonates in this lake. In the DJX-pit, however, the Fe/Mn oxide and residual fractions play a more significant role for U sequestration. Accordingly, the Fe/Mn oxide fraction may represent U sorbed to amorphous Fe/Mn oxide, while the residual fraction might represent U incorporated into more recalcitrant, crystalline Fe oxides, such as hematite (Tessier *et al.*, 1979, Sheppard and Thibault, 1992; Duff *et al.*, 2002). Hematite was detected in most D-pit and some DJX-pit samples (Table B.2). The high abundance of U in the Fe/Mn oxide fraction in the deep DJX-pit samples compared to D-pit can be explained with the oxic/suboxic conditions in the deep monimolimnion, which differs from the anoxic monimolimnion of D-pit (Chapter 2). Therefore, this Fe/Mn oxide fraction might release U upon the establishment of anoxia in DJX-pit.

Troyer *et al.* (2014) investigated U tailings and mining affected stream and pond sediments (North Cave Hills, South Dakota, USA) and found that most U was in the acid soluble carbonate fraction and the reducible Fe oxyhydroxide fraction, which is similar to findings of this study. However, at the toe of the tailings pile, Troyer *et al.* (2014) found that the exchangeable fraction was dominant. In our study, the exchangeable fraction was rather low, suggesting that the sediment do not contain easily mobilized U. In the two pit lakes at Cluff Lake, the acid soluble (carbonates) and Fe/Mn oxide oxides fractions contributed the most to the U pool in the sediments, which on average accounted together for 78% of total U (Tables B.3-B.12).

Arsenic, which was dominant in the two most resilient fractions (Fe/Mn oxides and residual), can be expected to be stable within the sediments. A similar distribution and total concentrations of As were reported by Troyer *et al.* (2014). Pichler *et al.* (2000) analyzed the distribution of metals in the tailings of another U mine in northern Saskatchewan and found that As was bound to amorphous Fe oxyhydroxides rather than to crystalline Fe oxides or residual fractions. In the Cluff Lake pits, the amorphous Fe oxide phase was generally not as important for As as compared to the residual fraction. Similarities in the distribution of As and P can be explained by their similar chemical behavior and the possibility of phosphate and arsenate co-precipitation (Dungkaew *et al.*, 2012). The observed similarities with respect to Fe distributions, would further suggest that As and P are competing for sorption sites on Fe oxides (Hongshao and Stanforth, 2001).

Similar Ni, Co, and Mn distributions are likely the result of these metals being associated with Mn oxides (Larsen and Postma, 1997). Perhaps surprisingly, Ni was not especially abundant in the deeper sediment samples in DJX-pit, compared to the Ni-poor D-pit.Complexation with sulfate and the depressed pH conditions in the DJX-pit promote Ni remaining in solution (Larsen and Postma, 1997), an interpretation consistent with previous thermodynamic modeling done in Chapter 2. The lower pH values of the deeper DJX-pit layers (>20 m) could also decrease the abundance of Ni within the exchangeable fraction in those sediments, as lower pH values may lead to a decrease in the abundance of negatively charged surface sites available for Ni^{2+} sorption. Notable is the absence of Ni in the residual fraction in shallow DJX-pit sediments.

The observed microbial communities are consistent with the geochemistry of the two pits. Due to anoxic conditions in D-pit, anaerobic species, such as a relative of the Fe(III) reducer *Rhodoferax ferrireducens* or methanogens (*Methanosarcina*, *Methanobacterium, Methanosaeta*) were abundant in the D-pit sediment community, in accordance with the constrained ordinations analysis (Figure B.9). Anoxic conditions likely also favor slightly higher average TOC concentrations in the D-pit (average for sequenced samples 1.1 % vs. 0.6% in the DJX-pit samples) because of limited organic matter degradation. In DJX-pit, high sulfate concentrations allow for the presence of sulfate reducing bacteria, even with the presence of traces of oxygen in deeper layers. Sulfate reducers might play an important role in both pit lakes, considering that the freshly precipitated sediments collected in sediment traps contained

Fe-S phases, such as pyrite. The 16S rRNA data, however, cannot constrain how active potential sulfate reducers might be in the DJX-pit sediments. Interestingly, U sediment concentrations seem to drive the community composition in the deep DJX-pit sediments. The high U concentrations might limit the activity of certain microbes through toxicity effects (VanEngelen *et al.*, 2010), which, in turn, might induce a higher environmental stress on corresponding communities and lower their species richness and diversity. The response of the communities to Ni remains unclear, likely because of the widely varying Ni concentrations found in pit sediment samples (Figure 3.5).

3.6.3 Importance of the U micro-grains

Both minerals identified in the U-rich grains in the pit sediments, vandendriesscheite and gauthierite, are alteration products of a uraninite precursor, which were previously found in U mines such as the Shinkolobwe mine in Congo (Burns, 1997; Olds *et al.*, 2017) and the Jáchymov mine in Czech Rebuplic (Ondrus *et al.*, 1997). The majority of the grains were classified as vandendriesscheite, an early alteration product (Plášil, 2014), which has the lowest concentration of Pb of all lead oxide hydrates (Burns, 1997). According to Burns (1997), due to the accumulation of Pb, this alteration product requires long-term exposure to oxidizing conditions, and therefore, it is unlikely that this mineral formed during the sample recovery and preparation. As some grains did not show any identifiable diffraction pattern or produce a satisfactory fit to a known mineral standard (Table B.18), it can be inferred that some form of non-crystalline uraninite was present (Alessi *et al.*, 2014a), an assertion confirmed by XANES spectra which indicated that the predominant oxidation state of U was 4+, with 44-67% U(IV). Bacterial U reduction in the sediments of the pits might be limited, as traces of oxygen (0.9 mg/L) and nitrate (1.6 mg/L) in the DJX-pit might be responsible for the suppression of potential U(VI) reducing organisms (Finneran *et al.*, 2002). In D-pit, high abundances of Fe oxides might suppress microbial U(VI) reduction through competition of U(VI) and Fe(III) as electron acceptors (Wielinga *et al.*, 2000). Therefore, it is likely that the observed micro-crystals of vandendriesscheite and gauthierite are the result of the alterations of detrital uraninite or amorphous pitchblende in the mining pits, which were exposed to wet and oxic conditions over 4 years, i.e., during the mining operations and initial flooding. Detected monazite particles are likely detriatal as well, given their crystalline appearance (Figures 3.6 and 3.9). Their origin could be the exposed rock of the pit banks and nearby waste rock, which is in contact with groundwater entering the pits. This portion of U is therefore not forming in the pit lake water column, but does, however, contribute to the measured overall sequestration rate. It was established above that this detriatal U is likely ending up in the oxidizable fraction of the bottom sediments. This means that its overall contribution to the total sequestered mass is relatively small, given that the oxidizable fraction makes up less than 5% in the analyzed samples (see U in Figure 3.5).

The dominance of As(III) in the U-rich grains and the high correlation between As and U (Table B.18 to Table B.20) are consistent with previous findings as vandendriesscheite, and similar uraninite alteration products, can contain up to 1.7% As_2O_3 impurities (Deditius *et al.*, 2007). It also suggests that the grains

are not highly matured, as it has been observed that over time As(III) and As(-I) in flooded mine tailings are generally oxidized to As(V) and form stable arsenates, such as scorodite ($FeAsO_4 \cdot 2H_2O$) (Warner and Rowson, 2007). This phase was, however, not identified in our samples. The U-rich micro-grains seem to generally benefit the overall stability of U, as suggested by the sequential extractions and corresponding SEM-EDS analyses.

Over time, in the Ca- and Si-rich environments of the D-pit and DJX-pit water-sediment-boundary (Chapter 2), the vandendriesscheite (and possibly gauthierite) grains could be expected to form uranophane ($CaU_2Si_2O_{11} \cdot 6H_2O$) and masuyite ($PbU_3O_{10} \cdot 3H_2O$) assuming no kinetics barriers (Finch and Ewing, 1991). Masuyite can further alter to curite ($Pb_3U_8O_{27} \cdot 6H_2O$), kasolite ($PbUSiO_6 \cdot H2O$), and soddyite ($U_2SiO_8 \cdot 2H_2O$) in the presence of silica (Finch and Ewing, 1991). The uranyl silicate minerals are generally less soluble than uranyl oxic hydrates or uranyl carbonates (Gorman-Lewis *et al.*, 2008), which would be beneficial for U stability in the pit sediments. Furthermore, curite would promote the precipitation of uranyl phosphates (Finch and Ewing, 1991), which are even more insoluble than uranyl silicates (Gorman-Lewis *et al.*, 2008). Uranyl phosphates would be more favored in the slightly acidic environment of DJX-pit deeper water, although, the formation of the required curite may be suppressed (Plášil, 2014). In D-pit, on the other hand, although the formation of curite might be favored, the precipitation of phosphates and/or arsenates could be suppressed by the elevated pH conditions characteristic in the D-pit (Plášil, 2014).

3.7 Concluding remarks

The observations in the water columns of the two flooded mining pits support the possibility of metal sequestration by colloidal pumping (Figure 3.10). Trace metals accumulate onto colloidal particles, such as Ca-O and Fe-O particles in the D-pit, and Ca-S-O particles in the DJX-pit. Colloidal aggregation and precipitation can then lead to the removal of metals from the water column. We observed that in the two investigated pits, Fe-S particles are able to sorb trace metals, such as Ni and Co. Uranium is likely being removed by a similar process and also by monazite-(Ce) crystals. In addition, aluminosilicates can sorb U in the DJX-pit environment. Although different in their water chemistry, both pits express a similar precipitation rate for U below the chemocline of about 0.9 g/m^2/year. In the bottom sediments, the stability of metals could be summarized as Ni<U<As. Nickel, having large exchangeable and acid soluble fractions, might be easily mobilized by changes in the ionic strength and acidity of the water. Similarly, pH changes in the water might strongly affect U, and some U from the reducible fraction might be released into the DJX-pit water when the monimolimnion turns anaerobic. The stratification regime and its future development in the DJX-pit is, however, not yet fully understood (Chapter 2). In addition, observed U mineral phases, such as vandendriesscheite might benefit U stability over longer periods of time. The sediment chemistry likely exerts a strong environmental control on the microbial communities, as indicated by their low species richness and diversity in deep sediments of the DJX-pit. Continuous monitoring of the pit will allow observation regarding the environmental stability moving forward, and if necessary, identify if

intervention is required to counter any environmentally detrimental development. This study demonstrates the importance of the colloid/sediment interactions in mine pit lakes and their potential influence on microbial communities and metal mobility, which has significant implications for other mining sites that involve open pit mining and that aim to use pit lakes and bioremediation techniques as decommissioning strategies. Results presented here indicate that colloidal fractions with particle sizes >0.45 µm might be overlooked when applying standard monitoring techniques and might not reveal the full extent of metal distribution in pit lake environments.

4 COLLOIDAL METAL TRANSPORT ALONG TWO PERMEABLE REACTIVE BARRIERS IN A MINING-AFFECTED SPHAGNUM PEATLAND

4.2 Summary

The biogeochemistry of two alkaline permeable reactive barriers (PRBs) installed for remediation in a mining affected wetland was investigated in order to assess the importance of colloidal particles on metal removal processes in such systems. At the time of investigation, both PRBs were effective in removing U, Cu, and Zn (>95%) from groundwater but were slightly less efficient for Ni and Co (<90%). Previously installed groundwater wells allowed an in-depth analysis of groundwater passing through the first PRB. Here, in an alkaline environment (pH 6.0-9.7), 11-14% of Ni, 36-37% of Co, 77-81% of Cu, 14-17% of U, and 10-19% of Fe were associated with organic matter and inorganic colloids, while in the more acidic environments (pH <6.0) of the surrounding wetland, ionic species and complexes (e.g., Co^{2+}, Ni^{2+}, Cu^{2+}, $UO_2H_3SiO_4^+$) dominated. Larger colloidal fractions (>1 kDa) favored the removal of Cu and U, which were more strongly bound to the solid phase, suggesting ongoing metal sequestration processes. Uranium removal was likely further enhanced by U(VI) reduction in the alkaline and oxygen-depleted conditions of the PRBs. The less efficient removal of Ni and Co, being major target metals, was explained by their high solubility, their limited association with colloids, and unfavorable redox and pH conditions (for the formation of sulfides) created by the alkaline PRBs, considerations that are critical in the design of future PRBs for the remediation of similar systems.

4.3 Introduction

PRBs are an *in situ* technology applied to the remediation of both organic and inorganic contaminants in groundwater (Powell *et al.*, 1998). Typically a trench is excavated perpendicular to the flow of contaminated groundwater and then backfilled with a mixture of reactive and permeable material. Contaminants are removed by sorption or precipitation, or, if the contaminant is organic, they are degraded by redox processes (Powell *et al.*, 1998). The transport behavior of trace metals in aqueous environments is strongly affected by redox conditions, pH, available ligands (e.g., organic acids), and potential sorption sites (Borch *et al.*, 2010; Violante *et al.*, 2010). However, colloidal particles (1-1000 nm and up to 10 μm in some environments), which are little-affected by gravitational setting, can substantially alter the transport behavior of trace metals (Honeyman, 1991; Dai *et al.*, 1995; Gustafsson and Gschwend, 1997). Despite this, few studies have investigated the importance of colloidal transport of trace metals in mining affected wetlands (e.g., Wang *et al.*, 2013) and their importance in the performance of PRBs.

In this study, we investigated PRBs installed in a wetland (fen type, *Sphagnum* dominated) at a decommissioned mine in Cluff Lake, northern Saskatchewan, Canada (Figure 4.1), that was reported to receive inputs of U, Mn, Fe, Ni, Co, Zn and traces of Cu and Mo due to previous mining activities (see

previous chapters). The two experimental PRBs were designed and installed in 2006 and 2007 by the site owner to intercept the waste stream originating at a waste rock pile and to reduce contaminant flow into a nearby stream, with a major focus on the removal of U. The 2006 PRB (PRB2) contained a mixture of gravel (50%) and peat (50%) with additions of lime and limestone (unknown amounts). The 2007 PRB (PRB1) was installed further upgradient of groundwater flow and was backfilled with gravel (60%), peat (35%), lime (3%) and limestone (2%). The dimensions of PRB2 are not well documented, but it is longer but narrower compared to the PRB1, which was originally 124 m long, 2 m wide and 4-9 m deep (see Figure 4.2 for photos). A previous study showed that the reactive barriers efficiently removed U, which was the major metal of concern in the groundwater. However, the barriers did not remove Co and Ni to a similar extent (AREVA, 2013). Nevertheless, the wetland itself successfully diminished metals concentrations further downgradient of the PRBs. The reasons for the suppressed performance of the PRBs in regards to Co and Ni were not further investigated by the site owner.

In order to better understand how biogeochemical factors, and in particular the role of colloidal metal associations could affect the barrier performance and metal removal, we applied geochemical modeling, metal speciation investigations (using sequential extractions), colloidal analyses (using filtrations and asymmetrical flow field flow fractionation, or AF4), and 16S rRNA gene sequencing to obtain an integrated understanding of the PRB environment. The results from this study provide vital information for future mining waste management scenarios and for PRB designs in similar environments.

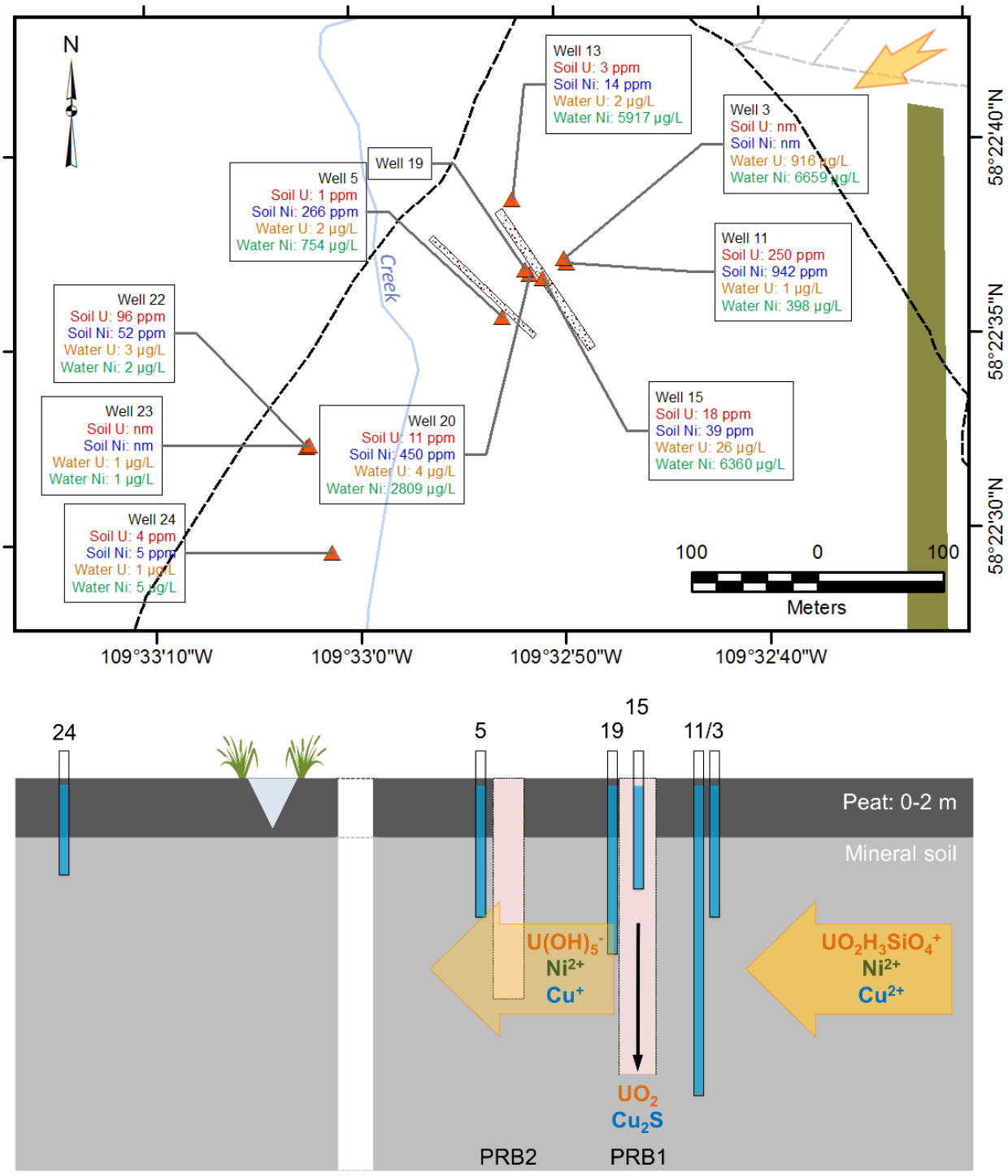

Figure 4.1 Top: overview map of the sampling locations. In the map, values for U and Ni represent groundwater and soil concentrations and outlines of the PRB2 (southwest) and the PRB1 (northeast) are drawn as textured rectangles between well 5 (downgradient) and wells 03/11 (upgradient). General groundwater flow direction is indicated by the arrows. Bottom: artistic depiction of a cross section cutting through the PRBs (not too scale).

Figure 4.2 Photos of the two PRBs. Top: The partially water logged 2006 PRB (PRB2). Bottom: The drier 2007 PRB (PRB1). Arrows point to the locations of wells 5 (top) and 15 (bottom), respectively.

4.4 Materials and Methods

4.4.1 Peat and soil samples

All sampling was organized along a transect passing through both permeable reactive barriers and utilizing existing groundwater wells (Figure 4.1). In 2017, surface samples were collected to a depth of 20-30 cm ("surface", S) using a hand auger 2 m away from the wells. At PRB1, an additional 90-100 cm deep sample was collected (15D). In 2018, at selected locations, deeper soil samples from the peat/mineral soil interface were collected. The sampling depths are given in Table 4.1. All peat/soil samples were placed into plastic bags and sealed for transportation.

Table 4.1 Sampling depths, pH values, and carbon and nitrogen data from surface peat (S) and mineral soil (M) from the transect cutting through the PRBs. Samples 15 were taken from the PRB material. See Figure 1 for spatial distribution of locations.

Location	Depth cm	Year collected	pH	TN wt%	TC wt%	TOC wt%
11 S	20-30	2017	4.10	1.4	44.8	40.2
11 M	110-120	2018	4.94	0.0	0.7	0.7
13 S	20-30	2017	3.25	0.7	44.3	42.5
15 S	20-30	2017	9.72	0.1	6.7	6.1
15 D	90-100	2017	-	0.1	6.8	6.2
15 M	200-210	2018	8.75	0.4	22.6	21.3
20 S	20-30	2017	5.27	0.7	31.3	31.2
20 M	190-200	2018	7.31	0.0	0.6	0.6
05 S	20-30	2017	4.06	1.0	38.9	33.9
05 M	110-120	2018	3.66	0.1	1.4	1.3
22 S	20-30	2017	5.93	0.7	15.5	15.0
24 S	20-30	2017	5.07	1.4	43.0	40.9
24 M	200-210	2018	2.90	0.1	0.7	0.7

In the laboratory, subsamples of the collected peat and soil were dried (105 °C) to determine the water content by mass loss. The dried samples were then ground by a mortar and pestle and analyzed for total carbon (TC), total organic carbon (TOC), and total nitrogen (TN) using a Thermo Scientific Flash 2000 elemental analyzer at the University of Alberta (UofA). Mineralogy of the mineral soil samples and all samples taken from PRB1 (15S, 15D, and 15M) were determined at the UofA with an Ultima IV X-ray diffraction (XRD) unit (Rikagu) with a cobalt X-ray source (λ = 1.790260) using the JADE 9.5 software packages and databases (2013 ICDD, 2015-1 ICSD) for interpretation. Samples from the PRB were also separated through a set of sieves (2 mm, 1 mm, 0.075 mm) to determine the size distribution of the upper layers. The pH of selected samples was measured in a water slurry using a 1:5 mass to volume ratio using air dried, ground, and sieved (<2 mm) solids (Rayment and Higginson, 1992), which required hand-squeezing for wetted peat samples due to their high water absorption (Stanek, 1972).

To distinguish the concentrations and binding affinities of trace metals in the wetland, a sequential extraction technique based on the Community Bureau of Reference (CBR) method (Quevauviller *et al.*, 1993), with modifications as described in von Gunten *et al.* (2017), was performed on the 2017 peat, the 2018 mineral soil, and all PRB1 samples. This method allows for the extraction of organic-rich substrates and considered the following four metal fractions: (1) exchangeable/acid soluble (metals weakly adsorbed to the substrate and to carbonates), (2) easily reducible (Fe/Mn oxyhydroxides), (3) oxidizable (metals sorbed/precipitated to organic matter and sulfides), and (4) residual (strongly bound metals). Extractions were performed with 0.5 g samples in 50 mL PP centrifuge tubes (here further referred to as "reaction tubes"). To reduce sample losses during sample transfer between the extractions, 0.45 μm PVDF filter centrifuge tubes (Thermo Scientific) were used for solution recovery. For this, after each extraction, the suspensions in the reaction tubes were transferred to the centrifuge filter tubes and centrifuged at 2000 g for 8 min to recover the solution, which was then analyzed for metal concentrations using an Agilent 8800 Triple Quadrupole Inductively Coupled Plasma – Mass Spectrometer (ICP-MS). During ICP-MS analyses, He, H_2, and O_2 were used as collision and reaction gases to remove polyatomic interferences (Sakai, 2015). Residual material in the reaction tubes after each extraction step was transferred to the filter tubes with the addition of ultrapure water and centrifuged again. Additional ultrapure water was added to wash the sample for the next extraction step. After flushing, the solids were transferred back into the reaction tube with additions of water and dried at 60 °C prior to the next step. No ashing was performed for the last digestion step, however an increased amount of 70% nitric acid (10 mL) was used in the digestion to completely digest the peat-rich samples.

4.4.2 Groundwater samples

In 2017, groundwater from wells was sampled using a MasterFlex E/S portable sampler (Cole-Parmer). The wells were purged (three well volumes, according to Vail, 2013). Water samples were filtered (0.45 μm) and acidified (pH <2) prior to analysis by ICP-MS. For selected samples, sulfate-S and nitrate-N were measured by colorimetry according to EPA (1983).

In 2018, selected wells were similarly purged, and physical/chemical parameters were then recorded on site using an YSI Professional multimeter submerged in a bucket filled with fresh water from the well. Samples filtered through 0.45 μm membranes were collected for asymmentrical flow field-flow fractionation linked to an ICP-MS (AF4-ICP-MS), which was done to analyze the distribution of trace metals in different colloid types. This method is documented to differentiate between dissolved species, species bound to dissolved organic carbon (DOM), and those bound to inorganic colloids (mainly clays and oxyhydroxides) (Cuss *et al.*, 2017). In order to sample anaerobically, inline-filtered water was pumped directly into a glove bag (Fisher Scientific), which was first purged three times with nitrogen gas. Water samples were collected in duplicate, filled into acid washed 150 mL glass serum bottles, and sealed inside of the glove bag with rubber stoppers.

In the laboratory, the samples were stored in an anaerobic glove box (98% nitrogen, 2% hydrogen) prior to analysis by AF4-ICP-MS. To prevent oxidation during the measurements, glass autosampler vials were used (filled in an anaerobic glove box) and the instrument eluent was bubbled with Ar for 72 hours before analyses. Ultrapure water and HCl were used to adjust pH and conductivity of the carrier fluid buffer (ammonium carbonate) to the sample properties. The method is described in full detail in Cuss *et al.* (2017).

In addition to the AF4 samples, to investigate the size distribution of colloidal particles in groundwater, water pumped from the wells was instantly filtered using in-line 1.2 μm, 0.45 μm, and 0.2 μm high-turbidity filters (Waterra) and ultrafiltration cartridges (Pellicon XL, Millipore, 500 kDa and 10 kDa), both fed with the 0.2 μm permeate. All permeate samples were analyzed for metals and metalloids using the ICP-MS.

4.4.3 Geochemical modeling

Geochemical modeling was performed with PHREEQC V. 3.4.0.12927 and the Minteq.v4 (Parkhurst and Appelo, 2013) database to model the conditions found in the shallow groundwater upgradient of PRB1 by using elemental concentrations measured in upgradient well 3 as input values (Table C.2). To simulate the percolation of this water through the PRB, the pH was adjusted based on geochemical conditions in well 15 (Table 4.1), which is located within PRB1 (Figure 4.2). Temperature was adjusted as measured in wells 3 and 15 (5.5 °C) and the redox conditions (p_e) were set based on oxygen concentrations (Table 4.2). For reduced scenarios, a p_e of -3 was chosen based on the highest p_e values generally found for sulfur reducing environments (Libes, 2009).

Table 4.2 Metal concentrations, anions, and chemical parameters measured in pore water and groundwater as determined on June 2017 samples (well 19 data and oxygen concentrations from June 2018). Removal efficiency was calculated by comparing data from well 3 (upgradient) and well 5 (downgradient). Mo was <0.001 ppm except for groundwater samples 03 and 22 (0.001 ppm). The detection limit for dissolved oxygen was 0.1 ppm.

Site	Depth	Ca	Mg	S	Mn	Fe	Co	Ni	Cu	Zn	U	O_2	Cond	pH
	m	ppm	ppm	ppm	ppm	ppm	ppm	ppm	ppm	ppm	ppm	ppm	µS/cm	
03	5.0	257	475	1079	14.9	6.6	1.898	6.659	0.073	1.049	0.916	0.2	2837	4.6
11	11.8	394	292	878	4.7	12.2	0.110	0.398	0.002	0.050	<0.001	-	3472	6.4
13	3.1	191	441	918	15.7	2.3	1.864	5.917	0.003	1.169	0.002	-	2651	4.9
15	4.4	184	450	951	11.7	0.4	1.409	6.360	0.002	0.015	0.026	0.1	2895	6.0
19	5.8	210	417	969	12.9	1.4	1.798	6.544	<0.001	0.535	0.171	0.2	3320	5.3
20	10.1	332	360	936	11.9	15.5	0.812	2.809	0.004	0.338	0.004	-	3784	5.7
05	5.0	212	374	829	6.9	3.8	0.195	0.754	0.003	0.048	0.002	0.2	3259	6.7
22	1.6	10	4	3	0.1	10.6	0.001	0.001	0.003	0.011	0.003	-	122	6.3
23	6.8	32	9	21	0.8	7.2	<0.001	0.001	0.001	0.009	0.001	-	227	6.3
24	3.0	116	96	277	2.3	17.3	0.001	0.005	0.001	0.016	0.001	4.3	1404	6.1
Removal efficiency (formula: 1 - concentration in 5 / concentration in 3)														
		18%	21%	23%	54%	42%	90%	89%	96%	95%	100%			

4.4.4 *Stable isotopes of water*

To investigate groundwater and surface water interactions, we investigated the δ^2H and $\delta^{18}O$ isotopic composition in rain water, groundwater from several wells in the wetland and its surroundings, as well as surface water from creeks and lakes (for locations see Table C.1). Water samples were collected in June and September 2017 and June 2018 using a MasterFlex E/S portable sampler (see above). Samples were filtered (0.45 μm), and then analyzed for δ^2H and $\delta^{18}O$ values (delta notations, relative to the Vienna Standard Mean Ocean Water, VSMOW) using the Picarro Cavity Ring-Down Spectroscopy L2130-i Isotopic Water Analyzer at the UofA with analytical uncertainties of 0.2‰ and 0.6‰ for $\delta^{18}O$ and δ^2H, respectively. In addition, water samples were analyzed for their chemical composition using the ICP-MS (Table C.1).

4.4.5 *16S-rRNA gene sequencing*

To better understand the biogeochemical conditions in the investigated environment and the potential impact of the waste stream on microbes, DNA was extracted from peat (2017) and mineral soil (2018) samples from the field. DNA was isolated using the FastDNA SPIN Kit for soil (MP Biomedicals) and 16S rRNA was amplified by polymerase chain reaction (PCR) following the 16S Metagenomic Sequencing Library Preparation Guide by Illumina (Illumina, 2016) and using the universal bacterial and archaeal primers F515 (5'-GTGCCAGCMGCCGCGGTAA-3') and R806 (5'-GGACTACHVGGGTWTCTAAT-3') (von Gunten *et al.*, 2018). Sequencing was performed on an Illumina MiSeq platform for pair-end reads using the Illumina NexteraXT library preparation kit. Obtained data was processed using the MetaAmp version 2.0 pipeline (Dong *et al.*, 2017). The amplicons were trimmed to a length of 250 base pairs with a minimum length overlap of 50 base pairs (no mismatches in overlap) and no mismatches were allowed for the primer sequences. Reference alignments were done to the SILVA version 123 database (Yilmaz *et al.*, 2014). Operational taxonomic unit (OTU) clustering was performed at 99% similarity level (Edgar, 2018), and singletons, unknowns and eukaryotic sequences were removed. R version 3.4.1 and the PHYLOSEQ package were used to plot the community composition (McMurdie & Holmes, 2013; R Core Team, 2017). The distribution of predicted metabolisms was estimated with the METAGENassist tool by Arndt *et al.* (2012). Selected OTU sequences were aligned with the National Center for Biotechnology Information (NCBI) database using BLAST (Altschul *et al.*, 1990). Raw sequence reads were submitted to the National Center for Biotechnology Information (NCBI) database under the bioproject accession number PRJNA513194.

4.5 *Results*

4.5.1 *Mineralogy*

Sieving of the PRB1 material (15S) indicated that the soil particles comprised the following size fractions: >2 mm (83%), 2-1 mm (5%), 1-0.075 mm (11%), <0.075 mm (1%). Therefore, the sieving supports the reported dominance of the gravel-sized fraction (AREVA, 2013). The pH of this top PRB1

material was between 8.95-9.72, which is relatively high compared to the groundwater flowing through the PRB1 (pH 6, Table 4.1), indicating strongly alkaline conditions.

XRD analyses on the soils collected in close proximity to the groundwater wells 11, 20, 5, and 24 (refer to Figure 4.1) indicated the presence of quartz (SiO_2), microcline ($KAlSi_3O_8$), clinochlore ($(Mg_5Al)(AlSi_3)O_{10}(OH)_8$) and muscovite ($K(Al_{2.9}Si_{3.1}O_{10})(OH)_2$). Traces of pyrite ($FeS_2$) were found in sample 5M, downgradient of both PRBs. XRD on the PRB1 samples (15S, 15D, and 15M) indicated the presence of quartz, natrolite ($K_{14.93}(Al_2Si_3O_{10})_8$), microcline, dolomite ($CaMg(CO_3)_2$) and calcite ($Ca(CO_3)$), kaolinite ($Al_2Si_2O_5(OH)_4$), muscovite and clinochlore. Further, the following phosphate, sulfate and sulfide minerals were found: millisite ($(Na,K)CaAl_6(PO_4)_4(OH)_9 \cdot 3H_2O$), bassanite ($Ca(SO_4) \cdot 0.5H_2O$), and pyrite.

4.5.2 Solid metal speciation

Generally, higher trace metal concentrations were found in the topsoil (20-30 cm) as compared to the mineral soil (90-100 cm). Nickel, for example, had a concentration of 910 ppm at the surface upgradient of the PRBs (Figure 4.3) and only 16 ppm in the underlying mineral soil. Exceptions to this pattern were Cu (all samples except upgradient of PRBs), S and Fe (downgradient of PRBs), in which cases the mineral soil contained higher concentrations of those elements. The PRB1 metal concentrations were generally low compared to the surrounding peat, a result of the higher density of the PRB1 material which mainly consists of gravel. The PRB samples, however, had higher abundances of Fe and Mn, likely due to the high abundance of clay and the presence of pyrite.

Sequential extractions revealed a high fraction of metals in the oxidizable fraction of the peat and the mineral soil below (Figure 4.3). This fraction includes organic matter and certain easily oxidizable sulfides (Tessier *et al.*, 1979) and contains more than 70% of Ni, Cu, and U in the surface peat. The average abundance for all trace elements shown in Figure 4.3 was 57%, while the contribution of the oxidizable fraction in the mineral soil samples was on average lesser (30%). Nickel and Co both exhibited similar distributions; the first two soil fractions averaged 24% and 51% in the surface samples, respectively, and 84% in the mineral samples, suggesting high potential mobility. Copper, on the other hand, was mainly present in the oxidizable and residual fractions (78% and 13%, respectively) in surface and mineral samples, suggesting higher recalcitrance, which was similar to U (62% and 22%).

In the PRB1 samples, many elements (e.g., Ni, Co, and Cu) showed high recalcitrance with up to 100% of those metals being bound to the two more stable fractions (oxidizable and residual). For U, the more mobile exchangeable/acid soluble fraction made up to 61%, suggesting the presence of uranyl carbonates. Like U, sulfur (on average 75% exchangeable/acid soluble) was also mobile, likely due to highly soluble sulfates such as bassanite. Similarly, Mn was generally mobile and dominant (average of 63%) in the first two fractions (exchangeable/acid soluble and reducible), indicating the presence of sorbed Mn^{2+} and amorphous Mn oxyhydroxides.

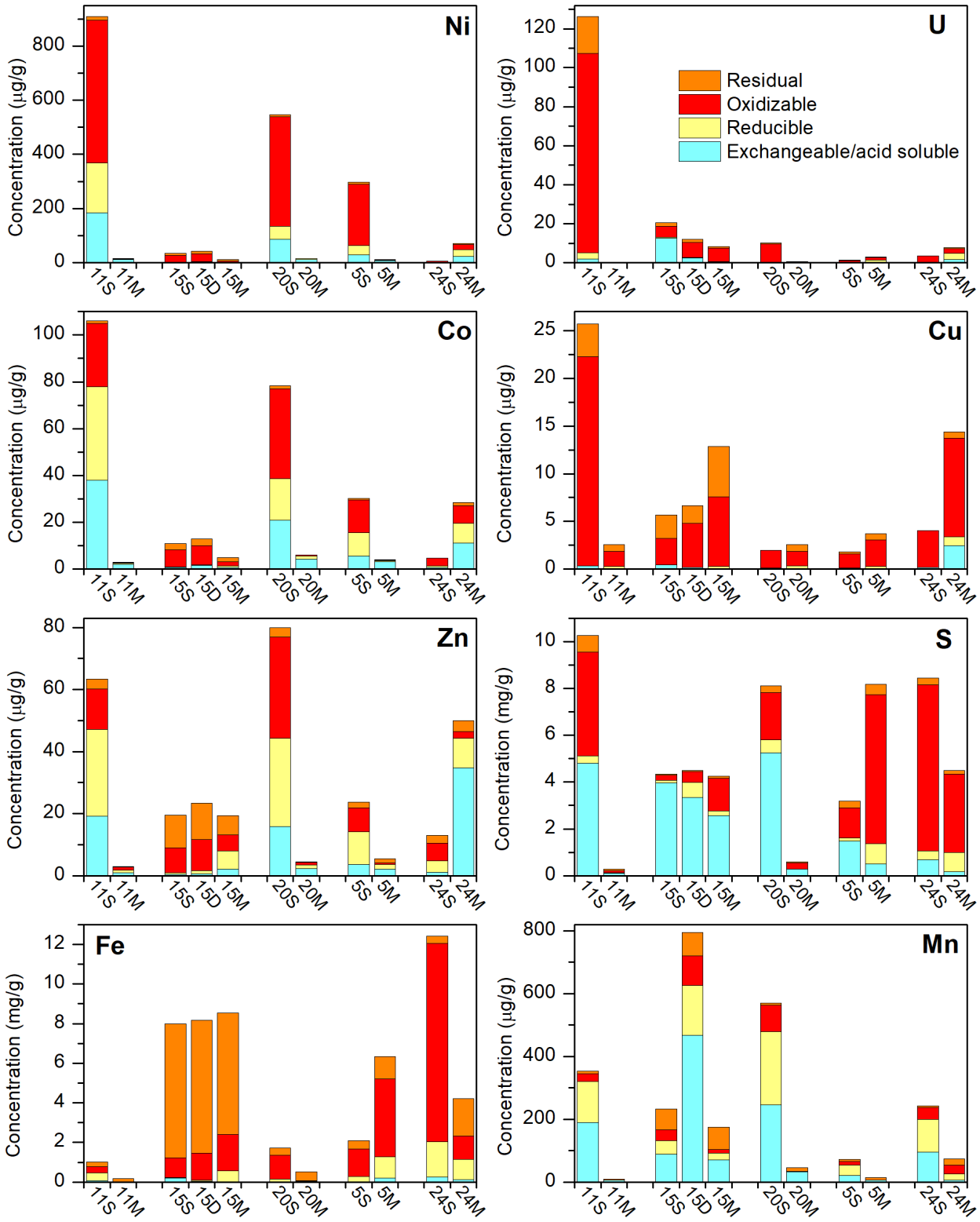

Figure 4.3 Metal distribution over the four solid fractions in peat and PRB samples determined by sequential extraction.

4.5.3 Aqueous geochemical trends and speciation modeling

Groundwater had elevated metal concentrations at the upgradient locations (stations 3 and 11) compared to downgradient sampling points (Table 4.2). Shallow groundwater collected at 5 m depth from well 3 (upgradient of the PRB1) had considerably higher concentrations of metals compared to the deeper groundwater collected at 12 m from well 11. For example, in well 3, Ni and U were 6659 ppb and 916 ppb, respectively, compared to 398 ppb and <1 ppb, respectively, in well 11. At the PRB1 (location 15), groundwater did not show elevated Ca concentrations as would be expected due to the presence of lime and limestone, and was still rich in U (26 ppb), Ni (6360 ppb) and Co (1409 ppb). Downgradient of the two PRBs (site 5), groundwater had lower concentrations of most elements, with the exception of S (829 ppm). The overall removal efficiencies in groundwater for transition metals and U were >43%, with U, Cu, and Zn having the highest values (Table 4.2).

The specific conductivity (Table 4.2) was elevated in all wells in proximity of the PRBs and also at the isolated location 24 (Figure 4.1), suggesting that a fraction of the waste plume could be passing underneath the PRB. This observation is further supported by high metal concentrations in well 24 (e.g., 17 ppm for Fe). Dissolved oxygen values measured in June 2018 varied from 0.1 ppm to 0.2 ppm in the surrounding of the PRBs, suggesting a low oxygen environment. At the same time, no nitrate-N could be detected in the wells 15 and 20. Sulfate-S was high for wells 15 and 20 with 1083 ppm and 1031 ppm, respectively, suggesting a sulfate-reducing environment. This confirmed the strong sulfide smell of disturbed peat and mineral soil samples in the field, indicating active sulfur reduction.

Geochemical modeling suggested that in the shallow groundwater coming from the direction of well 3 and flowing southwest (Figure 4.1), mostly divalent metal species dominated (e.g., Mn^{2+}, Co^{2+}, Ni^{2+}) while Fe and U were expected to be in their oxidized forms as $Fe(OH)_2^+$ and $UO_2H_3SiO_4^+$ (Table 4.3, graphical summary in Figure 4.1). When this water reaches the PRB, the pH rose to a maximum of pH 9, as measured in the PRB1 solids (Table 4.2). Under oxidized conditions, especially Fe and Cu would more readily form aqueous hydroxide species, e.g. $Fe(OH)_4^-$ and $Cu(OH)_2^0$. The O_2 measurements were, however, close to the detection limit of the instrument and the distinct smell of sulfide suggested anaerobic conditions in the groundwater. When taking this into account (Table 4.3, right columns), most major species would change at the upgradient conditions (pH 4.6), forming sulfides, e.g., $Cu(HS)_3^-$ and $Zn(HS)_2^0$, and reduced species, e.g., $Fe(HS)_2$ and $U(OH)_4$. Exceptions are Mn, Co and Ni, present almost exclusively in their divalent forms. At pH 9 under anaerobic conditions, free ionic species (monovalent and divalent) were favored for all investigated metals except U (forming $U(OH)_5^-$). Precipitating species, predicted based on their saturation indices (Table 4.3), indicated that under oxic conditions several Mn, Fe, Co, Cu, Zn, and U species could precipitate, mostly as oxides (e.g., $CoFe_2O_4$), hydroxides (e.g., $Co(OH)_3$, $UO_2(OH)_2$), and sulfates (e.g., $Zn_4(OH)_6SO_4$). No Ni phases were found to be favorable for precipitation, indicating their high mobility at oxygenated surface conditions. Under anoxic conditions, generally less precipitates were predicted to form due to decreased formation of oxides, hydroxides and

sulfates, although, the reducing conditions would favor the formation of sulfides, e.g., pyrite, CoS, NiS, Cu_2S, and reduced U species (e.g., amorphous UO_2).

Table 4.3 Summary of the PHREEQC modeling results for groundwater based on the composition found in well 3 (upgradient of PRB1) with varied pH and p_e values. In the solids section below, saturation indices are positive (bold) for species that are expected to precipitate. "am": amorphous.

		pH 4.6, pe 14.9		pH 9, pe 11.4		pH 4.6, pe -3		pH 9, pe -3	
		Aqueous species (major species and abundance)							
Element		Species	%	Species	%	Species	%	Species	%
Mn		Mn^{2+}	74	Mn^{2+}	74	Mn^{2+}	100	Mn^{2+}	74
Fe		$Fe(OH)_2^+$	99	$Fe(OH)_4^-$	87	$Fe(HS)_2^0$	54	Fe^{2+}	66
Co		Co^{2+}	70	Co^{2+}	65	Co^{2+}	100	Co^{2+}	65
Ni		Ni^{2+}	61	Ni^{2+}	59	Ni^{2+}	100	Ni^{2+}	59
Cu		Cu^{2+}	60	$Cu(OH)_2$	75	$Cu(HS)_3^-$	100	Cu^+	100
Zn		Zn^{2+}	52	Zn^{2+}	36	$Zn(HS)_2^0$	83	Zn^{2+}	36
U		$UO_2H_3SiO_4^+$	63	$UO_2H_3SiO_4^+$	47	$U(OH)_4^0$	48	$U(OH)_5^-$	100
S		SO_4^{2-}	68	SO_4^{2-}	69	H_2S^0	99	SO_4^{2-}	69
		Potential precipitates							
Solid	Formula	Saturation index		Saturation index		Saturation index		Saturation index	
Birnessite	MnO_2	-1.0		**9.7**		-36.5		-19.0	
MnS	MnS	-128.0		-135.4		-4.2		-20.5	
Ferrihydrite	$Fe(OH)_3$	**1.1**		**4.4**		-11.7		**1.7**	
Magnesioferrite	Fe_2MgO_4	-3.2		**12.4**		-28.4		**7.0**	
Magnetite	Fe_3O_4	**3.6**		**12.7**		-16.8		**18.9**	
Goethite	FeOOH	**3.9**		**7.3**		-8.8		**4.5**	
Mackinawite	FeS	-129.4		-143.3		-0.8		-16.7	
Pyrite	FeS_2	-207.3		-235.6		**9.1**		-22.8	
Na-Jarosite	$NaFe_3(SO_4)_2(OH)_6$	**4.5**		**1.4**		-72.5		-6.9	
$Co(OH)_3$	$Co(OH)_3$	-7.9		**1.9**		-25.5		-12.5	
$CoFe_2O_4$	$CoFe_2O_4$	**15.8**		**31.3**		-9.5		**25.8**	
CoS(α)	CoS	-120.9		-128.4		**2.8**		-13.4	
$Ni(OH)_2$	$Ni(OH)_2$	-9.4		-0.6		-9.1		-0.6	
NiS(α)	NiS	-122.1		-129.6		**1.7**		-14.6	
$Cu(OH)_2$	$Cu(OH)_2$	-6.8		**0.8**		-19.6		-3.1	
Chalcocite	Cu_2S	-123.8		-126.9		**9.8**		**9.2**	
Antlerite	$Cu_3(OH)_4SO_4$	-12.2		**1.6**		-70.1		-9.9	
Cupricferrite	$CuFe_2O_4$	**4.3**		**18.6**		-34.0		**9.3**	
Cuprousferrite	$CuFeO_2$	-0.4		**9.6**		-8.1		**17.4**	
Chalcopyrite	$CuFeS_2$	-225.7		-248.3		**13.7**		-10.5	
Covellite	CuS	-106.2		-115.0		**4.5**		-3.8	
$Zn(OH)_2$	$Zn(OH)_2$	-8.5		**0.2**		-12.4		**0.2**	
$Zn_4(OH)_6SO_4$	$Zn_4(OH)_6SO_4$	-24.9		**1.0**		-59.7		**1.0**	
ZnS(am)	ZnS	-119.4		-127.0		**0.3**		-12.0	
UO_2(am)	UO_2	-28.0		-25.5		**1.8**		-2.3	
Uraninite	UO_2	-22.0		-19.5		**7.8**		**3.7**	
$UO_2(OH)_2$(β)	$UO_2(OH)_2$	-4.1		**0.2**		-10.1		-5.3	

4.5.4 Water isotopic data

Using $\delta^{18}O$ and δ^2H data obtained from rain-, ground-, and surface waters, the local evaporation line (LEL) was constructed yielding the equation: $\delta^2H = 4.88\ \delta^{18}O - 57.8$ (Figure 4.4). The LEL slope is typical of those for high latitudes (Gibson *et al.*, 2016). The June 2017 values plot in the lighter region, indicating

that evaporation left behind heavier water in September 2017. The local meteoric water line (LMWL) was obtained by plotting a fit through the rain water samples and samples measured from the deeper wells that did not show large variation between June and September. The latter group of samples turned out to be from the investigated wetland, suggesting that those wells did not experience enrichment of heavier isotopes by evaporation processes. Thus, groundwater in the wetland likely originated from relatively rapid percolation of precipitation through the waste rock pile located in the northeast (see Chapter 1). The obtained slope of the LMWL was 7.7, which corresponds to the Saskatchewan average of 7.7 (Pham *et al.*, 2009). Additionally, δ^2H and $\delta^{18}O$ of surface water collected on top of both PRBs was similar to groundwater from the wetland wells (see Table C.1 for details), suggesting that this water is strongly influenced by groundwater and is not simply accumulated rain water.

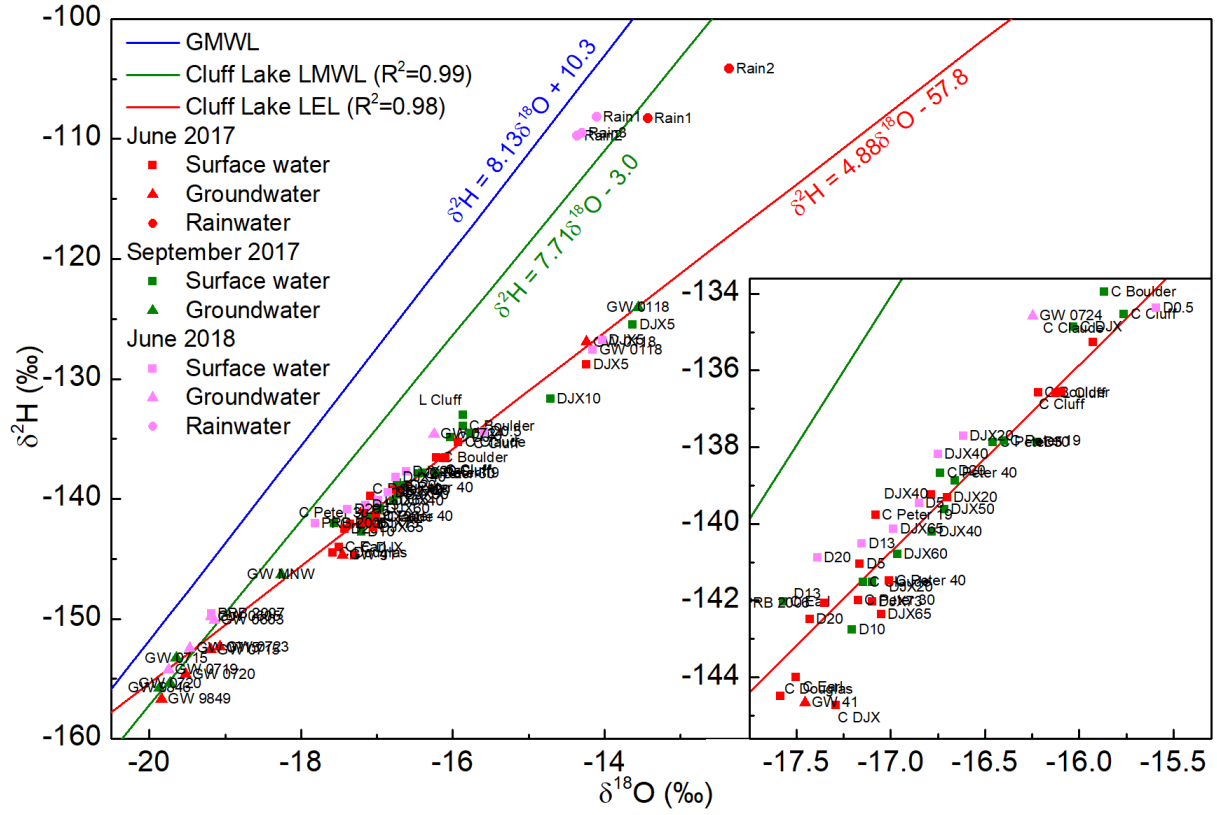

Figure 4.4 Summary of water isotope data showing the global meteoric water line (GMWL), the local meteoric water line (LMWL) and the local evaporation line (LEL). The inset map shows a zoomed view on the major point cluster containing mainly surface water from creeks ("C"), the flooded pits ("D" and "DJX"), the lake ("L") and shallow groundwater wells ("GW"). See Table C.1 for details on sampling locations.

4.5.5 Colloidal metal distribution

AF4-ICP-MS analyses revealed colloid-associated trace metals in the 0.45 µm filtered water, especially for the transition metals Co, Ni, Cu, and the heavier elements Pb, Th, and U (Figure 4.5). Cobalt and Ni were strongly associated with the DOM fraction at PRB1 (well 15) and in the isolated well 24 beyond the creek. Both have relatively high water pH levels (*ca.* pH 6) and this suggests complexation with organic

acids (i.e., humic acids). Compared to Co and Ni, Cu showed an even stronger association with DOM and also with inorganic colloids, especially at well 15, but also in the downgradient locations (wells 19, 5, and 24). Judging by the low abundance of colloidal Fe, and Mn, the inorganic particles likely consisted of clay particles. The following metals dominated the free ionic species: Ca, Mg (data not shown), Mn, Mo, Zn, and As. Increased acidity of the deep upgradient well 3 water (pH 4.6) favored free ionic species for the majority of the metals, with exceptions of Al, Th and U. Uranium is known to form strong complexes with humic acids even at low pH values in both common oxidation states: U(IV) and U(VI) (Li *et al.*, 1980).

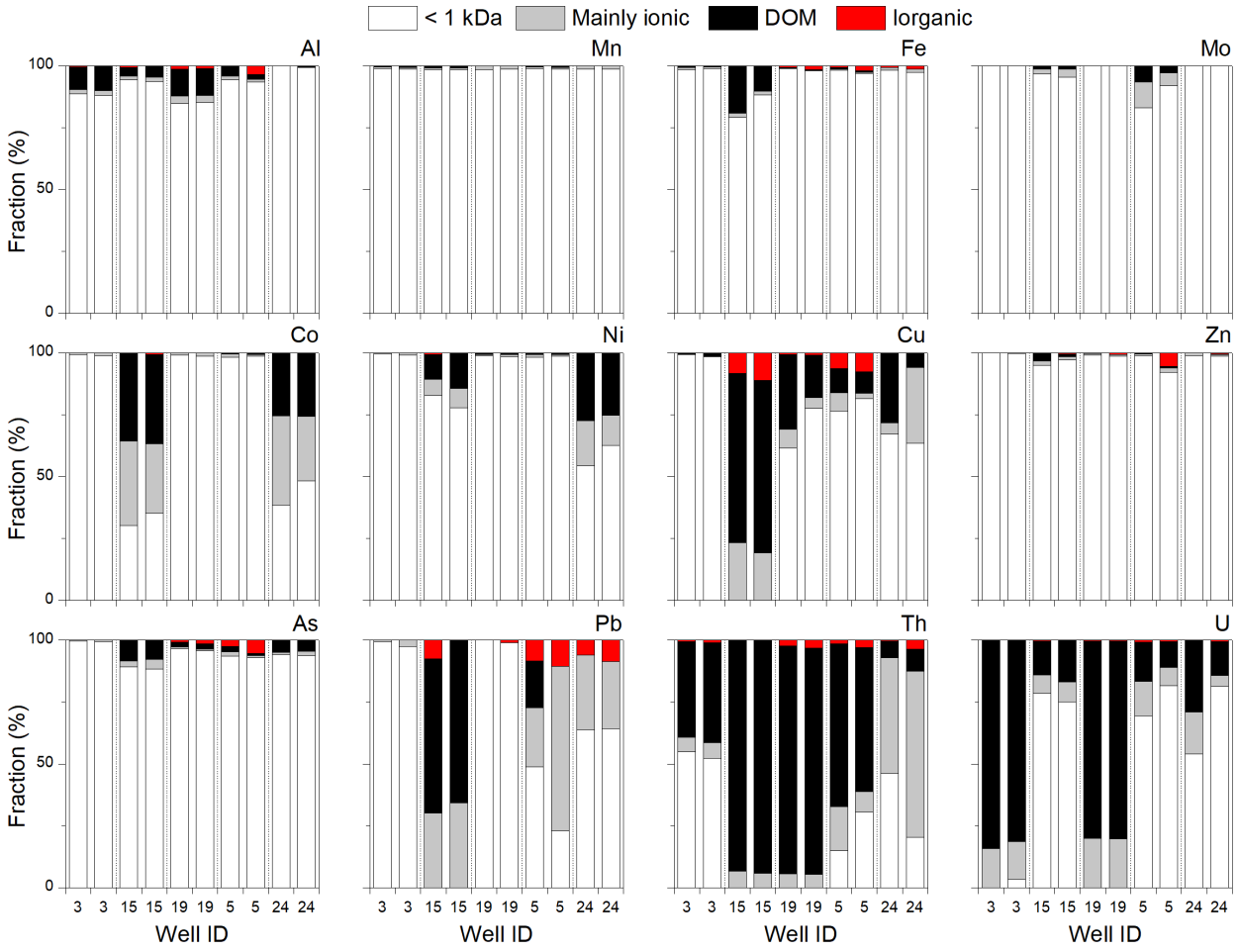

Figure 4.5 AF4-ICP-MS results for selected elements. Each well was measured in duplicates. For well locations, see Figure 4.1.

Sequential filtration results (Figure C.1) confirmed the AF4-ICP-MS findings, indicating that Ni and Co express similar colloidal distributions. In the upgradient water (well 3), clear differences in concentrations were not found for all size fractions, suggesting that the majority of Ni and Co was in the dissolved form (<10 kDa). Water from well 19 (between both PRBs) contained large particles (>1.2 µm) which carried substantial amounts of Ni, Co, Zn, As, and Al. These particles were likely well sediments disturbed by pumping. Filtration results for TOC suggest that the observed DOM particles mentioned above were mostly low molecular weight (LMW), i.e., <10 kDa for the wells 3 and 19 (i.e., upgradient and middle).

Approximately 75% of the TOC in the groundwater at well 15 (PRB1) was <10 kDa, the rest being up to 200 nm in size, suggesting that the DOM increased in size at PRB1. About 80% of the TOC in the isolated groundwater well 24 was in the 10-500 kDa fraction, with the rest being <10 kDa. At PRB1, many elements (e.g., Al, Co, Ni, Cu, Zn, and As) became evident in the colloidal fractions >450 nm, suggesting the formation of larger colloids in the alkaline environment of the reactive medium.

4.5.6 Prokaryotic community changes

16S rRNA gene sequencing indicated that all surface peat samples in the proximity of the PRB (11S, 20S, 5S) had similar microbial communities (Figure 4.6). These communities were dominated by bacterial classes Alpha- and Betaproteobacteria, Acidobacteria, and Sphingobacteriia. The mineral soil samples (i.e., 11M, 20M, 5M, 24M), in general, showed a higher abundance of the classes Anaerolineae, Deltaproteobacteria, Nitrospira, and in the case of the locations 11 (upgradient) and 24 (isolated), Methanomicrobia. Many of the dominant OTUs found in the upgradient sample 11S were closely related to fermentative and acidotolerant microbes, such as *Pseudolabrys*, *Ignavibacterium*, *Bryobacter*, *Acidothermus*, and a representative of the Verrucomicrobia phylum (Table C.3), many of which were previously found in wetlands (Kämpfer *et al.*, 2006; Drake *et al.*, 2009; Kulichevskaya *et al.*, 2010; Iino *et al.*, 2010; Juottonen *et al.*, 2017). At PRB1, the shallow and deep samples (15S and 15M) showed a similar distribution of classes, dominated by Bacteroidia and Clostrodia (Figure 4.6). Compared to the surrounding samples, more OTUs related to alkalitolerant and alkaliphilic microbes were found, such as the genera *Alkalibacterium*, *Chitinispirillum*, *Geosporobacter*, *Proteiniclasticum, Desulfatirhabdium, Geofilum, Erysipelothrix*, *Desulfomicrobium, Caldicoprobacter,* and *Draconibacterium* (Rozanova *et al.*, 1988; Balk et al, 2008; Zhang *et al.*, 2010; Miyazaki *et al.*, 2012; Bouanane-Darenfed *et al.*, 2014; Yumoto *et al.*, 2014; Hong *et al.*, 2015; Wang & Riley, 2015; Sorokin *et al.*, 2016).

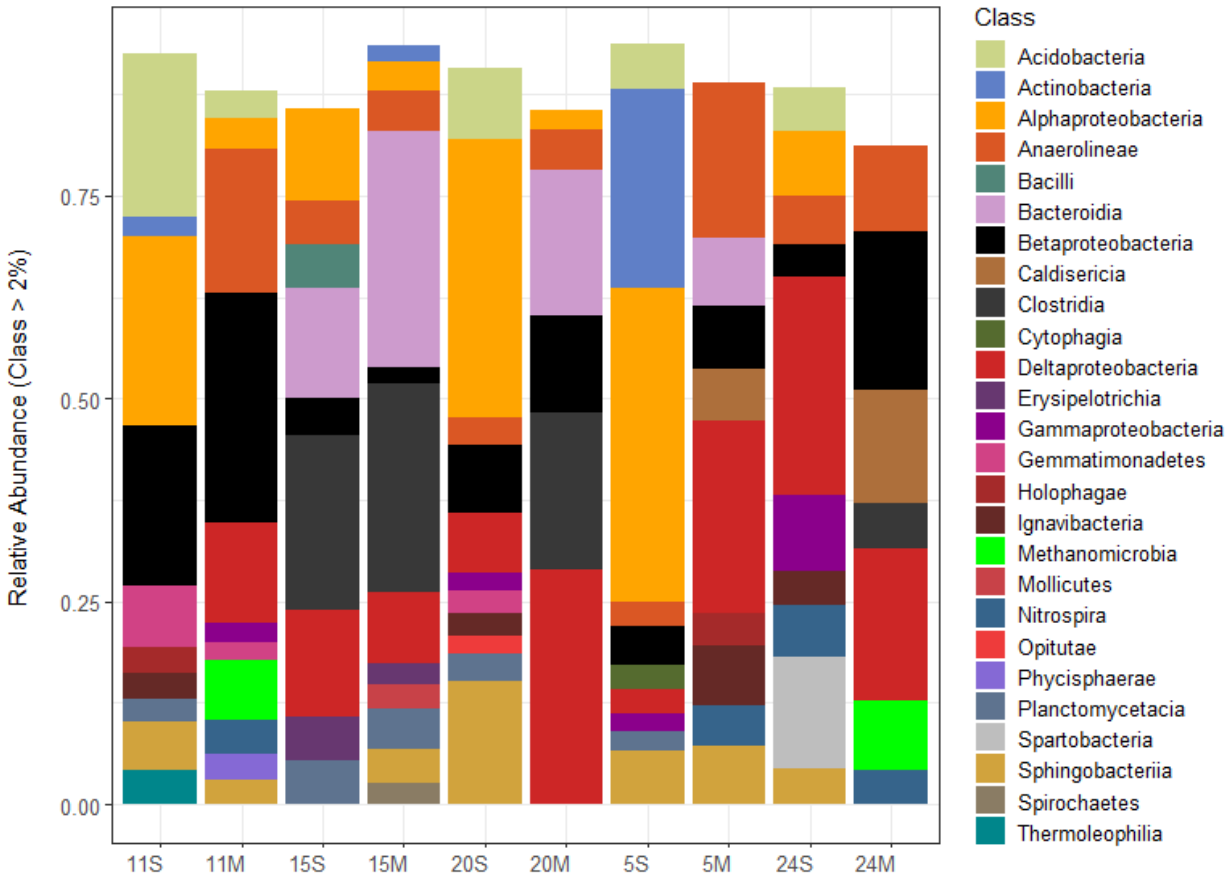

Figure 4.6 Microbial class composition of surface peat ("S") and mineral soil ("M") samples. Only classes with an abundance >2% are shown.

Species richness (i.e., Chao1 index) was generally lower in the mineral soil samples (Figure 4.7), indicating that fewer species were able to become established in the sandy till compared to the overlaying peat. The diversity (inverse Shannon index), on the other hand, was relatively similar between peat and corresponding mineral soil samples. PRB1 showed the highest inverse Shannon indices, suggesting that the reactive medium supported a more diverse microbial community. This PRB effect lasted also further down gradient (location 20).

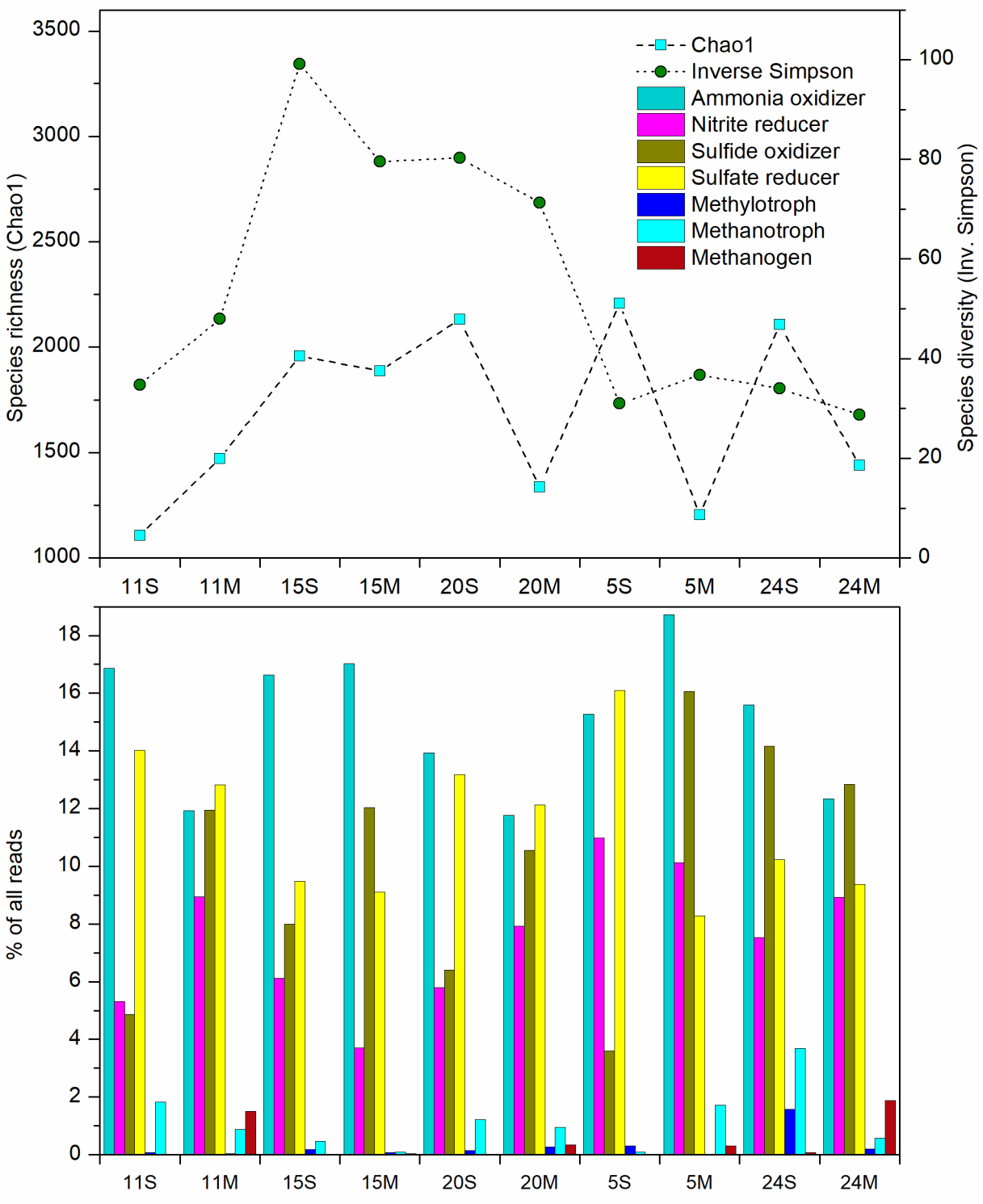

Figure 4.7 Species richness, diversity and potential metabolisms in the analyzed surface peat ("S") and mineral soil ("M") samples.

METAGENassist analyses suggested that ammonia oxidizers, sulfide oxidizers, and sulfate reducers were the most represented metabolisms, making 12-19%, 4-16%, and 8-16% of the community, respectively (Figure 4.7). Redox conditions were likely dominated by sulfur reduction as suggested above, which is typical for non-iron PRBs (Powell *et al.*, 1998). As expected, methanotrophs (overall 0.091-3.684%) were often dominant in the surface exposed peat layers, whereas methanogens (overall 0.003-1.878%) were more abundant in deeper mineral soil. Given that Co, Ni, Cu, and Zn were highly concentrated in the waste stream and are known to be important co-factors for methanogens and methanotrophs (Scheller *et al.*, 2010; Glass & Orphan, 2012), it was expected that they would enhance the presence of those metabolisms, as was previously demonstrated in laboratory and field studies (Patel & Sprott, 1990; Basiliko & Yavitt, 2001). However, no clear increase of these metabolic groups could be observed in this study. The isolated location 24 and the upgradient location 11 showed similar abundances of methanogens and methanotrophs. This overall low abundance of methane-related metabolisms could be related to their suppression by sulfate-reducing bacteria (Oude Elferink *et al.*, 1994; Dise & Verry, 2001).

To test for methanotropy, surface peat from the locations 5 (downgradient of PRBs) and 11 (upgradient of PRBs) was incubated anaerobically (Figure C.2). Methane became detectable after 2 months of incubation. The less contaminated peat from location 5 generated relatively more methane with a lighter $\delta^{13}C\text{-}CH_4$ signature (Figure C.2), suggesting higher activity of methanogens. This finding was supported by 16S rRNA gene sequencing on those samples, showing 10x more sequences related to potential methanogens in the incubated location 5 sample than in sample 11, without substantial differences in the amount of methanotrophy-related sequences (Figure C.2). The major potential methanogen was an archaeon related to *Methanosarcina*, while dominant presumed methanotrophs were relatives of *Methylocella* and *Methylovirgula*. This test indicated that in the case of the Cluff Lake PRB1, the increased concentrations of transition metals are likely not promoting methanogenesis in the near-surface soil.

Relatives of bacteria being potentially capable of reducing U(VI) were mostly found in the upgradient mineral soil sample 11M, the deep PRB1 sample 15M, and the mineral sample located between the two PRBs, 20M. Examples include *Clostridium* (Gao & Francis, 2008), *Geobacter* and *Shewanella* (Newsome *et al.*, 2014b), *Desulfovibrio* (Lovley *et al.*, 1993b), and *Desulfosporosinus* (Suzuki *et al.*, 2004; Alessi *et al.*, 2014a) with abundances up to 0.051%, 0.150%, 0.005%, 0.309%, and 1.141%, respectively (Table C.4). Species of *Desulfosporosinus*, one of the most prominent potential U(VI) reducers, are known to grow autotrophically on hydrogen and sulfate and were found to enzymatically reduce U(VI) under bicarbonate depletion, a condition likely dominant around the PRB1 due to an elevated pH.

4.6 Discussion

4.6.1 Biogeochemical fate of metals passing through the PRB

Due to the distinct hydrogen sulfide smell and the possibility that measured oxygen concentrations in groundwater were artificially elevated due to oxygenation during the pumping, it can be assumed that the reduced scenarios shown in Table 4.3 are more likely applicable to the investigated PRB environment. This is supported by the dominance of sulfate-reducing microbial metabolisms predicted by METAGENassist. Under such reducing conditions and at a pH <5, limited metal removal processes could be expected. Nonetheless, several metal sulfides would be prone to precipitation, such as pyrite, CoS, NiS, Cu_2S, and ZnS. Interestingly, as soon as this water reaches the PRB and the pH rises to 9 and higher, the precipitation of most metals becomes less favorable under reducing conditions. In particular, Mn, Co, and Ni are not prone to precipitation, which explains their high mobility through the PRBs. While pyrite precipitation is not predicted to be favorable, traces of pyrite found in the PRB1 material and the relatively acidic pH of 6 measured in the well 15 (inside the PRB1) suggest that the bulk pH is considerably lower than 9 and that a degree of sulfide precipitation is possible. This difference between the solid pH >9 and pH 6 of the groundwater shows that groundwater does not reside within the PRB for a sufficient time to reach chemical equilibrium. Sulfides of Co, Ni, Cu and Zn have a wide range of solubility constants (reported here as log K_{sp}, 25°C). For Co, reported values range from -24.7 to -20.4, while the Ni, Cu, and Zn values are -25.7 to -18.5, -47.6 to -35.2, and -23.8 to -21.6, respectively (Table 8.6 in Dean, 1999). Therefore, the solubility of those sulfides can be roughly ordered as Ni > Co > Zn > Cu. Correspondingly, while Cu and Zn more readily precipitate even at low sulfide concentrations (Sheoran & Sheoran, 2006), Co and Ni remain highly mobile. In this regard, the presence of the PRBs may have worsened the situation by creating unfavorable conditions for Co and Ni removal.

Metal sorption could also play an important role in metal removal by the PRBs. However, competition reactions with other metals can have a detrimental effect on the degree of sorption, particularly for metals such as Ni that bond more weakly than other divalent cations. For example, sorption of Cu can outcompete Ni, due to stronger bond formation (Ho *et al.*, 1996). Copper is especially strongly binding to organic matter (Yang *et al.*, 2015), which explains the large oxidizable fraction determined by sequential extraction and the large colloidal DOM fraction determined by AF4 for Cu. Ni could potentially sorb to microbial biomass under low pH conditions (Zandvoort *et al.*, 2006) but that would depend on the composition of the organic material, i.e., the availability of organic ligands that deprotonates at low pH. Although, an increase of colloidal TOC at PRB1 (Figure C.1) suggests some increase in microbial activity, and Ni (with Co) are indeed partially bound to colloidal DOM particles, the degree of biomass growth is likely insufficient to remove large amounts of Ni, reasons for which are elaborated below.

Uranium, as the major target metal for removal, is efficiently removed by several processes. Under anaerobic conditions, U(VI) can be reduced to U(IV) by Fe(II) species and various Fe(III) and sulfate

reducing bacteria. This might be responsible for the formation of a dominant oxidizable fraction for U as observed by the sequential extractions. Similarly, Newsome *et al.* (2014b) observed a large oxidizable fraction for U in clay-rich sediments that showed active bioreduction of U(VI). At PRB1, under low oxygen conditions, U(VI) likely precipitates by forming uranyl carbonates and possibly uranyl hydroxides, such as paulscherrerite, as supported by a large exchangeable/acid soluble soil fraction in the surface sample 15S and by thermodynamic modeling (Table 4.3).

4.6.2 Formation and role of colloidal particles

Larger (>0.45 μm) colloidal particles were found in the groundwater in the first PRB and the groundwater samples taken downgradient of it (e.g., wells 19, 5 and 24). Many DOM and inorganic colloids also emerge in the groundwater after passing through the PRB1 (Figure 4.5). The colloids are likely formed by the degradation of organic matter (decay of peat, microbial biomass) and the physical breakdown of clays. Taking this into account, major contaminants in water can be divided into 4 groups: (1) truly dissolved (Mn, Fe, Zn), (2) partially DOM-associated at the PRB and in the isolated well (Ni, Co), (3) DOM-associated at pH ≥6 (Cu), and (4) mostly DOM-associated (U). Thorium, although not a major contaminant, is associated with the latter group as well. The overall small colloidal fractions of Mn, Fe, and Zn is likely related to the pH conditions, as previously shown by thermodynamic modeling. Furthermore, reducing conditions within the peat would favor divalent species of most transition metals, and, therefore increase their mobility. Similar effects play an important role for the 2nd group for Ni and Co, however, the environments within PRB1 and at well 24 (isolated) seem to favor their binding to DOM. For the 3rd group, the previously discussed affinity of Cu to organic matter is responsible for the high abundance of DOM-associated Cu, especially at PRB1. Finally, in the 4th group, U is strongly bound to DOM, except for environments with higher pH values (e.g., PRB1 and isolated location), suggesting that the formation of carbonates is the controlling factor. Thorium, being an actinide such as U, behaves similarly, although it does not show as strong changes to pH as U (Figure 4.5). It also has a greater DOM-associated fraction, likely due to its inability to be easily oxidized from its major oxidation state Th(IV) (Adams *et al.*, 1959) and due to its high affinity to organic ligands (Langmuir & Herman, 1980).

Metals with higher colloid-associated fractions also exhibit a stronger binding in the solid phase. For example, the average colloidal fraction of Fe is higher (4%) than that of Mn (<1%) and Fe is more strongly bound to the solid phase (88% oxidizable and residual vs. 37% for Mn). Copper and U that have high removal rates in groundwater (Table 2), are largely in the colloidal phase for all groundwater samples (on average 28% and 43%, respectively) and are strongly bound to the solid phase (oxidizable and residual: 88.4% and 72.5%, respectively). On the other hand, Co and Ni both have lower removal rates, have a small colloidal fraction (on average 13% and 8%, respectively) and are relatively mobile (oxidizable and residual: 30% and 31%, respectively). These results suggest that colloidal particles scavenge metals from the groundwater and promote removal processes. In the case of U, this is different than the observations of Wang *et al.* (2013) and Graham *et al.* (2011) for wetland and clay-loam soil pore- and groundwater,

where colloidal particles contributed to a higher mobility of U. Our results are similar to those of Tran *et al.* (2018), who observed that in a carbonate-rich environment, U (and Cs) are likely sequestered by attachment to colloidal particles. Therefore, the alkaline conditions of the PRBs contribute to an efficient removal of actinides (U, Th) and the transition metals Cu and Zn by colloids (i.e., colloidal pumping, Honeyman & Santschi, 1991) but have a limited or even detrimental effect on the removal of Ni, Co, Mn, and Fe.

4.6.3 Further considerations and potential improvement possibilities

Divalent metals can be removed from wetlands either by aerobic processes involving sorption, or anaerobic processes such as sulfate reduction. In an experiment by Eger (1994), the first method was shown to efficiently remove Ni, provided the water level on the surface was not in excess of 5 cm to allow sufficient contact with the peat at the bottom. At our field site, other than the creek flowing through the wetland, no additional surface water flow is documented, although the older 2006 PRB was observed to develop substantial amounts of standing water on top (likely groundwater seepage as indicated by water isotopes), while PRB1 showed some puddles on the surface (Figure 4.2). Therefore, aerobic processes are not likely to contribute significantly to the removal of transition metals in this environment. According to Eger (1994), an efficient anaerobic treatment would require (1) the establishment of anaerobic conditions at the treatment zone, (2) sufficient amounts of bioavailable sulfate, and (3) an easily degradable substrate that would increase the activity of sulfate reducing bacteria. By using the metal concentrations and pH conditions found in well 3 upgradient of the PRBs, and using the formula by Eger (1994), one can estimate the total requirement of sulfate, assuming that all Al and Fe is in the trivalent form and considering divalent metal concentrations of Mn, Co, Ni, Cu, and Zn. This approach yields 0.014 M of sulfate required, half the concentration of seawater but more than 10 times higher than in surrounding freshwater (e.g., Cluff Lake as reported in Chapter 2), except for mining sites (e.g., up to 0.052 M in Benner *et al.*, 1999). In the case of well 3, the water contains approximately 0.034 M of S_{tot}, indicating that sufficient sulfate is present. Critically, the presence of potential sulfate-reducing bacteria was also confirmed by METAGENassist. However, peat itself, which was used as filling material in the PRB, is likely not a good substrate for this purpose, as other organic materials, such as compost, saw dust, or manure are more efficiently degraded through microbial respiration (Eger, 1994; Powell *et al.*, 1998). During PRB construction, those materials were not easily accessible at the treatment site due to the remoteness of the location. Nevertheless, metal concentrations found in groundwater generally showed a strong decrease after passing through the PRBs. While the observed removal efficiencies are still relatively high for PRBs as compared to other case studies (Powell *et al.*, 1998), they do not reduce the concentrations of Ni to the recommended level in soil (89 ppm, industrial soil quality guideline, Canadian Council of Ministers of the Environment), leaving Ni as a potential residual concern at this site.

The design and installation of PRBs, especially in remote locations with poor accessibility, appears to be an attractive, cost-effective, passive technology (Powell *et al.*, 1998; Thiruvenkatachari *et al.*, 2008).

Future PRB applications in similar environments and for similar scenarios should consider the modest tendency of Ni and Co to sorb to solids or precipitate as a part of secondary mineral phases. Stronger microbial activity might be induced by the use of more degradable organic matter in the construction of the PRB, for example compost or sawdust provided by logging operations. The thickness of the PRB should be properly assessed to make sure that under the dominant groundwater flow conditions, the contaminated stream has sufficient time to react with the PRB medium. More importantly, in the case of an alkaline PRB, the amount of base-generating material (e.g., limestone) should be properly adjusted to the long-term acid generation potential of the waste stream. At the same time, the pH change should not induce detrimental changes in the surface environment, such as potential Fe or P limitation in plants (Wilkinson, 2000). Water isotope investigations suggest that precipitation at the site rapidly percolates through the waste rock pile and reaches the wetland without evaporation. Upgradient modifications, e.g., the establishment of a dense vegetation cover, could help to slow down water infiltration and help to retain contaminated groundwater in the source area. At Cluff Lake, the waste rock pile is being revegetated (AREVA, 2013) and future observations might reflect the success of this measure. Measurements of conductivity and metal concentrations further suggest that the waste stream may be partially passing the PRBs and the creek leading to a metal signature at isolated locations (e.g., station 24). Deeper placement of the PRBs or the use of an underground funneling installation to guide the groundwater flow through the reactive medium would likely have enhanced the PRB performance.

5 CONCLUSIONS AND RECOMMENDATIONS FOR FUTURE STUDIES

Indisputably, mining is a process that helped to form modern human society since the beginning of the Copper Age in Mesopotamia before 4000 BC (Matthews and Fazeli, 2004). Since then, mining has become an essential part of our cultures and economies, ranging from iron mining for tools to uranium mining for warfare and energy supplies and peaked in the creation of iconic cities such as Johannesburg and Yekaterinburg. However, the rapid expansion of mining has generated vast quantities of mining-related wastes, which will continue to be a major challenge for the mining industry in the coming decades. The Cluff Lake project created approximately 2.4 Mm^3 of tailings (CNSC, 2003), which is modest when compared with larger Canadian mining projects, such as the partially decommissioned Giant gold mine near Yellowknife (Nordwest Territories), with more than 11 Mm^3 of arsenic-loaded tailings (INAC, 2018), or the copper and zinc Kidd Creek mine in northern Ontario, Canada, which is expected to produce more than 90 Mm^3 of tailings by 2023 (Hudson-Edwards *et al.*, 2011). Still, the Cluff Lake site presents a unique, well-documented site to assess the historical performance of pit lakes and permeable reactive barriers, as it contains inorganics like U, As, Ni, and Co as major contaminants of concern present in surface and groundwater that pose threats to local flora and fauna.

While methods now exist to deal with such contaminations in an engineered and scientifically-supported way, many aspects are not yet fully understood. In this thesis, contamination management by two established, relatively low-cost technologies was investigated. Although those technologies were shown to be successful in many studies, one still needs to consider that these are relatively new tools and their long-term performance is not known. Eventually, such systems, as in the case of Cluff Lake, will be abandoned over extended periods of time and will slowly become part of their surroundings. On the example of Cluff Lake, it was shown that in order to understand elemental cycling, it is important to consider not just the elements of concern but also other chemical and biological actors using a biogeochemical approach. Despite the differences between the two investigated technologies (meromictic pit lakes and permeable reactive barriers) similar tools can be applied to assess metals biogeochemistry and ultimately make predictions about future performance. For example, sequential extractions proved to be crucial in investigating speciation of metals and metalloids and could be corroborated with spectroscopic (e.g., XANES) and crystallographic (e.g., XRD) techniques. To investigate the mobility and the colloidal nature of contaminants in the aqueous phase, sequential filtrations and AF-4 proved to be useful yet challenging techniques, requiring special equipment in the field and the laboratory (e.g., anaerobic glove bags and boxes and filtration cartridges). To investigate potential microbial interactions, 16S rRNA showed to be a powerful technique allowing for a broad and quick assessment of archean and bacterial communities. Overlying all of it, thermodynamic modeling (e.g., using PHREEQC) was an important tool to explain reaction mechanisms and corroborate observations.

Meromictic pit lakes were shown to be an efficient remediation technology for cold regions. Sequestration rates obtained in Chapter 3 indicate that considerable amounts of metals and metalloids (in the range of kg/year for each lake) are removed from the surface water. Overall, in regard to remediation, a meromictic pit lake with fully developed anoxia would likely be more beneficial for sequestration of U. Increased precipitation of sulfide phases would also benefit the precipitation of transition metals (e.g., Ni, Co, Mo) and eventually even As, that could be bound into residual phases such as arsenopyrite. It was shown that the cycling of Fe and Ca in the D-pit and DJX-pit at Cluff Lake was not only important for the stabilization of the stratification (i.e., meromixis) of these pit lakes, but also influenced the sequestration of contaminants by allowing them to sorb to colloidal particles made of Fe-O, Fe-S, and Ca-S phases. While this seems beneficial for the surface water quality, it is important to understand that artificially-induced meromixis is a fairly labile state. Estimates done in Chapter 2 indicated that the D pit at Cluff Lake might remain meromictic for about 83 years, given that the stratification remains stabilized by metal precipitation and dissolution processes (e.g., Fe oxyhydroxides). We could assume the same or a longer lifetime for the meromixis in the DJX-pit. During this meromictic time the lakes will sequester contaminants from the water columns into the sediments. Using the sequestration rates obtained in Chapter 3 a careful estimate of the total amount of sequestered contaminants can be done, yielding more than 1.1 t of U and about 6.0 t of As for the D-pit and about 6.5 t of U and 4.1 t of Ni for the DJX-pit (Table 5.1). Obviously those numbers are very rough estimates based on the extrapolations and need to be considered with care. Nevertheless, the orders of magnitude are striking, e.g., when considering that the whole mine produced about 28000 t of U. Changes of the water balance of the lakes, the climate, and vegetation density, as well as potential anthropogenic disturbances through recreational use will shift the intrinsic elemental cycles in the lakes and may eventually lead to deviations from this optimistic scenario. While anoxia in the monimolimnion might be a more beneficial scenario for U sequestration, it is a more difficult state to maintain in an artificial lake, where chemocline migration may ultimately lead to an overturning of the lake and induce oxygenation of deeper water layers. This means that such lakes need to be carefully monitored to prevent the loss of meromixis. Continuous freshwater supply for the mixolimnion or fertilization could be potential management techniques to maintain meromixis.

Table 5.1 Estimates on total sequestered metals by the meromictic pits

	D-pit	DJX-pit
U sequestration rate (g/m^2/year)	0.90	0.91
As sequestration rate (g/m^2/year)	4.67	0.04
Ni sequestration rate (g/m^2/year)	0.11	0.57
Years of meromixis (years)	83	100
Surface area (m^2)	15400	85900
U sequestered (kg)	1150	6488
As sequestered (kg)	5969	285
Ni sequestered (kg)	141	4064

Over time accumulations of contaminants in the pit lake sediments and the permeable reactive barrier material will become a liability for future generations. While techniques, such as dredging and excavation exist, they will pose a challenge due to the remoteness of Cluff Lake and similar mining sites. Proper controls such as signage will be required to prevent risks of exposure to humans. Such signage was present at the boundaries of the mining area and near the wetland at the time of the field campaigns performed in Chapters 2-4, however, none existed in the immediate proximity of the pits. Remobilization of contaminants into groundwater and surface water from covered waste rock piles and from exposed and oxidized bedrock in the pits will pose further risks and will need to be investigated in future.

The permeable reactive barriers at Cluff Lake did not fail in terms of U retention, however, they were not sufficient in remediating transition metals, likely due to improper design and construction, as was discussed in Chapter 4. Furthermore, the low pH environment might even have worsened the situation for Ni and Co, counteracting the natural retention of those metals in the slightly acidic environment of the peatland. This demonstrates how important it is to evaluate the performance of remediation installations after longer periods of time.

Microbes played a key role in both the pit lakes and the reactive barriers. Microbial species diversity was highest at the zones having the largest physical (e.g., temperature) and chemical gradients (e.g., pH, redox, chemical species). In the pits, this applied to chemoclines in the open water and to the shallow sediments, where the difference between sediment and water in terms of chemistry was the largest (Chapters 2 and 3). In the case of the reactive barrier, this applied to the zone where the groundwater hit the reactive material, generating a strong chemical gradient (Chapter 4). Furthermore, similar microbial groups were identified in all 3 systems (water, sediments, soil). The classes Alphaproteobacteria, Deltaproteobacteria, and Clostridia were well represented at the gradient zones and sometimes even the same representative genera were found (e.g., *Geobacter*, *Desulfosporosinus*, *Rhodoferax*). This is not very surprising given that all those environments were affected by the same kind of redox-sensitive species, such as U, Fe, and S (mainly in the form of SO_4^{2-}). The microbes were important players, driving the kinetics in those systems, a universal concept that allows to apply bioremediation to a variety of scenarios and to control the outcome by promoting or suppressing microbial activity. Knowing the dominant microbial groups for a given scenario may allow for better targeted and therefore more efficient bioremediation, especially in the case of reactive barriers (e.g., biobarriers, see Chapter 1). By altering parameters, such as available carbon sources, electron acceptors and pH conditions, one could steer bioremediation systems to perform desired biological activities.

Continuous monitoring over longer periods of time should be considered for both remediation installments at Cluff Lake investigated in this thesis, as this would provide valuable data in terms of long-term performance of those technologies. Further studies need to focus on the geochemical evolution of pit lakes. Particularly interesting would be the investigation of biogeochemical changes happening in an overturning pit lake, making a transition from a meromictic lake into a holomictic lake, which will

dramatically shift equilibria of chemical species and strongly impact present biota. Presently, RNA-based investigations of microbial communities in the pelagic zone of the pit lakes and in the permeable reactive medium could help to understand the activity of microorganisms and their ultimate role in metal/metalloid cycling. Synchrotron-based spectroscopy on the reactive barrier medium could further help to get an in-depth understanding of the U retention on the micro scale.

The biogeochemical approach used in the studies of this thesis could be similarly applied to other mining sites worldwide that have to manage contaminated water. A careful limnological characterization of surface water bodies and pedological and hydrogeological investigations related to groundwater problems can be used to delineate the systems and following investigations of geochemical and biological processes involved in contaminant cycles could help to explain mechanisms important for remediation.

BIBLIOGRAPHY

Abdelouas, A., Lutze, W. and Nuttall, E., 1998. Chemical reactions of uranium in ground water at a mill tailings site. *Journal of Contaminant Hydrology*, *34*(4): 343-361.

Adams, J.A., Osmond, J.K., & Rogers, J.J. (1959). The geochemistry of thorium and uranium. *Physics and Chemistry of the Earth, 3*, 298-348.

Albuquerque, L., França, L., Rainey, F.A., Schumann, P., Nobre, M.F., and da Costa, M.S., 2011. Gaiella occulta gen. nov., sp. nov., a novel representative of a deep branching phylogenetic lineage within the class Actinobacteria and proposal of Gaiellaceae fam. nov. and Gaiellales ord. nov. *Systematic and applied microbiology*, *34*(8): 595-599.

Alessi, D.S., Lezama-Pacheco, J.S., Janot, N., Suvorova, E.I., Cerrato, J.M., Giammar, D.E., Davis, J.A., Fox, P.M., Williams, K.H., Long, P.E., Handley, K.M., Bernier-Latmani, R., Bargar, J.R., 2014a. Speciation and reactivity of uranium products formed during in situ bioremediation in a shallow alluvial aquifer. *Environmental Science & Technology, 48*(21): 12842-12850.

Alessi, D.S., Lezama-Pacheco, J.S., Stubbs, J.E., Janousch, M., Bargar, J.R., Persson, P., and Bernier-Latmani, R., 2014b. The product of microbial uranium reduction includes multiple species with U (IV)–phosphate coordination. *Geochimica et Cosmochimica Acta*, *131*: 115-127.

Alexandre, P., Kyser, K., Layton-Matthews, D., Beyer, S.R., Hiatt, E.E., and Lafontaine, J., 2015. Formation of the enigmatic Matoush uranium deposit in the Paleoprotozoic Otish Basin, Quebec, Canada. *Mineralium Deposita, 50*(7): 825-845.

Algeo, T.J., and Tribovillard, N., 2009. Environmental analysis of paleoceanographic systems based on molybdenum–uranium covariation. *Chemical Geology*, *268*(3-4): 211-225.

Altschul, S.F., Gish, W., Miller, W., Myers, E.W., and Lipman, D.J., 1990. Basic local alignment search tool. *Journal of Molecular Biology, 215*: 403-410.

AMOK, 1974. The Carswell circular structure and Cluff Lake uranium ore-bodies. Saskatchewan Geological Society Special Publication Number 2: FUELS: a geological appraisal. Proceedings of a symposium. Accessed April 2018. URL: http://archives.datapages.com/data/sgs/1974/047/images/047.pdf

Anderson, M.J., and Willis, T.J., 2003. Canonical analysis of principal coordinates: a useful method of constrained ordination for ecology. *Ecology*, *84*(2): 511-525.

Anderson, R. F., 1984. A method for determining the oxidation state of uranium in natural waters. *Nuclear Instruments and Methods in Physics Research, 223*(2-3): 213-217.

Anderson, R.F., Fleisher, M.Q., and LeHuray, A.P., 1989. Concentration, oxidation state, and particulate flux of uranium in the Black Sea. *Geochimica et Cosmochimica Acta, 53*(9): 2215-2224.

Andreesen, J.R., Bahl, H., and Gottschalk, G., 1989. Introduction to the physiology and biochemistry of the genus Clostridium. In P.M. Nigel, and D.J. Clarke (eds.) *Clostridia* (pp. 27-62). Springer, Boston, MA, USA.

AREVA, 2009. Cluff Lake project. Detailed decommissioning plan, version 2. AREVA Resources Canada Inc.

AREVA, 2013. Cluff lake project: 2012 annual report. AREVA Resources Canada Inc.

Arndt, D., Xia, J., Liu, Y., Zhou, Y., Guo, A.C., Cruz, J.A., Sinelnikov, I., Budwill, K., Nesbø, C.L., and Wishart, D.S., 2012. METAGENassist: a comprehensive web server for comparative metagenomics. *Nucleic acids research*, *40*(W1): W88-W95.

Bai, J., Yin, X., Zhu, Y., Fan, F., Wu, X., Tian, W., Tan, C., Zhang, X., Wang, Y., Cao, S., and Fan, F., 2016. Selective uranium sorption from salt lake brines by amidoximated Saccharomyces cerevisiae. *Chemical Engineering Journal, 283*: 889-895.

Baker, J.E., Capel, P.D., and Eisenreich, S.J., 1986. Influence of colloids on sediment-water partition coefficients of polychlorobiphenyl congeners in natural waters. *Environmental science & technology, 20*(11): 1136-1143.

Balk, M., Altınbaş, M., Rijpstra, W.I.C., Damste, J.S.S., & Stams, A.J., 2008. Desulfatirhabdium butyrativorans gen. nov., sp. nov., a butyrate-oxidizing, sulfate-reducing bacterium isolated from an anaerobic bioreactor. *International Journal of Systematic and Evolutionary Microbiology, 58*(1): 110-115.

Bargar, J.R., Williams, K.H., Campbell, K.M., Long, P.E., Stubbs, J.E., Suvorova, E.I., Lezama-Pacheco, J.S., Alessi, D.S., Stylo, M., Webb, S.M., Davis, J.A., Giammar, D.E., Blue, L.Y., and Bernier-Latmani, R., 2013. Uranium redox transition pathways in acetate-amended sediments. *Proceedings of the National Academy of Sciences, 110*(12): 4506-4511.

Basiliko, N., and Yavitt, J.B., 2001. Influence of Ni, Co, Fe, and Na additions on methane production in Sphagnum-dominated Northern American peatlands. *Biogeochemistry, 52*(2): 133-153.

Bell, K., 1985. Geochronology of the carswell area, northern saskatchewan: in the carswell structure uranium deposits, saskatchewan. *Geological Association of Canada Special Paper 29*: 34-46.

Beller, H.R., 2005. Anaerobic, nitrate-dependent oxidation of U (IV) oxide minerals by the chemolithoautotrophic bacterium Thiobacillus denitrificans. *Applied and Environmental Microbiology, 71*(4): 2170-2174.

Benner, S.G., Blowes, D.W., Gould, W.D., Herbert, R.B. & Ptacek, C.J. (1999). Geochemistry of a permeable reactive barrier for metals and acid mine drainage. *Environmental Science & Technology, 33*(16), 2793-2799. https://doi.org/10.1021/es981040u

Berestovskaya, J.J., Kotsyurbenko, O.R., Tourova, T.P., Kolganova, T.V., Doronina, N.V., Golyshin, P.N., and Vasilyeva, L.V., 2012. Methylorosula polaris gen. nov., sp. nov., an aerobic, facultatively methylotrophic psychrotolerant bacterium from tundra wetland soil. *International journal of systematic and evolutionary microbiology*, *62*(3): 638-646.

Bleise, A., Danesi, P. R., and Burkart, W., 2003. Properties, use and health effects of depleted uranium (DU): a general overview. *Journal of Environmental Radioactivity, 64*(2): 93-112.

Boehrer B., von Rohden C., and Schultze M., 2017. Physical Features of Meromictic Lakes: Stratification and Circulation. In R. Gulati, E. Zadereev, and A. Degermendzhi (eds.) *Ecology of Meromictic Lakes* (vol 228, pp. 15-34). Springer, Cham, Switzerland.

Boehrer, B., and Schultze, M., 2008. Stratification of lakes. *Reviews of Geophysics, 46*(2).

Bohu, T., Akob, D.M., Abratis, M., Lazar, C.S., and Küsel, K., 2016. Biological low-ph mn(ii) oxidation in a manganese deposit influenced by metal-rich groundwater. *Applied and Environmental Microbiology, 82*(10): 3009-3021.

Borch, T., Kretzschmar, R., Kappler, A., Cappellen, P. V., Ginder-Vogel, M., Voegelin, A., and Campbell, K., 2010. Biogeochemical redox processes and their impact on contaminant dynamics. *Environmental Science & Technology, 44*(1): 15-23.

Borggaard, O.K., 1992. Dissolution of poorly crystalline iron oxides in soils by EDTA and oxalate. *Zeitschrift für Pflanzenernährung und Bodenkunde*, *155*(5): 431-436.

Bouanane-Darenfed A., Fardeau ML., and Ollivier B., 2014. The Family Caldicoprobacteraceae, In E. Rosenberg, E.F., DeLong, S. Lory, E. Stackebrandt, and F. Thompson (eds.), *The Prokaryotes* (pp. 13-18). Sprigner, Berlin, Heidelberg, Germany.

Brassier-Lecarme, C., Baron, P., Chevalier, J.L., and Madic, C., 1997. Acidic organophosphorus solvent extraction process for the purification of molybdenum in tailings from uranium ore treatment. *Hydrometallurgy*, *47*(1): 57-67.

Burns, P.C., 1997. A new uranyl oxide hydrate sheet in vandendriesscheite; implications for mineral paragenesis and the corrosion of spent nuclear fuel. *American Mineralogist*, *82*(11-12): 1176-1186.

Campos, V.L., Escalante, G., Yañez, J., Zaror, C.A., and Mondaca, M.A., 2009. Isolation of arsenite-oxidizing bacteria from a natural biofilm associated to volcanic rocks of Atacama Desert, Chile. *Journal of Basic Microbiology, 49*(S1).

CAN (Canadian Nuclear Assocaition), 2015. Nuclear fuel cycle. Accessed February 2018. URL: https://cna.ca/technology/energy/nuclear-fuel-cycle/

Caporaso, J.G., Lauber, C.L., Walters, W.A., Berg-Lyons, D., Huntley, J., Fierer, N., Owens, S.M., Betley, J., Fraser, L., Bauer, M., and Gormley, N., 2012. Ultra-high-throughput microbial community analysis on the Illumina HiSeq and MiSeq platforms. *The ISME journal*, *6*(8): 1621.

Castro, J.M., and Moore, J.N., 2000. Pit lakes: their characteristics and the potential for their remediation. *Environmental Geology, 39*(11): 1254-1260.

Chang, S.S., and Kang, D.H., 2004. Alicyclobacillus spp. in the fruit juice industry: history, characteristics, and current isolation/detection procedures. *Critical Reviews in Microbiology, 30*(2): 55-74.

Church, C.D., Wilkin, R.T., Alpers, C.N., Rye, R.O., and McCleskey, R.B., 2007. Microbial sulfate reduction and metal attenuation in pH 4 acid mine water. *Geochemical Transactions, 8*(1): 10.

CNSC (Canadian Nuclear Safety Commission), 2003. Comprehensive study report, Cluff Lake decommissioning project. Accessed February 2019. URL: https://ceaa.gc.ca/41B79974-docs/report_e.pdf

CNSC (Canadian Nuclear Safety Commission), 2018. Uranium mines and mills waste. Accessed February 2019. URL: http://nuclearsafety.gc.ca/eng/waste/uranium-mines-and-millswaste/index.cfm

Cowan, G.A., 1976. A natural fission reactor. *Scientific American, 235*(1): 36-47.

Croteau, M.N., Cain, D.J., and Fuller, C.C., 2013. Novel and nontraditional use of stable isotope tracers to study metal bioavailability from natural particles. *Environmental science & Technology, 47*(7) : 3424-3431.

Curie P, Curie M, and Bémont G, 1898. Sur une nouvelle substance fortement radio-active contenue dans la pechblende. *Comptes rendus de l'Académie des Sciences, 127*: 1215–1218.

Cuss, C.W., and Guéguen, C., 2012. Determination of relative molecular weights of fluorescent components in dissolved organic matter using asymmetrical flow field-flow fractionation and parallel factor analysis. *Analytica Chimica Acta, 733*: 98-102.

Cuss, C.W., Grant-Weaver, I., and Shotyk, W., 2017. AF4-ICPMS with the 300 Da Membrane To Resolve Metal-Bearing “Colloids”< 1 kDa: Optimization, Fractogram Deconvolution, Advanced Quality Control. *Analytical Chemistry, 89*(15): 8027-8035.

Dahlkamp, F.J., 2013. *Uranium ore deposits.* Springer Science & Business Media, Berlin, Germany.

Dai, M., Martin, J.M., and Cauwet, G., 1995. The significant role of colloids in the transport and transformation of organic carbon and associated trace metals (Cd, Cu and Ni) in the Rhône delta (France). *Marine Chemistry*, *51*(2): 159-175.

Dalla Vecchia, E., Veeramani, H., Suvorova, E.I., Wigginton, N.S., Bargar, J.R. and Bernier-Latmani, R., 2010. U (VI) reduction by spores of Clostridium acetobutylicum. *Research in Microbiology, 161*(9): 765-771.

Dean, J. A., 1999. *Lange's handbook of chemistry* (Fifteenth Edition). New York, NY, USA: McGraw-Hill, Inc.

Deditius, A.P., Utsunomiya, S., and Ewing, R.C., 2007. Alteration of UO2+ x under oxidizing conditions, Marshall Pass, Colorado, USA. *Journal of alloys and compounds*, *444*: 584-589.

Dessouki, T.C., Hudson, J.J., Neal, B.R., and Bogard, M.J., 2005. The effects of phosphorus additions on the sedimentation of contaminants in a uranium mine pit-lake. *Water Research*, *39*(13): 3055-3061.

Diez-Ercilla, M., Sánchez-España, J., Yusta, I., Wendt-Potthoff, K., and Koschorreck, M., 2014. Formation of biogenic sulphides in the water column of an acidic pit lake: biogeochemical controls and effects on trace metal dynamics. *Biogeochemistry, 121*(3): 519-536.

Dise, N.B., and Verry, E.S., 2001. Suppression of peatland methane emission by cumulative sulfate deposition in simulated acid rain. *Biogeochemistry, 53*(2), 143-160.

Donahue, R., Hendry, M.J., and Landine, P., 2000. Distribution of arsenic and nickel in uranium mill tailings, Rabbit Lake, Saskatchewan, Canada. *Applied Geochemistry, 15*(8): 1097-1119.

Dong, X., Kleiner, M., Sharp, C.E., Thorson, E., Li, C., Liu, D., and Strous, M., 2017. Fast and simple analysis of MiSeq amplicon sequencing data with MetaAmp. *Frontiers in Mirobiology, 8*, 1461.

Donner, M.W., Javed, M.B., Shotyk, W., Francesconi, K.A., and Siddique, T., 2017. Arsenic speciation in the lower Athabasca River watershed: a geochemical investigation of the dissolved and particulate phases. *Environmental Pollution, 224*: 265-274.

Drake, H.L., Horn, M.A., and Wüst, P.K., 2009. Intermediary ecosystem metabolism as a main driver of methanogenesis in acidic wetland soil. *Environmental Microbiology Reports, 1*(5), 307-318.

Du, X., Boonchayaanant, B., Wu, W.M., Fendorf, S., Bargar, J., and Criddle, C.S., 2011. Reduction of uranium (VI) by soluble iron (II) conforms with thermodynamic predictions. *Environmental science & Technology*, *45*(11): 4718-4725.

Duff, M.C., Coughlin, J.U., and Hunter, D.B., 2002. Uranium co-precipitation with iron oxide minerals. *Geochimica et Cosmochimica Acta*, *66*(20): 3533-3547.

Dungkaew, W., Haller, K.J., Flood, A.E., and Scamehorn, J.F., 2012. Arsenic removal by precipitation with calcium phosphate hydroxyapatite. In T. Tunkasiri (ed.) *Advanced Materials Research* (Vol. 506, pp. 413-416). Trans Tech Publications, Zürich, Switzerland.

Edgar, R.C., 2018. Updating the 97% identity threshold for 16S ribosomal RNA OTUs. *Bioinformatics, 34*(14): 2371-2375.

Eger, P., 1994. Wetland treatment for trace metal removal from mine drainage: the importance of aerobic and anaerobic processes. *Water Science and Technology, 29*(4): 249-256.

Emerson, D., and Moyer, C., 1997. Isolation and characterization of novel iron-oxidizing bacteria that grow at circumneutral ph. *Applied and Environmental Microbiology, 63*(12): 4784-4792.

EPA (United States Environmental Protection Agency), 1983. *Methods for Chemical Analysis of Water and Wastes.* EPA/600/4-79/020. Washington, DC, USA: Office of Research and Development. Accessed November 2018. URL: https://www.wbdg.org/FFC/EPA/EPACRIT/epa600_4_79_020.pdf

Erickson, B.E., and Helz, G.R., 2000. Molybdenum (VI) speciation in sulfidic waters: stability and lability of thiomolybdates. *Geochimica et Cosmochimica Acta, 64*(7): 1149-1158.

Falagán, C., Sánchez-España, F. J., and Johnson, D. B., 2013. Microbiological communities in two acidic mine pit lakes in the Iberian Pyrite Belt (IPB), Spain. *Advanced Materials Research, 825*: 19-22.

Falagán, C., Sánchez-España, J., and Johnson, D. B., 2014. New insights into the biogeochemistry of extremely acidic environments revealed by a combined cultivation-based and culture-independent study of two stratified pit lakes. *FEMS microbiology ecology, 87*(1): 231-243.

Feng, R., Dolton, W., Igarashi, R., Wright, G., Bradford, M., and McIntyre, S., 2010. Commissioning of the VESPERS beamline at the Canadian light source. In *AIP Conference Proceedings* (Vol. 1234, No. 1, pp. 315-318). AIP.

Feng, R., Gerson, A., Ice, G., Reininger, R., Yates, B., and McIntyre, S., 2007. VESPERS: a beamline for combined XRF and XRD measurements. In *AIP Conference Proceedings* (Vol. 879, No. 1, pp. 872-874). AIP.

Filella, M., 2006. Colloidal Properties of Submicron Particles in Natural Waters. In K.J. Wilkinson, and J.R. Lead (eds.) *Environmental Colloids and Particles: Behaviour, Separation and Characterisation* (vol. 10, pp. 17-93). John Wiley & Sons, Ltd, Chichester, UK.

Finch, R.J., and Ewing, R.C., 1991. Alteration of natural uranyl oxide hydrates in Si-rich groundwaters: implications for uranium solubility. *MRS Online Proceedings Library Archive*, *257*: 465-472.

Finneran, K.T., Housewright, M.E., and Lovley, D.R., 2002. Multiple influences of nitrate on uranium solubility during bioremediation of uranium-contaminated subsurface sediments. *Environmental Microbiology, 4*(9): 510-516.

Finneran, K.T., Johnsen, C.V., and Lovley, D.R., 2003. Rhodoferax ferrireducens sp. nov., a psychrotolerant, facultatively anaerobic bacterium that oxidizes acetate with the reduction of Fe (III). *International Journal of Systematic and Evolutionary Microbiology*, *53*(3): 669-673.

Fisher, T.S., and Lawrence, G.A., 2006. Treatment of acid rock drainage in a meromictic mine pit lake. *Journal of Environmental Engineering, 132*(4): 515-526.

Fomina M., Charnock J. M., Hillier S., Alvarez R., Livens F., and Gadd G. M., 2008. Role of fungi in the biogeochemical fate of depleted uranium. *Current Biology, 18*(9): R375–R377.

Foti, S.C,. and Freiling, E.C., 1964. The determination of the oxidation states of tracer uranium, neptunium and plutonium in aqueous media. *Talanta*, *11*(3): 385-392.

Frondel C., 1958. Systematic mineralogy of uranium and thorium. Geological Survey Bulletin 1064. US Government Printing Office, Washington.

Gadd, G. M., 2010. Metals, minerals and microbes: geomicrobiology and bioremediation. *Microbiology, 156*(3): 609-643.

Gao, W., and Francis, A.J., 2008. Reduction of uranium (VI) to uranium (IV) by Clostridia. *Applied and environmental microbiology, 74*(14): 4580-4584.

GBC Scientific Equipment. 2013. The determination of aluminum, iron and silicon in rock samples. Accessed February 2017. URL: http://www.gbcscientific.com/appnotes/AA_app_note_001. pdf

Geller, W., Schultze, M., Kleinmann, B., and Wolkersdorfer, C. 2012. Acidic pit lakes: the legacy of coal and metal surface mines. Springer Science & Business Media, Berlin, Germany.

Gibson, J. J., Birks, S. J., Yi, Y., Moncur, M. C., and McEachern, P. M., 2016. Stable isotope mass balance of fifty lakes in central Alberta: Assessing the role of water balance parameters in determining trophic status and lake level. *Journal of Hydrology: Regional Studies, 6*: 13-25.

Giloteaux, L., Holmes, D.E., Williams, K.H., Wrighton, K.C., Wilkins, M.J., Montgomery, A.P., Smith, J.A., Orellana, R., Thompson, C.A., Roper, T.J., and Long, P.E., 2013. Characterization and transcription of arsenic respiration and resistance genes during in situ uranium bioremediation. *The ISME Journal, 7*(2): 370-383.

Gimpel, J., Zhang, H., Davison, W., and Edwards, A. C., 2003. In situ trace metal speciation in lake surface waters using DGT, dialysis, and filtration. *Environmental science & Technology, 37*(1): 138-146.

Glass, J., and Orphan, V.J., 2012. Trace metal requirements for microbial enzymes involved in the production and consumption of methane and nitrous oxide. *Frontiers in Microbiology, 3*: 61.

Golab, A.N., Peterson, M.A., and Indraratna, B., 2006. Selection of potential reactive materials for a permeable reactive barrier for remediating acidic groundwater in acid sulphate soil terrains. *Quarterly Journal of Engineering Geology and Hydrogeology, 39*(2): 209-223.

Gorman-Lewis, D., Burns, P.C., and Fein, J.B., 2008. Review of uranyl mineral solubility measurements. *The Journal of Chemical Thermodynamics*, *40*(3): 335-352.

Graham, M.C., Oliver, I.W., MacKenzie, A.B., Ellam, R.M., and Farmer, J.G., 2011. Mechanisms controlling lateral and vertical porewater migration of depleted uranium (DU) at two UK weapons testing sites. *Science of the Total Environment, 409*(10): 1854-1866.

Graham, T., 1861. Liquid diffusion applied to analysis. *Philosophical Transactions of the Royal Society of London, 151*: 183-224.

Guéguen, C., and Cuss, C.W., 2011. Characterization of aquatic dissolved organic matter by asymmetrical flow field-flow fractionation coupled to uv-visible diode array and excitation-emission matrix fluorescence. *Journal of Chromatography A, 1218*(27): 4188-4198.

Gupta C., and Singh H., 2003. *Uranium resource processing – secondary resources*. Springer, Berlin, Heidelberg, Germany.

Gustafsson, C., and Gschwend, P.M., 1997. Aquatic colloids: concepts, definitions, current challenges. *Limnology and Oceanography, 42*(3): 519-528.

Gustafsson, C., and Gschwend, P.M., 1997. Aquatic colloids: Concepts, definitions, and current challenges. *Limnology and Oceanography, 42*(3): 519-528.

Harper, C.T., 1981. Uranium metallogenic studies: Cluff Lake area. Accessed April 2019. URL: http://publications.gov.sk.ca/documents/310/85533-Harper_1981_MiscRep81-4.pdf

Harper C.T., 1982. Geology of the carswell structure, central part. Saskatchewan Geological Survey Report 214. Accessed April 2019. URL: http://publications.gov.sk.ca/documents/310/90719-Report-214_Geology_Of_The_Carswell_Structure-Central_Part.pdf

Harter, R.D., 1983. Effect of Soil pH on Adsorption of Lead, Copper, Zinc, and Nickel. *Soil Science Society of America Journal, 47*(1): 47-51.

Hollings, P., Hendry, M.J., and Kerrich, R., 1999. Sequential filtration of surface and ground waters from the Rabbit Lake uranium mine, northern Saskatchewan, Canada. *Water Quality Research Journal*, *34*(2): 221-248.

Holmes, D.E., and Smith, J.A., 2016. Chapter One - Biologically produced methane as a renewable energy source. In S. Sariaslani, and G.M. Gadd (eds.) *Advances in applied microbiology* (vol. 97, pp. 1-61). Academic Press, Cambridge, MA, USA.

Honeyman, B.D., 1991. Surface chemistry, colloids and trace-element scavenging. In D.C., Hurd, and D.W. Spencer (eds.) *Marine Particles: Analysis and Characterization* (pp. 437-451). American Geophysical Union, Washington DC, USA.

Honeyman, J.T., and Santschi, P.H., 1991. Coupling adsorption and particle aggregation laboratory studies of “colloidal pumping” using “Fe-labeled hematite. *Environmental science & Technology, 25*(10): 1739-1747.

Hong, H., Kim, S.J., Min, U.G., Lee, Y.J., Kim, S.G., Jung, M.Y., Seo, Y.S., and Rhee, S.K., 2015. Geosporobacter ferrireducens sp. nov., an anaerobic iron-reducing bacterium isolated from an oil-contaminated site. *Antonie van Leeuwenhoek, 107*(4): 971-977.

Hongshao, Z., and Stanforth, R., 2001. Competitive adsorption of phosphate and arsenate on goethite. *Environmental Science & Technology*, *35*(24): 4753-4757.

Huang, J. W., Blaylock, M. J., Kapulnik, Y., and Ensley, B. D., 1998. Phytoremediation of uranium-contaminated soils: role of organic acids in triggering uranium hyperaccumulation in plants. *Environmental science & Technology, 32*(13): 2004-2008.

Huang, J.H., 2014. Impact of microorganisms on arsenic biogeochemistry: a review. *Water, Air, & Soil Pollution, 225*(2): 1848.

Hudson-Edwards, K.A., Jamieson, H.E., and Lottermoser, B.G., 2011. Mine wastes: past, present, future. *Elements*, *7*(6): 375-380.

Huerta-Diaz, M.A., Tessier, A., and Carignan, R., 1998. Geochemistry of trace metals associated with reduced sulfur in freshwater sediments. *Applied geochemistry*, *13*(2): 213-233.

Huffman, D., 2014. Cluff Lake project - iaea - rsls workshop. Accessed February 2019. URL: https://gnssn.iaea.org/RTWS/rsls-public/Shared%20Documents/Meetings/2nd%20Workshop,%202014,%20Canada/Presentations/Dale%20Huffman,%20Cluff%20Lake%20Project%20-May%202,%202014.pdf

Hunter, P., 2008. A toxic brew we cannot live without: Micronutrients give insights into the interplay between geochemistry and evolutionary biology. *EMBO reports, 9*(1): 15-18.

IEA (International Energy Agency), 2018a. Key world energy statistics 2018. IEA, Paris. URL: https://webstore.iea.org/world-energy-balances-2018-overview

IEA (International Energy Agency), 2018b. World Energy Outlook 2018, IEA, Paris. URL: https://doi-org.login.ezproxy.library.ualberta.ca/10.1787/weo-2018-en.

Iino, T., Mori, K., Uchino, Y., Nakagawa, T., Harayama, S., and Suzuki, K.I., 2010. Ignavibacterium album gen. nov., sp. nov., a moderately thermophilic anaerobic bacterium isolated from microbial mats at a terrestrial hot spring and proposal of Ignavibacteria classis nov., for a novel lineage at the periphery of green sulfur bacteria. *International Journal of Systematic and Evolutionary Microbiology, 60*(6): 1376-1382.

Illumina. 2016. 16S Metagenomic sequencing library preparation. Accessed October 2016. URL: https://pdfs.semanticscholar.org/bcd6/dc1196f3f906498d58aa39868895b18fa51d.pdf

INAC (Indigenous and Native Affaires Canada), 2018. Remediating the surface of Giant Mine. Accessed April 2019. URL: https://www.aadnc-aandc.gc.ca/eng/1100100027407/1100100027408

ITRC (Interstate Technology & Regulatory Council), 2011. Permeable Reactive Barrier: Technology Update. PRB-5. Washington, D.C.: Interstate Technology & Regulatory Council, PRB: Technology Update Team. Accessed February 2019. URL: https://www.itrcweb.org/GuidanceDocuments/PRB-5-1.pdf

Iyaka, Y.A., 2011. Nickel in soils: a review of its distribution and impacts. *Scientific Research and Essays, 6*(33): 6774-6777.

Jaeger, D., 1994. Effects of hypolimnetic water aeration and iron-phosphate precipitation on the trophic level of Lake Krupunder. *Hydrobiologia, 275*(1): 433-444.

Jefferson, C., Thomas, D., Gandhi, S., Ramaekers, P., Delaney, G., Brisbin, D., Cutts, C., Portella, P., and Olson, R., 2007. Unconformity-associated uranium deposits of the athabasca basin, saskatchewan and alberta. *Bulletin - Geological Survey of Canada, 588*: 23.

Joseph, S., Visalakshi, G., Venkateswaran, G., and Moorthy, P.N., 1996. Dissolution of haematite in citric acid-EDTA-ascorbic acid mixtures. *Journal of nuclear science and technology*, *33*(6): 479-485.

Juottonen, H., Eiler, A., Biasi, C., Tuittila, E.S., Yrjälä, K., & Fritze, H., 2017. Distinct anaerobic bacterial consumers of cellobiose-derived carbon in boreal fens with different CO2/CH4 production ratios. *Applied and Environmental Microbiology, 83*(4): e02533-16.

Kämpfer, P., Young, C.C., Arun, A.B., Shen, F.T., Jäckel, U., Rossello-Mora, R., Lai, W.A., and Rekha, P.D., 2006. Pseudolabrys taiwanensis gen. nov., sp. nov., an alphaproteobacterium isolated from soil. International *Journal of Systematic and Evolutionary Microbiology, 56*(10): 2469-2472.

Kijjanapanich, P., Annachhatre, A.P., Esposito, G., and Lens, P.N., 2014. Use of organic substrates as electron donors for biological sulfate reduction in gypsiferous mine soils from Nakhon Si Thammarat (Thailand). *Chemosphere, 101*: 1-7.

Kipp, G.G., Stone, J.J., and Stetler, L.D., 2009. Arsenic and uranium transport in sediments near abandoned uranium mines in Harding County, South Dakota. *Applied Geochemistry, 24*(12): 2246-2255.

Klaproth, M.H., 1789. Chemische Untersuchung des Uranits, einer neuentdeckten metallische Substanz. *Chemische Annalen für die Freunde der Naturlehre, 2*: 387–403.

Ku, T.-L., Knauss, K.G., and Mathieu, G.G., 1977. Uranium in open ocean: concentration and isotopic composition. *Deep Sea Research, 24*(11): 1005–1017.

Kulichevskaya, I.S., Suzina, N.E., Liesack, W., and Dedysh, S.N., 2010. Bryobacter aggregatus gen. nov., sp. nov., a peat-inhabiting, aerobic chemo-organotroph from subdivision 3 of the Acidobacteria. *International Journal of Systematic and Evolutionary Microbiology, 60*(2): 301-306.

Kumar, A., Rout, S., Narayanan, U., Mishra, M.K., Tripathi, R.M., Singh, J., Kumar, S., and Kushwaha, H.S., 2011. Geochemical modelling of uranium speciation in the subsurface aquatic environment of Punjab state in India. *Journal of Geology and Mining Research, 3*(5): 137-146.

Laird, K.R., Das, B., and Cumming, B.F., 2014. Enrichment of uranium, arsenic, molybdenum, and selenium in sediment cores from boreal lakes adjacent to northern Saskatchewan uranium mines. *Lake and Reservoir Management*, *30*(4): 344-357.

Langmuir, D., and Herman, J.S., 1980. The mobility of thorium in natural waters at low temperatures. *Geochimica et Cosmochimica Acta, 44*(11): 1753-1766.

Langmuir, D., 1978. Uranium solution-mineral equilibria at low temperatures with applications to sedimentary ore deposits. *Geochimica et Cosmochimica Acta*, *42*(6): 547-569.

Larios, R., Fernández-Martínez, R., and Rucandio, I., 2013. Assessment of a sequential extraction procedure for arsenic partitioning and application to samples from different pollution sources. *Analytical Methods*, *5*(16): 4096-4104.

Larsen, F., and Postma, D., 1997. Nickel mobilization in a groundwater well field: release by pyrite oxidation and desorption from manganese oxides. *Environmental science & Technology, 31*(9): 2589-2595.

Leigh, M.B., Wu, W.M., Cardenas, E., Uhlik, O., Carroll, S., Gentry, T., Marsh, T.L., Zhou, J., Jardine, P., Criddle, C.S., and Tiedje, J.M., 2015. Microbial communities biostimulated by ethanol during uranium (vi) bioremediation in contaminated sediment as shown by stable isotope probing. *Frontiers of Environmental Science & Engineering, 9*(3): 453-464.

Li, G.Y., Hu, N., Ding, D.X., Zheng, J.F., Liu, Y.L., Wang, Y.D., and Nie, X.Q., 2011. Screening of plant species for phytoremediation of uranium, thorium, barium, nickel, strontium and lead contaminated soils from a uranium mill tailings repository in South China. *Bulletin of Environmental Contamination and Toxicology, 86*(6): 646-652.

Li, W.C., Victor, D.M., and Chakrabarti, C.L., 1980. Effect of pH and uranium concentration on interaction of uranium (VI) and uranium (IV) with organic ligands in aqueous solutions. *Analytical Chemistry, 52*(3): 520-523.

Li, X., Coles, B.J., Ramsey, M.H., and Thornton, I., 1995. Sequential extraction of soils for multielement analysis by ICP-AES. *Chemical Geology*, *124*(1-2): 109-123.

Libes, S., 2009. *Introduction to marine biogeochemistry* (Second edition). Academic Press, Cambridge, MA.

Liger, E., Charlet, L., and van Cappellen, P., 1999. Surface catalysis of uranium (VI) reduction by iron (II). *Geochimica et Cosmochimica Acta, 63*(19): 2939-2955.

Lipscomb, W.N., and Sträter, N., 1996. Recent advances in zinc enzymology. *Chemical Reviews*, *96*(7): 2375-2434.

Lopez A., Lazaro N., Priego J., and Marques A., 2000. Effect of ph on the biosorption of nickel and other heavy metals by pseudomonas fluorescens 4f39. *Journal of Industrial Microbiology and Biotechnology, 24*(2): 146–151.

Lovley, D.R., Giovannoni, S.J., White, D.C., Champine, J.E., Phillips, E.J.P., Gorby, Y.A., and Goodwin, S., 1993a. Geobacter metallireducens gen. nov. sp. nov., a microorganism capable of coupling the complete oxidation of organic compounds to the reduction of iron and other metals. *Archives of Microbiology, 159*(4): 336-344.

Lovley, D.R., Roden, E.E., Phillips, E.J.P. and Woodward, J.C., 1993b. Enzymatic iron and uranium reduction by sulfate-reducing bacteria. *Marine Geology, 113*(1-2): 41-53.

Lücker, S., Schwarz, J., Gruber-Dorninger, C., Spieck, E., Wagner, M., and Daims, H., 2015. Nitrotoga-like bacteria are previously unrecognized key nitrite oxidizers in full-scale wastewater treatment plants. *The ISME journal*, *9*(3): 708.

Lueders, T., and Friedrich, M.W., 2002. Effects of amendment with ferrihydrite and gypsum on the structure and activity of methanogenic populations in rice field soil. Applied and *Environmental Microbiology, 68*(5): 2484-2494.

Macomber, L., and Hausinger, R.P., 2011. Mechanisms of nickel toxicity in microorganisms. *Metallomics, 3*(11): 1153-1162.

Matthews, R., and Fazeli, H., 2004. Copper and complexity: Iran and Mesopotamia in the fourth millennium BC. *Iran*, *42*(1): 61-75.

May, T.W., and Wiedmeyer, R.H., 1998. A table of polyatomic interferences in icp-ms. *Atomic Spectroscopy, 19*: 150-155.

McArdle, B.H., and Anderson, M.J., 2001. Fitting multivariate models to community data: A comment on distance-based redundancy analysis. *Ecology, 82*: 290–297.

McMurdie P.J., and Holmes S., 2013 phyloseq: an R package for reproducible interactive analysis and graphics of microbiome census data. *PloS ONE* 8(4): e61217.

Merkel, B.J., Planer-Friedrich, B., and Nordstrom, D., 2005. Groundwater geochemistry. A Practical Guide to Modeling of Natural and Contaminated Aquatic Systems (Second edition). Springer, Berlin, Heidelberg, Germany.

Miyazaki, M., Koide, O., Kobayashi, T., Mori, K., Shimamura, S., Nunoura, T., Imachi, H., Inagaki, F., Nagahama, T., Nogi, Y., and Deguchi, S., 2012. Geofilum rubicundum gen. nov., sp. nov., isolated from deep subseafloor sediment. *International Journal of Systematic and Evolutionary Microbiology, 62*(5): 1075-1080.

Moffett, D., and Tellier, M. 1977. Uptake of radioisotopes by vegetation growing on uranium tailings. *Canadian Journal of Soil Science, 57*(4): 417–424.

Morrison, S.J., and Spangler, R.R., 1992. Extraction of uranium and molybdenum from aqueous solutions: A survey of industrial materials for use in chemical barriers for uranium mill tailings remediation. *Environmental Science & Technology*, *26*(10): 1922-1931.

NEA/IAEA (Nuclear Energy Agency/International Atomic Energy Agency), 2018. Uranium 2018: Resources, Production and Demand, OECD Publishing, Paris. URL: https://doi.org/10.1787/uranium-2018-en.

Nelson, D.M., Penrose, W.R., Karttunen, J.O. and Mehlhaff, P., 1985. Effects of dissolved organic carbon on the adsorption properties of plutonium in natural waters. *Environmental science & Technology, 19*(2): 127-131.

Neubauer, E., Kammer, F., and Hofmann, T., 2013. Using flowfff and hpsec to determine trace metal-colloid associations in wetland runoff. *Water Research, 47*(8): 2757-2769.

Newsome, L., Morris, K., and Lloyd, J.R., 2014a. The biogeochemistry and bioremediation of uranium and other priority radionuclides. *Chemical Geology, 363*: 164-184.

Newsome, L., Morris, K., Trivedi, D., Atherton, N., and Lloyd, J.R., 2014b. Microbial reduction of uranium (VI) in sediments of different lithologies collected from Sellafield. *Applied geochemistry, 51*: 55-64.

NRC (National Research Council), 1977. *Arsenic: medical and biologic effects of environmental pollutants.* National Academic Press, Washington, USA.

Olds, T.A., Plášil, J., Kampf, A.R., Škoda, R., Burns, P.C., Čejka, J., Bourgoin, V., and Boulliard, J.C., 2017. Gauthierite, KPb [(UO2) 7O5 (OH) 7]· 8H2O, a new uranyl-oxide hydroxy-hydrate mineral from Shinkolobwe with a novel uranyl-anion sheet-topology. *European Journal of Mineralogy*, *29*(1): 129-141.

Ondrus, P., Veselovsky, F., Hlousek, J., Skala, R., Vavrin, I., Fryda, J., Cejka, J., and Gabasova, A., 1997. Secondary minerals of the Jáchymov (Joachimsthal) ore district. *Journal of Geosciences*, *42*(4): 3-76.

Oude Elferink, S.J.W.H., O., Visser, A., Pol, H., Look, W., and Stams, A.J., 1994. Sulfate reduction in methanogenic bioreactors. *FEMS Microbiology Reviews, 15*(2-3): 119-136.

Parkhurst, D.L., and Appelo, C.A.J., 2013. Description of input and examples for PHREEQC version 3: a computer program for speciation, batch-reaction, one-dimensional transport, and inverse geochemical calculations (No. 6-A43). Denver, CO, USA: US Geological Survey. Accessed March 2019. URL: https://pubs.usgs.gov/tm/06/a43/

Patel, G.B., and Sprott, G.D., 1990. Methanosaeta concilii gen. nov., sp. nov.(“Methanothrix concilii”) and Methanosaeta thermoacetophila nom. rev., comb. nov. *International Journal of Systematic and Evolutionary Microbiology, 40*(1): 79-82.

Paul, D., Poddar, S., and Sar, P., 2014. Characterization of arsenite-oxidizing bacteria isolated from arsenic-contaminated groundwater of west Bengal. *Journal of Environmental Science and Health, Part A, 49*(13): 1481-1492.

Pelletier C.A., Wen M.E., and Poling G.W., 2009. Flooding pit lakes with surface water. In D.N. Castendyk, and L.E. Eary (eds.) *Mine pit lakes – Characteristics, predictive modeling and sustainability* (pp. 239-248). Society for Mining, Metallurgy and Exploration, Littleton, CO, USA.

Perry, D.L., Klainer, S.M., Bowman, H.R., Milanovich, F.P., Hirschfeld, T., and Miller, S., 1981. Detection of ultratrace levels of uranium in aqueous samples by laser-induced fluorescence spectrometry. *Analytical Chemistry*, *53*(7): 1048-1050.

Pham, S.V., Leavitt, P.R., McGowan, S., Wissel, B., and Wassenaar, L.I., 2009. Spatial and temporal variability of prairie lake hydrology as revealed using stable isotopes of hydrogen and oxygen. *Limnology and Oceanography, 54*(1): 101-118.

Pichler, T., Hendry, M.J., and Hall, G.E.M., 2001. The mineralogy of arsenic in uranium mine tailings at the Rabbit Lake In-pit Facility, northern Saskatchewan, Canada. *Environmental Geology*, *40*(4-5): 495-506.

Pieters, R., and Lawrence, G.A. 2014. Physical processes and meromixis in pit lakes subject to ice cover. *Canadian Journal of Civil Engineering, 41*(6): 569-578.

Plasil, J., 2014. Oxidation-hydration weathering of uraninite: the current state-of-knowledge. *Journal of Geosciences*, *59*(2): 99-114.

Pokrovsky, O. S., Dupré, B., and Schott, J., 2005. Fe–Al–organic colloids control of trace elements in peat soil solutions: results of ultrafiltration and dialysis. *Aquatic Geochemistry, 11*(3): 241-278.

Porsch, K., and Kappler, A., 2011. Feii oxidation by molecular o2 during hcl extraction. *Environmental Chemistry, 8*(2): 190-197.

Powell, R.M., Blowes, D.W., Gillham, R.W., Schultz, D., Sivavec, T., Puls, R.W., Vogan, J.L., Powell, P.D., & Landis, R., 1998. *Permeable reactive barrier technologies for contaminant remediation.* EPA/600/R-98/125. United States Environmental Protection Agency, Washington, DC.

Quast, C., Pruesse, E., Yilmaz, P., Gerken, J., Schweer, T., Yarza, P., Peplies, J., and Glöckner, F.O., 2012. The SILVA ribosomal RNA gene database project: improved data processing and web-based tools. *Nucleic acids research*, *41*(D1): D590-D596.

Quevauviller, P., Rauret, G., and Griepink, B., 1993. Single and sequential extraction in sediments and soils. *International Journal of Environmental Analytical Chemistry, 51*(1-4): 231-235.

R Core Team, 2017. R: A language and environment for statistical computing. R Foundation for Statistical Computing, Vienna, Austria. URL: https://www.R-project.org/.

Raessler, M., 2018. The Arsenic Contamination of Drinking and Groundwaters in Bangladesh: Featuring Biogeochemical Aspects and Implications on Public Health. *Archives of environmental contamination and toxicology, 75*(1): 1-7.

Ramette, A., 2007. Multivariate analyses in microbial ecology. *FEMS microbiology ecology*, *62*(2): 142-160.

Ramos, O.E.R., Cáceres, L.F., Munoz, M.R.O., Bhattacharya, P., Quino, I., Quintanilla, J., Sracek, O., Thunvik, R., Bundschuh, J., and García, M.E., 2012. Sources and behavior of arsenic and trace

elements in groundwater and surface water in the Poopó Lake Basin, Bolivian Altiplano. *Environmental earth sciences*, *66*(3): 793-807.

Ratnaike, R.N., 2003. Acute and chronic arsenic toxicity. *Postgraduate medical journal, 79*(933): 391-396.

Ravel, B., and Newville, M., 2005. ATHENA, ARTEMIS, HEPHAESTUS: data analysis for X-ray absorption spectroscopy using IFEFFIT. *Journal of synchrotron radiation*, *12*(4): 537-541.

Rayment, G.E. and Higginson, F.R., 1992. *Australian laboratory handbook of soil and water chemical methods.* Inkata Press Pty Ltd., Melbourne, Australia.

Rhulmann, F., 1985. Mineralogy and metallogeny of uraniferous occurrences in the Carswell structure: in the Carswell structure uranium deposits, Saskatchewan. *Geological Association of Canada Special Paper 29*: 105-120.

Richter S., Alonso A., De Bolle W., Wellum R., and Taylor P., 1999. Isotopic “finger- prints” for natural uranium ore samples. *International Journal of Mass Spectrometry, 193*(1): 9–14.

Ross, J. M. and Sherrell, R. M., 1999. The role of colloids in tracemetal transport and adsorption behavior in New Jersey Pinelands streams. *Limnology and Oceanography, 44*(4): 1019-1034.

Rozanova, E.P., Nazina, T.N., and Galushko, A.S., 1988. Isolation of a new genus of sulfate-reducing bacteria and description of a new species of this genus, Desulfomicrobium apsheronum gen. nov., sp. nov. *Microbiology (Mikrobiologiya), 57*(5), 514-520.

Sadashivaiah, C., Ramakrishnaiah, C.R., and Ranganna, G., 2008. Hydrochemical analysis and evaluation of groundwater quality in Tumkur Taluk, Karnataka State, India. *International Journal of Environmental Research and Public Health, 5*(3): 158-164.

Sakai, K., 2015. Routine soil analysis using an Agilent 8800 ICP-QQQ. Application note 5991-6409EN. Agilent Technologies. Accessed February 2018. URL: https://www.agilent.com/en-us/library/applications

Sánchez-España, J., Yusta, I., Gray, J., and Burgos, W.D., 2016. Geochemistry of dissolved aluminum at low pH: Extent and significance of Al–Fe (III) coprecipitation below pH 4.0. *Geochimica et Cosmochimica Acta, 175*: 128-149.

Saunders, J.A., Lee, M.K., Dhakal, P., Ghandehari, S.S., Wilson, T., Billor, M.Z., and Uddin, A., 2018. Bioremediation of arsenic-contaminated groundwater by sequestration of arsenic in biogenic pyrite. *Applied geochemistry*, *96*: 233-243.

Scheller, S., Goenrich, M., Boecher, R., Thauer, R. K., and Jaun, B., 2010. The key nickel enzyme of methanogenesis catalyses the anaerobic oxidation of methane. *Nature 465*(7298): 606-608.

Schultze M., Boehrer B., Wendt-Potthoff K., Sánchez-España J., and Castendyk D., 2017. Meromictic Pit Lakes: Case Studies from Spain, Germany and Canada and General Aspects of Management and

Modelling. In R. Gulati, E. Zadereev, and A. Degermendzhi (eds.) *Ecology of Meromictic Lakes* (vol 228, pp. 235-276). Springer, Cham, Switzerland.

Schultze, M., Castendyk, D., Wendt-Potthoff, K., Sánchez-España, J., and Boehrer, B., 2016. On the relevance of meromixis in mine pit lakes - an update. In Proceedings IMWA 2016 Annual Conference, Freiberg, Germany. Accessed December 2016. URL: www.imwa.info/docs/imwa_2016/IMWA2016_Schultze_27.pdf

Schulze, R., Spring, S., Amann, R., Huber, I., Ludwig, W., Schleifer, K. H., and Kämpfer, P., 1999. Genotypic diversity of Acidovorax strains isolated from activated sludge and description of Acidovorax defluvii sp. nov. *Systematic and Applied Microbiology, 22*(2): 205-214.

Sharp, J.H., 1973. Size classes of organic carbon in seawater. *Limnology and Oceanography, 18*(3): 441-447.

Shelobolina, E.S., Vrionis, H.A., Findlay, R.H., and Lovley, D.R., 2008. Geobacter uraniireducens sp. nov., isolated from subsurface sediment undergoing uranium bioremediation. *International Journal of Systematic and Evolutionary Microbiology, 58*(5): 1075-1078.

Sheoran, A.S., and Sheoran, V., 2006. Heavy metal removal mechanism of acid mine drainage in wetlands: a critical review. *Minerals Engineering, 19*(2), 105-116.

Sheppard, M.I., and Thibault, D.H., 1992. Desorption and extraction of selected heavy metals from soils. *Soil Science Society of America Journal*, *56*(2): 415-423.

Slowey, A.J., Johnson, S.B., Newville, M., and Brown, G.E., 2007. Speciation and colloid transport of arsenic from mine tailings. *Applied Geochemistry, 22*(9): 1884-1898.

Bailey, B.L., Smith, L.J., Blowes, D.W., Ptacek, C.J., Smith, L., and Sego, D.C., 2013. The Diavik Waste Rock Project: Persistence of contaminants from blasting agents in waste rock effluent. *Applied geochemistry, 36*: 256-270.

SMA (Saskatchewan Mining Association), 2016. Uranium in Saskatchewan, facts on the industry for 2016. Accessed February 2019. URL: http://saskmining.ca/ckfinder/userfiles/files/EmergencyResponseCompetitionPhotos/SMA%20-%20Uranium%20Fact%20Sheets%202016ti.pdf

Sobolewski, A., 1999. A review of processes responsible for metal removal in wetlands treating contaminated mine drainage. *International Journal of Phytoremediation, 1*(1): 19-51.

Soni, A., Mishra, B., and Singh, S., 2014. Pit lakes as an end use of mining: A review. *Journal of Mining and Environment*, *5*(2): 99-111.

Sorokin, D.Y., Rakitin, A.L., Gumerov, V.M., Beletsky, A.V., Sinninghe Damsté, J.S., Mardanov, A.V., and Ravin, N.V., 2016. Phenotypic and genomic properties of Chitinispirillum alkaliphilum gen. nov., sp.

nov., a haloalkaliphilic anaerobic chitinolytic bacterium representing a novel class in the phylum Fibrobacteres. *Frontiers in Microbiology, 7*: 407.

Sparkes, G.W., Dunning, G.R., and Langille, A., 2017. The Michelin deposit: an example of albitite-hosted uranium mineralization within the Central Mineral Belt of Labrador. Newfoundland and Labrador Department of Natural Resources Geological Survey, Report 17-1: 219-238.

Speer, B.R., 1997. Photosynthetic pigments. Accessed October 2015. URL: http://www.ucmp.berkeley.edu/glossary/gloss3/pigments.html [cited October 2015].

Stackebrandt, E., Sproer, C., Rainey, F. A., Burghardt, J., Päuker, O., and Hippe, H., 1997. Phylogenetic analysis of the genus Desulfotomaculum: evidence for the misclassification of Desulfotomaculum guttoideum and description of Desulfotomaculum orientis as Desulfosporosinus orientis gen. nov., comb. nov. *International Journal of Systematic and Evolutionary Microbiology, 47*(4): 1134-1139.

Stanek, W., 1973. Comparisons of methods of pH determination for organic terrain surveys. *Canadian Journal of Soil Science, 53*(2): 177-183.

Stookey, L.L., 1970. Ferrozine---a new spectrophotometric reagent for iron. *Analytical Chemistry, 42*(7): 779-781.

Suyama, T., Shigematsu, T., Takaichi, S., Nodasaka, Y., Fujikawa, S., Hosoya, H., Tokiwa, Y., Kanagawa, T., and Hanada, S., 1999. Roseateles depolymerans gen. nov., sp. nov., a new bacteriochlorophyll a-containing obligate aerobe belonging to the β-subclass of the Proteobacteria. *International Journal of Systematic and Evolutionary Microbiology*, *49*(2): 449-457.

Suzuki, Y., Kelly, S.D., Kemner, K.M., and Banfield, J.F., 2004. Enzymatic U (VI) reduction by Desulfosporosinus species. *Radiochimica acta, 92*(1): 11-16.

Tamura N., 2014. XMAS: A versatile tool for analyzing synchrotron X-ray microdiffraction data. In R. Barabash, and G. Ice (eds.) *Strain and Dislocation Gradients from Diffraction – Spatially-Resolved Local Structure and Defects* (pp. 125-155). Imperial College Press, London, UK.

Tang, G., Wu, W.M., Watson, D.B., Parker, J.C., Schadt, C.W., Shi, X., and Brooks, S.C., 2013. U (VI) bioreduction with emulsified vegetable oil as the electron donor–microcosm tests and model development. *Environmental science & Technology, 47*(7): 3209-3217.

Tang, Y., and Reeder, R.J., 2009. Enhanced uranium sorption on aluminum oxide pretreated with arsenate. Part I: Batch uptake behavior. *Environmental science & technology*, *43*(12), 4446-4451.

Taylor, S.R., 1964. Abundance of chemical elements in the continental crust: a new table. *Geochimica et Cosmochimica Acta, 28*(8): 1273-1285.

Taylor, S.R., and McLennan, S.M., 1985. *The continental crust: its composition and evolution.* Blackwell Scientific Pub., Oxford, UK.

Tessier, A., Campbell, P.G., and Bisson, M., 1979. Sequential extraction procedure for the speciation of particulate trace metals. *Analytical chemistry*, *51*(7): 844-851.

Thiruvenkatachari, R., Vigneswaran, S., and Naidu, R., 2008. Permeable reactive barrier for groundwater remediation. *Journal of Industrial and Engineering Chemistry, 14*(2): 145-156.

Tran, E.L., Teutsch, N., Klein-BenDavid, O., and Weisbrod, N., 2018. Uranium and Cesium sorption to bentonite colloids under carbonate-rich environments: Implications for radionuclide transport. *Science of the Total Environment, 643*: 260-269.

Tranvik, L., 1994. Effects of colloidal organic matter on the growth of bacteria and protists in lake water. *Limnology and oceanography*, *39*(6): 1276-1285.

Troyer, L.D., Stone, J.J., and Borch, T., 2014. Effect of biogeochemical redox processes on the fate and transport of As and U at an abandoned uranium mine site: an X-ray absorption spectroscopy study. *Environmental Chemistry*, *11*(1): 18-27.

Vail, J., 2013. Groundwater sampling. Operating procedure. U.S. Environmental Protection Agency Science and Ecosystem Support Division. Athens, Georgia. Accessed June 2017. URL: www.epa.gov/sites/production/files/2015-06/documents/Groundwater-Sampling.pdf

van Emden, B., Thornber, M.R., Graham, J., and Lincoln, F.J., 1997. The incorporation of actinides in monazite and xenotime from placer deposits in Western Australia. *The Canadian Mineralogist*, *35*(1): 95-104.

Van Nostrand, J.D., Wu, L., Wu, W.M., Huang, Z., Gentry, T.J., Deng, Y., Carley, J., Carroll, S., He, Z., Gu, B., and Luo, J., 2011. Dynamics of microbial community composition and function during in situ bioremediation of a uranium-contaminated aquifer. *Applied and Environmental Microbiology, 77*(11): 3860-3869.

Vandenhove, H., Vanhoudt, N., Duquène, L., Antunes, K., and Wannijn, J., 2014. Comparison of two sequential extraction procedures for uranium fractionation in contaminated soils. *Journal of environmental radioactivity*, *137*: 1-9.

VanEngelen, M.R., Szilagyi, R.K., Gerlach, R., Lee, B.D., Apel, W.A., and Peyton, B.M., 2010. Uranium exerts acute toxicity by binding to pyrroloquinoline quinone cofactor. *Environmental science & Technology*, *45*(3): 937-942.

Veeramani, H., Scheinost, A.C., Monsegue, N., Qafoku, N.P., Kukkadapu, R., Newville, M., Lanzirotti, A., Pruden, A., Murayama, M., and Hochella Jr, M.F., 2013. Abiotic reductive immobilization of U (VI) by biogenic mackinawite. *Environmental Science & Technology, 47*(5): 2361-2369.

Violante, A., Cozzolino, V., Perelomov, L., Caporale, A. G., and Pigna, M., 2010. Mobility and bioavailability of heavy metals and metalloids in soil environments. *Journal of soil science and plant nutrition, 10*(3): 268-292.

Viollier, E., Inglett, P. W., Hunter, K., Roychoudhury, A. N., and Van Cappellen, P., 2000. The ferrozine method revisited: fe (ii)/fe (iii) determination in natural waters. *Applied Geochemistry, 15*(6): 785-790.

von Gunten, H.R., Sturm, M., and Moser, R.N., 1997. 200-year record of metals in lake sediments and natural background concentrations. *Environmental Science & Technology, 31*(8):2193-2197.

von Gunten, K., Alam, M.S., Hubmann, M., Ok, Y.S., Konhauser, K.O., and Alessi, D.S., 2017. Modified sequential extraction for biochar and petroleum coke: Metal release potential and its environmental implications. *Bioresource technology*, *236*: 106-110.

von Gunten, K., Hamilton, S.M., Zhong, C., Nesbø, C., Li, J., Muehlenbachs, K., Konhauser, K.O., and Alessi, D.S., 2018. Electron donor-driven bacterial and archaeal community patterns along forest ring edges in Ontario, Canada. *Environmental microbiology reports*, *10*(6): 663-672.

Von Gunten, U., and Schneider, W., 1991. Primary products of the oxygenation of iron (II) at an oxic—anoxic boundary: Nucleation, aggregation, and aging. *Journal of Colloid and Interface Science*, *145*(1): 127-139.

Wang, Q., and Riley, T.V., 2015. Chapter 47 - Erysipelothrix rhusiopathiae, In Y. Tang., M. Sussman, D. Liu, I. Poxton, and J. Schwartzman (eds.) *Molecular Medical Microbiology* (Second Edition, pp. 859-872). Academic Press, Boston, MA, USA.

Wang, Y., Frutschi, M., Suvorova, E., Phrommavanh, V., Descostes, M., Osman, A.A., Geipel, G., and Bernier-Latmani, R., 2013. Mobile uranium (IV)-bearing colloids in a mining-impacted wetland. *Nature communications*, *4*: 2942.

Warner, J., and Rowson, J., 2007. Technical Report: *In-situ* Monitoring and Validation of a Uranium Mill Tailings Management Facility Design Using X-ray Absorption Near Edge Structure (XANES) Spectroscopy. *Synchrotron Radiation News*, *20*(3): 14-17.

Wartiainen, I., Hestnes, A.G., McDonald, I.R., and Svenning, M.M., 2006. Methylobacter tundripaludum sp. nov., a methane-oxidizing bacterium from arctic wetland soil on the Svalbard Islands, Norway (78 n). *International Journal of Systematic and Evolutionary Microbiology, 56*(1): 109-113.

Watson, D.B., Wu, W.M., Mehlhorn, T., Tang, G., Earles, J., Lowe, K., Gihring, T.M., Zhang, G., Phillips, J., Boyanov, M.I., and Spalding, B.P., 2013. In situ bioremediation of uranium with emulsified vegetable oil as the electron donor. *Environmental Science & Technology, 47*(12): 6440-6448.

Wersin, P., Hochella, M.F., Persson, P., Redden, G., Leckie, J.O., and Harris, D.W., 1994. Interaction between aqueous uranium (vi) and sulfide minerals: spectroscopic evidence for sorption and reduction. *Geochimica et Cosmochimica Acta, 58*(13): 2829-2843.

WFD (World Forecast Directory), 2019. Cluff Lake average monthly climate data & extremes. Accessed February 2019. URL: http://www.eldoradocountyweather.com/canada/climate2/Cluff%20Lake.html

WHO (World Health Organization), 2001. Depleted uranium - sources, exposure and health effects. Technical report, Department of Protection of the Human Environment

Wielinga, B., Bostick, B., Hansel, C.M., Rosenzweig, R.F., and Fendorf, S., 2000. Inhibition of bacterially promoted uranium reduction: Ferric (hydr) oxides as competitive electron acceptors. *Environmental science & Technology*, *34*(11): 2190-2195.

Wiessner, A., Müller, J.A., Kuschk, P., Kappelmeyer, U., Kästner, M., Liu, Y.J., and Stottmeister, U., 2014. Environmental pollution by wastewater from brown coal processing–a remediation case study in Germany. *Journal of Environmental Engineering and Landscape Management, 22*(1): 71-83.

Wilkinson, R.E. (ed.), 2000. *Plant-Environment Interactions* (Vol. 77). CRC Press, Griffin, GA, USA.

Williams, K.H., Bargar, J.R., Lloyd, J.R., and Lovley, D.R., 2013. Bioremediation of uranium-contaminated groundwater: a systems approach to subsurface biogeochemistry. *Current opinion in biotechnology, 24*(3): 489-497.

Williams, K.H., Long, P.E., Davis, J.A., Wilkins, M.J., N'Guessan, A.L., Steefel, C.I., Yang, L., Newcomer, D., Spane, F.A., Kerkhof, L.J., and McGuinness, L., 2011. Acetate availability and its influence on sustainable bioremediation of uranium-contaminated groundwater. *Geomicrobiology Journal, 28*(5-6): 519-539.

Wilmarth, W.R., Mills, J.T., Dukes, V.H., and Sullivan, R.C., 2006. Effects of In-Tank Precipitation of Sodium Aluminosilicate on Uranium Chemistry. *Separation science and Technology*, *41*(11): 2325-2340.

WNA (World Nuclear Association), 2018a. Geology of Uranium Deposits. Accessed February 2019. URL: http://www.world-nuclear.org/information-library/nuclear-fuel-cycle/uranium-resources/geology-of-uranium-deposits.aspx

WNA (World Nuclear Association), 2018b. World uranium mining production. Accessed February 2019. URL: http://www.world-nuclear.org/information-library/nuclear-fuel-cycle/mining-of-uranium/world-uranium-mining-production.aspx

Wright, M.T., Stollenwerk, K.G., and Belitz, K., 2014. Assessing the solubility controls on vanadium in groundwater, northeastern San Joaquin Valley, CA. *Applied Geochemistry, 48*: 41-52.

Xu, M., Wu, W.M., Wu, L., He, Z., Van Nostrand, J.D., Deng, Y., Luo, J., Carley, J., Ginder-Vogel, M., Gentry, T.J., and Gu, B., 2010. Responses of microbial community functional structures to pilot-scale uranium in situ bioremediation. *The ISME Journal, 4*(8): 1060-1070.

Yang, K., Miao, G., Wu, W., Lin, D., Pan, B., Wu, F., and Xing, B., 2015. Sorption of Cu 2+ on humic acids sequentially extracted from a sediment. *Chemosphere, 138*, 657-663.

Yilmaz, P., Parfrey, L.W., Yarza, P., Gerken, J., Pruesse, E., Quast, C., Schweer, T., Peplies, J., Ludwig, W., and Glöckner, F.O., 2013. The SILVA and “all-species living tree project (LTP)” taxonomic frameworks. *Nucleic acids research*, *42*(D1): D643-D648.

Yumoto, I., Hirota, K., & Nakajima, K. (2014). The genus Alkalibacterium, In W.H. Holzapfel, and B.J.B Wood (eds.), *Lactic Acid Bacteria: Biodiversity and Taxonomy* (pp. 147-156). John Wiley & Sons, Oxford, UK.

Zandvoort, M.H., Van Hullebusch, E.D., Fermoso, F.G., and Lens, P.N.L., 2006. Trace metals in anaerobic granular sludge reactors: bioavailability and dosing strategies. *Engineering in Life Sciences, 6*(3), 293-301.

Zhang Z., Schwartz S., Wagner L., and Miller W., 2000. A greedy algorithm for aligning DNA sequences. *Journal of Computational Biology, 7*(1-2): 203-214.

Zhang, K., Song, L., and Dong, X., 2010. Proteiniclasticum ruminis gen. nov., sp. nov., a strictly anaerobic proteolytic bacterium isolated from yak rumen. *International Journal of Systematic and Evolutionary Microbiology, 60*(9), 2221-2225.

Zhilina, T. N., Zavarzina, D. G., Kolganova, T. V., Lysenko, A. M., and Tourova, T. P., 2009. Alkaliphilus peptidofermentans sp. nov., a new alkaliphilic bacterial soda lake isolate capable of peptide fermentation and fe (iii) reduction. *Microbiology, 78*(4): 445-454.

Zul, D., Wanner, G., and Overmann, J., 2008. Massilia brevitalea sp. nov., a novel betaproteobacterium isolated from lysimeter soil. *International Journal of Systematic and Evolutionary Microbiology, 58*(5): 1245-1251.

APPENDIX A
SUPPLEMENTARY INFORMATION FOR CHAPTER 2

Tables

Table A.1 Setup of the 8800 ICP-MS Triple Quad system (Agilent). Selected masses in Q1 and Q2 (first and second mass separation step), gas injected into the reaction chamber (between Q1 and Q2) and detection limits. Argon was used as the carrier gas. External calibration was done with elemental mixes diluted in 2% HNO_3 and 0.5% HCl (R^2>0.99). Indium (500 ppb) was the internal standard. The samples were diluted 2 to 20 times with 2% HNO_3 and 0.5% HCl prior to analysis to adjust the matrix and to be in the external calibration range. At least 4 measurements (average instrumental precision: 4.7%) were performed for each sample or standard with 300 scans per measurement. Helium and hydrogen were introduced into the reaction chamber between Q1 and Q2 with a flow rate of 3 mL/min to knock out potential polyatomic interferences summarized by May and Wiedmeyer (1998). For arsenic, oxygen was introduced into the reaction chamber (10% O_2) and a mass shift of m/z *16 was applied in the second mass analyzer.*

Element	Masses Q1 → Q2	Reaction/collision gas	Detection limit ppb
Li	7 → 7	No gas	1
B	11 → 11	No gas	10
Na	23 → 23	No gas	50
Mg	24 → 24	No gas	50
Al	27 → 27	No gas	1
Si	28 → 28	No gas	50
P	31 → 31	He	50
K	39 → 39	He	50
Ca	40 → 40, 44 → 44	H_2, He	50
V	51 → 51	He	1
Cr	52 → 52	He	1
Mn	55 → 55	He	1
Fe	56 → 56	He	10
Co	59 → 59	He	1
Ni	60 → 60	He	1
Cu	63 → 63	He	1
Zn	66 → 66	No gas	1
As	75 → 91	O_2	1
Br	79 → 79	No gas, He	50
Sr	88 → 88	No gas	1
Mo	95 → 95	He	1
Cd	111 → 111	No gas	1
Ba	138 → 138	No gas	1
Pb	208 → 208	No gas	1
U	238 → 238	No gas	1

Table A.2 PHREEQC modeling results for U, As, and Ni at selected depths. Saturation indices (SI) shown for solid species. The electrical balance error is defined by: 100(Cat-\|An\|)/(Cat+\|An\|). Sulfate was entered as total S, nitrate as total N, and TIC as total C, allowing PHREEQC to calculate the redox speciation as a function of concentrations, ORP, and pH. For As and Ni values, which were below the detection limit of the ICP-MS/MS, AF4-ICP-MS (for Ni) and IC-ICP-MS (for As) results were used. Electron potential pe was calculated based on: pe ≈ 16.9(ORP), where ORP was entered in V (Merkel et al., 2005). Pressure was considered based on depth, and atmospheric exchange was not included to keep pe at the measured value.*

			D-pit					DJX-pit		
Element	Ox. state	Species	0.5 m	5 m	10 m	13 m	20 m	0.5 m	50 m	80 m
U	U(IV)	$U(OH)_5^-$	4.20E-14	2.60E-14	4.07E-14	5.37E-07	3.78E-07	4.48E-13	2.62E-15	9.82E-14
		$U(OH)_4$	1.08E-16	5.91E-16	1.31E-15	6.77E-09	2.77E-10	1.28E-15	3.85E-16	1.19E-14
	U(V)	UO_2^+	8.03E-12	7.50E-11	1.50E-10	6.29E-09	8.90E-14	7.20E-11	1.41E-09	2.20E-08
	U(VI)	$UO_2(CO_3)_2^{2-}$	4.18E-07	9.49E-08	6.35E-08	3.29E-10	9.99E-16	4.49E-07	8.97E-09	2.34E-08
		UO_2CO_3	6.84E-08	1.83E-07	2.02E-07	2.57E-10	3.04E-17	1.66E-07	1.03E-06	3.98E-06
		$UO_2(CO_3)_3^{4-}$	1.65E-08	1.73E-09	7.26E-10	1.71E-11	1.38E-15	1.40E-08	4.98E-12	1.36E-11
		UO_2OH^+	9.08E-10	1.04E-09	1.30E-09	1.10E-12	9.19E-20	4.76E-09	7.51E-08	6.37E-07
		UO_2^{2+}	9.94E-12	2.20E-10	3.97E-10	1.40E-13	6.91E-22	7.72E-11	1.40E-07	1.22E-06
		UO_2SO_4	1.87E-13	2.47E-12	4.60E-12	7.82E-16	2.72E-33	2.81E-11	5.63E-08	7.78E-07
		$UO_2H_3SiO_4^+$	6.24E-11	2.78E-10	3.68E-10	3.65E-13	2.31E-20	2.25E-10	2.38E-08	2.16E-07
		$UO_2(SO_4)_2^{2-}$	3.33E-16	4.14E-15	8.01E-15	7.41E-19	-	1.48E-12	6.34E-09	2.14E-07
	SI	U_3O_8	-3.67	-4.55	-4.31	-2.95	-16.04	-1.31	-2.78	0.64
		U_4O_9	-6.37	-4.12	-3.12	14.34	4.31	-2.40	-3.72	1.73
		UO_2	-2.70	-1.69	-1.34	5.37	3.98	-1.59	-1.88	-0.39
		$USiO_4$	-3.70	-2.37	-2.00	4.78	3.27	-2.79	-2.49	-0.97
As	As(III)	H_3AsO_3	1.25E-14	5.53E-11	2.90E-10	2.13E-07	9.94E-07	3.14E-14	4.39E-12	4.40E-11
		$H_2AsO_3^-$	1.10E-16	3.72E-14	1.37E-13	2.57E-10	2.07E-08	2.37E-16	4.60E-16	5.55E-15
	As(V)	$HAsO_4^{2-}$	1.02E-08	1.27E-08	1.31E-08	2.65E-14	1.26E-15	8.21E-09	4.09E-10	1.97E-09
		$H_2AsO_4^-$	3.12E-09	2.73E-08	4.00E-08	3.07E-14	8.43E-17	2.46E-09	4.92E-09	1.77E-08
Ni		$NiCO_3$	4.03E-08	2.14E-08	2.25E-08	5.94E-08	3.23E-08	9.07E-07	7.60E-08	5.00E-08
		Ni^{2+}	9.70E-09	4.29E-08	7.40E-08	5.41E-08	1.23E-09	6.93E-07	1.73E-05	2.56E-05
		$NiHCO_3^+$	1.01E-09	3.57E-09	5.30E-09	5.66E-09	1.83E-10	2.69E-08	9.76E-08	5.93E-08
		$NiSO_4$	7.60E-11	2.91E-10	5.19E-10	1.84E-10	2.91E-21	1.10E-07	4.16E-06	9.83E-06
		$NiCl^+$	1.10E-12	5.64E-12	9.54E-12	1.08E-11	3.86E-13	1.34E-10	5.39E-09	2.61E-08
Electrical balance error			5.2%	4.9%	14.0%	25.5%	18.7%	5.1%	8.0%	6.5%

Table A.3 D-pit total inorganic and organic carbon, nitrogen, and concentrations of major anions. GW1: groundwater sample (DWW0041G). 'n.d.': not detected. No phosphate was detected in any of the samples (not shown). September 2015 sampling results can be found in Table A.9.

Depth	TIC ppm	TOC ppm	TN ppm	Cl^- ppm	NO_3^--N ppm	SO_4^{2-}-S ppm
0.5 m	13.59	7.03	n.d.	1.94	n.d.	1.78
1 m	13.66	6.42	n.d.	1.84	n.d.	1.76
2 m	14.02	6.19	n.d.	1.92	n.d.	1.83
3 m	17.34	5.02	n.d.	2.22	n.d.	1.49
4 m	18.85	5.4	0.012	2.23	0.19	1.79
5 m	18.38	7.15	0.12	2.29	0.21	1.84
6 m	19.6	4.09	0.078	2.24	0.24	1.83
7 m	19.98	5.2	0.071	2.22	0.24	1.82
8 m	20.18	5.16	0.149	2.23	0.24	1.82
9 m	21.15	5.18	0.14	2.27	0.25	1.85
10 m	20.27	5.5	0.161	2.25	0.25	1.84
11 m	21.93	5.33	0.148	2.29	n.d.	2.03
12 m	24.06	5.41	0.258	2.39	n.d.	2.02
13 m	28.29	8.6	0.719	3.69	n.d.	1.03
14 m	32.48	11.69	1.087	4.47	n.d.	n.d.
15 m	31.84	13.03	1.463	5.34	n.d.	n.d.
16 m	30.07	11.89	1.558	5.75	n.d.	n.d.
17 m	33.89	12.85	1.687	5.91	n.d.	n.d.
18 m	33.4	12.26	1.553	5.53	n.d.	n.d.
19 m	32.27	11.45	1.76	6.12	n.d.	n.d.
20 m	31.1	9.78	1.619	6.01	n.d.	n.d.
21 m	33.57	12.88	1.757	6.25	n.d.	n.d.
22 m	34.73	11.05	1.851	6.42	n.d.	n.d.
23 m	35.14	10.73	1.828	6.42	n.d.	n.d.
GW1	16.61	5.32	n.d.	2.27	n.d.	1.67

Table A.4 D-pit metal concentrations. GW1: groundwater sample (DWW0041G). Elements with values <5 ppb throughout the column are not shown. They include: V, Cr, Cu, Cd, Pb. Samples were diluted 1-2x prior to analysis.

Depth	Li	B	Na	Mg	Al	Si	K	Ca	Mn	Fe	Co	Ni	Zn	As	Br	Sr	Mo	Ba	U
	ppm	ppm	ppm	ppm	ppm	ppm	ppm	ppm	ppm	ppm	ppm	ppm	ppm	ppm	ppm	ppm	ppm	ppm	ppm
0.5 m	0.005	0.047	2.257	7.283	0.060	3.087	1.784	10.951	0.160	0.794	<0.002	0.003	<0.002	<0.002	0.020	0.064	<0.002	0.004	0.120
1 m	0.006	0.048	2.227	7.208	0.060	3.086	1.797	10.767	0.170	0.813	<0.002	0.003	<0.002	0.002	0.017	0.063	<0.002	0.004	0.100
2 m	0.005	0.047	2.237	7.145	0.087	3.174	1.744	10.408	0.210	0.917	<0.002	0.004	0.005	0.004	0.016	0.062	<0.002	0.004	0.095
3 m	0.005	0.046	2.435	8.174	0.068	3.703	1.793	11.888	0.507	1.190	<0.002	0.004	0.003	0.003	0.019	0.070	<0.002	0.006	0.075
4 m	0.005	0.050	2.624	8.687	0.066	4.004	1.881	12.733	0.588	1.676	<0.002	0.004	0.003	0.002	0.018	0.074	<0.002	0.006	0.069
5 m	0.005	0.053	2.710	8.886	0.065	4.143	1.907	12.715	0.644	2.123	<0.002	0.004	0.002	0.003	0.021	0.076	<0.002	0.006	0.067
6 m	0.005	0.052	2.724	8.867	0.059	4.186	1.930	12.686	0.750	3.088	<0.002	0.004	0.003	0.004	0.019	0.076	<0.002	0.007	0.066
7 m	0.005	0.053	2.731	8.842	0.065	4.183	1.907	12.914	0.832	3.367	<0.002	0.004	<0.002	0.003	0.020	0.076	<0.002	0.008	0.064
8 m	0.005	0.054	2.776	8.937	0.066	4.245	1.960	12.876	0.944	3.607	<0.002	0.004	<0.002	0.003	0.020	0.077	<0.002	0.008	0.066
9 m	0.004	0.055	2.793	8.954	0.065	4.260	1.944	12.896	1.043	3.623	<0.002	0.004	<0.002	0.003	0.019	0.077	<0.002	0.009	0.065
10 m	0.004	0.056	2.877	9.024	0.073	4.281	1.968	13.187	1.331	3.311	0.003	0.006	<0.002	0.004	0.018	0.078	<0.002	0.010	0.064
11 m	0.004	0.061	2.983	9.154	0.069	4.290	1.969	13.358	1.937	2.196	0.006	0.007	0.005	0.002	0.020	0.080	0.002	0.012	0.064
12 m	0.004	0.072	3.372	9.711	0.066	4.758	2.115	13.788	2.869	15.805	0.009	0.009	0.005	0.005	0.039	0.093	0.003	0.020	0.096
13 m	0.005	0.090	4.324	10.266	0.067	5.030	2.461	14.149	3.184	36.414	0.006	0.007	0.003	0.016	0.051	0.130	0.015	0.030	0.131
14 m	0.006	0.098	4.741	10.464	0.058	4.971	2.531	15.008	3.230	41.824	0.004	0.005	<0.002	0.024	0.051	0.145	0.019	0.037	0.121
15 m	0.006	0.111	5.390	10.842	0.058	4.520	2.665	16.056	3.290	46.444	0.003	<0.002	0.004	0.049	0.062	0.162	0.025	0.053	0.102
16 m	0.006	0.114	5.580	10.612	0.063	4.068	2.681	16.391	3.266	49.201	0.003	<0.002	<0.002	0.069	0.064	0.164	0.027	0.059	0.091
17 m	0.006	0.122	5.965	11.000	0.057	3.981	2.688	17.316	3.282	50.143	0.002	<0.002	0.012	0.075	0.069	0.171	0.028	0.065	0.091
18 m	0.005	0.123	6.085	11.186	0.068	3.929	2.703	17.635	3.273	50.054	0.003	<0.002	0.003	0.082	0.070	0.175	0.029	0.068	0.090
19 m	0.005	0.124	6.042	11.036	0.062	3.857	2.671	18.048	3.245	47.859	0.002	<0.002	0.005	0.085	0.070	0.172	0.029	0.065	0.089
20 m	0.005	0.125	6.046	11.088	0.066	3.887	2.656	18.002	3.226	47.702	0.003	<0.002	<0.002	0.076	0.071	0.171	0.028	0.065	0.090
21 m	0.004	0.127	6.126	11.063	0.056	3.826	2.644	18.459	3.231	52.700	0.002	<0.002	0.005	0.080	0.072	0.172	0.030	0.067	0.092
22 m	0.004	0.132	6.319	11.126	0.048	3.631	2.648	18.760	3.242	54.273	0.002	<0.002	<0.002	0.095	0.073	0.175	0.030	0.071	0.090
23 m	0.004	0.132	6.324	11.160	0.065	3.658	2.629	18.363	3.243	54.665	0.002	<0.002	<0.002	0.091	0.073	0.174	0.031	0.071	0.090
GW1	0.004	0.049	2.248	7.210	0.069	3.564	1.938	11.390	0.195	0.463	<0.002	0.003	<0.002	0.002	0.010	0.062	-	0.008	0.061

Table A.5 DJX-pit total inorganic and organic carbon, nitrogen, and concentrations of major anions. GW2: groundwater sample 1 (MNW6210G). GW3: groundwater sample 2 (HYD9846AG). 'n.d.': not detected. 'n.m.': not measured. No phosphate was detected in any of the samples (not shown). September 2015 sampling results can be found in Table A.9.

Depth	TIC ppm	TOC ppm	TN ppm	Cl^- ppm	NO_3^--N ppm	SO_4^{2-}-S ppm
0.5 m	6.522	4.638	n.d.	4.01	n.d.	70.10
2 m	6.481	4.509	n.d.	3.84	n.d.	69.70
4 m	6.259	4.671	n.d.	3.88	n.d.	71.80
6 m	7.175	5.035	n.d.	4.21	n.d.	75.90
8 m	7.716	4.064	n.d.	4.66	n.d.	79.80
10 m	7.706	4.524	n.d.	4.42	n.d.	78.00
12 m	7.837	4.463	n.d.	4.47	n.d.	78.00
14 m	7.819	4.601	n.d.	4.57	n.d.	79.20
16 m	7.832	4.408	n.d.	4.46	n.d.	78.40
18 m	7.809	3.641	0.06	6.50	0.31	140.3
20 m	7.748	3.202	0.018	6.72	0.34	154.7
22 m	8.076	3.414	0.041	6.63	0.33	159.6
24 m	7.958	3.282	0.062	6.68	0.34	159.8
26 m	8.302	3.528	0.079	6.72	0.36	164.2
28 m	4.949	3.079	0.079	6.69	0.35	163.5
30 m	7.04	2.96	0.111	6.74	0.34	166.4
32 m	8.38	3.42	0.108	6.75	0.35	168.7
34 m	8.213	3.647	0.092	6.76	0.34	167.4
36 m	8.115	3.655	0.111	6.87	0.34	169.6
38 m	6.586	3.323	0.107	6.93	0.35	170.5
40 m	7.282	3.078	0.087	6.87	0.33	170.3
42 m	7.195	3.295	0.076	6.91	0.34	172.7
44 m	7.246	3.324	0.115	6.88	0.33	171.3
46 m	8.166	3.624	0.115	7.00	0.37	172.2
48 m	6.241	3.5	0.132	7.19	0.42	172.4
50 m	7.544	3.486	0.102	7.50	0.38	175.7
55 m	8.97	3.26	0.163	8.33	0.40	140.6
60 m	10.22	3.59	0.687	18.37	0.85	236.0
65 m	8.825	3.845	0.876	19.25	0.98	265.0
70 m	1.501	3.865	2.289	28.47	1.91	474.8
75 m	4.196	4.215	2.166	29.80	1.76	479.2
80 m	3.319	4.293	2.043	30.41	1.56	474.70
82 m	3.794	4.129	3.794	30.87	1.55	475.80
GW2	-	-	-	81.2	n.d.	291.3
GW3	-	-	-	6.6	n.d.	11.6

Table A.6 iCAP Q ICP-MS results for D-pit (As, V) and DJX-pit (As, V, Cd, Pb, Sb, Tl, Se). 'LOD': limit of detection. Vanadium shows an increasing trend with depth, indicating that anaerobic conditions were favoring higher V concentrations, probably by the formation of more soluble V(III) complexes with Cl (Wright et al., 2014).

Pit	Depth	^{78}Se ppb	^{75}As ppb	^{51}V ppb	^{111}Cd ppb	^{207}Pb ppb	^{121}Sb ppb	^{205}Tl ppb
D-pit	0.5	<LOD	1.58	0.35	<LOD	<LOD	<LOD	<LOD
D-pit	5	<LOD	2.45	0.59	<LOD	<LOD	<LOD	<LOD
D-pit	10	<LOD	3.56	0.73	<LOD	<LOD	<LOD	<LOD
D-pit	13	<LOD	16.52	4.23	<LOD	<LOD	<LOD	<LOD
D-pit	15	<LOD	46.83	4.40	<LOD	<LOD	<LOD	<LOD
D-pit	18	<LOD	75.38	3.71	<LOD	<LOD	<LOD	<LOD
D-pit	20	<LOD	69.87	3.52	<LOD	<LOD	<LOD	<LOD
D-pit	23	<LOD	85.43	3.77	<LOD	<LOD	<LOD	<LOD
DJX-pit	0.5	0.29	0.96	0.07	0.02	0.03	0.04	0.03
DJX-pit	10	0.31	0.92	0.07	0.05	0.05	0.04	0.02
DJX-pit	30	1.36	0.42	0.07	0.17	0.06	0.05	0.06
DJX-pit	50	1.42	0.44	0.06	0.18	0.03	0.06	0.08
DJX-pit	60	1.97	0.62	0.06	0.28	0.07	0.11	0.14
DJX-pit	70	6.39	1.53	0.07	0.58	0.02	0.17	0.25
DJX-pit	80	5.91	1.48	0.07	0.59	0.02	0.17	0.27

Table A.7 DJX-pit metal concentrations. GW2: groundwater sample 1 (MNW6210G). GW3: groundwater sample 2 (HYD9846AG). Elements with values <5 ppb throughout the column are not shown. They include: V, Cr, As, Cd, Pb. Samples were diluted 1-2x prior to analysis.

Depth	Li	B	Na	Mg	Al	Si	K	Ca	Mn	Fe	Co	Ni	Cu	Zn	Br	Sr	Mo	Ba	U
	ppm	ppm	ppm	ppm	ppm	ppm	ppm	ppm	ppm	ppm	ppm	ppm	ppm	ppm	ppm	ppm	ppm	ppm	ppm
0.5 m	0.028	0.226	10.266	30.592	0.073	1.843	2.627	47.712	0.004	0.009	<0.002	0.102	<0.002	0.003	0.023	0.301	0.018	0.008	0.151
2 m	0.029	0.231	10.524	30.435	0.077	1.839	2.659	47.554	<0.002	0.008	<0.002	0.102	<0.002	<0.002	0.020	0.296	0.017	0.008	0.132
4 m	0.028	0.236	10.236	31.017	0.074	1.870	2.683	47.227	<0.002	0.008	<0.002	0.105	0.002	<0.002	0.019	0.301	0.019	0.008	0.127
6 m	0.029	0.234	10.092	30.415	0.082	1.886	2.665	46.901	<0.002	0.009	<0.002	0.104	<0.002	0.009	0.017	0.300	0.018	0.008	0.129
8 m	0.031	0.265	11.472	34.034	0.068	1.945	2.951	52.948	<0.002	0.013	<0.002	0.122	0.002	<0.002	0.023	0.336	0.021	0.009	0.140
10 m	0.031	0.270	11.395	33.905	0.076	2.200	2.975	52.128	<0.002	0.012	<0.002	0.124	<0.002	<0.002	0.023	0.337	0.021	0.009	0.136
12 m	0.031	0.270	11.474	34.209	0.110	2.133	2.983	52.954	0.007	0.017	<0.002	0.129	0.002	<0.002	0.024	0.339	0.021	0.009	0.138
14 m	0.031	0.268	11.443	34.262	0.059	2.144	2.991	53.200	0.031	0.017	<0.002	0.148	0.003	0.073	0.023	0.339	0.020	0.009	0.135
16 m	0.031	0.266	11.312	34.240	0.074	2.237	2.981	53.109	0.061	0.022	0.004	0.133	0.003	0.032	0.021	0.341	0.020	0.009	0.132
18 m	0.031	0.269	11.623	35.651	0.096	2.336	2.964	53.931	0.109	0.028	0.008	0.148	0.003	<0.002	0.021	0.347	0.020	0.009	0.127
20 m	0.070	0.489	20.381	64.698	0.166	4.733	3.343	89.080	1.924	<0.002	0.243	1.242	0.006	0.121	0.043	0.649	0.016	0.009	0.204
22 m	0.074	0.524	21.529	67.854	0.256	4.863	3.391	93.687	2.006	0.003	0.258	1.285	0.009	0.137	0.043	0.682	0.017	0.008	0.257
24 m	0.074	0.523	21.398	68.226	0.227	4.843	3.364	91.533	1.982	<0.002	0.255	1.277	0.009	0.124	0.044	0.677	0.016	0.008	0.256
26 m	0.074	0.550	21.985	69.508	0.263	5.010	3.383	96.439	2.033	0.003	0.261	1.287	0.009	0.147	0.043	0.704	0.015	0.008	0.275
28 m	0.074	0.548	22.286	70.005	0.263	4.913	3.427	95.485	2.061	<0.002	0.262	1.294	0.010	0.156	0.043	0.699	0.015	0.008	0.266
30 m	0.073	0.559	22.399	70.516	0.264	4.959	3.452	97.560	2.076	0.003	0.264	1.297	0.010	0.127	0.045	0.705	0.015	0.008	0.277
32 m	0.075	0.582	22.873	71.706	0.292	5.025	3.541	101.243	2.137	0.003	0.270	1.307	0.011	0.128	0.048	0.726	0.014	0.008	0.279
34 m	0.074	0.576	22.691	71.709	0.291	4.988	3.434	99.463	2.081	<0.002	0.264	1.275	0.010	0.131	0.046	0.718	0.013	0.008	0.280
36 m	0.075	0.590	22.838	71.996	0.320	5.044	3.446	100.083	2.103	<0.002	0.265	1.286	0.010	0.146	0.046	0.733	0.013	0.008	0.281
38 m	0.075	0.594	22.917	71.514	0.304	5.047	3.453	102.644	2.104	<0.002	0.265	1.287	0.010	0.133	0.045	0.736	0.014	0.008	0.282
40 m	0.074	0.588	23.028	72.631	0.302	4.994	3.471	102.776	2.122	<0.002	0.266	1.293	0.011	0.130	0.047	0.728	0.014	0.008	0.282
42 m	0.075	0.594	23.202	72.769	0.300	5.026	3.449	104.844	2.119	<0.002	0.265	1.283	0.010	0.129	0.047	0.735	0.014	0.008	0.288
44 m	0.075	0.598	23.246	72.903	0.299	4.997	3.463	103.703	2.102	<0.002	0.265	1.270	0.010	0.134	0.047	0.737	0.013	0.008	0.283
46 m	0.076	0.607	23.493	72.499	0.330	5.012	3.469	104.142	2.129	0.018	0.267	1.275	0.012	0.136	0.048	0.750	0.015	0.011	0.302
48 m	0.073	0.612	23.993	72.865	0.295	5.046	3.505	104.180	2.135	<0.002	0.266	1.278	0.010	0.131	0.048	0.753	0.017	0.008	0.307
50 m	0.073	0.630	25.122	73.967	0.306	4.986	3.542	107.352	2.203	<0.002	0.266	1.267	0.010	0.352	0.052	0.771	0.018	0.008	0.319
55 m	0.071	0.688	28.762	76.036	0.256	5.006	3.776	113.494	2.229	<0.002	0.261	1.230	0.009	0.144	0.062	0.836	0.025	0.009	0.371
60 m	0.062	0.842	55.978	86.994	0.156	4.850	5.253	146.135	2.245	<0.002	0.262	1.258	0.009	0.254	0.162	1.197	0.060	0.011	0.571
65 m	0.062	0.870	59.039	88.470	0.150	4.861	5.421	147.933	2.282	0.003	0.259	1.257	0.010	0.267	0.171	1.233	0.065	0.011	0.594
70 m	0.081	1.486	120.950	152.140	0.401	5.258	10.252	283.070	3.896	0.007	0.422	2.193	0.025	0.676	0.269	2.426	0.116	0.017	1.623
75 m	0.082	1.535	124.860	155.780	0.419	5.282	10.198	284.176	3.896	0.005	0.419	2.165	0.025	0.687	0.270	2.482	0.126	0.017	1.708
80 m	0.079	1.603	128.501	155.708	0.376	5.242	10.488	289.883	4.240	0.005	0.424	2.090	0.021	0.626	0.294	2.552	0.120	0.016	1.744
82 m	0.079	1.618	129.586	155.623	0.355	5.203	10.227	290.857	4.257	0.005	0.415	1.992	0.019	0.563	0.299	2.563	0.119	0.016	1.674
GW2	0.090	1.233	125.854	49.501	0.133	0.114	12.470	155.396	0.193	0.273	<0.002	<0.002	<0.002	<0.002	0.870	1.726	-	0.027	<0.002
GW3	0.013	1.024	22.033	7.495	<0.002	3.486	1.755	16.080	0.024	<0.002	<0.002	<0.002	<0.002	<0.002	0.070	0.207	-	0.008	<0.002

Table A.8 ICP-MS/MS results for filtered water samples from the D-pit and DJX-pit at different depths collected in September 2015. Values with a '<' sign indicate that the value detected (dilution factors 1-10x) was lower than the lowest external calibration standard.

Element	D-0 m ppb	D-5 m ppb	D-10 m ppb	D-15 m ppb	DJX-0 m ppb	DJX-20 m ppb	DJX-70 m ppb
Li	<1.0	<1.0	<1.0	<1.0	21.5	23.9	54.0
B	17.9	32.6	45.4	88.2	184.1	204.6	1378.7
Na	2628.0	3094.9	3424.9	5572.5	11472.0	12376.6	120206.2
Mg	8836.7	10153.2	10788.6	11826.7	31488.8	34542.0	152704.9
Al	7.6	7.7	4.9	<1.0	8.1	3.4	339.3
Si	3676.4	4439.3	4738.6	4480.7	1691.6	2496.3	4755.5
K	1809.8	1964.3	2011.4	2608.7	2556.3	2266.7	5532.3
Ca	11018.5	12695.8	13565.0	15495.2	24823.7	24392.9	171325.3
Cr	<1.0	<1.0	<1.0	<1.0	<1.0	<1.0	<1.0
Mn	73.8	574.3	2612.9	2688.7	3.3	46.1	3566.9
Fe	4561.3	4986.1	7486.2	32801.2	3938.8	4257.8	4563.3
Ni	<12.1	<12.1	<12.1	<12.1	60.7	101.9	1524.9
Cu	<12.1	<12.1	<12.1	<12.1	<12.1	<12.1	13.1
Zn	4.5	4.5	10.6	<1.0	4.5	14.7	929.1
As	3.8	2.3	3.9	77.7	1.4	1.6	<1.0
Br	<49.4	<49.4	<49.4	78.1	<49.4	<49.4	189.9
Sr	63.7	75.4	81.3	152.2	294.5	334.0	2403.2
Ba	<5.5	8.1	20.8	56.3	7.5	9.1	13.6
Pb	<12.1	<12.1	<12.1	<12.1	<12.1	<12.1	<12.1
U	41.0	49.7	43.9	62.0	102.9	108.1	1600.6

Table A.9: TOC, TN and selected anion concentrations in the water samples from D-pit and DJX-pit at different depths collected in September 2015.'n.d.': not detected. '-': not measured.

Location	Treatment	Depth m	TOC ppm	TN ppm	TOC/TN	TIC ppm	Cl^- ppm	NO_3^--N ppm	PO_4^{3-}-P ppm	SO_4^{2-}-S ppm
D-Pit	0.2 µm	0	6.7	0.5	13	86.2	4.1	n.d.	n.d.	2.1
D-Pit	0.2 µm	5	6.3	0.7	8	90.5	3.7	n.d.	n.d.	2.4
D-Pit	0.2 µm	10	6.0	0.7	8	109.	4.5	n.d.	n.d.	2.6
D-Pit	0.2 µm	15	7.7	1.9	4	137.	6.7	n.d.	n.d.	0.7
D-Pit	Unfiltered	0	8.00	0.1	67	-	-	-	-	-
D-Pit	Unfiltered	5	8.6	0.3	25	-	-	-	-	-
D-Pit	Unfiltered	10	9.4	0.3	26	-	-	-	-	-
D-Pit	Unfiltered	15	12.	1.2	10	-	-	-	-	-
DJX-Pit	0.2 µm	0	4.4	0.4	10	51.0	6.2	n.d.	n.d.	73.8
DJX-Pit	0.2 µm	20	4.5	0.6	7	51.5	7.1	n.d.	n.d.	79.0
DJX-Pit	0.2 µm	70	3.4	2.6	1	16.9	32.7	4.7	n.d.	550.2
DJX-Pit	Unfiltered	0	6.1	0.0	187	-	-	-	-	-
DJX-Pit	Unfiltered	20	6.4	0.3	22	-	-	-	-	-
DJX-Pit	Unfiltered	70	4.2	2.4	2	-	-	-	-	-

Table A.10 Fractionation of selected metals in the D-pit surface and groundwater near D-pit (GW1). 'DOM': metals associated with dissolved organic matter. 'Oxyhyd': metals associated with oxyhydroxides.

Sample	Element	Total ppb	Free	DOM	Oxyhyd	Sample	Element	Total ppb	Free	DOM	Oxyhyd
	7Li	0.832	100%	0%	0%		7Li	0.547	100%	0%	0%
	24Mg	13745	100%	0%	0%		24Mg	11644	100%	0%	0%
	27Al	15.1	37%	38%	25%		27Al	6.64	40%	34%	26%
	51V	0.414	91%	2%	7%		51V	0.394	61%	7%	32%
	55Mn	529	100%	0%	0%		55Mn	1079	98%	1%	1%
	56Fe	928	86%	1%	13%		56Fe	2449	67%	1%	32%
	59Co	1.29	96%	2%	2%		59Co	1.56	92%	3%	5%
	60Ni	2.62	79%	21%	0%		60Ni	3.61	77%	23%	0%
Dpit GW	63Cu	1.48	74%	23%	3%	D pit 10 m	63Cu	0.311	27%	61%	11%
	66Zn	2.02	93%	7%	0%		66Zn	2.54	97%	3%	0%
	75As	1.20	88%	4%	9%		75As	2.58	55%	3%	42%
	88Sr	61.7	100%	0%	0%		88Sr	61.6	99%	1%	0%
	95Mo	1.22	100%	0%	0%		95Mo	0.914	100%	0%	0%
	137Ba	8.748	95%	3%	3%		137Ba	10.4	91%	5%	4%
	208Pb	0.076	59%	3%	39%		208Pb	0.070	15%	5%	80%
	232Th	0.058	47%	17%	35%		232Th	0.028	0%	13%	87%
	238U	18.4	94%	4%	3%		238U	28.1	85%	3%	12%
	7Li	0.322	100%	0%	0%		7Li	0.134	100%	0%	0%
	24Mg	4605	100%	0%	0%		24Mg	2168	100%	0%	0%
	27Al	3.75	0%	67%	33%		27Al	1.17	48%	52%	0%
	51V	0.086	77%	23%	0%		51V	0.319	100%	0%	0%
	55Mn	65.5	95%	2%	2%		55Mn	450	94%	3%	3%
	56Fe	333	83%	1%	16%		56Fe	5296	98%	1%	1%
	59Co	0.070	68%	24%	8%		59Co	0.291	93%	3%	4%
	60Ni	2.23	66%	34%	0%		60Ni	0.330	75%	25%	0%
D pit 0.5 m	63Cu	0.314	17%	74%	9%	Dpit 15m	63Cu	0.032	25%	75%	0%
	66Zn	1.48	100%	0%	0%		66Zn	0.685	87%	13%	0%
	75As	1.00	78%	10%	12%		75As	4.99	98%	1%	2%
	88Sr	36.7	99%	1%	0%		88Sr	16.9	99%	1%	0%
	95Mo	1.91	100%	0%	0%		95Mo	2.57	100%	0%	0%
	137Ba	3.13	86%	7%	7%		137Ba	6.15	87%	7%	7%
	208Pb	0.026	15%	14%	71%		208Pb	0.004	65%	35%	0%
	232Th	0.010	0%	14%	86%		232Th	0.007	75%	9%	16%
	238U	5.74	98%	2%	0%		238U	8.42	91%	8%	2%
	7Li	0.492	100%	0%	0%		7Li	0.140	100%	0%	0%
	24Mg	11027	100%	0%	0%		24Mg	2050	100%	0%	0%
	27Al	3.27	0%	67%	33%		27Al	0.724	65%	20%	15%
	51V	0.275	52%	11%	37%		51V	0.246	98%	2%	0%
	55Mn	520	97%	1%	1%		55Mn	435	93%	3%	3%
	56Fe	1558	68%	1%	31%		56Fe	5004	99%	0%	0%
	59Co	0.442	87%	9%	3%		59Co	0.199	92%	3%	5%
	60Ni	2.65	72%	28%	0%		60Ni	0.181	0%	100%	0%
D pit 5 m	63Cu	0.271	12%	74%	14%	Dpit 20m	63Cu	0.022	0%	100%	0%
	66Zn	1.66	92%	8%	0%		66Zn	0.262	48%	52%	0%
	75As	1.87	68%	3%	29%		75As	6.88	99%	1%	0%
	88Sr	59.0	100%	0%	0%		88Sr	19.6	99%	1%	0%
	95Mo	0.890	100%	0%	0%		95Mo	2.87	100%	0%	0%
	137Ba	6.14	93%	4%	4%		137Ba	7.03	84%	8%	8%
	208Pb	0.040	25%	5%	70%		208Pb	0.007	86%	14%	0%
	232Th	0.029	0%	12%	88%		232Th	0.005	88%	7%	4%
	238U	31.1	90%	3%	7%		238U	6.18	92%	8%	0%

Table A.11 Fractionation of selected metals in the DJX-pit surface water. 'DOM': metals associated with dissolved organic matter. 'Oxyhyd': metals associated with oxyhydroxides. 'LOD': limit of detection.

Sample	Element	Total ppb	Free	DOM	Oxyhyd
DJX 0.5 m	7Li	14.64	100%	0%	0%
	24Mg	8582	100%	0%	0%
	27Al	8.99	41%	59%	0%
	51V	0.05	90%	10%	0%
	55Mn	0.94	98%	2%	0%
	56Fe	7.32	80%	3%	17%
	59Co	0.27	67%	9%	24%
	60Ni	57.14	60%	6%	34%
	63Cu	0.45	18%	65%	17%
	66Zn	2.88	84%	16%	0%
	75As	0.80	88%	3%	9%
	88Sr	285.07	100%	0%	0%
	95Mo	13.97	100%	0%	0%
	137Ba	6.94	88%	8%	4%
	208Pb	0.007	0%	25%	75%
	232Th	0.000	0%	20%	80%
	238U	101.92	98%	1%	0%
DJX 10 m	7Li	15.52	100%	0%	0%
	24Mg	26429	100%	0%	0%
	27Al	2.74	62%	15%	23%
	51V	0.03	100%	0%	0%
	55Mn	5.72	98%	1%	1%
	56Fe	5.96	72%	4%	25%
	59Co	0.27	95%	2%	3%
	60Ni	67.95	89%	2%	9%
	63Cu	0.86	61%	29%	10%
	66Zn	3.93	90%	10%	0%
	75As	0.74	96%	4%	0%
	88Sr	321.52	100%	0%	0%
	95Mo	15.82	100%	0%	0%
	137Ba	7.97	92%	4%	4%
	208Pb	0.006	100%	0%	0%
	232Th	0.001	67%	33%	0%
	238U	108.41	100%	0%	0%
DJX 30 m	7Li	59.13	100%	0%	0%
	24Mg	109196	100%	0%	0%
	27Al	103.89	98%	1%	2%
	51V	<LOD	100%	0%	0%
	55Mn	2336.24	100%	0%	0%
	56Fe	1.24	98%	2%	0%
	59Co	259.94	100%	0%	0%
	60Ni	1222.87	99%	1%	0%
	63Cu	5.53	98%	2%	0%
	66Zn	96.24	95%	2%	3%
	75As	0.43	99%	1%	0%
	88Sr	846.93	100%	0%	0%
	89Y	8.47	100%	0%	0%
	95Mo	14.06	100%	0%	0%
	137Ba	8.34	100%	0%	0%
	208Pb	0.026	92%	8%	0%
	232Th	0.011	99%	1%	0%
	238U	275.94	83%	0%	17%

Sample	Element	Total ppb	Free	DOM	Oxyhyd
DJX 50 m	7Li	59.41	100%	0%	0%
	24Mg	119105	100%	0%	0%
	27Al	88.44	98%	1%	1%
	51V	<LOD	0%	0%	0%
	55Mn	2694.73	100%	0%	0%
	56Fe	2.11	100%	0%	0%
	59Co	284.33	100%	0%	0%
	60Ni	1269.56	99%	1%	0%
	63Cu	5.56	98%	2%	0%
	66Zn	105.20	95%	2%	3%
	75As	0.45	95%	5%	0%
	88Sr	943	100%	0%	0%
	89Y	8.60	100%	0%	0%
	95Mo	18.37	99%	1%	0%
	137Ba	8.62	100%	0%	0%
	208Pb	0.008	76%	24%	0%
	232Th	0.002	86%	14%	0%
	238U	313.42	84%	0%	16%
DJX 80 m	7Li	64.07	100%	0%	0%
	24Mg	274156	100%	0%	0%
	27Al	177.25	98%	0%	1%
	51V	<LOD	0%	0%	0%
	55Mn	6261.20	100%	0%	0%
	56Fe	3.35	100%	0%	0%
	59Co	460.35	100%	0%	0%
	60Ni	2042.41	99%	0%	0%
	63Cu	11.68	99%	1%	0%
	66Zn	342.13	97%	1%	2%
	75As	1.48	99%	1%	0%
	88Sr	3061.69	100%	0%	0%
	89Y	46.4	100%	0%	0%
	95Mo	104.44	100%	0%	0%
	137Ba	15.84	100%	0%	0%
	208Pb	0.011	97%	3%	0%
	232Th	0.003	87%	13%	0%
	238U	1547.79	84%	0%	16%

Table A.12 Selected U, Fe, S, and N-cycles related bacteria found in the surface water samples (September 2016) from the D-pit and the DJX-pit using the 16S rRNA assay. Selected taxa are marked

with symbols: '' uranium reducers, '$' sulfate reducers, '#' Fe(III) reducers, '!' galena, hydrogen and HS oxidizers, '+' Fe(II) oxidizers, '§' hydrogen oxidizer, 'Ø' methane oxidizers.*

Identity	Class	D-0m	D-5m	D-10m	D-15m	DJX-0m	DJX-20m	DJX-70m
Glaciibacter superstes strain AHU1791	Actinobacteria	1.03%	2.62%	5.11%	1.78%	0.95%	0.59%	0.87%
Arthrobacter sp. PclMES1	Actinobacteria	0.44%	1.08%	0.22%	0.53%	0.31%	6.26%	0.41%
Mongoliicoccus roseus strain MIM28	Cytophagia	0.00%	2.11%	0.15%	0.00%	0.00%	0.01%	0.00%
Flavobacterium sp. 7B-412	Flavobacteriia	1.00%	2.65%	12.94%	1.15%	1.33%	15.01%	2.80%
Flavobacteria bacterium KF030	Flavobacteriia	0.00%	0.14%	0.03%	0.20%	0.30%	0.00%	2.71%
Chitinophaga sp. AKB-2008-JO108	Sphingobacteriia	0.00%	0.01%	0.00%	0.00%	3.87%	0.07%	0.27%
Pedobacter sp. R-36962	Sphingobacteriia	0.00%	0.13%	0.03%	0.00%	0.00%	0.01%	2.51%
Synechococcus sp. WH 8020	Cyanobacteria	5.18%	0.01%	0.06%	0.04%	0.00%	0.00%	0.00%
Clostridium bowmanii strain DSM 14206	Clostridia	0.40%	2.14%	0.64%	0.86%	0.62%	0.20%	1.11%
Alkaliphilus peptidifermentans strain Z-7036 #	Clostridia	0.00%	1.60%	0.23%	0.24%	0.07%	0.00%	0.31%
*Clostridium acetobutylicum **</sup>	Clostridia	0.27%	0.79%	0.08%	0.58%	0.18%	0.03%	0.18%
*Desulfosporosinus orientis strain DSM 765 *$*	Clostridia	0.15%	1.24%	0.39%	0.37%	0.13%	0.12%	0.25%
Brevundimonas variabilis strain HWS1051	Alphaproteobacteria	0.11%	0.50%	0.18%	0.64%	0.05%	4.08%	0.06%
Brevundimonas sp. H1-27	Alphaproteobacteria	3.89%	3.89%	5.14%	31.67%	0.65%	7.97%	0.48%
Caulobacter sp. K935	Alphaproteobacteria	0.20%	3.48%	0.22%	0.39%	3.69%	6.78%	0.08%
Chelativorans multitrophicus strain 8S	Alphaproteobacteria	0.19%	9.03%	1.83%	2.91%	0.13%	0.01%	2.14%
Pseudoxanthobacter soli strain CC4	Alphaproteobacteria	0.00%	0.00%	0.00%	0.00%	1.75%	0.03%	0.01%
Rhodobacter blasticus	Alphaproteobacteria	0.05%	1.76%	0.31%	0.29%	0.00%	0.00%	0.41%
Paracoccus sp. DFMS01	Alphaproteobacteria	0.02%	3.49%	0.69%	1.22%	0.03%	0.02%	0.85%
Novosphingobium sediminis strain YG-17	Alphaproteobacteria	0.85%	0.04%	0.00%	0.00%	0.06%	5.98%	0.49%
Sphingomonas sp. 5B	Alphaproteobacteria	2.28%	0.06%	0.00%	0.64%	16.62%	0.00%	0.00%
Sphingomonas sp. DP_00007	Alphaproteobacteria	0.05%	0.37%	1.11%	0.38%	4.35%	0.11%	0.52%
Sphingomonas aerolata strain NA215	Alphaproteobacteria	6.98%	2.41%	16.87%	2.41%	2.46%	0.51%	2.96%
Sphingopyxis rigui strain 01SU5-P	Alphaproteobacteria	0.20%	0.18%	0.06%	0.02%	6.88%	0.44%	0.00%
Polynucleobacter necessarius strain: MAT15	Betaproteobacteria	1.47%	1.32%	3.50%	1.46%	3.07%	0.73%	1.26%
Arsenic-oxidizing bacterium C05	Betaproteobacteria	0.00%	1.82%	0.03%	0.01%	0.00%	0.00%	0.00%
Polaromonas sp. JS666	Betaproteobacteria	0.18%	1.03%	0.42%	0.43%	0.70%	0.80%	16.93%
Acidovorax defluvii strain BSB411	Betaproteobacteria	1.05%	0.19%	0.19%	0.05%	1.83%	0.50%	0.07%
Hydrogenophaga defluvii strain BSB 9.5 §	Betaproteobacteria	0.00%	0.05%	0.07%	0.00%	3.01%	0.17%	0.52%
Rhodoferax ferrireducens isolate TB-2 #	Betaproteobacteria	0.48%	2.35%	4.95%	3.35%	0.63%	0.97%	1.05%
Noviherbaspirillum aurantiacum strain SUEMI08	Betaproteobacteria	0.24%	1.23%	0.36%	0.24%	0.66%	0.08%	0.59%
Massilia brevitalea strain byr23-80	Betaproteobacteria	0.20%	2.13%	0.10%	0.21%	0.17%	1.08%	0.75%
Thiobacillus plumbophilus strain Gro7 !	Betaproteobacteria	0.29%	1.47%	0.37%	1.33%	0.45%	0.09%	1.27%
Sideroxydans lithotrophicus strain LD-1 +	Betaproteobacteria	0.00%	0.45%	4.25%	2.07%	0.13%	0.01%	1.16%
Pelobacter propionicus strain DSM 2379	Deltaproteobacteria	0.03%	0.32%	0.74%	5.51%	0.09%	0.05%	0.17%
*Geobacter uraniireducens strain Rf4 *#*	Deltaproteobacteria	0.07%	0.58%	0.12%	0.23%	0.14%	0.03%	0.82%
*Geobacter sulfurreducens strain PCA *#*	Deltaproteobacteria	0.01%	0.01%	0.03%	0.00%	0.20%	0.06%	0.27%
*Geobacter metallireducens GS-15 *#*	Deltaproteobacteria	0.00%	0.10%	0.00%	0.16%	0.00%	0.00%	0.11%
Rheinheimera sp. F8	Gammaproteobacteria	31.45%	0.60%	0.31%	0.03%	0.00%	0.02%	0.00%
Methylobacter tundripaludum strain SV96 Ø	Gammaproteobacteria	0.00%	0.52%	4.11%	1.96%	0.00%	0.00%	0.98%
Acinetobacter lwoffii strain T24	Gammaproteobacteria	2.67%	7.85%	0.39%	3.68%	1.00%	16.01%	1.63%
Pseudomonas sp. BPA-6	Gammaproteobacteria	0.33%	3.64%	1.38%	2.09%	0.30%	5.99%	1.84%
Pseudomonas syringae strain NSM38	Gammaproteobacteria	16.56%	0.32%	0.05%	0.08%	0.00%	0.46%	0.00%

Figures

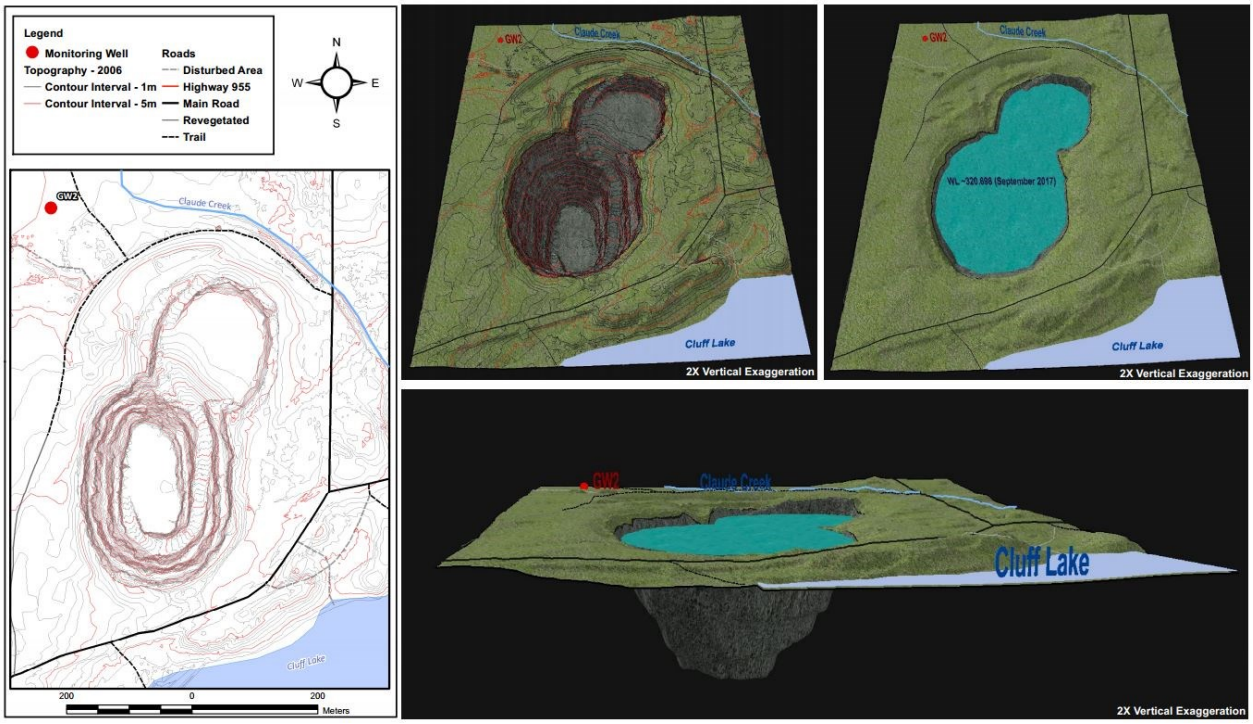

Figure A.1 3D model of the DJX-pit and the location of the groundwater well GW2.

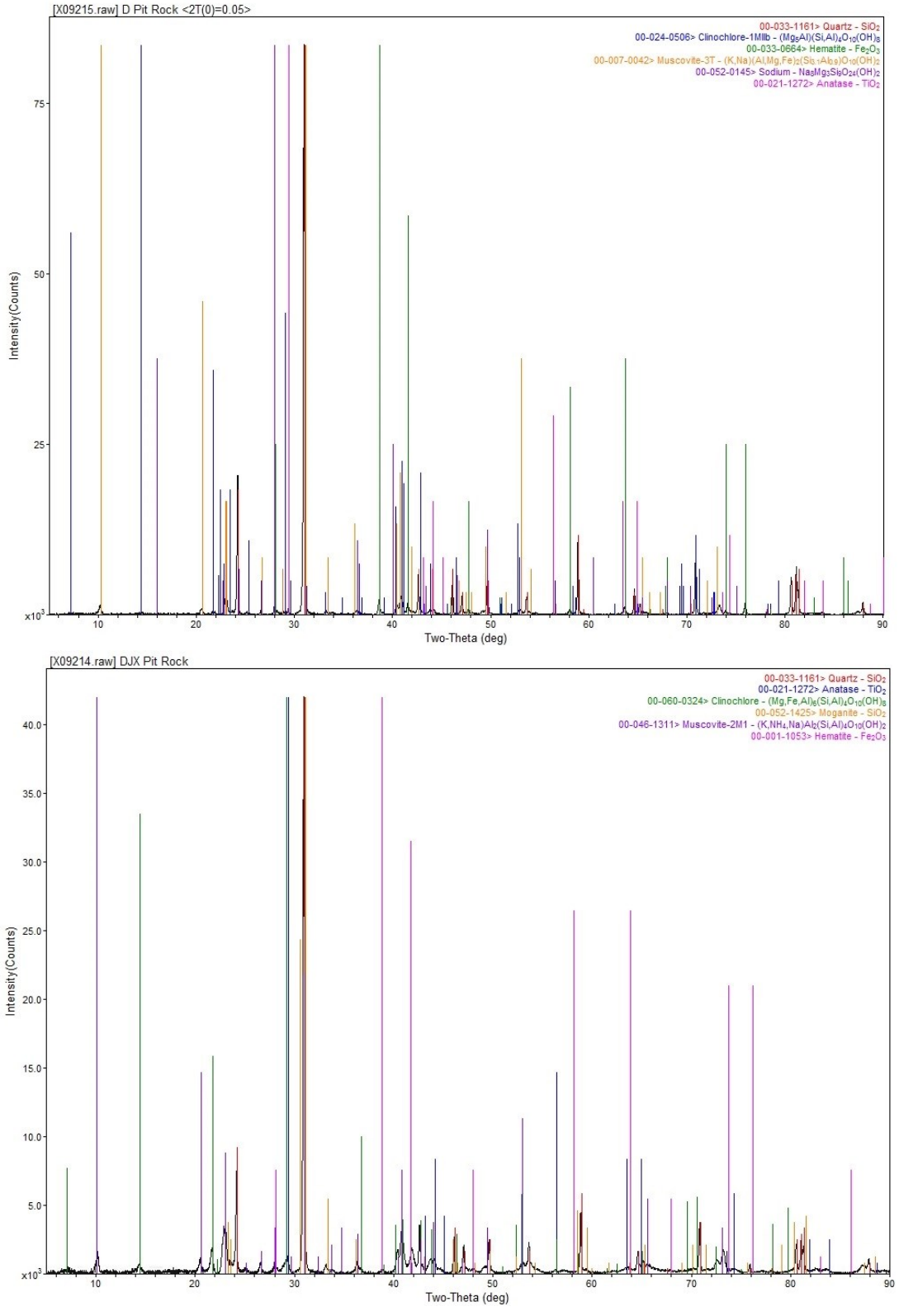

Figure A.2 RockD (top) and RockDJX (bottom) XRD spectra.

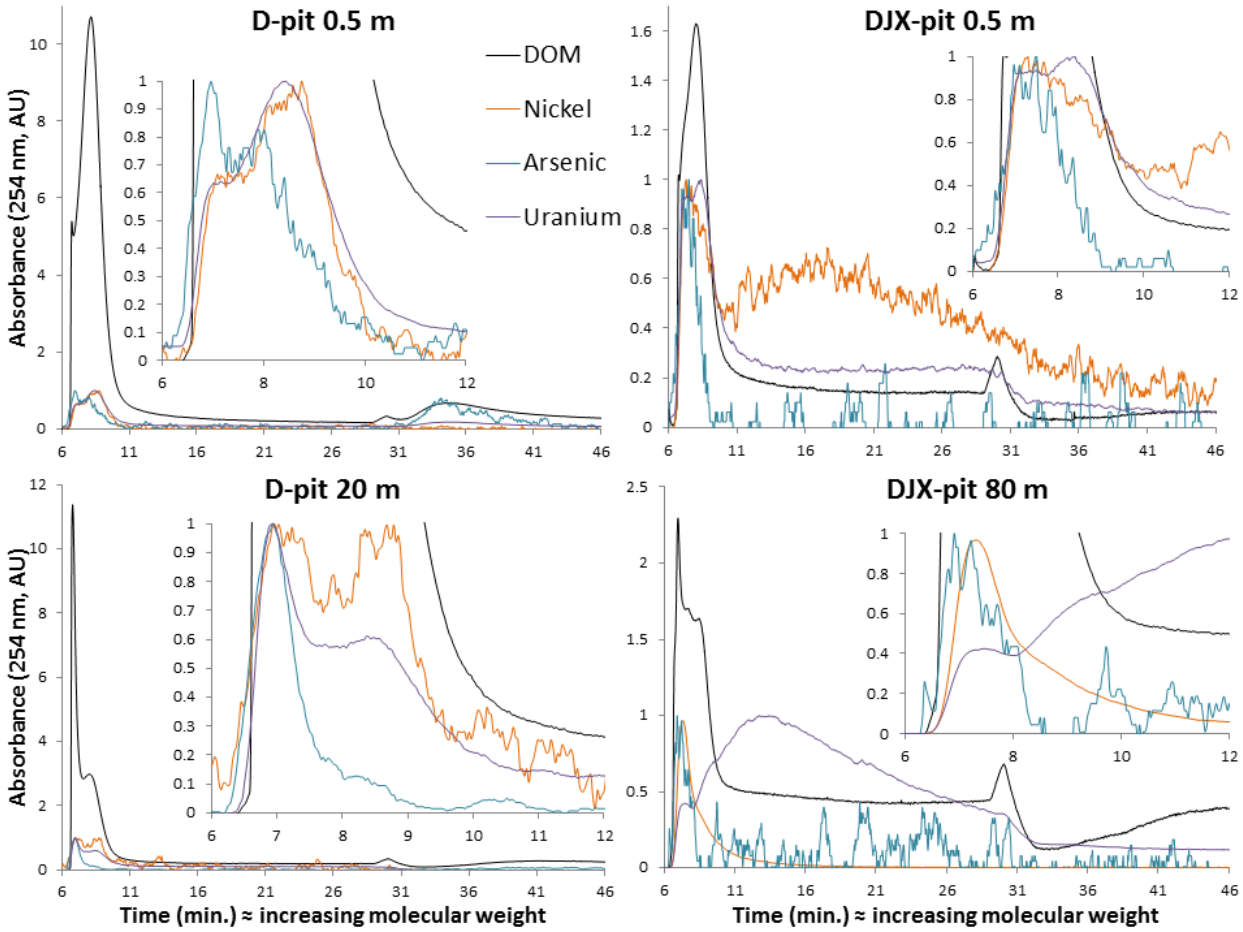

Figure A.3 AF4-ICP-MS example fractograms for D-pit and DJX-pit water samples.

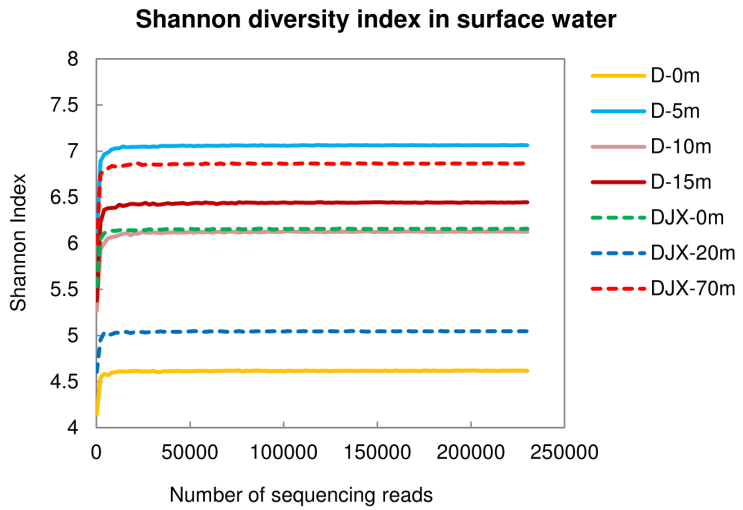

Figure A.4 Calculated Shannon diversity indexes for the sequenced samples from the water columns of D-pit and DJX-pit (September 2015 samples).

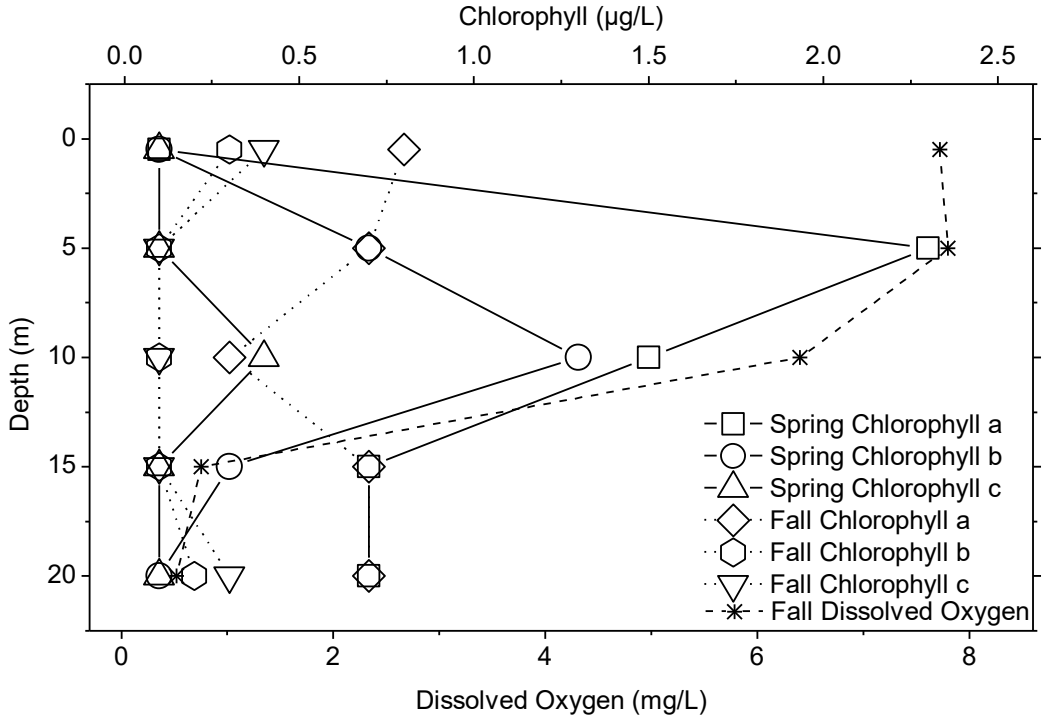

Figure A.5 Chlorophyll a, b and c concentrations in the D-Pit, measured in spring (March to May) and fall (September) 1987, and dissolved oxygen concentrations (field measurements) from fall (September) 1992 (based on data provided by AREVA). A clear concentration peak can be seen for the spring 1987 samples between 5-15 m indicating that primary production was most efficient in the mixolimnion close to the chemocline. Chlorophyll a is the most important photosynthetic pigment found in many pro- and eukaryots. Chlorophyll b on the other hand is typical for green algae and plants and chlorophyll c for diatoms and dinoflagellates (Speer, 1997). Surprisingly chlorophyll b and c concentrations in fall 1987 are higher at 20 m depth than at 15 m depth.

Figure A.6 Top: view from the center of the D-pit towards northeast. Bottom: view on the DJX-pit from the northern shore; Cluff Lake is seen near the end of the DJX-pit. The steep shores of both pits are favoring rock falls and landslides that might influence meromixis stability.

APPENDIX B
SUPPLEMENTARY INFORMATION FOR CHAPTER 3

Rock and ore samples

Two unidentified ore samples from Cluff Lake were provided by the mineralogy museum at the University of Alberta and were used for a qualitative description of the different ore types. Characteristic rock samples were collected along the shores of both pits in June 2016 (Figure 3.1). The rock and ore chemistry and mineralogy was investigated using total digestion, alkaline fusion and XRD analyses, similar to the sediment samples (see main text, Chapter 3).

The ore sample “Red Ore” had a similar reddish oxidation tone as rocks found around the D-pit and is likely representative of the ore body that was mined in the D-pit (AMOK, 1974; Harper, 1981; Harper, 1982). The other ore (“White Ore”) was white and brittle with visible black uraninite grains and was likely similar to deeper ore types, as mined in DJX/DJN. Correspondingly, the Red Ore showed similar mineralogy as the D-pit sediments and contained uraninite as well as wurzite ([Zn,Fe]S), calcite, magnesite, hematite, and goethite, while the White Ore mainly consisted of clay minerals, quartz, and uraninite (Table B.2). Digestion results from rock samples collected around the pits and the ore samples are provided in Table B.15. Rock D was more enriched in Ca, P, Mn, Fe, and As compared to Rock DJX, while Rock DJX, contained more Ni. This is consistent with the previously reported water chemistry for the two pits (see Chapter 2). The analyzed ore samples contained similar amounts of U with 16-19% by weight. Both ores also contained As and Ni, with 87-277 ppm and 267-245 ppm, respectively. These concentrations were generally similar to the ones found in the sediment samples of both pits. The Red Ore was also found to contain more Ca and Fe, again consistent with the corresponding rock sample, Rock D. The White Ore showed higher concentrations in Mo, similarly to the water column in the DJX-pit.

VESPERS beamline details

VESPERS uses a bending magnet as an X-ray source, a double crystal and multilayer monochromator as energy selector and has a spectral range of 2-30 keV with a beam size of 2-4 µm x 2-4 µm. XRF maps in this work were collected using a polychromatic X-ray beam with an energy range of 2-30 keV and a spot size of 2-4 µm. High resolution XRF maps were collected using a step size of 5 µm. Broad maps for localization were done with a step size of 10-50 µm. The beam was attenuated by 0.8 mm thick aluminum filter and the detector was situated 50-140 mm away from the samples depending on the signal strength. Maps were acquired for U (Lα1), K (Kα1), Ca (Kα1), Ti (Kα1), Cr (Kα1), Ni (Kα1), Cu (Kα1), Zn (Kα1), Y (Kα1), Pb (Lβ1), Fe (Kα1), Mn (Kα1), As (Kα1), and Rb (Kα1). The XRF signal was normalized to the flux of incoming X-ray beam measured by a N_2-filled ionization chamber.

XANES measurements were collected in fluorescence mode using a double crystal Si (111) monchromator with an energy resolution of 0.01%. The fluorescence detector was positioned 90° in respect to the incoming beam in the horizontal plane. The sample distance was 35-40 mm for μ-XANES, and 50-75 mm for bulk XANES measurements, respectively. XANES spectra were recorded for U (Lα1), Ni (Kα1), and As (Kα1) from 100 eV before the edge and 8k after the edge with varying energy increments for the pre-edge (10 eV), near-edge (0.5 eV), and post-edge regions (0.05k). Absorption energy was acquired at 5 sec per step (up to 15 sec for noisy signals). The As content of the glass slide and its influence on the XRF and μ-XANES results were verified by comparing the obtained results to the ones obtained from thin sections mounted on As-free quartz glass. Minor shift in As speciation was observed due to As present in the glass slides as discussed in the results section, however, no changes in the relative As signal in the XRF maps were detected.

In Athena (Demeter 0.9.24 XAS Processing Software), the spectra were background corrected by determining the pre-edge line before −30 eV, the post-edge line after +50 eV, and choosing a normalization order of 2. Calibration of spectra recorded at different dates was done using a Zr foil (for U), Au foil (for As) and Ni foil (for Ni). To determine the valence of the As and U hotspots, linear combination fitting of the XANES spectra was performed (in μ(E)) ranging from −20 eV before the edge to +80 eV after the edge) and by forcing the sum of components to 1. Fits were evaluated by visual comparison to the recorded data and a selection was made based on the lowest r-factors and X^2 values. For U, uranyl(VI) acetate and chemogenic uraninite standards, spectra from Alessi *et al.* (2014b) were used. The spectra were recorded at the Stanford Linear Accelerator Laboratory (SLAC) at the Stanford Synchrotron Radiation Lightsource (SSRL). The uranyl acetate spectra was shifted to match a uranyl nitrate hexahydrate spectrum recorded on the VESPERS beamline. The same energy shift was applied on the uraninite spectrum. For comparison two mineral spectra were recorded; autunite (Ruggles mine, NH, USA) and uraninite mixed with zippeite (Jachymov mine, Czech Republic). For As and Ni, previously recorded standard spectra were provided by the VESPERS beamline. For As, the following spectra were used for fitting: As_2O_3, As_2O_5, As_2S_3, $Ca_3(AsO_4)_2$, FeAsS, and Na_2HAsO_4. For Ni the sample data was compared to the following spectra: $NiCl_2$, $Ni(NO_3)_2$, NiO, NiS, NiSe.

For Laue diffraction, the Pilatus Pixel Array Detector (Dectris) was placed 90^o relative to the incident X-ray beam in vertical plane with the sample positioned 45^o relative to the beam. The sample-to-detector distance was calibrated to be 158.2 mm. For each beamline visit, detector calibration parameters vere adjusted. Laue patterns were recorded for 30-300 sec. The processing software XMAS v.6 by Nobumichi Tamura can be downloaded here: https://sites.google.com/a/lbl.gov/bl12-3-2/user-resources (last visited December 2017). Imported images were rotated by 270° clockwise to match the experimaental geometry and at least 10 peaks were identified before fitting. Laue indexing was done with an angular tolerance of

0.1° and using available and custom made crystal structure files[3]. The number of total peaks and the number of indexed peaks was recorded. A fit was considered successful when no other crystal file could be found with a better fit.

Tables

Table B.1 Mass analyzer settings and measurement modes of the 8800 ICP-MS Triple Quad system (Agilent). Q1 and Q2 are the m/z selected for the first and second mass separation step. For the measurements argon was used as the carrier gas. External calibration was done with elemental mixtures diluted in 2% HNO_3 and 0.5% HCl. Indium (500 ppb) was used as internal standard. The samples were diluted 2 to 20 times with 2% HNO_3 and 0.5% HCl prior to analysis to adjust the matrix and to be in the external calibration range. At least 3 measurements (instrumental precision: <5%) were performed for each sample or standard with 300 scans per measurement. Helium (He) and hydrogen (H_2) were introduced into the reaction chamber between Q1 and Q2 with a flow rate of 3 mL/min to knock out potential polyatomic interferences summarized by May and Wiedmeyer (1998). For As, P and S, oxygen was introduced into the reaction chamber (10% O_2) and a mass shift of m/z 16 was applied in the second mass analyzer to select for monooxygenated cations. The average recoveries of the certified STSD-3 values for the applied total digestions are shown in the last column.

Metal	*m/z* Q1 → Q2	Reaction/collision	Quantification limit	STSD-3 average recovery
Li	7 → 7	No gas	1	122
B	11 → 11	No gas	10	122
Na	23 → 23	No gas	50	99
Mg	24 → 24	No gas	50	98
Al	27 → 27	No gas, He	50	91
Si	28 → 28	H_2, He	50	95
P	31 → 31, 31	He, O_2	50	105
S	32 → 48	O_2	50	144
K	39 → 39	No gas, He	50	98
Ca	40 → 40, 44	H_2, No gas	50	91
V	51 → 51	He	1	90
Cr	52 → 52	No gas, He	1	85
Mn	55 → 55	No gas, He	1	95
Fe	56 → 56	No gas, He	10	94
Co	59 → 59	No gas, He	1	105
Ni	60 → 60	No gas, He	1	114
Cu	63 → 63	No gas, He	1	101
Zn	66 → 66	No gas, He	1	119
As	75 → 91	O_2	1	96
Br	79 → 79	No gas, He	50	-
Sr	88 → 88	No gas	1	111
Mo	96 →96	He	1	122
Cd	111 → 111	No gas	1	113
Ba	138 → 138	No gas, He	1	100
Ce	140 →140	No gas	1	101
Pb	208 → 208	No gas	1	114
Th	232 → 232	No gas, He	1	95
U	238 → 238	No gas	1	91

[3] abernathyite, agricolite, albite, anorthite, arsenopyrite, autunite, billietite, boltwoodite, coffinite, curite, davidite, dessauite, dewindtite, dymkovite, ferrihydrite, fourmarierite, galena, gauthierite, grimselite, hallimondite, hematite, hugelite, ianthinite, K[(UO2)(AsO4)](H2O)3, kasolite, mapiquiroite, masuyite, metaschoepite, monazite-(Ce), muscovite, Ni[UO2AsO4]2(H2O)12, nickeline, nielsbohrite, novacekite, parsonsite, phosphuranylite, plumbomicroclite, pyrochlore, quartz, rauchite, richetite, rutherfordine, sayrite, schoepite, soddyite, spriggite, stepite, UAs, uraninite, uranophane, uranopilite, vandendriesscheite, vanmeersscheite, vysokyite, widenmannite. Crystal structure files assembled with data from the American Mineralogist Crystal Structure Database (http://rruff.geo.arizona.edu/AMS/amcsd.php).

Table B.2 Mineral composition, nitrogen, and carbon content of sediment samples from D-pit and DJX-pit and the Cluff Lake ore samples. Alb: albite. Ano: anorthite. Cal: calcite. Chs: clinohypersthene. Cli: clinochlore. Dol: dolomite. Ens: enstatite. Goe: goethite. Gyp: gypsum. Hem: hematite. Ilt: illite. Kao: kaolinite. Mag: magnesite. Mic: microcline. Mus: muscovite. Ort: orthoclase. Phl: phlogopite. Pyr: pyrite. Ppf : phosphoferrite. Qrz: quartz. Rut: rutile. Ura: uraninite. Wur: wurtzite. n.m.: not measured. TN, TC and TOC given in weight-%.

Sample	Tectosilicates	Clays	Inosilicates	Oxides	Sulfides/ sulfates/ phosphates	Carbonates	TN	TC	TOC
D-1	Qrz	Mus, Ilt, Cli		Hem			0.01	<0.10	<0.10
D-2	Qrz	Mus, Ilt, Cli		Hem			0.01	<0.10	<0.10
D-3	Qrz, Ano	Mus, Ilt, Cli		Hem			0.03	0.23	0.25
D-4	Qrz, Ano	Mus, Ilt, Cli		Hem		Dol	0.06	0.67	0.65
D-5	Qrz, Ano	Mus, Ilt, Cli		Hem			0.01	<0.10	<0.10
D-6	Qrz, Ano	Mus, Ilt, Cli		Hem		Dol	0.13	1.46	1.44
D-7	Qrz, Ano, Alb	Mus, Ilt, Cli		Hem		Dol	0.06	0.73	0.72
D-8	Qrz, Ano	Mus, Ilt, Cli		Hem			0.06	0.82	0.75
D-9	Qrz, Ano, Alb	Mus, Ilt, Cli		Hem			0.07	0.75	0.80
D-10	Qrz, Ano	Mus, Ilt, Cli		Hem		Dol	0.07	0.94	0.91
D-22m	Qrz, Alb, Ort	Mus, Cli,		Hem			0.08	0.96	0.96
DJX-	Qrz, Alb, Ort	Cli, Phl					0.10	2.02	1.64
DJX-	Qrz, Alb, Ort	Cli, Phl					0.03	0.35	0.34
DJX-	Qrz, Alb, Ort	Mus, Cli					0.02	0.20	0.17
DJX-	Qrz, Alb, Ort	Mus, Cli					0.01	0.13	0.12
DJX-8	Qrz, Alb, Mic	Mus, Cli		Hem			0.35	4.20	3.52
DJX-4a	Qrz, Ort	Mus, Cli	Ens	Hem, Rut			0.07	1.16	0.87
DJX-4b	Qrz, Alb, Ort	Mus, Cli			Pyr	Dol	0.05	0.65	0.52
DJX-4c	Qrz, Alb, Ort	Mus, Cli				Dol	0.07	0.85	0.72
DJX-68	Qrz, Mic	Mus, Cli,					0.07	1.04	1.04
DJX-87	Qrz, Mic	Ilt, Cli, Kao					0.03	0.51	0.50
DJX-91	Qrz, Ort	Mus, Cli,	Chs				0.03	0.32	0.32
Red	Qrz	Ilt, Cli		Hem,	Wur	Cal, Mag	n.m.	n.m.	n.m.
White	Qrz	Mus, Ilt,		Ura			n.m.	n.m.	n.m.
Soil1	Qrz, Mic	Mus, Cli					0.04	0.62	0.62
Soil2	Qrz				Ppf		0.01	0.09	0.08
Trap D	Qrz	Mus		Mag			0.72	11.50	9.36
Trap	Qrz	Mus, Cli		Mag	Gyp		0.82	7.86	7.09

Table B.3 Sequential extraction results for D-6 in triplicates. Exch: exchangeable. Carb: bound to carbonates. Fe/Mn: bound to amorphous iron and manganese oxides. OrgM: bound to organic matter. Res: residual (calculated). Conc: average concentration of three measurements. Stdev: standard deviation (n=3).

	Exch		Carb		Fe/Mn		OrgM		Res	Total	
Element	Conc	Stdev	Conc	Stdev	Conc	Stdev	Conc	Stdev	Conc	Conc	Stdev
	µg/g	µg/g	µg/g	µg/g	µg/g	µg/g	µg/g	µg/g	µg/g	µg/g	µg/g
Al	109.7	54.0	104.2	7.2	436.9	17.1	510.3	4.2	88535.6	89696.7	8177.5
As	5.6	0.5	10.6	0.4	76.7	1.7	2.5	0.1	354.7	450.1	37.9
B	4.5	1.2	<0.1		0.5	0.1	<0.1		414.4	419.5	37.8
Ba	30.9	0.9	14.0	0.8	9.8	0.3	2.9	0.04	239.2	296.8	29.1
Ca	430.2	17.7	40.6	2.4	20.4	0.7	7.8	0.5	1576.5	2075.4	173.3
Cr	0.3	0.1	1.1	0.1	3.4	0.2	1.5	0.01	108.8	115.1	11.3
Cu	2.9	0.3	4.2	1.0	5.5	0.3	14.6	0.2	10.9	38.1	3.5
Fe	259.7	57.8	1709.2	53.9	7126.1	235.2	471.4	7.7	27946.7	37513.1	3079.6
K	1173.3	41.7	103.4	8.5	24.1	0.4	14.4	0.3	34292.9	35608.1	3229.7
Li	2.5	0.7	0.7	0.1	1.4	0.02	1.1	0.03	77.2	82.8	7.1
Mn	220.4	8.8	149.3	9.0	26.6	0.8	3.6	0.01	53.6	453.5	60.3
Ni	69.1	2.9	25.2	1.1	29.8	1.0	21.6	0.2	37.9	183.5	19.7
P	1.3	0.3	22.2	1.0	119.4	4.5	7.7	1.6	634.2	784.7	119.3
Pb	0.1	0.01	0.3	0.1	2.2	0.05	0.7	0.02	10.0	13.4	1.3
S	358.8	27.8	279.0	4.3	167.5	21.1	1299.2	101.8	1533.3	3637.8	242.9
Si	29.3	7.5	43.8	14.7	46.4	5.0	35.4	1.6	348433.5	348588.4	13289.5
Sr	15.9	0.6	1.8	0.1	0.7	0.03	0.2	0.01	204.6	223.2	21.4
U	1.6	0.5	203.8	11.6	86.9	0.7	12.0	0.6	51.8	356.1	28.7
Zn	2.8	0.4	3.2	0.7	2.9	0.2	<0.1		47.4	56.2	5.5

Table B.4 Sequential extraction results for D-9 in triplicates. Exch: exchangeable. Carb: bound to carbonates. Fe/Mn: bound to amorphous iron and manganese oxides. OrgM: bound to organic matter. Res: residual (calculated). Conc: average concentration of three measurements. Stdev: standard deviation (n=3).

	Exch		Carb		Fe/Mn		OrgM		Res	Total	
Element	Conc	Stdev	Conc	Stdev	Conc	Stdev	Conc	Stdev	Conc	Conc	Stdev
	µg/g	µg/g	µg/g	µg/g	µg/g	µg/g	µg/g	µg/g	µg/g	µg/g	µg/g
Al	148.5	10.3	111.5	6.0	578.1	7.6	553.4	19.3	90783.9	92175.3	534.5
As	8.2	0.02	14.8	0.1	63.6	1.0	2.5	0.1	288.2	377.4	17.5
B	2.3	0.2	<0.1		1.3	0.1	<0.1		400.9	404.6	12.1
Ba	40.7	1.8	11.4	0.2	7.4	0.1	2.4	0.1	210.0	271.9	1.1
Ca	415.7	19.3	62.6	5.0	36.3	1.0	18.3	2.7	1590.7	2123.6	51.6
Cr	0.2	0.03	0.7	0.02	2.9	0.04	1.5	0.1	98.1	103.5	1.2
Cu	5.6	2.5	5.7	1.7	3.6	0.1	4.7	0.2	23.8	43.5	0.7
Fe	146.4	16.7	748.4	2.1	4832.8	58.5	243.3	11.1	38026.9	43997.8	139.3
K	1292.9	64.9	117.8	3.2	34.2	0.4	17.9	1.1	35163.7	36626.5	159.0
Li	1.4	0.2	0.5	0.1	2.3	0.03	1.0	0.1	78.0	83.2	2.4
Mn	135.6	5.5	25.1	0.4	23.4	0.3	4.7	0.2	208.1	396.8	3.3
Ni	27.5	1.2	11.5	0.6	36.8	0.3	8.3	0.3	93.3	177.4	2.8
P	1.0	0.1	16.7	0.9	92.5	4.2	5.3	0.5	659.8	775.2	141.9
Pb	0.8	0.1	1.5	0.1	3.5	0.05	1.5	0.1	7.5	14.9	1.0
S	320.1	4.1	81.9	0.4	53.5	2.7	241.7	3.4	303.9	1001.0	49.0
Si	69.6	54.5	4.4	4.3	51.9	4.0	28.2	3.3	307481.1	307635.1	15784.4
Sr	17.9	0.8	1.7	0.1	0.8	0.03	0.2	0.01	187.6	208.2	3.9
U	8.6	3.5	148.6	6.0	99.6	2.3	34.2	5.0	176.4	467.4	9.9
Zn	1.8	0.3	1.7	0.6	7.3	0.3	<0.1		123.2	134.2	5.2

Table B.5 Sequential extraction results for D-10 in triplicates. Exch: exchangeable. Carb: bound to carbonates. Fe/Mn: bound to amorphous iron and manganese oxides. OrgM: bound to organic matter. Res: residual (calculated). Conc: average concentration of three measurements. Stdev: standard deviation (n=3).

	Exch		Carb		Fe/Mn		OrgM		Res	Total	
Element	Conc	Stdev	Conc	Stdev	Conc	Stdev	Conc	Stdev	Conc	Conc	Stdev
	µg/g	µg/g	µg/g	µg/g	µg/g	µg/g	µg/g	µg/g	µg/g	µg/g	µg/g
Al	108.0	50.3	92.6	8.2	487.3	49.5	560.3	13.0	70207.7	71455.8	6826.3
As	8.8	1.1	17.7	0.6	74.7	6.5	3.3	0.2	208.1	312.5	11.3
B	1.5	0.3	<0.1		1.0	0.2	<0.1		134.1	136.6	11.4
Ba	34.5	3.0	10.9	0.2	6.6	0.6	2.3	0.04	270.0	324.4	29.8
Ca	357.9	29.1	57.0	0.6	29.7	2.3	18.8	3.2	1306.3	1769.8	183.6
Cr	0.2	0.1	0.8	0.03	2.6	0.2	1.6	0.04	98.0	103.2	9.5
Cu	3.6	0.9	3.8	0.04	2.7	0.4	5.2	0.2	47.4	62.8	5.4
Fe	110.3	39.0	835.5	29.6	4255.9	409.5	283.3	12.5	40982.4	46467.3	4346.0
K	1133.2	93.6	116.3	7.1	27.1	3.1	17.9	0.4	26627.0	27921.6	2772.9
Li	1.0	0.1	0.3	0.01	1.8	0.1	1.0	0.03	51.8	56.0	5.5
Mn	111.4	9.7	22.9	0.8	20.2	2.0	4.5	0.2	462.9	621.9	50.1
Ni	26.2	2.8	12.6	0.2	32.9	3.3	9.6	0.4	142.9	224.3	19.5
P	0.9	0.04	16.6	0.5	103.3	4.9	6.0	0.5	702.6	829.4	8.8
Pb	0.6	0.1	1.2	0.01	2.9	0.3	1.4	0.04	5.6	11.6	1.2
S	313.1	15.1	87.4	2.6	56.9	1.8	287.2	10.5	409.2	1153.9	24.3
Si	27.4	14.8	17.9	10.0	46.1	6.2	29.4	1.5	295936.0	296056.9	3709.1
Sr	15.8	1.4	2.4	0.6	0.7	0.1	0.2	0.01	119.0	138.1	12.1
U	5.5	2.2	140.0	5.7	75.3	8.6	34.0	7.3	178.2	433.1	44.4
Zn	2.8	2.9	0.6	0.2	6.4	0.7	<0.1		129.2	139.0	18.1

Table B.6 Sequential extraction results for D-22 in triplicates. Exch: exchangeable. Carb: bound to carbonates. Fe/Mn: bound to amorphous iron and manganese oxides. OrgM: bound to organic matter. Res: residual (calculated). Conc: average concentration of three measurements. Stdev: standard deviation (n=3).

	Exch		Carb		Fe/Mn		OrgC		Res	Total	
Element	Conc	Stdev	Conc	Stdev	Conc	Stdev	Conc	Stdev	Conc	Conc aver	Stdev
	µg/g	µg/g	µg/g	µg/g	µg/g	µg/g	µg/g	µg/g	µg/g	µg/g	µg/g
Al	39.4	6.1	86.5	20.1	875.4	111.9	945.1	21.5	81575.1	83521.5	4331.2
As	5.9	0.3	11.6	0.1	75.4	4.0	25.9	1.5	115.3	234.2	5.3
B	18.4	2.1	3.1	0.2	2.5	0.1	0.2	0.04	614.7	638.9	8.4
Ba	126.2	2.3	50.3	0.7	64.8	3.1	22.2	1.4	489.2	752.6	62.1
Ca	609.0	11.2	92.9	4.3	165.3	11.8	226.0	11.7	2248.6	3341.8	234.0
Ce	1.5	0.04	3.6	0.1	8.0	0.3	8.3	0.5	89.3	110.7	19.2
Co	3.1	0.05	1.9	0.03	12.4	0.5	1.5	0.1	5.3	24.3	0.4
Cr	<0.3		0.7	0.1	3.4	0.3	2.1	0.03	78.9	85.5	0.9
Cu	1.4	0.03	2.4	0.4	2.7	0.4	9.2	0.3	16.3	32.0	0.4
Fe	129.4	18.6	751.9	64.4	6451.2	427.9	815.3	55.3	26427.0	34574.8	206.7
K	154.3	17.2	80.3	4.4	56.7	2.8	19.7	0.7	31293.5	31604.5	894.6
Li	5.0	0.9	6.6	2.4	2.2	0.2	0.9	0.03	61.6	76.3	3.8
Mn	97.7	0.9	23.1	0.8	69.9	2.8	8.1	0.5	97.4	296.2	6.2
Mo	1.6	0.2	5.7	0.2	26.9	1.3	12.6	0.4	42.1	88.8	0.7
Ni	15.3	0.3	7.6	0.4	56.9	2.3	11.7	0.8	58.7	150.2	2.3
P	2.2	1.6	8.4	1.6	43.4	7.7	120.4	6.2	465.8	640.4	23.1
Pb	0.5	0.01	1.1	0.1	4.3	0.2	1.2	0.05	7.4	14.6	0.1
S	311.4	7.5	75.9	5.9	157.2	0.1	303.2	16.7	594.6	1442.4	37.0
Si	<0.4		<0.4		104.1	64.2	<0.1		329438.6	329543.6	4103.4
Sr	9.5	0.1	2.0	0.1	1.7	0.1	0.6	0.1	192.5	206.4	36.9
Th	<0.3		0.3	0.01	0.2	0.0	1.1	0.03	20.9	22.9	2.4
Ti	<0.3		0.4	0.1	0.3	0.04	5.6	0.2	4512.0	4518.6	26.7
U	10.1	0.05	171.9	1.8	105.5	0.8	24.6	1.0	5.9	317.9	15.4
V	0.1	0.1	0.4	0.2	7.4	0.5	2.1	0.1	137.8	147.8	2.5
Zn	2.7	0.3	4.0	5.0	11.7	0.7	2.6	0.2	22.1	43.1	2.6

Table B.7 Sequential extraction results for DJX-13b in triplicates. Exch: exchangeable. Carb: bound to carbonates. Fe/Mn: bound to amorphous iron and manganese oxides. OrgM: bound to organic matter. Res: residual (calculated). Conc: average concentration of three measurements. Stdev: standard deviation (n=3).

	Exch		Carb		Fe/Mn		OrgM		Res	Total	
Element	Conc	Stdev	Conc	Stdev	Conc	Stdev	Conc	Stdev	Conc	Conc	Stdev
	µg/g	µg/g	µg/g	µg/g	µg/g	µg/g	µg/g	µg/g	µg/g	µg/g	µg/g
Al	3.9	1.6	104.6	9.3	887.3	23.2	515.7	85.8	43558.8	45070.3	5235.6
As	1.3	0.6	0.3	0.1	1.8	0.1	1.1	0.02	8.5	13.0	1.1
Ba	0.2	0.02	8.2	0.4	7.8	0.8	1.9	0.3	441.0	459.0	11.3
Ca	432.5	15.2	63.0	5.5	83.4	2.5	43.1	6.3	1562.8	2184.9	93.0
Co	1.8	0.1	5.0	0.3	47.5	1.6	2.5	0.4	3.6	60.3	1.7
Cr	<0.2		<0.3		2.2	0.1	1.2	0.2	29.7	33.6	1.2
Cu	0.6	0.1	5.8	0.3	12.0	0.4	<0.7		11.3	30.3	0.6
Fe	4.3	2.0	161.8	11.4	2861.0	101.8	<0.7		12084.1	15111.8	1555.7
K	3.9	7.8	111.5	8.1	85.4	33.1	51.4	7.8	24255.8	24508.1	3001.5
Mn	56.6	1.6	102.1	7.4	381.0	16.1	13.3	2.4	68.2	621.2	11.5
Ni	6.6	1.1	26.9	1.8	75.7	2.7	5.8	1.1	7.5	122.4	2.3
P	0.8	0.1	2.0	0.2	56.9	5.9	6.0	0.3	85.4	151.0	9.2
Pb	<0.2		<0.2		2.0	0.1	<0.7		13.1	16.3	0.5
S	181.6	10.1	35.0	4.1	45.3	10.3	294.8	23.4	8.0	564.7	113.0
Si	<0.2		3.2	2.3	<6.8		21.5	4.6	285694.0	285725.7	18358.0
Sr	3.8	0.2	1.3	0.1	6.9	0.1	0.7	0.1	74.1	86.8	3.1
U	<0.2		46.6	3.5	14.5	0.6	1.8	0.3	0.6	63.8	4.4
V	<0.2		<0.2		2.6	0.1	1.2	0.2	47.1	51.4	0.8
Zn	6.1	2.6	7.1	0.9	11.0	1.1	<0.7		17.5	42.3	0.8

Table B.8 Sequential extraction results for DJX-8 in triplicates. Exch: exchangeable. Carb: bound to carbonates. Fe/Mn: bound to amorphous iron and manganese oxides. OrgM: bound to organic matter. Res: residual (calculated). Conc: average concentration of three measurements. Stdev: standard deviation (n=3).

	Exch		Carb		Fe/Mn		OrgM		Res	Total	
Element	Conc	Stdev	Conc	Stdev	Conc	Stdev	Conc	Stdev	Conc	Conc	Stdev
	µg/g	µg/g	µg/g	µg/g	µg/g	µg/g	µg/g	µg/g	µg/g	µg/g	µg/g
Al	3.2	0.8	63.6	5.0	494.6	31.2	318.8	25.1	29536.0	30416.1	1705.0
As	0.7	0.1	0.7	0.1	2.9	0.5	<0.6		7.0	11.8	1.4
Ba	1.5	0.7	4.0	0.3	6.8	0.2	<0.7		161.6	174.5	31.4
Ca	583.8	8.5	76.2	9.9	80.5	7.0	30.0	9.2	338.3	1108.8	58.4
Co	8.0	0.4	12.5	1.0	13.8	1.7	1.0	0.2	2.8	38.1	3.4
Cr	<0.2		<0.2		1.4	0.1	0.9	0.1	23.2	26.1	4.2
Cu	0.7	0.02	3.3	0.2	6.0	0.5	<0.6		8.0	18.6	2.1
Fe	3.9	0.6	212.8	15.8	1646.2	120.4	22.4	7.6	7715.6	9600.9	876.0
K	72.5	112.7	61.0	7.7	21.0	2.8	7.1	1.2	13854.7	14016.3	821.7
Mn	276.3	11.2	100.3	9.7	31.9	3.3	4.4	0.4	22.9	435.9	16.1
Ni	33.2	1.8	91.3	9.5	81.7	11.1	8.3	1.9	3.6	218.1	3.9
P	2.4	0.1	7.1	1.2	103.3	10.1	21.4	4.4	26.2	160.4	9.7
Pb	<0.2		0.3	0.03	1.0	0.1	<0.6		3.3	5.4	0.7
S	251.2	17.4	75.1	22.2	41.6	13.6	256.6	98.1	21.2	645.7	60.0
Si	<0.2		<0.3		<6.7		27.2	22.2	267921.9	267956.2	5478.1
Sr	3.8	0.4	1.0	0.1	6.9	0.2	0.6	0.01	65.8	78.0	7.0
U	0.3	0.02	32.4	2.7	7.6	1.3	1.3	0.2	0.8	42.2	4.3
V	0.3	0.01	<0.2		1.3	0.1	1.1	0.1	33.7	36.7	3.7
Zn	3.6	1.8	14.4	0.4	4.6	1.9	<0.6		9.0	32.3	4.4

Table B.9 Sequential extraction results for DJX-4c in triplicates. Exch: exchangeable. Carb: bound to carbonates. Fe/Mn: bound to amorphous iron and manganese oxides. OrgM: bound to organic matter. Res: residual (calculated). Conc: average concentration of three measurements. Stdev: standard deviation (n=3).

	Exch		Carb		Fe/Mn		OrgM		Res	Total	
Element	Conc	Stdev	Conc	Stdev	Conc	Stdev	Conc	Stdev	Conc	Conc	Stdev
	µg/g	µg/g	µg/g	µg/g	µg/g	µg/g	µg/g	µg/g	µg/g	µg/g	µg/g
Al	9.4	3.6	81.6	4.4	878.8	9.8	628.1	33.2	64843.6	66441.5	1696.9
As	0.3	0.02	0.6	0.1	7.0	0.1	<0.6		17.4	25.9	1.6
Ba	3.9	0.9	6.8	0.5	6.9	0.1	1.9	0.1	296.7	316.3	6.7
Ca	797.1	59.7	89.1	11.0	126.5	1.2	71.6	4.9	420.1	1504.6	131.6
Co	9.6	0.6	11.2	0.5	23.6	0.3	3.3	0.1	0.8	48.5	2.0
Cr	<0.2		1.1	1.0	2.8	0.2	1.8	0.1	75.3	81.2	2.5
Cu	1.3	0.1	6.4	0.5	7.1	0.02	0.9	0.7	14.2	29.9	3.9
Fe	9.3	3.7	377.9	45.1	4284.2	41.9	258.2	51.1	19324.5	24254.0	1306.0
K	126.3	103.7	96.2	6.7	52.8	0.1	13.9	5.1	27715.2	28004.4	558.9
Mn	219.8	10.2	73.4	6.0	65.7	0.5	9.5	0.4	45.0	413.4	5.2
Ni	45.2	3.2	55.4	4.3	123.1	1.3	17.9	1.1	0.8	242.4	3.5
P	0.5	0.2	2.0	0.1	37.6	4.0	2.5	0.3	221.6	264.2	23.3
Pb	<0.2		0.5	0.02	3.1	0.5	<0.6		3.7	8.0	0.4
S	426.7	4.7	79.1	3.6	42.1	3.4	628.7	16.8	328.1	1504.8	63.3
Si	<0.2		<0.2		<7.3		16.2	2.7	224427.1	224451.1	5466.5
Sr	5.7	1.1	1.3	0.05	7.0	0.1	0.6	0.01	72.2	86.7	7.6
U	0.5	0.1	62.9	4.0	23.7	0.3	5.2	0.3	2.0	94.2	3.7
V	0.3	0.02	<0.2		3.3	0.1	<0.6		121.3	125.7	1.0
Zn	15.0	5.5	7.8	0.9	8.2	0.1	<0.7		8.3	40.0	2.9

Table B.10 Sequential extraction results for DJX-68 in triplicates. Exch: exchangeable. Carb: bound to carbonates. Fe/Mn: bound to amorphous iron and manganese oxides. OrgM: bound to organic matter. Res: residual (calculated). Conc: average concentration of three measurements. Stdev: standard deviation (n=3).

	Exch		Carb		Fe/Mn		OrgC		Res	Total	
Element	Conc	Stdev	Conc	Stdev	Conc	Stdev	Conc	Stdev	Conc	Conc	Stdev
	µg/g	µg/g	µg/g	µg/g	µg/g	µg/g	µg/g	µg/g	µg/g	µg/g	µg/g
Al	51.6	0.7	643.2	26.2	4844.2	149.7	1017.8	32.4	111012.3	117569.1	3022.2
As	0.6	0.02	0.3	0.00	5.3	0.4	4.0	0.1	18.1	28.3	0.5
B	13.5	1.1	4.8	0.4	15.6	0.3	0.6	0.1	1087.4	1121.9	24.9
Ba	0.2	0.8	19.5	0.8	51.8	4.7	6.9	0.7	407.5	485.9	26.4
Ca	773.6	9.8	51.9	2.1	97.7	1.7	152.7	1.7	1568.2	2644.1	334.4
Ce	3.0	0.1	5.3	0.1	16.4	0.3	3.7	0.1	46.8	75.2	4.4
Co	2.3	0.02	4.0	0.2	55.9	1.5	3.3	0.1	7.3	72.7	2.8
Cr	<0.3		<0.3		1.7	0.05	0.5	0.03	98.3	101.2	0.1
Cu	2.6	0.1	19.6	3.8	55.1	1.9	76.5	4.6	76.6	230.5	21.3
Fe	59.7	7.6	321.3	24.4	9099.3	1566.9	565.3	5.0	17328.0	27373.5	1639.6
K	170.3	6.3	76.1	4.2	307.3	33.8	29.1	1.6	39377.1	39959.9	1349.2
Li	3.3	0.2	2.2	0.5	5.4	0.2	1.4	0.04	93.8	106.2	2.0
Mn	37.6	0.4	24.6	1.3	335.1	9.1	8.5	0.4	61.5	467.3	32.8
Mo	0.7	0.1	1.2	0.1	80.1	4.8	14.9	0.9	78.7	175.6	5.3
Ni	5.4	0.2	7.9	0.3	88.5	1.5	8.0	0.4	61.7	171.6	5.9
P	5.4	2.9	0.9	0.9	24.1	2.1	86.2	1.5	180.9	297.5	22.5
Pb	<0.3		0.5	0.02	8.7	1.0	0.4	0.02	10.8	20.7	0.4
S	982.7	21.2	344.7	17.4	1889.9	153.6	496.6	15.0	596.3	4310.1	172.4
Si	<0.3		<0.3		161.8	16.3	<0.1		285552.1	285714.6	5592.6
Sr	8.7	0.1	1.5	0.04	8.6	0.8	0.6	0.02	48.9	68.2	2.7
Th	<0.3		<0.3		1.3	0.02	0.9	0.01	17.2	20.0	1.9
Ti	<0.3		<0.3		0.5	0.01	1.7	0.04	3386.3	3389.1	150.4
U	36.9	0.8	612.6	9.4	818.4	33.7	19.0	0.8	145.7	1632.6	82.7
V	0.3	0.1	<0.3		5.3	0.2	0.9	0.02	972.3	979.1	10.8
Zn	7.3	0.3	4.3	0.1	57.1	0.6	8.7	0.3	48.9	126.3	1.2

Table B.11 Sequential extraction results for DJX-87 in triplicates. Exch: exchangeable. Carb: bound to carbonates. Fe/Mn: bound to amorphous iron and manganese oxides. OrgM: bound to organic matter. Res: residual (calculated). Conc: average concentration of three measurements. Stdev: standard deviation (n=3).

	Exch		Carb		Fe/Mn		OrgC		Res	Total	
Element	Conc	Stdev	Conc	Stdev	Conc	Stdev	Conc	Stdev	Conc	Conc	Stdev
	µg/g	µg/g	µg/g	µg/g	µg/g	µg/g	µg/g	µg/g	µg/g	µg/g	µg/g
Al	151.6	71.3	655.0	69.0	3325.2	394.4	759.4	40.0	110888.5	115779.7	8628.3
As	0.7	0.1	0.3	0.1	6.9	0.2	3.4	0.1	224.1	235.4	17.0
B	10.6	0.8	3.4	0.4	10.1	0.9	0.6	0.2	274.5	299.2	32.0
Ba	0.7	0.6	12.2	0.2	23.7	0.4	1.5	0.2	631.2	669.3	49.2
Ca	563.3	7.6	27.1	1.3	84.1	1.2	205.7	18.0	1180.2	2060.4	129.3
Ce	2.4	0.1	2.2	0.1	5.8	0.6	1.7	0.1	48.1	60.1	8.8
Co	1.3	0.2	1.7	0.1	19.0	1.9	3.3	0.3	<0.1	25.1	1.8
Cr	0.3	0.02	<0.3		1.5	0.2	0.3	0.03	119.5	122.0	7.9
Cu	1.1	0.2	2.9	0.3	25.8	0.7	93.7	5.8	<0.1	57.0	8.8
Fe	135.1	64.0	142.2	61.7	5977.7	3142.9	875.5	23.2	23823.2	30953.7	2043.1
K	201.9	13.7	66.1	8.5	191.9	8.9	15.1	1.4	34272.4	34747.4	2544.1
Li	2.7	0.2	1.1	0.1	2.6	0.0	1.0	0.1	115.7	123.2	8.9
Mn	14.4	0.5	3.4	0.4	40.4	7.9	2.3	0.2	91.7	152.2	12.0
Mo	0.8	0.3	1.4	0.4	32.6	0.9	5.1	0.4	244.8	284.7	18.7
Ni	2.2	0.4	4.0	0.3	40.4	3.4	5.8	0.4	58.1	110.5	7.2
P	6.8	0.9	<0.3		23.5	0.8	91.0	9.7	354.7	476.3	33.1
Pb	<0.3		0.7	0.1	5.2	0.2	0.2	0.04	20.6	27.1	1.6
S	633.9	38.8	181.0	13.1	1153.8	90.3	1144.2	39.0	2669.5	5782.5	322.1
Si	<0.3		<0.3		123.3	46.9	<0.1		302261.6	302385.6	28174.4
Sr	6.6	0.2	0.9	0.04	5.4	0.2	0.4	0.02	70.7	84.0	6.3
Th	<0.3		<0.3		<0.7		0.5	0.02	15.8	17.6	2.3
Ti	0.4	0.1	0.3	0.04	0.3	0.1	1.1	0.04	3286.8	3288.9	167.7
U	45.0	5.2	317.6	29.2	421.8	39.5	7.5	1.2	358.5	1150.5	99.6
V	0.6	0.1	<0.3		3.4	0.1	0.7	0.05	315.6	320.5	21.6
Zn	4.7	1.0	6.3	6.8	36.9	1.8	8.0	0.7	1.2	57.0	10.5

Table B.12 Sequential extraction results for DJX-91 in triplicates. Exch: exchangeable. Carb: bound to carbonates. Fe/Mn: bound to amorphous iron and manganese oxides. OrgM: bound to organic matter. Res: residual (calculated). Conc: average concentration of three measurements. Stdev: standard deviation (n=3).

	Exch		Carb		Fe/Mn		OrgC		Res	Total	
Element	Conc	Stdev	Conc	Stdev	Conc	Stdev	Conc	Stdev	Conc	Conc	Stdev
	µg/g	µg/g	µg/g	µg/g	µg/g	µg/g	µg/g	µg/g	µg/g	µg/g	µg/g
Al	50.3	2.7	913.2	17.4	4731.9	174.6	1357.7	63.5	83439.6	90492.7	1918.4
As	0.6	0.1	3.7	0.2	71.5	3.7	65.0	2.3	57.2	198.0	3.3
B	10.7	0.1	6.5	0.1	19.3	3.5	0.8	0.1	187.8	225.1	11.8
Ba	3.4	0.4	21.7	1.7	27.4	1.8	0.7	0.1	148.3	201.4	2.6
Ca	743.8	17.7	32.9	3.0	176.0	11.2	364.2	15.5	1302.3	2619.3	159.7
Ce	1.1	0.03	0.7	0.01	3.3	0.1	1.7	0.1	92.6	99.5	4.0
Co	0.5	0.02	1.0	0.01	12.9	0.3	4.8	0.1	2.6	21.8	0.1
Cr	<0.3		0.5	0.2	4.1	0.1	0.7	0.04	109.0	114.6	0.7
Cu	3.3	3.1	3.8	0.7	16.0	0.7	15.0	0.5	10.9	48.9	3.8
Fe	69.2	5.2	95.8	0.6	5084.0	763.4	1184.6	31.7	20325.3	26758.9	345.1
K	254.4	17.9	81.1	0.2	300.5	20.8	10.9	3.2	31916.4	32563.3	537.4
Li	2.7	0.04	0.9	0.02	4.8	0.2	1.1	0.03	80.9	90.4	0.7
Mn	10.6	0.2	2.2	0.03	23.0	0.8	3.1	0.1	83.2	122.1	0.3
Mo	1.4	0.01	10.2	0.3	165.1	9.5	20.4	2.7	87.6	284.6	4.4
Ni	1.2	0.04	2.0	0.1	43.0	1.6	10.3	0.2	44.4	100.9	1.4
P	5.8	2.3	<0.3		44.0	1.7	192.6	4.6	86.6	329.4	28.9
Pb	<0.3		0.7	0.01	5.8	0.4	0.3	0.1	18.3	25.3	0.4
S	1139.1	27.0	462.1	5.0	1402.9	93.8	1481.0	19.9	146.2	3770.4	94.7
Si	<0.3		<0.3		235.4	142.0	<0.1		241244.7	241480.9	39853.0
Sr	9.8	0.2	1.3	0.04	7.8	0.6	0.6	0.04	65.9	85.4	1.3
Th	<0.3		0.5	0.01	1.3	0.1	1.1	0.04	19.9	23.1	0.4
Ti	<0.3		<0.3		0.4	0.1	2.2	0.1	2711.9	2715.2	69.4
U	74.6	1.5	570.8	4.4	437.9	1.2	17.7	1.2	247.8	1348.7	40.4
V	0.5	0.1	<0.3		5.3	0.2	1.0	0.04	284.6	291.7	2.9
Zn	1.9	0.3	12.7	9.3	14.5	0.6	3.6	0.4	51.0	83.8	9.0

Table B.13 Sequential extraction results for soil Soil1 in triplicates. Exch: exchangeable. Carb: bound to carbonates. Fe/Mn: bound to amorphous iron and manganese oxides. OrgM: bound to organic matter. Res: residual (calculated). Conc: average concentration of three measurements. Stdev: standard deviation (n=3).

	Exch		Carb		Fe/Mn		OrgM		Res	Total	
	Conc	Stdev	Conc	Stdev	Conc	Stdev	Conc	Stdev	Conc	Conc	Stdev
	µg/g	µg/g	µg/g	µg/g	µg/g	µg/g	µg/g	µg/g	µg/g	µg/g	µg/g
Al	10.9	3.5	42.0	0.3	389.5	14.8	286.7	27.2	9689.9	10419.0	1645.1
K	277.9	2.6	30.2	0.3	10.7	0.6	8.1	1.2	3313.0	3639.9	506.6
P	0.5	0.1	1.3	0.1	28.4	1.7	74.7	9.2	39.9	144.7	25.8
S	36.1	1.9	3.5	0.4	10.5	1.2	148.9	10.1	<0.1	175.8	22.2
Ca	455.6	15.2	24.1	1.0	61.7	2.0	56.5	16.1	501.6	1099.5	208.5
V	0.1	0.004	<0.1		1.1	0.03	0.8	0.1	9.9	11.9	2.7
Cr	<0.1		0.1	0.003	1.0	0.02	1.5	0.1	<0.1	11.9	3.4
Mn	8.8	0.6	1.9	0.01	7.7	0.3	1.4	0.2	46.7	66.5	20.7
Fe	17.5	5.3	49.2	2.3	1072.2	37.0	393.2	18.8	4586.3	6118.3	1408.8
Co	0.2	0.01	0.1	0.001	0.5	0.02	0.2	0.02	1.4	2.3	0.5
Ni	0.4	0.04	0.2	0.01	1.5	0.04	0.7	0.1	3.8	6.6	1.2
Cu	0.7	0.1	0.3	0.01	1.0	0.01	3.3	0.4	2.1	7.4	1.2
Zn	<0.1		<0.1		1.2	0.1	0.4	0.1	<0.1	10.3	8.6
Sr	6.2	0.3	0.4	0.01	0.2	0.01	0.1	0.03	27.7	34.6	2.7
As	<0.1		<0.1		0.4	0.02	0.2	0.02	0.7	1.4	0.3
Se	<0.1		<0.1		<0.1		0.2	0.01	<0.1	0.2	0.1
Mo	<0.1		<0.1		0.1	0.003	0.3	0.02	0.1	0.5	0.1
Cd	<0.1		<0.1		<0.1		0.0	0.00	<0.1	<0.1	
Ba	5.1	0.2	1.6	0.04	1.5	0.1	0.8	0.1	88.9	97.9	10.8
Ce	0.2	0.02	1.2	0.04	2.5	0.1	4.0	0.5	16.6	24.4	2.5
Pb	<0.1		0.1	0.04	0.3	0.1	<0.1		<0.1	1.7	0.7
Th	<0.1		<0.1		<0.1		0.5	0.1	3.3	3.8	0.6
U	0.1	0.01	3.3	0.2	1.9	0.2	1.2	0.6	-0.1	6.4	1.0

Table B.14 Sequential extraction results for soil Soil2 in triplicates. Exch: exchangeable. Carb: bound to carbonates. Fe/Mn: bound to amorphous iron and manganese oxides. OrgM: bound to organic matter. Res: residual (calculated). Conc: average concentration of three measurements. Stdev: standard deviation (n=3).

	Exch		Carb		Fe/Mn		OrgM		Res	Total	
	Conc	Stdev	Conc	Stdev	Conc	Stdev	Conc	Stdev	Conc	Conc	Stdev
	µg/g	µg/g	µg/g	µg/g	µg/g	µg/g	µg/g	µg/g	µg/g	µg/g	µg/g
Al	22.2	3.1	46.4	6.0	335.1	14.4	163.3	27.1	7808.2	8375.2	652.0
K	271.8	9.9	24.6	1.5	7.3	0.3	8.8	0.9	2835.2	3147.7	326.2
P	0.4	0.1	1.1	0.1	27.8	1.3	43.6	6.4	36.4	109.2	4.5
S	10.2	0.9	<0.1		<0.1		<0.1		<0.1	25.1	3.3
Ca	162.6	11.4	4.1	0.4	60.7	0.5	79.9	24.1	1046.8	1354.1	259.6
V	0.1	0.01	<0.1		0.7	0.03	0.5	0.1	<0.1	7.7	2.1
Cr	<0.1		0.1	0.03	0.9	0.03	0.5	0.1	5.7	7.2	2.0
Mn	0.8	0.1	1.4	0.4	5.6	1.1	0.7	0.1	26.6	35.2	4.0
Fe	21.9	4.5	22.4	5.0	686.4	34.0	160.8	36.0	3352.3	4243.8	758.3
Co	<0.1		<0.1		0.3	0.03	0.1	0.01	0.9	1.3	0.3
Ni	0.1	0.01	<0.1		0.5	0.03	0.2	0.04	2.6	3.4	0.8
Cu	0.1	0.1	<0.1		<0.1		0.1	0.02	<0.1	2.0	0.3
Zn	<0.1		<0.1		0.2	0.1	<0.1		<0.1	13.8	2.0
Sr	3.8	0.3	0.1	0.003	0.1	0.002	0.1	0.01	34.1	38.2	6.8
As	<0.1		<0.1		<0.1		<0.1		0.6	0.6	0.1
Se	<0.1		<0.1		<0.1		<0.1		<0.1	<0.1	
Mo	<0.1		<0.1		<0.1		<0.1		<0.1	0.1	0.02
Cd	<0.1		<0.1		<0.1		<0.1		<0.1	<0.1	
Ba	4.0	0.4	1.0	0.1	1.0	0.1	0.2	0.05	82.2	88.4	5.5
Ce	0.2	0.02	0.2	0.03	0.8	0.03	0.9	0.2	11.9	14.0	1.7
Pb	<0.1		<0.1		<0.1		<0.1		<0.1	1.0	0.6
Th	<0.1		<0.1		<0.1		0.1	0.01	1.6	1.7	0.3
U	<0.1		0.1	0.01	0.1	0.004	<0.1		0.2	0.5	0.1

Table B.15 Total digestion results of rock samples found on the shores of the pit lakes, obtained ore samples, and the sediments collected by sediment traps. See section "Rock and ore samples mineralogy and chemistry results" of Appendix B for more details.

	Units	Rock D	Rock DJX	Red Ore	White Ore	D-pit trap	DJX-pit trap
Al	%	6.1	10.1	6.6	7.4	1.5	4.7
As	ppm	13.2	3.4	86.7	277.1	1953.6	55.3
B	ppm	189.0	268.0	1351.8	2117.0	114.7	442.6
Ba	ppm	59.6	40.6	844.8	1078.4	267.8	149.2
Ca	ppm	1262.6	201.7	23408.3	1506.6	5441.0	7463.8
Cd	ppm	-	-	-	-	0.1	0.5
Ce	ppm	37.6	9.9	193.5	121.9	144.1	92.2
Co	ppm	4.7	4.4	11.4	50.9	17.0	459.7
Cr	ppm	79.2	116.8	160.5	50.5	28.2	56.5
Cs	ppm	-	-	-	-	381.4	447.6
Cu	ppm	1.5	1.5	2563.8	867.6	17.6	254.6
Fe	%	2.4	0.8	15.7	1.8	22.3	4.5
K	%	2.6	3.4	2.0	3.9	0.5	2.0
Li	ppm	37.1	118.3	511.1	453.8	16.6	99.4
Mg	%	0.5	1.8	1.3	2.1	0.3	1.5
Mn	ppm	705.7	18.8	982.9	2448.1	2252.9	1893.1
Mo	ppm	1.8	1.1	16.0	422.4	19.1	207.2
Na	ppm	126.9	250.6	1143.8	1587.6	686.9	3564.4
Ni	ppm	23.8	61.1	266.6	244.9	46.5	896.4
P	ppm	554.8	75.3	705.9	307.7	792.7	639.5
Pb	ppm	3.0	2.1	21.3	256.7	15.8	29.3
S	ppm	50.1	56.0	633.6	337.1	3828.4	20919.0
Sr	ppm	29.6	18.1	301.2	73.8	75.4	94.6
Th	ppm	23.2	8.6	100.0	879.4	10.6	12.6
U	%	0.0006	0.0007	15.6	18.9	377.8 ppm	1449.7 ppm
V	ppm	119.2	123.8	2603.7	1562.9	60.0	176.5
Zn	ppm	14.8	94.8	240.2	9.9	12.7	175.7

Table B.16 Extraction of As, U and Ni from D-6 and D-9 sediments using weak oxalic and citric acids. The values represent the amount of elements relative to the value obtained by total digestion. For comparison, the amounts of the elements extracted by the sequential extraction steps 1-4 are shown (relative to the total amount).

	Acid (mM)	As	U	Ni
D-6 seq extr steps 1-4		21%	85%	79%
D-6 oxalic acid	6.5	2%	33%	30%
D-6 oxalic acid	31.9	25%	90%	67%
D-6 citric acid	6.8	4%	73%	52%
D-6 citric acid	17.7	49%	114%	77%
D-9 seq extr steps 1-4		24%	62%	47%
D-9 oxalic acid	6.8	5%	43%	19%
D-9 oxalic acid	35.0	32%	70%	49%
D-9 citric acid	6.6	11%	65%	33%
D-9 citric acid	33.9	31%	76%	47%

Table B.17 SEM/EDS results for U-rich hotspots found in D-pit and the DJX-pit sediments. "at%": normalized atom-%. The hotspot indices do not correspond to indices shown in the synchrotron results.

	Al	C	Ca	Ce	Cl	Fe	K	La	Mg	Nd	O	P	Pb	S	Th	Ti	U	O/U	U/Pb
Normal thin sections																			
D6_1	4.7	-	0.9	5.4	-	1.3	0.5	2.8	-	1.9	59.6	11.6	-	10.5	0.9	-	-	-	-
D9_1	6.8	-	-	-	-	2.1	-	-	1.1	-	57.9	-	2.8	15.5	-	1.2	12.7	4.6	4.5
D9_3	5.3	28.7	-	-	-	1.8	-	-	0.8	-	41.8	-	1.6	9.4	-	-	10.7	3.9	6.7
D9_4	8.7	-	-	-	-	1.7	-	-	2.4	-	57.8	-	1.4	13.2	-	-	14.9	3.9	10.6
D10_1	10.3	-	-	-	3.6	2.3	-	-	1.8	-	58.8	-	0.6	18.8	-	0.8	3.1	19.0	5.2
D10_2	5.1	34.2	2.1	-	-	1.2	-	-	0.7	-	38.3	-	0.9	9.3	-	-	8.2	4.7	9.1
D10_3	2.5	42.1	-	-	-	0.8	-	-	0.1	-	37.2	-	2.2	4.7	-	-	10.4	3.6	4.7
Quartz glass thin sections																			
D9_qrz_H	4.0	-	-	-	-	-	-	-	-	-	66.2	-	2.5	7.3	-	-	19.9	3.3	7.9
D9_qrz_H	6.4	-	-	-	-	-	-	-	-	-	65.7	-	2.7	10.6	-	-	14.6	4.5	5.3
D9_qrz_H	4.1	-	-	-	-	-	-	-	-	-	61.5	-	3.6	9.6	-	-	21.2	2.9	6.0
D9_qrz_H	4.5	-	-	-	-	-	-	-	-	-	62.6	-	2.1	8.4	-	-	22.4	2.8	10.5
D9_qrz_H	4.5	-	-	-	-	-	-	-	-	-	64.7	-	2.1	7.8	-	-	20.8	3.1	9.8
D10_qrz_	6.2	-	-	-	-	-	-	-	-	-	62.8	-	2.7	8.4	-	-	18.4	3.4	6.8
D10_qrz_	3.4	-	-	-	-	-	-	-	-	-	70.7	-	3.2	6.2	-	-	16.5	4.3	5.2
D10_qrz_	7.1	-	-	-	-	-	-	-	-	-	64.6	-	2.8	9.8	-	-	15.8	4.1	5.6
D10_qrz_	6.0	-	-	-	-	-	-	-	-	-	60.2	-	2.7	12.2	-	-	18.8	3.2	6.9
DJX13a_	3.1	-	-	8.1	-	-	-	3.5	-	-	59.0	16.4	-	9.1	0.9	-	-	-	-
DJX8_HS	2.9	-	-	8.9	-	-	-	5.3	-	-	58.7	14.8	-	9.4	-	-	-	-	-
DJX4c_H	3.3	-	-	7.4	-	-	-	3.5	-	-	63.0	15.6	-	6.5	0.8	-	-	-	-
DJX4c_H	4.5	-	-	-	-	-	-	-	-	-	63.4	-	2.3	12.9	-	-	17.0	3.7	7.5
DJX4c_H	4.2	-	-	-	-	-	-	-	-	-	71.6	-	2.1	10.2	-	3.0	8.9	8.1	4.1
DJX4c_H	3.1	-	-	-	-	-	-	-	-	-	66.0	-	3.0	10.3	-	-	17.6	3.7	5.9
Sequential extraction: selected hotpot EDS																			
D10 step	7.0	-	-	-	-	1.51	-	-	1.19	-	58.1	-	1.0	22.6	-	-	8.7	6.7	8.5
D10 step	4.7	-	-	-	-	2.47	-	-	0.86	-	63.3	-	3.2	11.3	-	-	14.2	4.5	4.4
D10 step	9.1	-	-	-	-	1.73	-	-	1.85	-	56.2	-	1.8	17.7	-	-	11.5	4.9	6.3

Table B.18 Uranium XANES and mineralogy (Laue indexing) data obtained at the VESPERS beamline for D-pit samples. Shown are (from left to right): XANES linear combination fitting results for bulk sediment samples and U-rich hotspots, Pearson's correlation indices calculated based on XRF elemental maps, and microdiffraction results. "gau": gauthierite. "van": vandendriesscheite. X^2 and r-factor are linear combination fitting parameters. See Figure B.1 for XANES data and fits.

Hotspot name	Linear combination fitting				Pearson's correlation factors for U											Laue fitting
	U(VI)	U(IV)	X^2	r-factor	As	Ca	Fe	K	Mn	Ni	Pb	S	Th	Zn	U	
D6_1_HS1	58%	42%	0.1975	0.0128	0.82	0.23	0.90	0.32	0.01	0.33	0.43	0.13	-	-	1.00	-
D6_2_HS1	-	-	-	-	-0.73	0.49	0.92	-	0.91	0.91	0.97	0.54	-	-	1.00	van (28/36)
D9_1_HS1	49%	51%	0.5143	0.0454	0.94	0.49	-0.43	0.70	0.69	0.70	0.99	0.39	-	-	1.00	van (23/23)
D9_2_HS1	38%	62%	0.1819	0.0117	0.97	0.32	0.26	0.79	0.31	-	-	-	-	-	1.00	-
D9_2_HS2	44%	56%	0.1768	0.0126	0.96	0.22	-0.15	0.60	0.19	-	-	-	-	-	1.00	-
D9_2_HS3	-	-	-	-	-0.72	0.52	0.92	-	0.91	0.94	0.97	0.62	-	-	1.00	van (235/261)
D9_4_HS1	39%	61%	0.1365	0.0102	0.92	0.07	0.03	0.84	0.22	0.44	1.00	0.19	-	-	1.00	gau (10/14)
D9_6_HS1	-	-	-	-	0.96	-0.13	0.12	-	0.09	0.36	0.99	0.18	-	-	1.00	van (38/52)
D9_7_HS1	38%	62%	0.1643	0.0122	0.99	0.55	-0.19	0.97	0.80	0.21	0.97	0.07	-	-	1.00	van (135/179)
D9_7_HS2	30%	70%	0.1356	0.0088	0.97	0.00	-0.09	0.38	-0.04	-	-	-	-	-	1.00	-
D9_7_HS3	32%	68%	0.1232	0.0087	0.99	0.16	0.30	0.56	0.28	-	-	-	-	-	1.00	-
D9_9_HS1	42%	58%	0.1821	0.0136	0.99	0.22	-0.14	0.92	0.00	-	-	-	-	-	1.00	no fit
D9_9_HS2	36%	64%	0.2129	0.0143	0.97	0.10	-0.12	0.65	0.13	-	-	-	-	-	1.00	no fit
D10_4_HS1	13%	87%	0.1184	0.0090	0.79	0.11	0.11	0.49	0.23	0.44	1.00	0.19	-	-	1.00	van (47/60)
D10_4_HS2	22%	78%	0.1006	0.0072	0.49	0.03	0.00	0.56	0.03	-	-	-	-	-	1.00	-
D10_5_HS1	-	-	-	-	0.29	0.12	0.20	-	0.29	0.34	0.99		-	-	1.00	van (67/90)
D10_6_HS1	45%	55%	0.1661	0.0109	0.93	0.12	0.01	0.48	0.16	-	-	-	-	-	1.00	van (21/27)
D10_7_HS1	40%	60%	0.1316	0.0099	0.80	0.22	0.53	0.39	0.64	-	-	-	-	-	1.00	no fit
D10_8_HS1	8%	92%	0.1977	0.0159	0.98	-0.05	-0.32	-	0.21	0.33	1.00	0.13	0.99	-	1.00	van (13/14)
D10_10_HS1	26%	74%	0.2185	0.0142	0.98	0.04	-0.06	0.67	0.11	-	-	-	-	-	1.00	van (35/36)
D10_11_HS1	0%	100%	0.1747	0.0120	0.91	0.73	0.52	-	0.80	0.91	0.91	-	0.86	-	1.00	no fit
D22_1_HS1	-	-	-	-	-0.02	0.05	0.04	-	0.03	-	0.12	-	0.32	-	1.00	van (62/87)
D22_1_HS2	-	-	-	-	0.12	-0.08	-0.06	-	-0.03	-	0.31	-	0.77	-	1.00	van (53/59)
D22_1_HS4	-	-	-	-	0.94	0.22	0.86	-	0.60	-	0.83	-	0.60	-	1.00	van (45/51)
D22_1_HS5	-	-	-	-	0.59	0.20	0.55	-	0.55	-	0.09	-	0.10	-	1.00	gau (67/77)
D22_1_HS6	38%	62%	2.8383	0.1369	0.94	0.87	-0.15	-	0.78	-	0.92	-	0.90	-	1.00	-
D22_1_HS7	21%	79%	0.2412	0.0138	0.98	0.02	-0.13	-	-0.06	-	0.99	-	0.50	-	1.00	-
D6_bulk	80%	20%	0.3118	0.0121	-	-	-	-	-	-	-	-	-	-	-	-
D8_bulk	77%	23%	0.1696	0.0073	-	-	-	-	-	-	-	-	-	-	-	-
D10_bulk	98%	2%	0.2589	0.0098	-	-	-	-	-	-	-	-	-	-	-	-
Hotspots average	33%	67%	0.3270	0.0200	0.69	0.22	0.16	0.62	0.33	0.54	0.79	0.27	0.63	-	1.00	-
Bulk average D-pit	85%	15%	0.2467	0.0098	-	-	-	-	-	-	-	-	-	-	-	-

Table B.19 Uranium XANES and mineralogy (Laue indexing) data obtained at the VESPERS beamline for DJX-pit samples. Shown are (from left to right): XANES linear combination fitting results for bulk sediment samples and U-rich hotspots, Pearson's correlation indices calculated based on XRF elemental maps, and microdiffraction results. "gau": gauthierite. "van": vandendriesscheite. X^2 and r-factor are linear combination fitting parameters. See Figure B.1 for XANES data and fits.

Hotspot name	Linear combination fitting				Pearson's correlation factors for U											Laue fitting
	U(VI)	U(IV)	X^2	r-factor	As	Ca	Fe	K	Mn	Ni	Pb	S	Th	Zn	U	
DJX4c_2_HS1	42%	58%	0.5686	0.0242	1.00	0.33	0.01	-	0.03	0.05	1.00	-	-	0.17	1.00	-
DJX4c_3_HS1	42%	58%	0.9121	0.0343	1.00	0.79	-0.14	-	0.02	0.56	0.97	-	-	0.69	1.00	-
DJX4c_4_HS2	84%	16%	0.2722	0.0113	0.33	0.92	0.14	-	0.73	0.58	0.08	-	-	0.11	1.00	-
DJX91_1_HS1	-	-	-	-	0.11	0.33	0.28	-	0.28	-	0.10		0.13	-	1.00	van (14/14)
DJX91_1_HS2	-	-	-	-	0.18	0.17	0.51	-	0.35	-	0.20		0.15	-	1.00	van (30/33)
DJX91_2_HS1	-	-	-	-	0.07	0.21	0.30	-	0.32	-	0.08		0.14	-	1.00	gau (18/22)
DJX13a_bulk	76%	24%	0.3381	0.0136	-	-	-	-	-	-	-	-	-	-	-	-
DJX8_bulk	83%	17%	0.8011	0.0410	-	-	-	-	-	-	-	-	-	-	-	-
DJX4c_bulk	78%	22%	0.2918	0.0140	-	-	-	-	-	-	-	-	-	-	-	-
Uranyl nitrate hexahydrate	98%	2%	0.2013	0.0147	-	-	-	-	-	-	-	-	-	-	-	-
Autunite	100%	0%	1.0637	0.0562	-	-	-	-	-	-	-	-	-	-	-	-
Uraninite/Zippeite	78%	22%	0.2437	0.0126	-	-	-	-	-	-	-	-	-	-	-	-
Hotspots average	56%	44%	0.5843	0.0233	0.45	0.46	0.18	-	0.29	0.40	0.41	-	0.14	0.32	1.00	-
Bulk average DJX-pit	79%	21%	0.4770	0.0228	-	-	-	-	-	-	-	-	-	-	-	-

Table B.20 Arsenic XANES data obtained at the VESPERS beamline for D-pit and DJX-pit samples. Shown are (from left to right): XANES linear combination fitting results for bulk sediment samples and U-rich hotspots, and Pearson's correlation indices calculated based on XRF elemental maps. Fitted species are indicated with letters A-E. A: $As^{III}_2O_3$. B: $As^{V}_2O_5$. C: $Ca_3(As^{V}O_4)_2$. D: $Na_2HAs^{V}O_4$. E: $As^{III}_2S_3$. X^2 and r-factor are linear combination fitting parameters. See Figure B.2 for XANES data and fits.

Hotspot name	Linear combination fitting						Pearson's correlation factors for As							
	As(III)	As(III) species	As(V) or As(-I)	As(V)/As(-I) species	X^2	r-factor	As	Ca	Fe	Mn	Ni	Zn	Pb	U
D6_HS1 (glass slide)	79%	A	21%	B	0.7854	0.0156	1.00	0.22	0.40	0.34	0.54	-	0.26	0.63
D9_1_HS1 (glass slide)	78%	A	22%	D	1.2488	0.0254	1.00	0.39	-0.04	0.54	0.80	-	0.97	0.96
D9_4_HS1 (glass slide)	77%	A	23%	D	1.1375	0.0229	1.00	0.32	0.16	0.34	0.47	-	0.75	0.75
D9_9_HS1 (glass slide)	82%	A	18%	B	1.2809	0.0256	1.00	0.15	-0.35	-0.23	0.03	-	0.76	0.89
D10_1_HS1	48%	A	52%	B	2.4683	0.0153	1.00	0.78	-0.22	0.31	0.32	0.47	0.98	0.99
D10_2_HS1	46%	A	54%	B	2.8374	0.0141	1.00	0.41	-0.46	0.28	0.19	0.26	0.98	0.99
D10_4_HS1	40%	A	60%	B	4.5953	0.0194	1.00	0.50	0.03	0.54	0.32	0.30	0.93	0.98
D10_5_HS1 (glass slide)	83%	33% A, 50% E	17%	D	0.0128	0.0037	1.00	0.30	0.21	0.26	0.36	-	0.28	0.29
D10_7_HS1 (glass slide)	70%	A	30%	C	0.7986	0.0162	1.00	0.50	0.81	0.41	0.90	-	0.88	0.87
D10_11_HS1 (glass slide)	74%	A	26%	C	0.9544	0.0201	1.00	0.75	0.49	0.83	0.91	-	0.95	0.99
D6 bulk	62%	A	38%	C	0.8795	0.0168	-	-	-	-	-	-	-	-
D8 bulk	65%	A	35%	C	1.2109	0.0225	-	-	-	-	-	-	-	-
D10 bulk	48%	A	52%	D	1.2940	0.0227	-	-	-	-	-	-	-	-
DJX4c_2_HS1*	22%	A	78%	B	36.5593	0.2616	1.00	0.34	0.03	0.04	0.06	0.18	1.00	1.00
DJX4c_3_HS1*	60%	E	40%	B	130.7905	0.7857	1.00	0.79	-0.17	0.02	0.58	0.69	0.97	1.00
DJX4c_4_HS2	33%	A	67%	D	9.3739	0.1959	1.00	0.36	0.12	0.38	0.76	0.57	0.07	0.33
DJX13a_bulk	0%		100%	87% D, 13% B	1.9167	0.0285	-	-	-	-	-	-	-	-
DJX8_bulk	42%	A	59%	D	0.9784	0.0184	-	-	-	-	-	-	-	-
DJX4c_bulk	45%	A	55%	D	1.2967	0.0246	-	-	-	-	-	-	-	-
Glass slide	70%	A	31%	B	7.8655	0.1197	-	-	-	-	-	-	-	-
Hotspot average D-pit	68%		32%		1.6119	0.0178	1.00	0.43	0.10	0.36	0.48	0.34	0.77	0.83
Hotspot average DJX-pit	33%		67%		9.3739	0.1959	1.00	0.58	-0.03	0.20	0.67	0.63	0.52	0.67
Bulk average D-pit	58%		42%		1.1281	0.0207	-	-	-	-	-	-	-	-
Bulk average DJX-pit	29%		71%		1.3973	0.0238	-	-	-	-	-	-	-	-

* noisy data (not included for average)

Table B.21 Nickel XANES data obtained at the VESPERS beamline for D-pit. Shown are (from left to right): XANES linear combination fitting results for bulk sediment samples and U-rich hotspots, and Pearson's correlation indices calculated based on XRF elemental maps. Fitted species are indicated with letters A-B. A: NiO. B: NiSe. X^2 and r-factor are linear combination fitting parameters. See Figure B.3 for XANES data and fits.

Hotspot name	Linear combination fitting					Linear correlation factors for Ni					
	$NiNO_3$	other	other species	X2	r-factor	As	Fe	Ni	Pb	Th	U
D10_5_HS2	78%	22%	B	1.5294	0.0143	0.87	0.76	1.00	0.66	0.66	0.53
D10_12_HS1	65%	35%	A	0.9089	0.0078	-0.01	0.83	1.00	0.18	0.55	-0.32
D10_13_HS1	71%	29%	A	1.2031	0.0094	-0.12	0.32	1.00	0.19	0.16	0.04
D10_16_HS1	51%	49%	A	1.8249	0.0166	0.91	0.24	1.00	0.16	0.05	0.08
Hotspot average	66%	31%		1.3666	0.0120	0.41	0.54	1.00	0.30	0.36	0.08

Table B.22 U speciation calculations for samples collected and treated based on Anderson (1984). "Dil" contains the sample dilution prior to sample treatment. The columns 3-5 show the measured U concentrations in solutions before and after HF addition and the resulting difference. The Ca column shows the Ca concentration of the added sample (considering dilution) and columns 7-8 show the corresponding slopes obtained by linear approximation. The linear combination fitting (LCF) results for with Ca and without Ca are shown in the last columns. Without Ca in the case of U(VI), 61% of U precipitated (slope 0.61), whereby in the case of U(IV), 93% (slope 0.93). With Ca, 57-83% of U(VI) precipitated with highest slopes obtained for low Ca concentrations, suggesting that Ca is competing with Nd for F, as was expected. In the Ca calibration solutions, 80-97% of U(IV) precipitated, again, with highest slopes for lowest Ca concentrations. No explanation was yet found for the fact that low Ca concentration calibration did not result in similar slopes as without Ca (especially in the oxic samples).

Sample		U (ppm)			Ca (ppm)	LCF with Ca				LCF without Ca	
Name	Dil	before HF	after HF	precipitated	before HF	U(VI) slope	U(IV) slope	U(VI)	U(IV)	U(VI)	U(IV)
D5	-	0.153	0.041	0.112	11.8	0.747	0.887	109%	-9%	64%	36%
D13	-	0.144	0.035	0.109	15.6	0.661	0.848	49%	51%	57%	43%
D20	-	0.074	0.014	0.060	17.3	0.624	0.830	7%	93%	43%	57%
DJX5	10x	0.017	0.005	0.012	3.7	0.831	0.974	176%	-76%	409%	-309%
DJX20	10x	0.029	0.007	0.022	6.4	0.803	0.945	129%	-29%	176%	-76%
DJX40	10x	0.038	0.009	0.029	7.1	0.796	0.937	127%	-27%	186%	-86%
DJX65	10x	0.164	0.043	0.121	19.8	0.569	0.805	28%	72%	78%	22%

Table B.23 SEM/EDS results for precipitates found in D-pit (spot nr. 18-33) and the DJX-pit (spot nr. 52-64) water samples after 7.5 months of storage. "wt%": normalized weight-%. "Ø": average value. Carbon wt% not included.

Spot Nr.	O (wt%)	Na (wt%)	Mg (wt%)	Al (wt%)	Si (wt%)	S (wt%)	Cl (wt%)	K (wt%)	Ca (wt%)	Fe (wt%)	Fe/O (mol/mol)	Al/Si (mol/mol)	Al/K (mol/mol)	Si/K (mol/mol)	Ca/S (mol/mol)
D-pit 20 m															
18	21.33				0.65				0.64	22.1	0.30				
19	20.60				0.52				0.61	20.02	0.28				
20	20.95								0.48	12.8	0.18				
21	15.51									6.24	0.12				
22	21.47				0.6				0.81	16.35	0.22				
23	16.59									4.34	0.07				
24	23.51				0.67				0.62	15.48	0.19				
25	22.66				0.80				0.69	16.39	0.21				
26	24.16				0.68				0.75	17.28	0.20				
27	22.67				0.87				0.80	19.49	0.25				
29	13.95									5.86	0.12				
30	14.72									7.35	0.14				
31	13.75									3.62	0.08				
32	13.06									5.16	0.11				
33	9.52									0.84	0.03				
Ø 18-	18.30				0.68				0.68	11.55	0.18				
DJX-pit 65 m															
52	25.60		0.76	5.27	6.05	0.24		1.36		0.97	0.01	0.90	5.59	6.19	
53	32.32		1.21	8.95	12.39	0.31		2.47		1.59	0.01	0.75	5.24	6.99	
54	30.93		1.30	8.07	8.76	0.34		2.10		1.48	0.01	0.96	5.54	5.80	
55	32.84		1.06	9.93	12.88	0.18		3.66		0.93	0.01	0.80	3.92	4.91	
Ø 52-	30.42		1.08	8.05	10.02	0.27		2.40		1.24	0.01	0.83	4.85	5.82	
56	21.13		0.23	3.74	4.62			2.03				0.84	2.66	3.17	
57	32.07	0.16	0.97	5.44	5.01			0.93				1.13	8.45	7.50	
58	25.59		0.53	3.55	4.51			1.44				0.82	3.56	4.36	
Ø 56-	26.26	0.16	0.58	4.24	4.71			1.47				0.93	4.18	4.48	
60	36.77	0.31	0.24	0.87	22.03	0.38						0.04			
61	36.67	2.72	4.05	2.26	2.98	7.00	0.45	0.73				0.79	4.49	5.70	
62	38.29	2.68	4.62	1.98	2.89	9.56	0.47	0.97				0.71	2.96	4.15	
63	31.63	3.95	9.69		0.32	18.73	1.24								
64	34.46	3.27	2.95		0.28	14.96	0.28		12.18						0.65
Ø 60-	35.57	2.59	4.31	1.70	5.70	10.13	0.61	0.85	12.18			0.31	2.90	9.35	0.96

Table B.24 SEM/EDS results for sediments collected by sediment traps from the D-pit and DJX-pit. "at%": normalized atom-%. "Ø": average value. Carbon, chloride, silver, and titanium at% not included.

Spot Nr.	O (at%)	Na (at%)	Mg (at%)	Al (at%)	Si (at%)	P (at%)	S (at%)	K (at%)	Ca (at%)	Mn (at%)	Fe (at%)	Co (at%)	Ni (at%)	Sr (at%)	La (at%)	Ce (at%)	Nd (at%)	Th (at%)	U (at%)
DJX1	53.76		0.76	5.45	2.51	1.56	0.48	0.25	0.21		0.41			0.15	0.08	0.19			
DJX2	52.23		2.56	5.80	5.78		0.32	0.87			1.31								
DJX3	50.62		1.28	4.21	4.74		0.54	0.67			1.35								
DJX4	44.90		0.79	2.72	4.27	0.73	0.33	0.55	0.19		0.66								
DJX5	46.60	0.40	0.91	3.26	3.81		0.54	0.55	0.10	0.05	1.11								
DJX6	50.27	0.44	1.16	3.62	4.55		0.80	0.65	0.11		1.06								
DJX7	51.96		0.58	3.63	4.81		0.39	1.08			1.04								
DJX8	41.75		0.28	1.90	1.96	3.52		0.14	0.16		0.53				0.91	1.79	0.68		
DJX9	50.52		0.75	2.96	3.32		0.72	0.36		0.19	8.56								0.03
DJX10	37.32		0.62	1.45	1.84		5.01	0.22			2.12	1.45	1.15						
DJX11	36.69		0.71	2.32	3.09		6.55	0.46			3.32								
DJX12	39.34		0.86	2.04	2.43		4.35	0.29			3.00	0.55	0.46						
Ø DJX	46.33	0.42	0.94	3.28	3.59	1.94	1.82	0.51	0.15	0.12	2.04	1.00	0.81	0.15	0.50	0.99	0.68	-	0.03
D1	44.59			0.56	0.97			0.11	0.19		5.29								
D2	25.12			0.22	0.34						1.12								
D3	49.19		0.16	0.68	1.62			0.17	0.18	0.12	6.65								
D4	37.34			0.49	0.90		3.60	0.09	0.13		4.95								
D5	45.02		0.73	1.30	1.57						4.01								
D6	29.78			0.30	0.50		4.42				3.34								
D7	37.83			1.75	0.55	3.81			0.15		1.27				1.02	2.10	0.72	0.04	
D8	40.03			1.23	0.90				0.31		6.28								
Ø D	39.05	0.42	0.67	1.30	1.52	2.87	4.29	0.26	0.19	0.12	3.62	1.00	0.81	0.15	0.76	1.54	0.70	0.04	0.03

Table B.25 Top 30 OTUs and their relative distribution in percent. All top 30 OTUs were Bacteria. The bottom of the table contains the total amount of identified OTUs, and α-diversity indices, such as species richness (Chao) and species diversity (Shannon, Inverse Simpson).

OTU	D6	D9	D10	DJX4a	DJX12a	DJX68	DJX87	DJX91a	DJX91b	Taxonomy
OTU1	0.00	0.01	0.00	0.01	0.01	6.97	14.20	9.26	19.00	Bacteroidetes: Sphingobacteriia: Sphingobacteriales: Chitinophagaceae
OTU2	0.02	0.09	0.04	0.01	0.01	0.00	0.03	30.95	0.01	Proteobacteria: Alphaproteobacteria: Rhizobiales
OTU3	0.00	0.00	0.03	0.00	0.00	0.22	1.42	2.70	18.94	Proteobacteria: Betaproteobacteria
OTU4	0.10	0.07	0.06	0.18	0.61	1.35	3.11	1.32	14.73	Actinobacteria: Actinobacteria: Micrococcales: Microbacteriaceae
OTU5	6.63	11.00	8.88	0.08	0.01	0.02	0.00	0.01	0.01	Firmicutes: Clostridia: Clostridiales: Clostridiaceae-1: Clostridium-sensu-stricto-13
OTU7	0.01	0.00	0.00	0.08	0.36	8.69	3.74	0.34	0.95	Chloroflexi: KD4-96
OTU8	5.42	6.34	4.69	0.23	2.42	0.39	0.39	0.50	0.27	Proteobacteria: Betaproteobacteria: Burkholderiales: Comamonadaceae: Rhodoferax
OTU9	0.12	0.29	0.42	0.08	0.07	0.54	1.34	7.02	0.68	Proteobacteria: Betaproteobacteria: Nitrosomonadales: Gallionellaceae: Candidatus-Nitrotoga
OTU6	1.49	7.89	9.73	0.03	0.03	0.02	0.02	0.00	0.01	Proteobacteria: Deltaproteobacteria: Desulfuromonadales: Geobacteraceae: Geobacter
OTU10	0.00	0.00	0.00	0.00	0.00	8.16	2.09	0.02	0.53	Acidobacteria: Holophagae: Holophagales: Holophagaceae
OTU15	0.00	0.00	0.00	0.04	0.08	3.37	1.56	3.87	0.48	Proteobacteria: Betaproteobacteria
OTU12	0.04	0.26	0.15	0.19	0.14	0.81	1.35	1.87	4.04	Proteobacteria: Alphaproteobacteria: Rhizobiales: Bradyrhizobiaceae
OTU11	0.70	0.16	0.29	0.01	0.02	2.26	3.97	0.49	2.48	Bacteroidetes: Sphingobacteriia: Sphingobacteriales: Chitinophagaceae: Sediminibacterium
OTU13	4.52	2.82	9.74	0.02	0.00	0.01	0.00	0.01	0.00	Firmicutes: Bacilli: Bacillales: Planococcaceae
OTU124	0.01	0.01	0.01	0.00	0.01	3.67	4.17	1.01	0.34	Chloroflexi: KD4-96
OTU21	0.00	0.00	0.00	0.00	0.00	1.96	1.80	2.20	0.66	Proteobacteria: Gammaproteobacteria: Xanthomonadales: Xanthomonadaceae: Rhodanobacter
OTU6433	0.00	0.00	0.00	0.02	0.11	0.11	0.37	1.13	3.95	Proteobacteria: Betaproteobacteria: Nitrosomonadales: Gallionellaceae
OTU16	0.02	0.02	0.01	0.08	0.13	0.42	1.32	0.48	3.47	Proteobacteria: Alphaproteobacteria: Rhizobiales: Xanthobacteraceae: Pseudolabrys
OTU7439	0.00	0.01	0.02	0.00	0.02	0.19	1.20	3.55	0.85	Proteobacteria: Betaproteobacteria: Burkholderiales: Comamonadaceae: Polaromonas
OTU237	0.03	0.03	0.05	0.22	1.60	1.68	1.11	0.08	0.96	Proteobacteria: Betaproteobacteria: Burkholderiales: Comamonadaceae
OTU27	1.47	1.73	1.59	2.95	0.16	0.01	0.01	0.00	0.00	Bacteroidetes: Bacteroidetes-vadinHA17
OTU18	0.01	0.03	0.02	0.00	0.00	1.39	1.40	1.81	0.63	Bacteroidetes: Sphingobacteriia: Sphingobacteriales: Chitinophagaceae
OTU14	0.36	5.59	2.59	0.00	0.00	0.00	0.00	0.00	0.00	Microgenomates
OTU23	0.01	0.02	0.00	0.01	0.12	0.55	1.23	0.00	2.52	Verrucomicrobia: Verrucomicrobiae: Verrucomicrobiales: Verrucomicrobiaceae: Prosthecobacter
OTU31	0.08	0.24	0.42	0.04	0.13	0.71	2.52	0.73	0.21	Bacteroidetes: Sphingobacteriia: Sphingobacteriales: Chitinophagaceae: Ferruginibacter
OTU17	0.00	0.00	0.00	0.00	0.00	0.14	4.89	0.00	0.38	Verrucomicrobia: Verrucomicrobia-Incertae-Sedis: Candidatus-Methylacidiphilum
OTU49	0.25	0.07	0.07	3.07	0.15	0.33	0.17	0.02	0.04	Chloroflexi: KD4-96
OTU19	0.00	0.00	0.00	0.00	0.00	1.10	2.37	0.88	0.23	Gemmatimonadetes: Gemmatimonadetes: Gemmatimonadales: Gemmatimonadaceae
OTU55	0.00	0.00	0.00	0.95	2.48	0.03	0.10	0.00	0.03	Verrucomicrobia: Spartobacteria: Chthoniobacterales: Chthoniobacteraceae: Chthoniobacter
OTU332	0.01	0.00	0.01	0.25	0.42	1.75	1.39	0.07	0.26	Bacteria: Proteobacteria: Betaproteobacteria: Burkholderiales: Comamonadaceae
Total OTUs	2690	3008	2543	3861	4647	2996	2280	1780	2064	
Chao	3291.7	2822.9	2936.7	4755.2	3892.0	3321.8	2559.1	1941.6	2205.0	
Shannon	5.7	4.9	4.9	6.6	6.4	5.0	4.7	3.5	3.5	
Inv. Simpson	70.5	32.1	29.1	206.1	217.4	38.5	29.7	8.5	10.0	

Table B.26 Water filtration results with fresh samples collected in June 2017 (performed in the field). More details on the filtration procedures and following calculations of the fractions are given in the text above.

	Mg	Al	Si	S	K	Ca	Mn	Fe	Co	Ni	Cu	As	Mo	U
D5 <10 kD	7.967	0.003	3.429	1.816	1.235	12.095	0.631	0.013	0.001	0.004	0.004	0.002	0.002	0.076
D5 10 - 500 kD	0.181	0.004	0.190	0.048	<0.001	0.272	0.033	0.501	<0.001	0.001	<0.001	<0.001	<0.001	0.001
D5 500 kD - 0.2 µm	0.125	<0.001	0.024	0.025	0.008	0.059	<0.001	<0.001	<0.001	<0.001	0.003	<0.001	<0.001	0.019
D5 0.2 - 0.45 µm	0.065	<0.001	0.123	0.009	<0.001	<0.001	<0.001	2.153	<0.001	<0.001	<0.001	0.002	<0.001	0.049
D5 >0.45 µm	0.052	<0.001	0.112	0.012	0.016	<0.001	<0.001	1.638	<0.001	<0.001	<0.001	0.002	<0.001	0.019
D13 <10 kD	9.697	0.001	4.007	0.766	1.599	15.782	2.559	29.507	0.004	0.005	0.001	0.012	0.014	0.151
D13 10 - 500 kD	0.212	<0.001	0.055	0.006	0.027	0.265	0.218	<0.001	<0.001	0.001	<0.001	<0.001	<0.001	0.013
D13 500 kD - 0.2 µm	0.142	<0.001	0.239	<0.001	0.024	0.369	<0.001	9.312	<0.001	<0.001	<0.001	0.008	0.001	<0.001
D13 0.2 - 0.45 µm	<0.001	<0.001	0.134	0.092	<0.001	<0.001	<0.001	1.823	<0.001	<0.001	<0.001	0.005	<0.001	<0.001
D13 >0.45 µm	0.083	0.001	0.128	0.011	<0.001	0.142	<0.001	1.526	<0.001	<0.001	<0.001	0.007	<0.001	<0.001
D20 <10 kD	9.992	0.001	2.320	0.114	1.891	17.262	2.568	30.700	0.002	0.001	0.001	0.026	0.024	0.062
D20 10 - 500 kD	0.234	<0.001	0.119	0.009	0.014	0.292	0.056	5.397	<0.001	<0.001	<0.001	0.007	0.001	0.006
D20 500 kD - 0.2 µm	0.116	<0.001	0.169	0.041	0.055	0.401	0.025	4.814	<0.001	<0.001	<0.001	0.017	0.001	0.001
D20 0.2 - 0.45 µm	<0.001	<0.001	0.196	<0.001	<0.001	0.106	0.002	9.699	<0.001	<0.001	<0.001	0.032	<0.001	0.007
D20 >0.45 µm	0.131	<0.001	0.139	0.034	<0.001	0.167	0.033	1.437	<0.001	0.001	<0.001	0.007	<0.001	0.003
DJX5 <10 kD	53.858	0.065	3.563	150.726	2.423	61.139	1.298	0.058	0.170	0.765	0.002	0.001	0.012	0.154
DJX5 10 - 500 kD	<0.001	<0.001	<0.001	<0.001	<0.001	<0.001	<0.001	<0.001	<0.001	<0.001	<0.001	<0.001	0.004	0.003
DJX5 500 kD - 0.2 µm	<0.001	<0.001	<0.001	<0.001	<0.001	<0.001	<0.001	<0.001	<0.001	<0.001	<0.001	<0.001	<0.001	0.026
DJX5 0.2 - 0.45 µm	<0.001	<0.001	<0.001	<0.001	<0.001	<0.001	<0.001	<0.001	<0.001	<0.001	<0.001	<0.001	<0.001	<0.001
DJX5 >0.45 µm	<0.001	<0.001	<0.001	<0.001	<0.001	<0.001	<0.001	<0.001	<0.001	<0.001	0.001	<0.001	<0.001	<0.001
DJX20 <10 kD	55.908	0.082	3.727	155.322	2.493	63.531	1.493	0.016	0.197	0.857	0.003	0.001	0.013	0.274
DJX20 10 - 500 kD	0.712	0.015	0.114	4.422	0.014	0.488	0.010	<0.001	0.004	0.008	<0.001	<0.001	<0.001	<0.001
DJX20 500 kD - 0.2 µm	0.433	0.038	0.030	<0.001	0.062	0.068	0.002	<0.001	<0.001	<0.001	0.002	<0.001	<0.001	0.023
DJX20 0.2 - 0.45 µm	<0.001	0.001	0.038	<0.001	<0.001	0.202	<0.001	0.009	<0.001	<0.001	<0.001	<0.001	<0.001	<0.001
DJX20 >0.45 µm	<0.001	0.001	<0.001	<0.001	<0.001	<0.001	<0.001	0.033	<0.001	<0.001	0.001	<0.001	<0.001	0.064
DJX40 <10 kD	58.845	0.144	4.100	171.331	2.693	70.386	1.665	0.007	0.211	0.880	0.005	0.001	0.011	0.377
DJX40 10 - 500 kD	1.796	0.019	0.175	3.275	0.062	2.206	0.038	0.013	0.004	0.019	<0.001	<0.001	<0.001	<0.001
DJX40 500 kD - 0.2 µm	<0.001	0.034	<0.001	<0.001	<0.001	<0.001	<0.001	<0.001	<0.001	<0.001	0.001	<0.001	<0.001	<0.001
DJX40 0.2 - 0.45 µm	<0.001	0.010	<0.001	<0.001	<0.001	<0.001	<0.001	<0.001	<0.001	<0.001	<0.001	<0.001	<0.001	<0.001
DJX40 >0.45 µm	<0.001	0.012	0.072	<0.001	<0.001	<0.001	<0.001	0.062	<0.001	<0.001	0.001	<0.001	0.001	0.068
DJX65 <10 kD	125.067	0.299	5.519	490.110	6.500	224.050	3.701	0.057	0.352	1.537	0.019	0.001	0.084	1.593
DJX65 10 - 500 kD	<0.001	<0.001	<0.001	1.013	0.006	<0.001	<0.001	<0.001	0.002	<0.001	<0.001	<0.001	<0.001	0.036
DJX65 500 kD - 0.2 µm	<0.001	0.010	<0.001	0.798	0.188	<0.001	0.052	0.010	<0.001	<0.001	<0.001	<0.001	0.002	0.008
DJX65 0.2 - 0.45 µm	<0.001	<0.001	<0.001	<0.001	<0.001	<0.001	<0.001	<0.001	<0.001	<0.001	<0.001	<0.001	<0.001	<0.001
DJX65 >0.45 µm	<0.001	0.114	<0.001	<0.001	<0.001	<0.001	<0.001	0.103	<0.001	<0.001	0.003	<0.001	<0.001	0.284

Table B.27 Water filtration results with mature samples collected in June 2017 (performed in glove box).

	Mg	Al	Si	S	K	Ca	Mn	Fe	Co	Ni	Cu	As	Mo	U
D5 <10 kD	9.032	0.005	3.665	1.998	1.391	10.508	0.515	0.015	<0.001	<0.001	<0.001	<0.001	<0.001	0.053
D5 10 - 500 kD	<0.001	<0.001	0.077	<0.001	<0.001	0.898	0.001	0.059	<0.001	0.003	<0.001	<0.001	<0.001	0.014
D5 500 kD - 0.2 µm	<0.001	0.005	0.072	0.584	<0.001	2.536	0.017	1.263	<0.001	<0.001	<0.001	0.002	<0.001	0.040
D5 0.2 - 0.45 µm	<0.001	<0.001	0.410	0.435	<0.001	0.519	0.006	0.886	<0.001	<0.001	<0.001	0.001	<0.001	0.003
D5 >0.45 µm	<0.001	<0.001	0.592	0.441	<0.001	0.546	0.004	0.640	<0.001	0.001	<0.001	0.001	<0.001	0.019
D13 <10 kD	10.511	0.004	5.041	1.382	1.630	15.294	2.621	30.241	0.004	<0.001	0.006	0.005	0.011	0.132
D13 10 - 500 kD	0.355	<0.001	0.167	<0.001	0.033	0.632	0.122	1.840	<0.001	0.005	<0.001	0.001	<0.001	<0.001
D13 500 kD - 0.2 µm	<0.001	<0.001	0.326	<0.001	0.043	0.141	0.039	3.610	<0.001	0.001	<0.001	0.003	<0.001	0.003
D13 0.2 - 0.45 µm	0.034	0.003	0.002	<0.001	<0.001	0.048	<0.001	2.588	<0.001	<0.001	<0.001	0.009	<0.001	0.003
D13 >0.45 µm	0.070	0.008	0.155	<0.001	<0.001	0.405	0.025	2.314	<0.001	0.001	<0.001	0.006	<0.001	0.006
D20 <10 kD	11.374	0.001	3.931	0.396	1.958	19.811	2.307	44.988	0.001	0.001	<0.001	0.030	0.026	0.068
D20 10 - 500 kD	0.198	<0.001	0.171	<0.001	0.050	0.586	0.070	3.137	<0.001	<0.001	<0.001	0.005	0.002	0.002
D20 500 kD - 0.2 µm	0.141	0.001	0.119	<0.001	0.058	0.186	0.021	3.026	<0.001	<0.001	<0.001	0.014	<0.001	<0.001
D20 0.2 - 0.45 µm	<0.001	0.002	0.051	<0.001	<0.001	<0.001	0.026	1.316	<0.001	<0.001	<0.001	0.010	<0.001	<0.001
D20 >0.45 µm	<0.001	0.008	0.117	<0.001	<0.001	0.060	0.585	0.937	<0.001	<0.001	<0.001	0.020	<0.001	<0.001
DJX5 <10 kD	41.456	0.038	3.826	192.498	2.447	62.351	1.021	0.257	0.121	0.626	<0.001	0.001	0.010	0.061
DJX5 10 - 500 kD	<0.001	<0.001	0.094	<0.001	0.047	0.744	0.014	<0.001	0.001	0.016	<0.001	<0.001	<0.001	0.010
DJX5 500 kD - 0.2 µm	<0.001	0.017	0.068	<0.001	0.041	0.512	0.019	<0.001	0.004	0.021	0.002	<0.001	0.003	0.151
DJX5 0.2 - 0.45 µm	<0.001	<0.001	0.124	<0.001	<0.001	<0.001	<0.001	<0.001	<0.001	0.007	<0.001	<0.001	<0.001	0.003
DJX5 >0.45 µm	<0.001	0.011	0.140	<0.001	<0.001	0.231	<0.001	<0.001	<0.001	0.026	<0.001	<0.001	<0.001	0.055
DJX20 <10 kD	52.674	0.086	5.032	236.360	2.642	75.930	1.721	0.091	0.195	1.015	<0.001	<0.001	0.007	0.058
DJX20 10 - 500 kD	<0.001	0.004	0.100	<0.001	<0.001	<0.001	<0.001	<0.001	<0.001	0.012	<0.001	<0.001	<0.001	0.005
DJX20 500 kD - 0.2 µm	11.051	0.052	<0.001	<0.001	0.011	2.709	0.012	<0.001	0.001	0.010	0.004	<0.001	0.005	0.188
DJX20 0.2 - 0.45 µm	<0.001	0.002	0.178	0.929	0.008	<0.001	0.004	<0.001	0.006	0.040	<0.001	<0.001	<0.001	0.017
DJX20 >0.45 µm	<0.001	0.017	0.068	3.496	<0.001	<0.001	<0.001	<0.001	0.004	0.004	<0.001	<0.001	<0.001	0.059
DJX40 <10 kD	62.529	0.100	5.239	278.426	3.118	72.867	2.016	0.222	0.221	1.023	<0.001	<0.001	0.007	0.133
DJX40 10 - 500 kD	9.286	<0.001	0.015	5.656	<0.001	1.602	0.005	<0.001	<0.001	0.012	0.001	<0.001	<0.001	0.054
DJX40 500 kD - 0.2 µm	<0.001	0.055	0.062	0.259	0.042	0.106	0.018	<0.001	<0.001	0.013	0.005	<0.001	0.009	0.245
DJX40 0.2 - 0.45 µm	<0.001	<0.001	0.333	0.015	<0.001	<0.001	<0.001	<0.001	<0.001	0.010	<0.001	<0.001	<0.001	0.001
DJX40 >0.45 µm	<0.001	0.014	0.288	<0.001	0.029	<0.001	0.016	<0.001	<0.001	0.048	<0.001	<0.001	<0.001	0.092
DJX65 <10 kD	137.632	0.128	5.803	644.202	7.878	199.435	3.763	0.086	0.341	1.738	0.005	<0.001	0.056	0.707
DJX65 10 - 500 kD	2.240	0.005	0.071	<0.001	0.127	7.969	0.074	<0.001	<0.001	0.034	<0.001	<0.001	<0.001	0.010
DJX65 500 kD - 0.2 µm	0.782	0.034	0.230	6.110	0.139	<0.001	0.043	<0.001	<0.001	0.032	0.009	<0.001	0.035	0.666
DJX65 0.2 - 0.45 µm	2.837	<0.001	0.014	10.345	<0.001	3.741	<0.001	<0.001	0.010	0.081	<0.001	<0.001	<0.001	0.026
DJX65 >0.45 µm	0.983	0.084	0.034	6.789	<0.001	0.775	<0.001	0.045	<0.001	0.014	0.001	<0.001	0.001	0.171

Table B.28 Water filtration results with fresh samples collected in June 2018 (performed in the field by closed inline filtration).

	Mg	Al	Si	S	K	P	Ca	Mn	Fe	Co	Ni	Cu	As	Mo	U
D5 <10 kD	8.478	0.003	3.889	2.469	1.339	0.001	13.723	0.554	0.012	0.001	0.005	0.000	0.001	0.001	0.079
D5 10 - 500 kD	0.142	<0.001	<0.001	<0.001	0.043	0.001	0.359	0.000	0.089	<0.001	<0.001	<0.001	0.000	<0.001	0.001
D5 500 kD - 0.2 µm	<0.001	0.002	0.032	<0.001	0.036	0.001	0.261	0.004	2.113	<0.001	<0.001	<0.001	0.002	<0.001	0.004
D5 0.2 - 0.45 µm	0.090	0.001	<0.001	<0.001	<0.001	<0.001	0.225	0.015	0.341	0.000	0.000	<0.001	<0.001	0.000	0.003
D5 0.45 - 1.2 µm	<0.001	0.000	0.074	<0.001	0.010	0.002	0.235	0.020	0.237	<0.001	<0.001	<0.001	0.000	0.000	<0.001
D5 >1.2 µm	<0.001	0.008	0.100	<0.001	<0.001	0.009	<0.001	0.011	0.739	<0.001	<0.001	<0.001	0.001	<0.001	0.000
D13 <10 kD	8.842	0.001	4.301	1.853	1.339	0.001	14.890	1.746	2.901	0.005	0.005	<0.001	0.002	0.002	0.056
D13 10 - 500 kD	0.328	0.002	<0.001	0.124	0.097	0.000	0.404	0.169	5.127	<0.001	0.003	<0.001	0.001	0.001	0.022
D13 500 kD - 0.2 µm	0.223	0.001	0.164	<0.001	0.081	0.001	1.175	0.130	7.511	<0.001	<0.001	<0.001	0.005	0.002	0.040
D13 0.2 - 0.45 µm	<0.001	<0.001	<0.001	0.001	<0.001	0.001	<0.001	<0.001	<0.001	<0.001	<0.001	<0.001	<0.001	<0.001	<0.001
D13 0.45 - 1.2 µm	<0.001	0.001	0.123	<0.001	<0.001	0.000	0.109	0.060	2.229	<0.001	<0.001	<0.001	0.002	0.001	0.009
D13 >1.2 µm	<0.001	0.030	<0.001	<0.001	<0.001	0.006	<0.001	<0.001	<0.001	<0.001	<0.001	<0.001	0.003	<0.001	<0.001
D20 <10 kD	10.981	0.002	2.850	0.389	2.024	0.001	21.076	2.482	12.699	0.002	0.001	<0.001	0.004	0.020	0.049
D20 10 - 500 kD	<0.001	<0.001	0.151	0.026	<0.001	0.001	0.308	0.044	12.286	<0.001	<0.001	<0.001	0.005	0.003	0.003
D20 500 kD - 0.2 µm	<0.001	<0.001	0.168	0.151	0.048	0.000	1.096	0.109	25.953	<0.001	<0.001	<0.001	0.028	0.004	0.009
D20 0.2 - 0.45 µm	<0.001	<0.001	0.016	<0.001	0.005	<0.001	0.072	<0.001	<0.001	<0.001	<0.001	<0.001	0.001	<0.001	0.001
D20 0.45 - 1.2 µm	0.459	0.010	<0.001	0.659	0.027	0.018	0.510	0.003	<0.001	0.001	0.005	<0.001	0.000	0.000	0.005
D20 >1.2 µm	<0.001	<0.001	<0.001	<0.001	<0.001	<0.001	<0.001	<0.001	<0.001	<0.001	<0.001	<0.001	<0.001	<0.001	<0.001
DJX5 <10 kD	26.857	0.008	1.713	89.511	1.698	0.001	35.601	0.004	0.002	0.002	0.068	0.001	0.001	0.013	0.102
DJX5 10 - 500 kD	2.015	0.000	<0.001	<0.001	0.226	0.000	2.788	<0.001	0.005	<0.001	0.005	0.002	0.000	0.000	0.000
DJX5 500 kD - 0.2 µm	2.911	0.003	<0.001	<0.001	0.316	<0.001	3.528	<0.001	0.012	<0.001	0.002	<0.001	0.000	0.000	0.007
DJX5 0.2 - 0.45 µm	<0.001	<0.001	<0.001	<0.001	<0.001	<0.001	0.092	0.002	<0.001	0.001	0.003	<0.001	<0.001	<0.001	0.009
DJX5 0.45 - 1.2 µm	<0.001	<0.001	<0.001	<0.001	<0.001	<0.001	<0.001	0.003	<0.001	0.001	0.006	0.000	<0.001	<0.001	0.005
DJX5 >1.2 µm	<0.001	0.017	<0.001	<0.001	<0.001	<0.001	1.024	0.029	0.015	0.006	0.014	<0.001	0.000	0.000	0.022
DJX20 <10 kD	63.679	0.105	4.611	165.783	2.623	0.001	77.703	1.563	0.004	0.178	0.858	0.007	0.000	0.013	0.229
DJX20 10 - 500 kD	0.828	0.009	<0.001	<0.001	0.072	0.000	1.592	<0.001	<0.001	0.000	0.000	<0.001	0.000	0.000	0.000
DJX20 500 kD - 0.2 µm	<0.001	<0.001	0.023	1.818	<0.001	<0.001	0.931	<0.001	<0.001	<0.001	<0.001	<0.001	<0.001	<0.001	0.006
DJX20 0.2 - 0.45 µm	<0.001	<0.001	<0.001	<0.001	<0.001	<0.001	<0.001	0.006	<0.001	0.000	<0.001	<0.001	0.000	<0.001	0.000
DJX20 0.45 - 1.2 µm	<0.001	<0.001	<0.001	<0.001	<0.001	<0.001	<0.001	<0.001	<0.001	<0.001	<0.001	<0.001	0.000	<0.001	<0.001
DJX20 >1.2 µm	<0.001	0.001	0.023	<0.001	<0.001	<0.001	0.522	<0.001	0.035	<0.001	<0.001	<0.001	<0.001	0.000	<0.001
DJX40 <10 kD	58.088	0.154	4.994	218.690	2.185	<0.001	74.151	1.476	0.003	0.164	0.744	0.006	0.000	0.011	0.259
DJX40 10 - 500 kD	11.027	0.035	<0.001	<0.001	0.703	<0.001	15.335	0.278	0.001	0.030	0.123	0.003	0.000	0.001	0.021
DJX40 500 kD - 0.2 µm	<0.001	0.005	<0.001	<0.001	0.011	<0.001	<0.001	<0.001	0.002	<0.001	<0.001	<0.001	0.000	<0.001	0.004
DJX40 0.2 - 0.45 µm	<0.001	<0.001	<0.001	<0.001	<0.001	<0.001	<0.001	<0.001	<0.001	<0.001	<0.001	<0.001	<0.001	<0.001	0.001
DJX40 0.45 - 1.2 µm	<0.001	<0.001	<0.001	<0.001	<0.001	<0.001	0.107	<0.001	0.000	<0.001	<0.001	<0.001	<0.001	<0.001	0.002
DJX40 >1.2 µm	<0.001	0.004	<0.001	<0.001	0.016	<0.001	0.026	<0.001	0.040	<0.001	<0.001	<0.001	0.000	<0.001	0.001
DJX65 <10 kD	117.163	0.147	4.786	408.889	6.443	0.001	194.430	2.836	0.008	0.276	1.261	0.010	0.001	0.072	0.936
DJX65 10 - 500 kD	2.653	0.029	<0.001	10.645	0.229	0.000	1.032	0.077	<0.001	0.004	0.038	0.001	0.000	0.002	0.140
DJX65 500 kD - 0.2 µm	2.911	0.016	0.129	8.162	0.176	<0.001	12.281	0.063	<0.001	0.003	0.008	0.000	0.000	0.002	<0.001
DJX65 0.2 - 0.45 µm	<0.001	<0.001	<0.001	<0.001	<0.001	<0.001	<0.001	<0.001	<0.001	<0.001	<0.001	<0.001	<0.001	<0.001	<0.001
DJX65 0.45 - 1.2 µm	<0.001	0.000	<0.001	0.057	<0.001	<0.001	<0.001	<0.001	<0.001	<0.001	<0.001	0.001	<0.001	<0.001	<0.001
DJX65 >1.2 µm	<0.001	0.003	<0.001	<0.001	<0.001	0.000	<0.001	<0.001	0.054	<0.001	<0.001	<0.001	0.000	<0.001	<0.001
Well 0118 <10 kD	27.918	0.005	2.642	76.333	1.774	0.000	38.929	0.242	7.081	0.018	0.046	<0.001	0.002	0.001	0.000
Well 0118 10 - 500 kD	0.261	<0.001	0.002	1.251	0.055	<0.001	0.488	0.008	0.104	0.001	0.001	<0.001	<0.001	<0.001	<0.001
Well 0118 500 kD - 0.2 µm	0.003	0.004	<0.001	<0.001	0.013	<0.001	0.530	<0.001	0.259	<0.001	0.001	<0.001	0.000	0.000	<0.001
Well 0118 0.2 - 0.45 µm	0.000	<0.001	<0.001	1.027	0.024	<0.001	<0.001	<0.001	0.007	0.000	<0.001	<0.001	0.000	0.000	<0.001
Well 0118 0.45 - 1.2 µm	<0.001	<0.001	<0.001	<0.001	<0.001	<0.001	<0.001	<0.001	0.035	<0.001	0.000	<0.001	<0.001	<0.001	<0.001
Well 0118 >1.2 µm	<0.001	0.001	<0.001	<0.001	<0.001	<0.001	<0.001	<0.001	<0.001	<0.001	<0.001	<0.001	<0.001	<0.001	<0.001

Figures

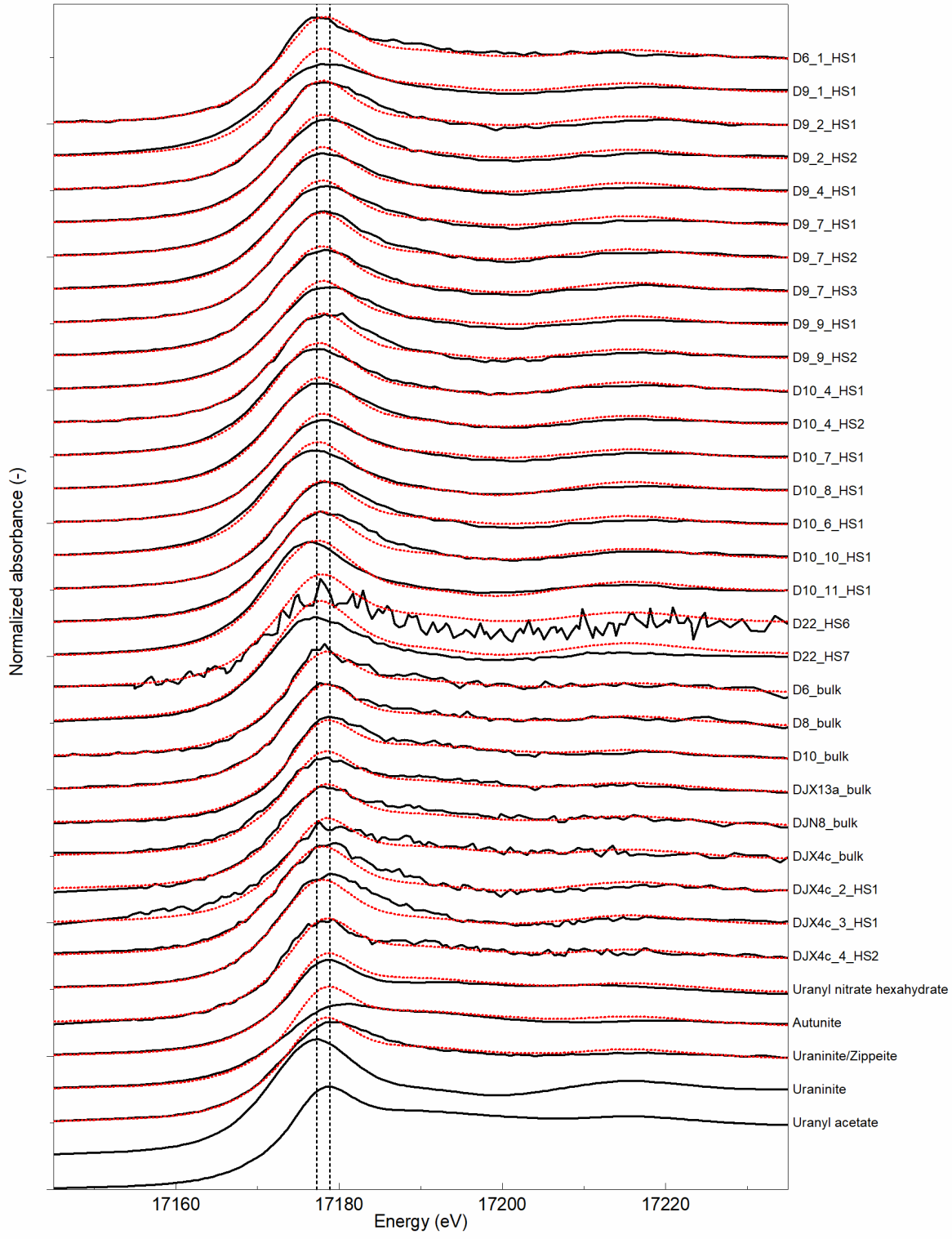

Figure B.1 Merged XANES spectra for U (black, solid) and fit (red, dotted) obtained by linear combination fitting.

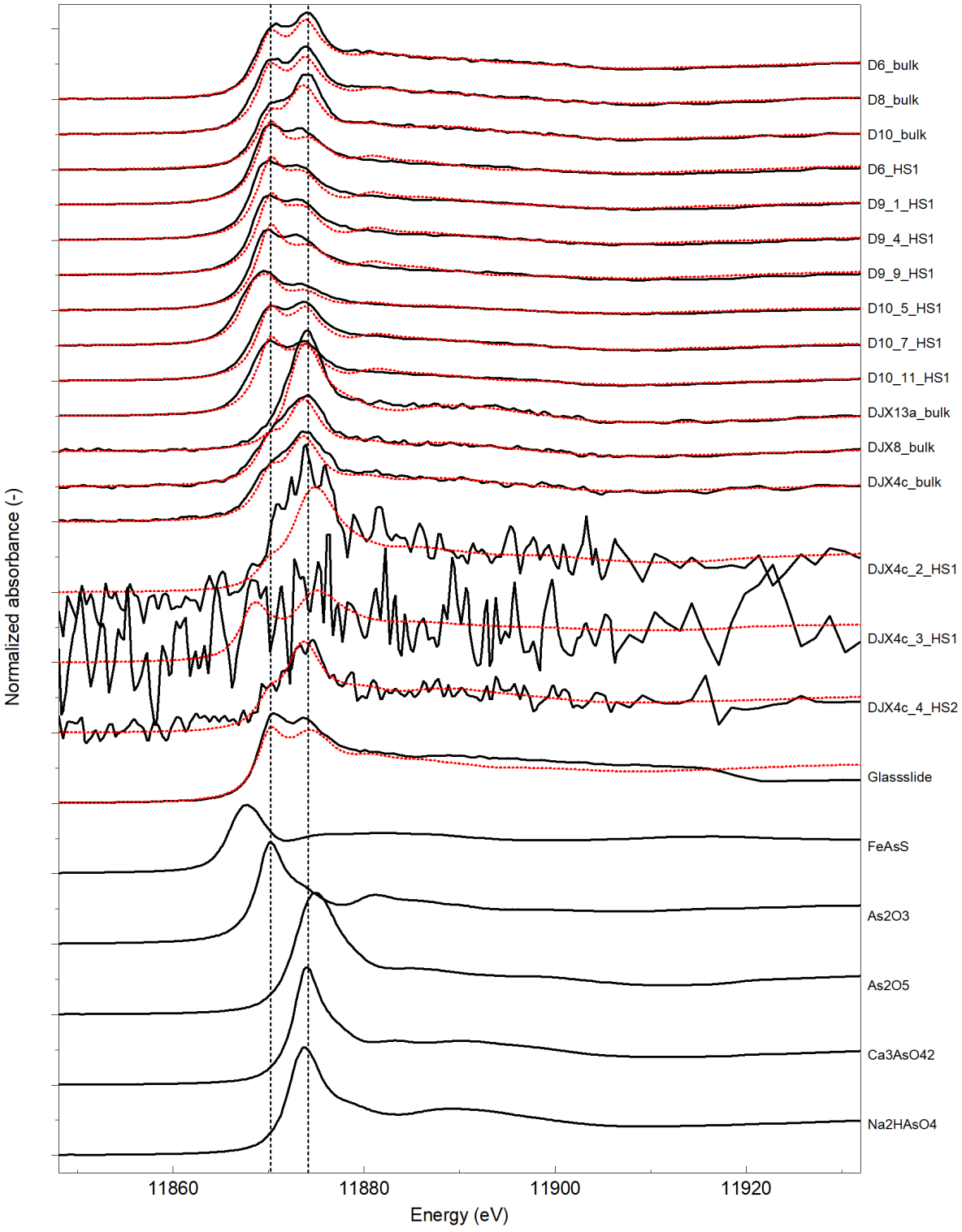

Figure B.2 Merged XANES spectra for As (black, solid) and fit (red, dotted) obtained by linear combination fitting. DJX4c_2_HS1 and DJX4c_3_HS1 were very noisy, which did not allow reliable fitting.

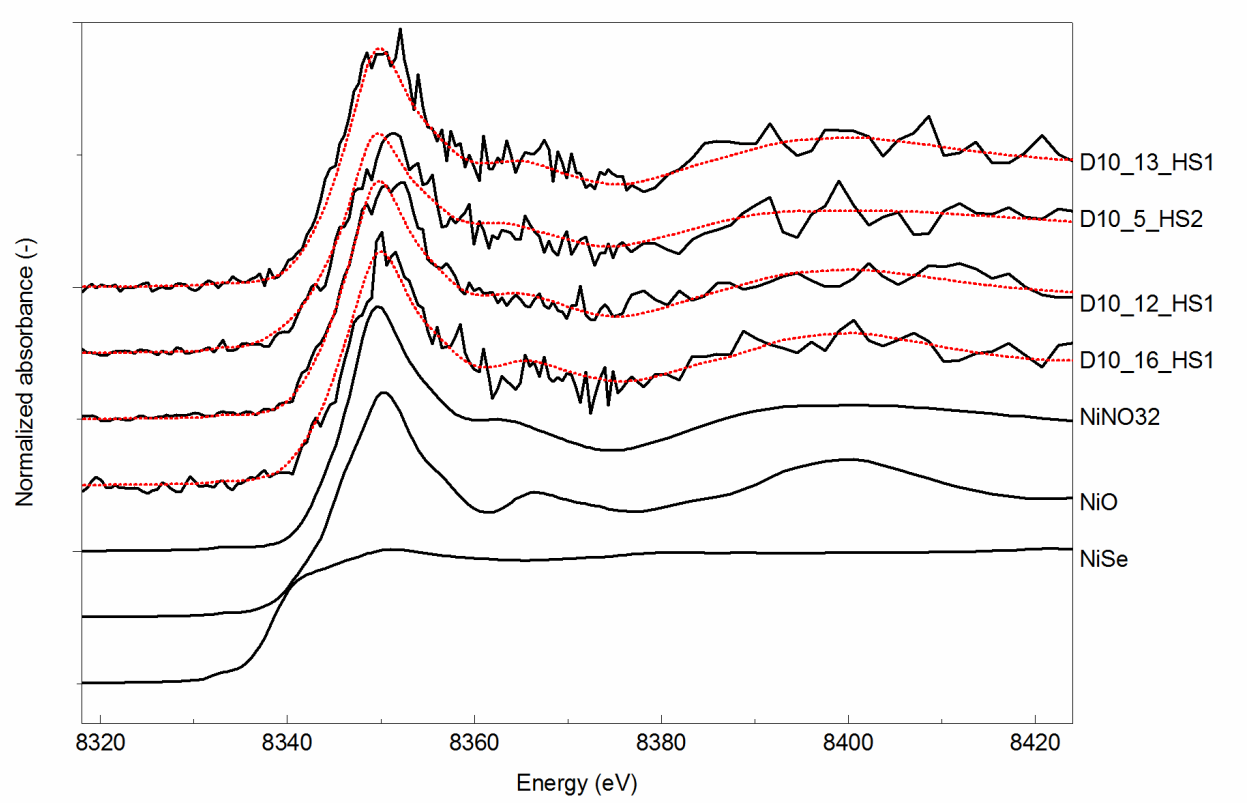

Figure B.3 Merged XANES spectra for Ni (black, solid) and fit (red, dotted) obtained by linear combination fitting.

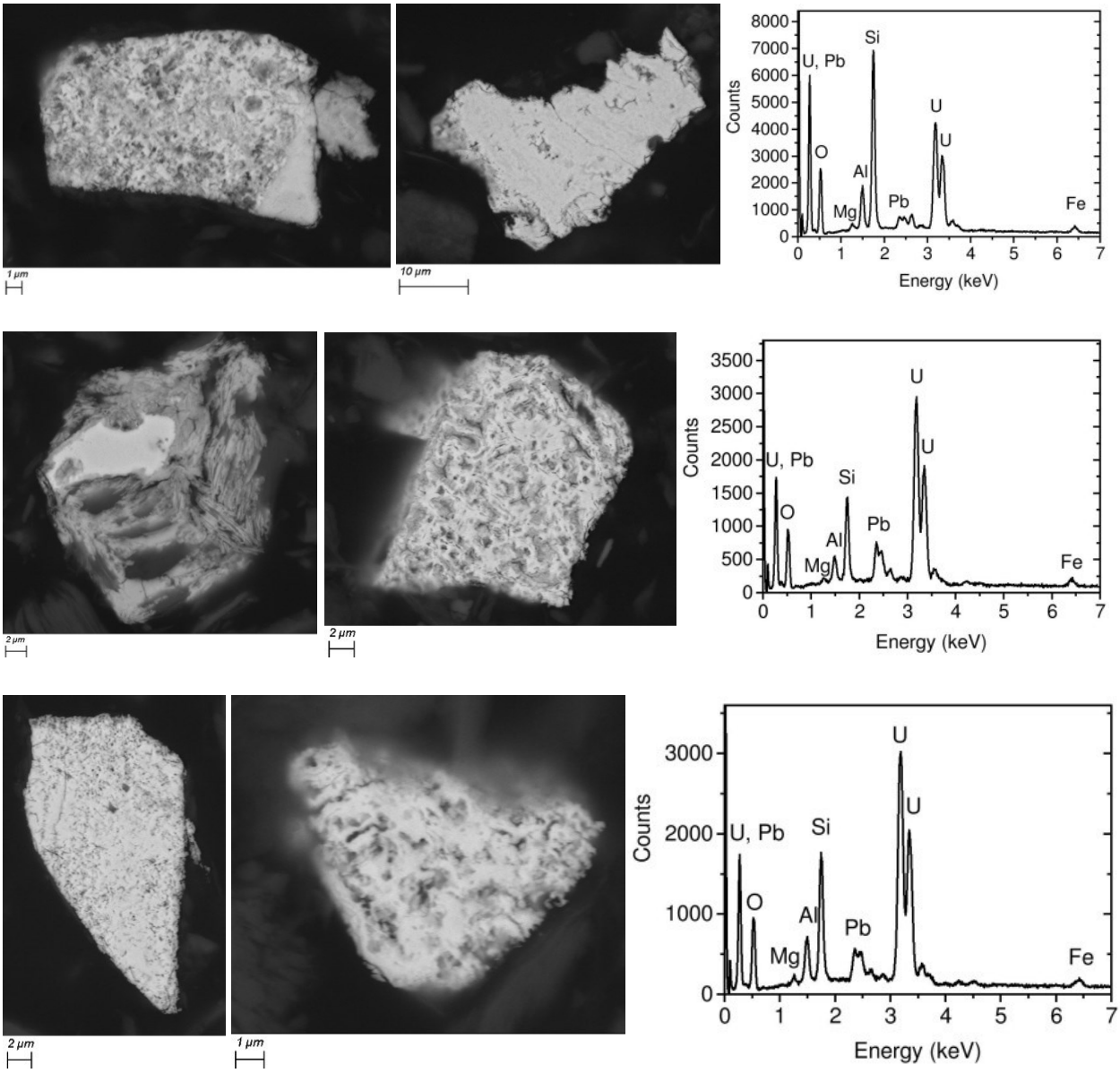

Figure B.4 Examples of U-rich accumulations found after sequential extraction step 1 (top), step 2 (middle) and step 3 (bottom). No grains were detected after step 4 and 5. The EDX spectra belong to the U grains on the right side.

D10 quartz glass area 1

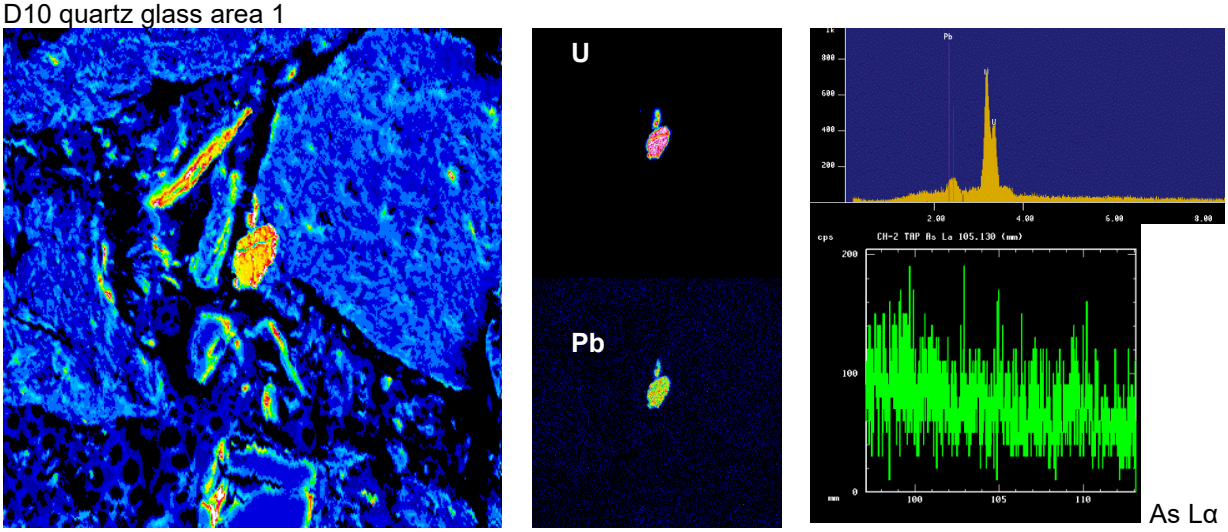

D10 quartz glass area 2

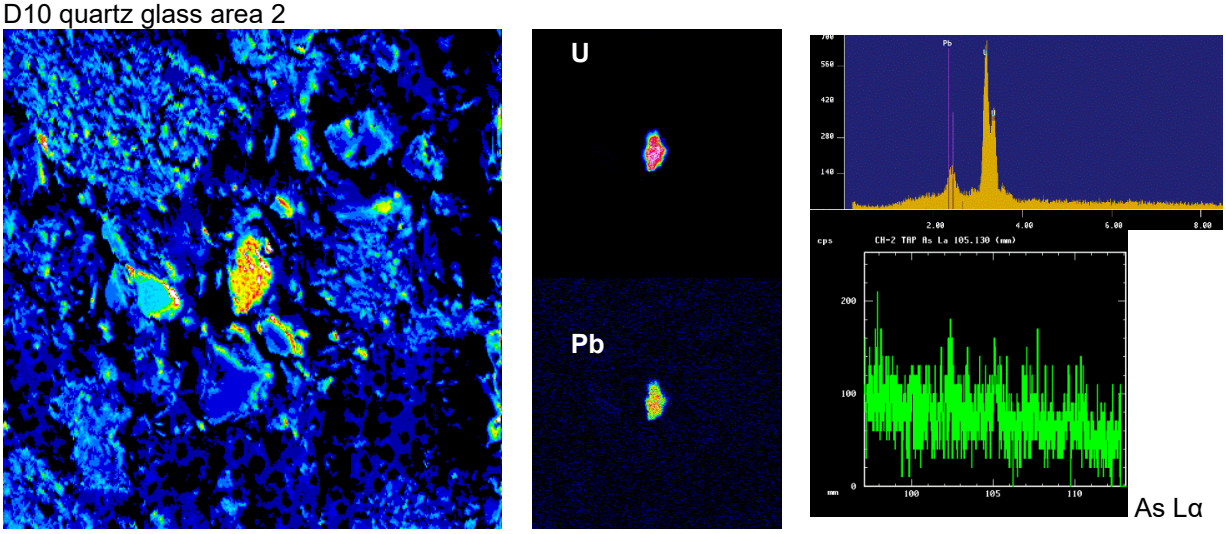

D10 quartz glass area 4

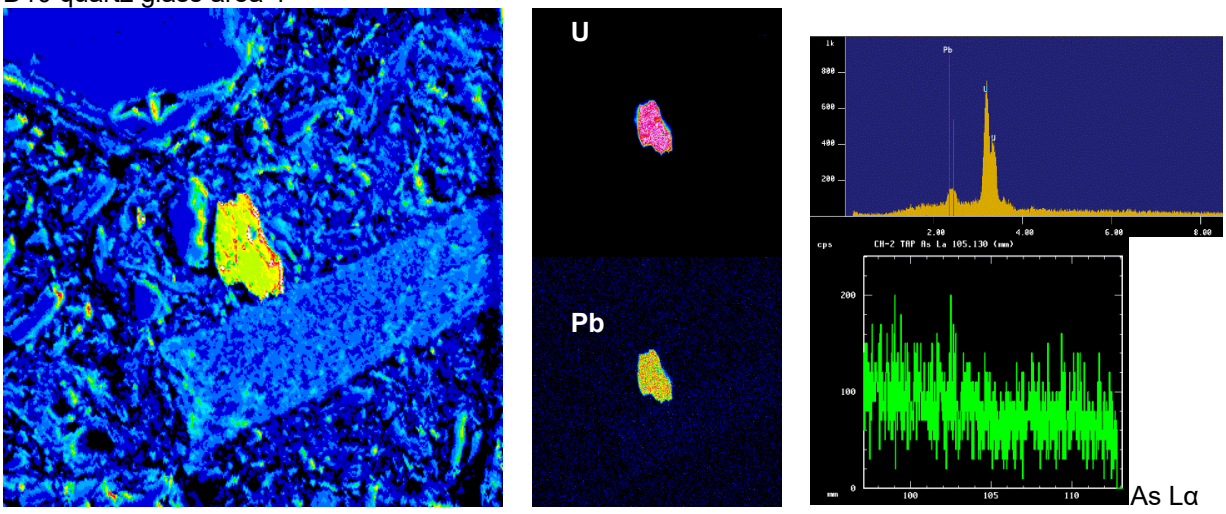

Figure B.5 Selected microprobe results for D-pit U-rich grains (sample D-10) showing the secondary electron image (left), selected elemental maps (middle) and the EDX spectrum with focus on the As Lα edge (right).

DJX4c quartz glass area 2

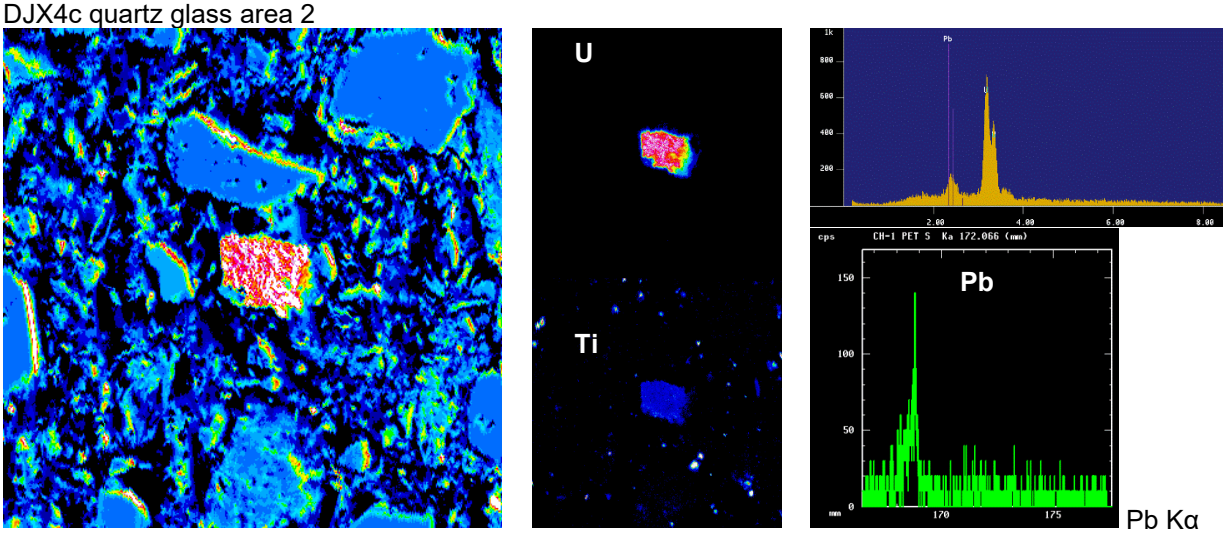

DJX4c quartz glass area 3

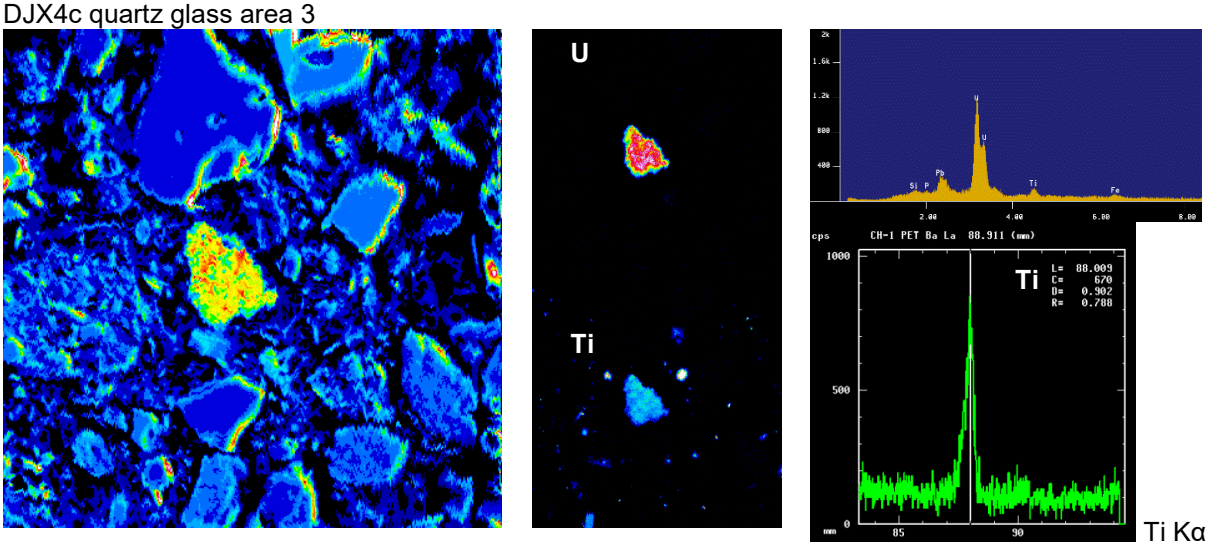

DJX4c quarz glass area 4

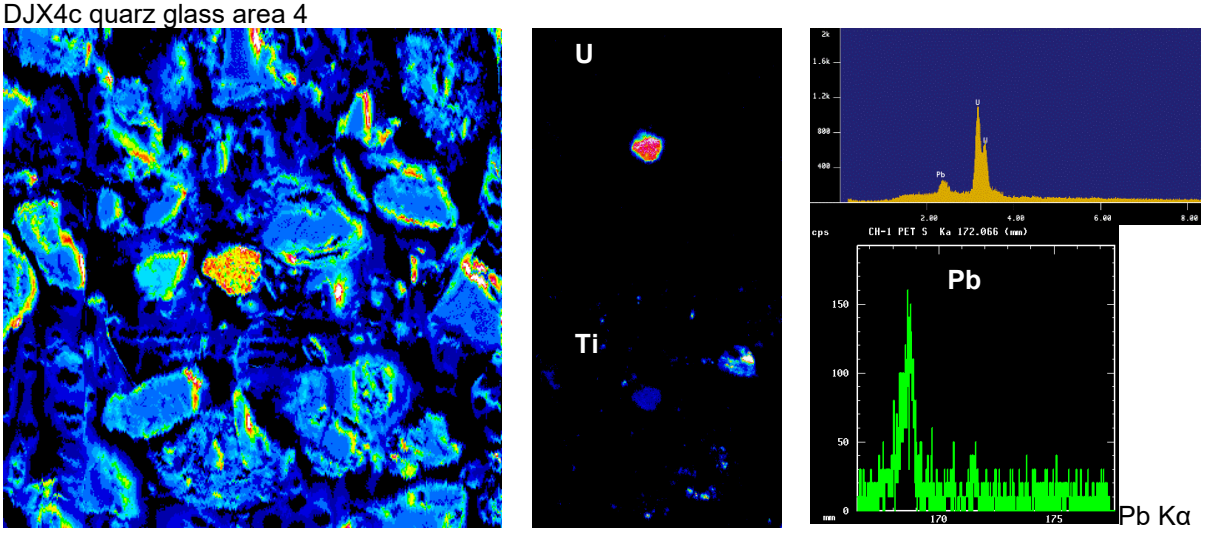

Figure B.6 Selected microprobe results for DJX-pit U-rich grains (sample DJX-4c) showing the secondary electron image (left), selected elemental maps (middle) and the EDX spectrum with focus on the Pb Kα and Ti Kα edges (right).

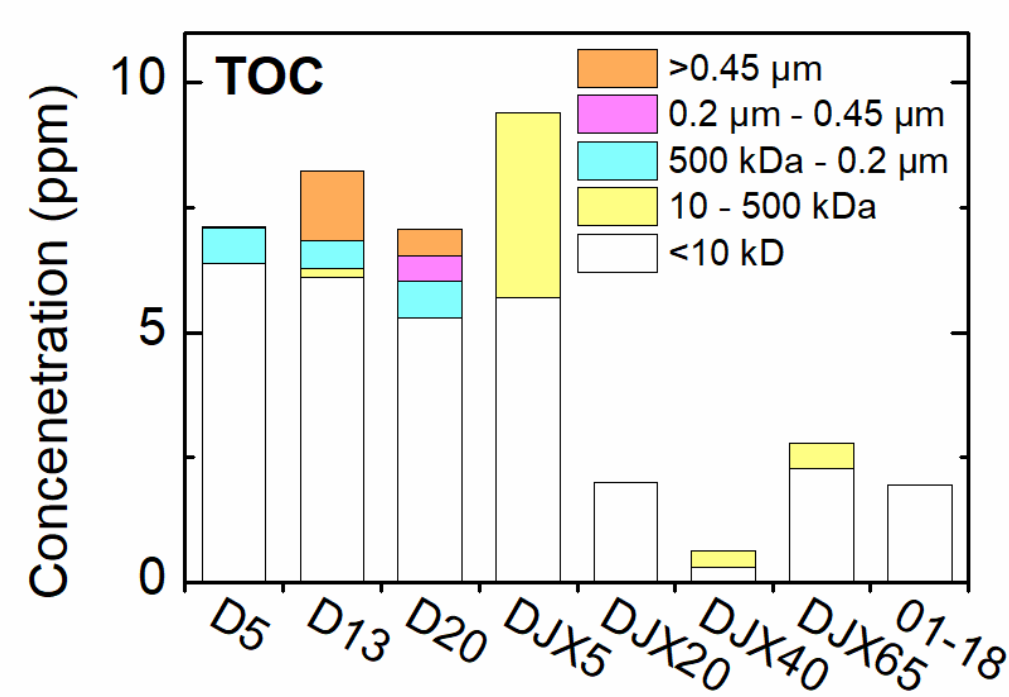

Figure B.7 Filtrations of June 2018 samples for TOC analysis. The majority of particles in both pits was present in the <10 kDa fraction. An exception was water from the deeper layers of the DJX-pit, where small colloids (10-500 kDa) were strongly represented. In the monimolimnion of the D-pit, larger colloids (>500 kDa) were found.

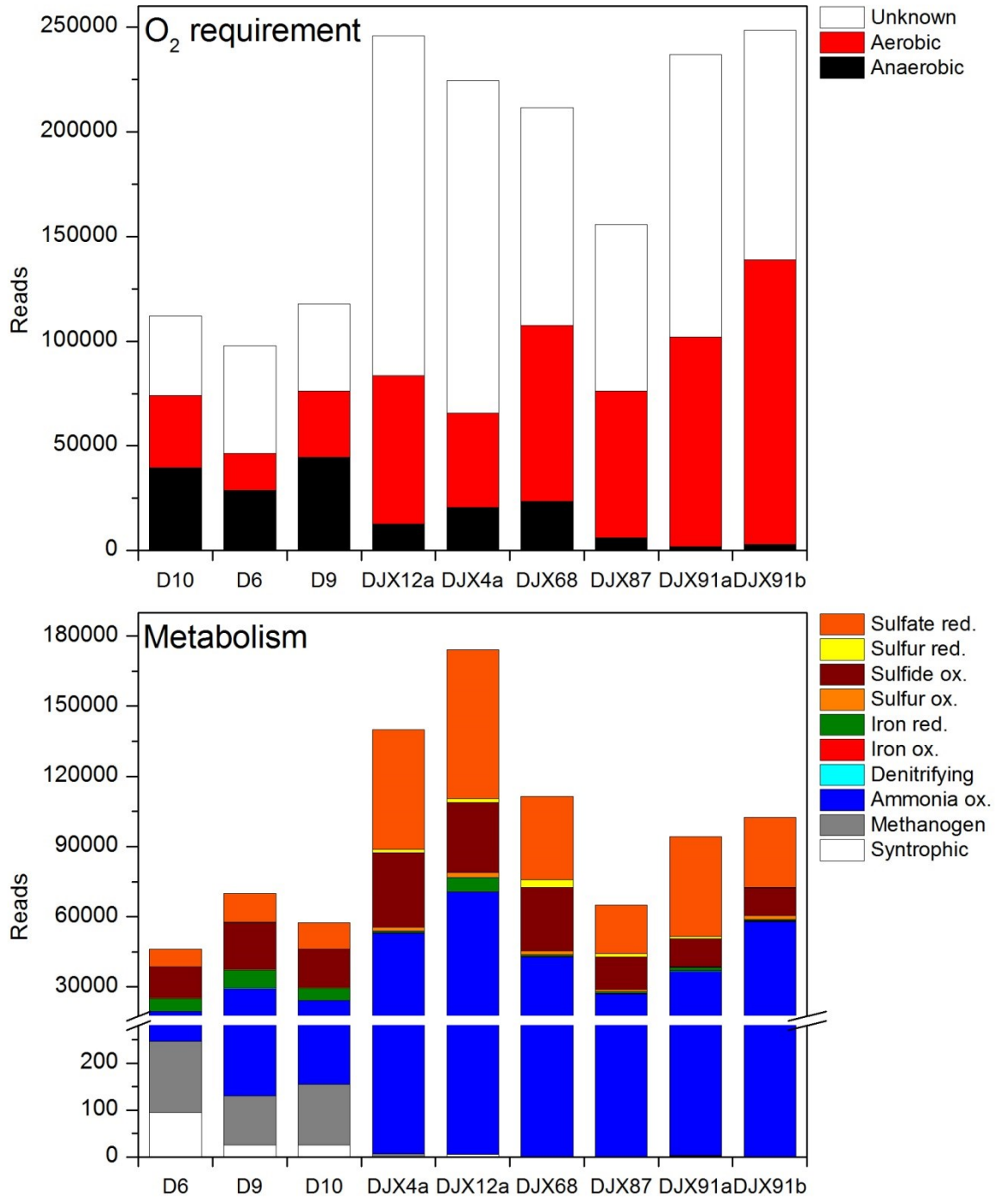

Figure B.8 Oxygen requirements (top) and predicted metabolism (bottom). For better visualization, selected metabolic pathways (e.g., dehalogenation, xylan degradation) and unknown counts are not shown in the bottom graph.

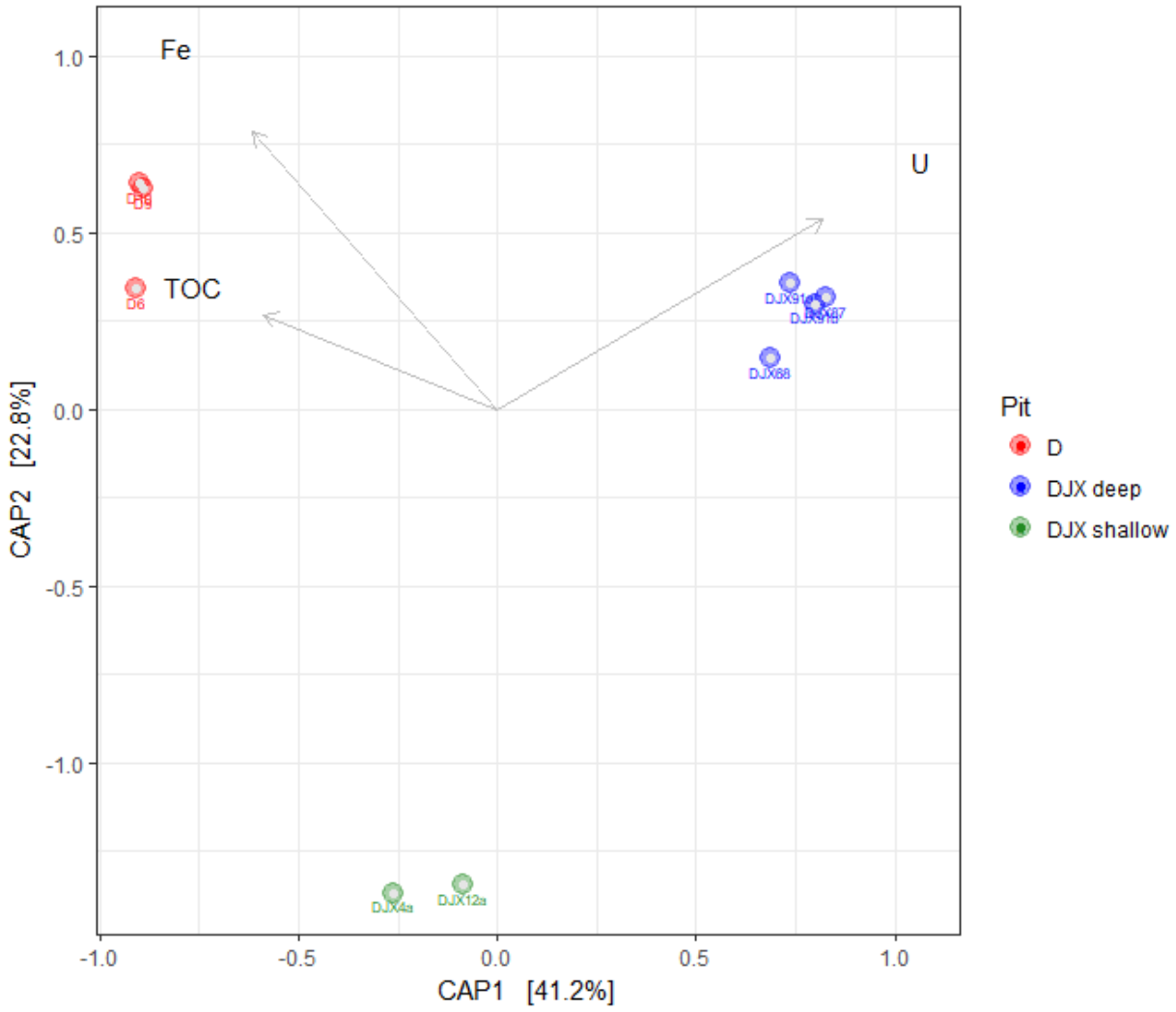

Figure B.9 Constrained ordination plot based on the Bray-Curtis algorithm. The shown axes explain 64% of the variation. Colors represent sample groups (D-pit, DJX-pit deep, DJX-pit shallow). Arrows show environmental variables. The significance of environmental variables was tested in R version 3.4.0 by applying the adonis function of the R phyloseq package and using the Bray-Curtis algorithm (McArdle and Anderson, 2001). Only significant variables are shown: TOC (total organic carbon, p=0.014), Fe (p=0.010), and U (p=0.001).

Figure B.10 Example photos of the sediment traps. Top left: two sediment traps with the aluminum pipes attached; the collection tube is inside the pipe; the funnel on top, made of a cut PET bottle had a surface area of 95 cm^2. Top right: sediment trap after deployment in the D-pit in June 2017. The white buoy is carrying the sediment trap below; the plastic water log is keeping the white buoy at a distance to the center buoy. Bottom: collected sediments from the sediment trap retrieved from the DJX-pit in June 2018 after removing the funnel and after sealing the tube.

APPENDIX C
SUPPLEMENTARY INFORMATION FOR CHAPTER 4

Tables

Table C.1 Water isotope results and other data for sampling locations at Cluff Lake.

Station details				June 2017					September 2017					June 2018	
Sample	Description	N	W	Ca (ppm)	Ni (ppm)	U (ppm)	d18O	d2H	Ca (ppm)	Ni (ppm)	U (ppm)	d18O	d2H	d18O	d2H
D0.5	D-pit 0.5m	58.362	109.514	-	-	-	-	-	-	-	-	-	-	-15.59	-134.38
D5	D-pit 5m	58.362	109.514	12.358	0.003	0.145	-17.16	-141.05	12.657	0.004	0.109	-16.22	-137.87	-16.85	-139.45
D13	D-pit 13m	58.362	109.514	16.277	0.005	0.151	-17.35	-142.07	14.360	0.006	0.128	-17.21	-142.76	-17.15	-140.51
D20	D-pit 20m	58.362	109.514	18.061	0.001	0.076	-17.43	-142.48	19.373	<0.001	0.021	-16.66	-138.88	-17.39	-140.88
DJX5	DJX-pit 5m	58.368	109.546	37.059	0.079	0.165	-14.24	-128.78	40.195	0.059	0.122	-13.63	-125.51	-14.03	-126.79
DJX10	DJX-pit 10m	58.368	109.546	-	-	-	-	-	42.917	0.077	0.141	-14.72	-131.68	-	-
DJX20	DJX-pit 20m	58.368	109.546	64.288	0.854	0.233	-16.70	-139.31	72.331	0.755	0.213	-17.10	-141.52	-16.62	-137.70
DJX40	DJX-pit 40m	58.368	109.546	70.971	0.892	0.319	-16.79	-139.24	81.540	0.853	0.298	-16.78	-140.20	-16.75	-138.19
DJX50	DJX-pit 50m	58.368	109.546	-	-	-	-	-	90.067	0.823	0.391	-16.72	-139.62	-	-
DJX60	DJX-pit 60m	58.368	109.546	-	-	-	-	-	89.224	0.836	0.157	-16.97	-140.79	-	-
DJX65	DJX-pit 65m	58.368	109.546	192.272	1.406	1.388	-17.05	-142.36	-	-	-	-	-	-16.99	-140.13
DJX73	DJX-pit 73m	58.368	109.546	232.472	1.472	1.622	-17.10	-142.03	-	-	-	-	-	-	-
C DJX	DJX seepage	58.370	109.546	53.179	0.208	0.004	-17.29	-144.73	64.963	0.172	0.006	-16.03	-134.87	-	-
GW 0118	Well btw DJX and Cluff	58.365	109.547	35.517	0.058	<0.001	-14.24	-126.91	32.495	0.052	<0.001	-13.56	-124.03	-14.15	-127.57
GW 9846	Well west of DJX	58.368	109.549						12.319	0.002	<0.001	-19.87	-155.75	-	-
GW 9849	Well btw DJX and Cluff L	58.364	109.549	27.624	0.004	0.026	-19.84	-156.67	-	-	-	-	-	-	-
GW-41	Groundwater near D-pit	58.362	109.515	13.789	0.002	0.021	-17.45	-144.66	-	-	-	-	-	-	-
GW MNW	Well north of DJX	58.371	109.549	-	-	-	-	-	60.734	<0.001	<0.001	-18.26	-146.31	-	-
GW 0603	Well upgradient of PRB1	58.377	109.547	-	-	-	-	-	-	-	-	-	-	-19.14	-150.09
PRB 2007	PRB1 surface water	58.377	109.547	-	-	-	-	-	-	-	-	-	-	-19.18	-149.58
GW 0715	Well in PRB1	58.377	109.547	212.387	6.360	0.026	-19.19	-152.58	221.100	4.214	0.026	-19.65	-153.27	-19.46	-152.41
GW 0719	Well between PRBs	58.377	109.548	-	-	-	-	-	-	-	-	-	-	-19.75	-154.23
PRB 2006	PRB2 surface water	58.377	109.548	-	-	-	-	-	-	-	-	-	-	-17.82	-142.06
GW 0605	Well downgradient of PRB2	58.377	109.548	-	-	-	-	-	-	-	-	-	-	-19.19	-149.80
GW 0720	Isolated groundwater well "20"	58.377	109.548	389.114	2.809	0.004	-19.52	-154.59	458.735	0.769	<0.001	-19.73	-155.38	-	-
GW 0723	Isolated groundwater well "23"	58.376	109.551	-	-	-	-19.07	-152.35	-	-	-	-	-	-	-
GW 0724	Isolated groundwater well "24"	58.375	109.550	-	-	-	-	-	-	-	-	-	-	-16.25	-134.58
C Boulder	Boulder Creek	58.361	109.516	8.610	<0.001	<0.001	-16.22	-136.57	10.373	<0.001	<0.001	-15.87	-133.96	-	-
L Cluff	Cluff Lake	58.363	109.549	15.648	0.001	0.003	-16.12	-136.59	14.443	<0.001	<0.001	-15.87	-132.99	-	-
C Cluff	Cluff Creek	58.332	109.600	15.545	0.001	0.001	-16.09	-136.56	13.793	<0.001	<0.001	-15.76	-134.54	-	-
C Peter	Peter River road crossing	58.367	109.540	19.091	0.001	<0.001	-17.17	-142.00	18.164	0.002	0.001	-16.46	-137.87	-	-
C Peter	Peter River	58.364	109.536	19.479	0.001	0.001	-17.01	-141.48	11.493	<0.001	<0.001	-16.74	-138.68	-	-
C Peter	Peter River mouth	58.368	109.539	18.882	0.001	0.001	-17.08	-139.77	16.821	0.001	<0.001	-16.40	-137.84	-	-
C Claude	Claude Creek	58.368	109.540	76.788	0.011	<0.001	-15.93	-135.26	87.517	0.011	<0.001	-17.15	-141.52	-	-
C Earl	Earl Creek road crossing	58.369	109.529	17.254	<0.001	<0.001	-17.50	-144.00	15.501	<0.001	<0.001	-17.57	-142.03	-	-
C Douglas	Douglas River	58.287	109.539	13.365	<0.001	<0.001	-17.59	-144.50	-	-	-	-	-	-	-
Rain1	Rain gauge 1	58.370	109.546	-	-	-	-13.43	-108.29	-	-	-	-	-	-14.10	-108.16
Rain2	Rain gauge 2	58.369	109.528	-	-	-	-12.36	-104.16	-	-	-	-	-	-14.36	-109.73
Rain3	Rain gauge 3	58.529	109.481	-	-	-	-	-	-	-	-	-	-	-14.30	-109.53

Table C.2 Input values for the geochemical model in PHREEQC. The p_e values were calculated based on the redox formula:

$0.25O_2+H^++e^- \leftrightarrow 0.5H_2O$

and a corresponding equation for electron activity:

$p_e = p_e^0 + 1/n * log_{10}([O_2]^{0.25}*[H^+])$

where p_e^0 is equal to 20.75 (Libes, 2011), n is the number of transferred e^- (=1), $[O_2]$ is assumed to be equal to the aqueous O_2 concentration (in mol/L) and $[H^+]$ is the proton concentrations (=10^{-pH}).

Temperature	5.5 °C
pH	4.57 or 9
p_e	14.87, 11.4 or -3
Redox based on	p_e
Units for elements	µmol/kg water
Al	351.6683
As	0.026
Ba	0.1101
Ca	6420.6412
Co	32.172
Cu	1.1553
Fe	117.5493
K	209.7058
Mg	20207.2237
Mn	270.5338
Na	4692.1433
Ni	110.9806
Pb	0.0141
Si	33709.0532
Sr	23.0831
U	3.8484
Zn	15.9159
S	33613.7072

Table C.3 Important OTUs found in peat and mineral soil samples ordered based on abundance in samples 11S (upgradient), 5S (downgradient), and 15S (2007 PRB). All abundance numbers in %. Query coverage of the matches was 100%.

OTU	11S	11M	15S	15	20S	20	5S	5M	24S	24	BLAST match	Identitie	Accession
15	**10.1**	0.15	0.0	0.0	0.5	0.0	0.39	0.0	0.0	0.0	*Uncultured bacterium clone SI-2M_C01*	99%	EF221531.1
2	**9.21**	10.3	0.0	0.0	3.5	4.0	0.05	0.1	0.0	0.0	*Candidatus Nitrotoga sp. KNB*	99%	LS423452.1
11	**5.86**	0.80	0.0	0.0	5.1	0.6	0.08	0.0	0.0	0.0	*Nitrosospira multiformis strain ATCC 25196*	96%	NR_074736.
42	**3.08**	0.00	0.0	0.0	0.0	0.0	0.13	0.0	0.0	0.0	*Steroidobacter denitrificans strain DSM 18526*	94%	CP011971.1
36	**2.58**	0.00	0.0	0.0	0.0	0.0	0.09	0.0	0.0	0.0	*Acidothermus cellulolyticus strain 11B*	98%	NR_074501.
70	**2.05**	0.10	0.0	0.0	0.1	0.0	0.00	0.0	0.0	0.0	*Gemmatimonas phototrophica strain AP64*	92%	CP011454.1
40	**1.60**	0.73	0.0	0.0	0.6	0.8	0.01	1.7	0.0	0.0	*Thermoanaerobaculum aquaticum strain MP-01*	96%	NR_109681.
20	**1.60**	0.11	0.0	0.0	0.1	0.0	0.00	0.0	0.0	0.0	*Ignavibacterium album strain 14rA*	92%	KF528150.1
39	**1.40**	0.01	0.0	0.0	0.0	0.0	0.00	0.0	0.0	0.0	*Candidatus Koribacter versatilis Ellin345*	95%	CP000360.1
30	**1.31**	0.77	0.0	0.0	2.2	0.3	0.13	0.0	0.0	0.0	*Pseudolabrys taiwanensis strain KIS20-7*	98%	EU938323.1
114	**1.24**	0.02	0.0	0.3	0.2	0.0	0.06	0.0	0.1	0.0	*Conexibacter stalactiti strain YC2-25*	95%	NR_157993.
100	**1.21**	0.00	0.0	0.0	0.1	0.0	0.15	0.0	0.0	0.0	*Bryobacter aggregatus strain MOB76*	92%	AM887762.1
48	**1.21**	0.01	0.0	0.0	0.5	0.1	0.48	0.0	0.2	0.0	*Bryobacter aggregatus strain MOB76*	89%	AM887762.1
5	0.01	0.00	0.1	0.0	0.0	0.0	**16.4**	0.0	0.0	0.0	*Arthrobacter pascens strain CRS-46*	100%	MH497219.1
38	0.00	0.01	0.0	0.0	0.5	0.0	**2.42**	0.0	0.0	0.0	*Methylocapsa aurea strain KYG*	97%	NR_116996.
168	0.00	0.00	0.0	0.0	0.0	0.0	**1.80**	0.0	0.0	0.0	*Massilia sp. strain cHCR2ah*	100%	KY302251.1
22	0.00	0.00	0.1	0.0	2.1	0.0	**1.65**	0.0	0.2	0.0	*Bacterium MI-40 (Rhizobiales, MNG7)*	97%	AB529706.1
118	0.00	0.00	0.0	0.0	0.1	0.0	**1.49**	0.0	0.0	0.0	*Woodsholea maritima*	91%	FM886859.2
31	0.00	0.00	0.0	0.0	5.5	0.0	**1.43**	0.0	0.0	0.0	*Terrimonas rhizosphaerae strain CR94*	98%	NR_156069.
112	0.00	0.00	0.0	0.0	0.1	0.0	**1.36**	0.0	0.0	0.0	*Chryseolinea serpens strain RYG*	94%	NR_108511.
123	0.00	0.00	0.0	0.0	0.1	0.0	**1.35**	0.0	0.0	0.0	*Rhizomicrobium electricum strain Mfc52*	91%	NR_108115.
17	0.00	0.00	**3.6**	2.6	0.0	0.1	0.00	0.0	0.0	0.0	*Geosporobacter ferrireducens strain IRF9*	96%	NR_148302.
10	0.00	0.00	**3.5**	1.7	0.0	3.2	0.00	0.0	0.0	0.0	*Proteiniclasticum ruminis strain D3RC-2*	99%	NR_115875.
23	0.00	0.00	**2.8**	0.7	0.0	0.3	0.00	0.0	0.0	0.0	*Desulfatirhabdium butyrativorans strain HB1*	95%	NR_043578.
14	0.00	0.00	**2.7**	2.8	0.0	1.5	0.00	0.0	0.0	0.0	*Geofilum rubicundum strain JAM-BA0501*	100%	NR_112717.
66	0.00	0.00	**2.0**	0.0	0.0	0.0	0.00	0.0	0.0	0.0	*Alkalibacterium sp. strain MB6*	100%	MG654646.1
51	0.00	0.00	**1.9**	0.6	0.0	0.0	0.00	0.0	0.0	0.0	*Chitinispirillum alkaliphilum strain 4S-PA-ChS2*	97%	MG264252.1
91	0.00	0.00	**1.9**	0.1	0.0	0.0	0.01	0.0	0.0	0.0	*Hydrogenophaga atypica strain M10*	100%	KT345668.1
47	0.00	0.00	**1.9**	0.3	0.0	0.9	0.00	0.0	0.0	0.0	*Desulfomicrobium baculatum strain HAQ-8*	100%	KF536747.1
46	0.00	0.00	**1.7**	1.2	0.0	0.0	0.00	0.0	0.0	0.0	*Erysipelothrix rhusiopathiae*	94%	AB055909.1
92	0.00	0.00	**1.6**	0.1	0.0	0.0	0.00	0.0	0.0	0.0	*Erysipelothrix sp. CE10*	99%	KX156786.1
68	0.00	0.00	**1.6**	1.3	0.0	0.4	0.00	0.1	0.0	0.0	*Draconibacterium orientale strain FH5*	90%	NR_121783.
339	0.00	0.00	**1.5**	0.2	0.0	0.0	0.00	0.0	0.0	0.0	*Youngiibacter multivorans*	98%	AB910755.1
99	0.00	0.00	**1.4**	0.5	0.0	0.0	0.00	0.0	0.0	0.0	*Caldicoprobacter sp. clone S1_A3*	97%	KX672185.1

Table C.4 Examples of OTUs with a similarity to potential U(VI) reducing bacteria. All summed abundance numbers in %.

OTUs	11S	11M	15S	15M	20S	20M	5S	5M	24S	24M	Taxonomy
57	0.0125	0.0430	0.0030	0.0511	0.0065	0.0506	0.0000	0.0605	0.0246	0.1193	*Clostridium-sensu-stricto-9*
58	0.0214	0.0095	0.1501	0.0070	0.1287	0.0405	0.0000	0.0000	0.0985	0.0070	*Geobacter*
3628	0.0000	0.0019	0.0007	0.0023	0.0000	0.0051	0.0000	0.0130	0.0000	0.0000	*Shewanella*
2234, 515, 2219, 3437, 8944	0.0000	0.0000	0.0007	0.3090	0.0130	0.0152	0.0000	0.0000	0.0457	0.0047	*Desulfovibrio*
338, 53, 8224, 8080, 9422	0.0727	0.0300	0.5495	0.9944	0.0400	1.1409	0.0000	0.0322	0.0000	0.0000	*Desulfosporosinus*

Figures

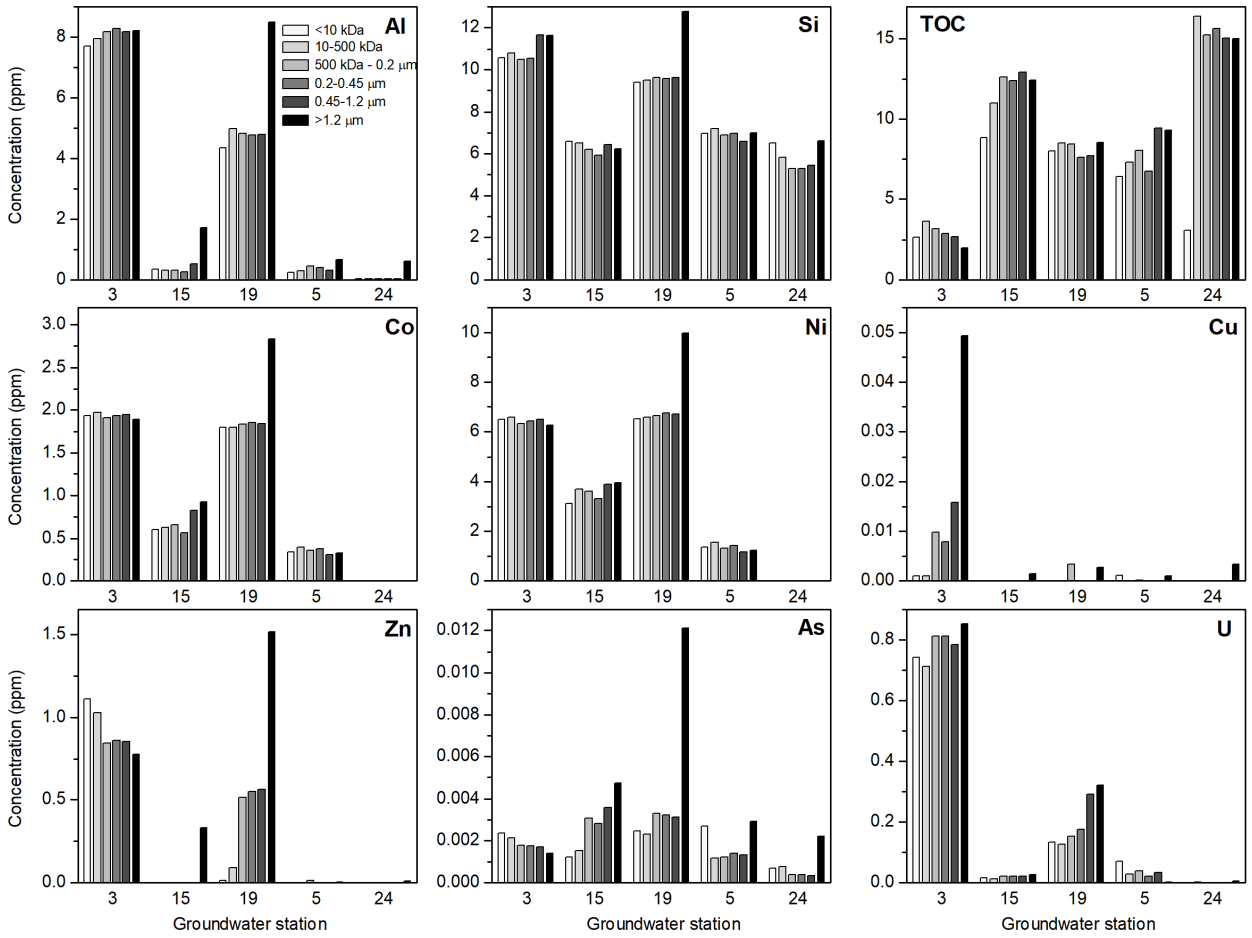

Figure C.1 Sequential filtration results for selected groundwater wells.

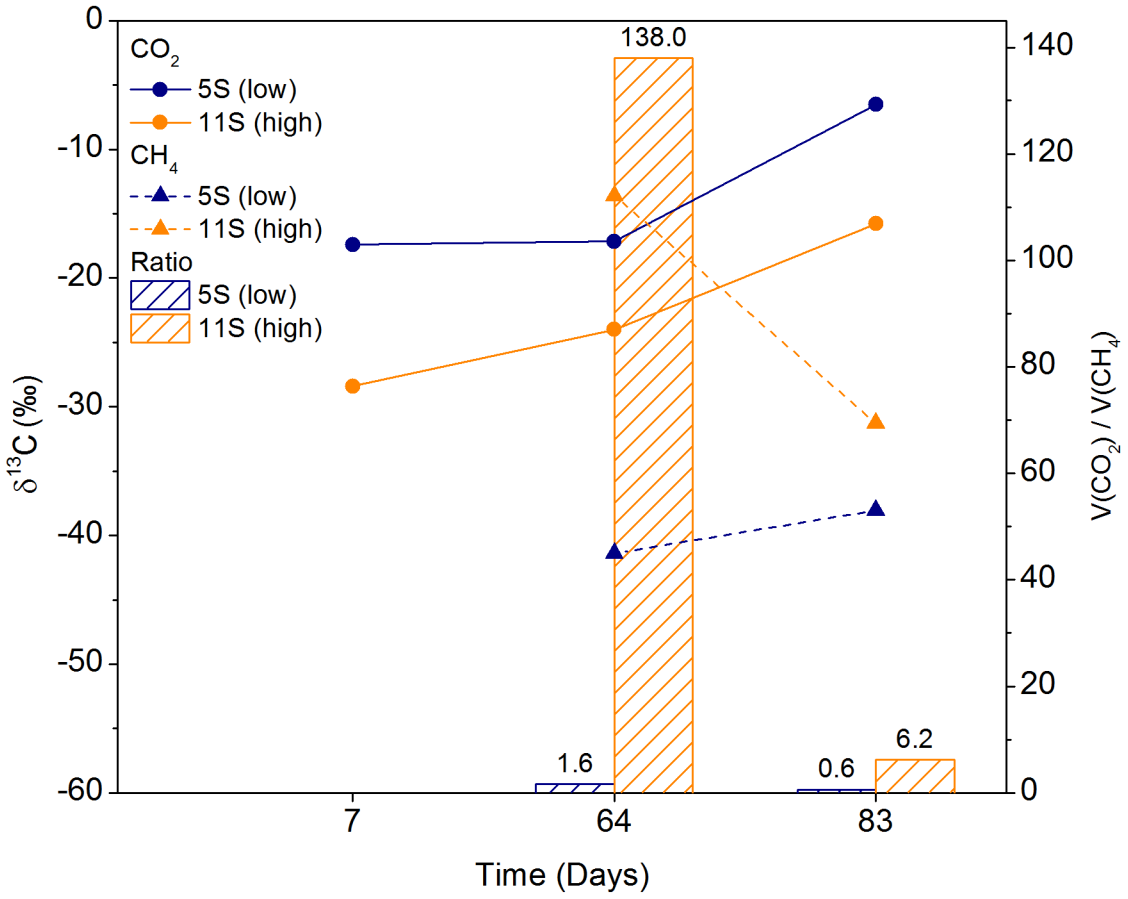

Figure C.2 $\delta^{13}C$ PDB of CO_2 and CH_4 and their peak volume ratios (see details below).

To monitor microbial changes that might have been induced due to increased transition metal inflow and to investigate how this might impact methanogens and methanotrophs, batch experiments were set up using sterile 150 mL serum bottles in duplicates. Peat form the location 5S (downgradient of PRBs) was used as a low contamination sample ("low"), whereby peat from the location 11S (upgradient of PRBs) was used as a high contamination sample ("high"). Each serum bottles was filled with 15 g wet peat (equal to 2.6 g of dry peat) and 40 mL of ultrapure water before sealing. The headspace was then flushed with Ar gas for 30 min. The bottles were then left in a dark place at room temperature. Carbon isotope analysis was performed on days 7, 64, and 83 on one replicate of each sample using an Agilent 6890 gas chromatograph. 100-2000 µL of headspace gas were injected. The $\delta^{13}C$ PDB of CO_2 and CH_4 and the peak volume ratios (signal CO_2 [Vs] / signal CH_4 [Vs]) were recorded. 66 days after incubation peat was extracted from the other replicates using sterile spatulas and the samples were used for 16S-rRNA gene sequencing as described in the main text. The abundance of potential methanogens and methanotrophs was quickly assessed by a search for taxa known for methanogenesis and methanotrophy. This showed that methanogens made about 2.90% and 0.29% of the 5S (low) and the 11S (high) communities, respectively, while methanotrophs made only 0.15% and 0.14% (data not shown).